Felsic metastability during continental subduction: The Norwegian Western Gneiss Complex as a case study

Thesis submitted in accordance with the requirements of the University of Adelaide for an Honours Degree in Geology

Teagan Laryssa Romyn

July 2020

THE UNIVERSITY of ADELAIDE

FELSIC METASTABILITY DURING CONTINENTAL SUBDUCTION: THE NORWEGIAN WESTERN GNEISS COMPLEX AS A CASE STUDY

METASTABILITY DURING CONTINENTAL SUBDUCTION

ABSTRACT

Ultra-high pressure (UHP) metamorphic terranes are thought to record the Earth's secular thermal evolution in their mineral assemblages. These mineral assemblages change from amphibolite-facies to eclogite-facies with increasing pressure during subduction. Mafic eclogite-facies rocks within UHP metamorphic terranes such as the Western Gneiss Complex (WGC), Norway, record deep burial and subsequent exhumation. Felsic orthogneisses encasing these mafic rocks are subjected to the same conditions but typically do not record UHP metamorphism. To date, it remains debated whether the felsic orthogneisses do not record UHP metamorphism because they remain metastable at eclogite-facies conditions. LA-ICP-MS ages of 416 ± 18 Ma and 399.8 ± 7.8 Ma, obtained from rutile grains within two mafic eclogites near Lavik, Norway, suggest this region underwent eclogite-facies metamorphism during the Caledonian Orogeny (~430–385 Ma). Mineral equilibria forward modelling shows garnet-bearing felsic gneiss in the study area did not record pressure-temperature (*P–T*) conditions exceeding ~8–9 kbar, ~650 °C. By comparison, nearby high strain mafic eclogite recorded peak metamorphic conditions of ~20–22 kbar, ~650 °C. Major element zonation patterns in garnet >600 μm from high strain mafic eclogite indicate peak metamorphism persisted for between ~10–20 Myr. A lack of high-pressure mineral phases in felsic orthogneisses imply they remained metastable in the WGC for at least this time period. The anhydrous nature (H_2O = 0.34 wt%) of the modelled gneiss may explain this metastability during the Caledonian Orogeny, as fluid is necessary to catalyse many metamorphic reactions. A lack of fluid would thus inhibit anhydrous felsic orthogneisses within the WGC from reacting beyond amphibolite facies. This metastability would inhibit the felsic orthogneiss from recording peak *P–T* conditions as hydrous mafic eclogites do. This kinetic inhibition implies anhydrous felsic orthogneisses within the WGC – and, possibly, other UHP metamorphic terranes – make poor recorders of UHP metamorphism.

KEYWORDS

Metastability, eclogite, UHP metamorphism, felsic gneiss

TABLE OF CONTENTS

LIST OF FIGURES AND TABLES

INTRODUCTION

Metamorphic rocks form the basis of critical datasets revealing deep Earth conditions. These rocks are subjected to pressure-temperature (*P–T*) variations as they cycle through tectonic and geodynamic processes over geological timescales. Therefore, *P–T* records – as stored in metamorphic mineral assemblages – retrieved from such rocks provide information about the evolution of deep Earth processes. The assumption that metamorphosed felsic and mafic rocks are equally competent in recording their *P–T* evolution is called into question in multiple UHP metamorphic terranes, including the Norwegian Western Gneiss Complex (WGC; Massonne, Willner & Gerya, 2007; Peterman, Hacker & Baxter, 2010; Proyer, 2003; Wain, Waters & Olijynk, 2000; Young & Kylander-Clark, 2015). In these terranes, the presence of UHP assemblages in the volumetrically minor (~2%; Hacker et al., 2010) mafic eclogites casts doubt on the reliability of adjacent felsic amphibolites as effective geodynamic indicators (Proyer, 2003). Though some rare UHP felsic gneisses do exist, most felsic rocks in these terranes typically do not record deep burial and exhumation (Hacker et al. 2010; Peterman et al., 2010; Proyer, 2003; Wain et al., 2000). Nonetheless it is assumed many metamorphic rocks reveal (a) the secular thermal evolution of the Earth and (b) rock behaviour in tectonic systems because their mineral assemblages change as a function of *P–T*.

The differing responses of mafic and felsic lithologies to subduction processes is problematic. Such variance implies large portions of the Earth's crust do not respond to changing *P–T* during subduction (Massonne et al., 2007; Peterman et al., 2010; Wain et

al., 2000). Consequently, the full extent of a region's metamorphic complexity remains uncaptured in the rock record, confusing attempts to understand the deep Earth processes such rocks supposedly record (Wain, 1997). The assumption that all metamorphic rocks are accurate tools for understanding the Earth's thermal and secular evolution may therefore be unrealistic, casting doubt upon numerous geological studies.

The WGC (Figure 1) is an extensively studied UHP metamorphic terrane (Cuthbert, Carswell, Krogh-Ravna & Wain, 2000; Griffin & Brueckner, 1985; Milnes, Wennberg, Skår & Koestler, 1997) which has undergone three orogenic events (Skår & Pedersen, 2003). The first two orogenies metamorphosed the bulk felsic gneiss to amphibolite facies, while a minor eclogite facies portion (garnet–clinopyroxene–phengite–rutile–coesite) indicates burial of >125 km during the Caledonian Orogeny ~430–385 Ma (Gaál & Gorbatschev, 1987; Hacker et al., 2003, 2010; Kullerud, Torudbakken & Ilebekk, 1986; Skår & Pedersen, 2003; Walsh & Hacker, 2004). The felsic rocks record little to no evidence of subduction processes and are typically dismissed by most studies (Cuthbert et al., 2000; Griffin & Brueckner, 1985; Wain et al., 2000).

Several mechanisms have been presented to explain low felsic gneiss reactivity in the WGC (Hacker et al., 2003; Proyer, 2003; Wain, Waters & Austrheim, 2001; Walsh & Hacker, 2004; Young & Kylander-Clark, 2015). Rare felsic eclogite in the northern WGC is typically associated with shear zones – concentrated areas of deformation and fluid flow (Wain et al., 2000, 2001). The low reactivity of most felsic orthogneiss within the WGC has been previously explained by lack of fluid (e.g. Proyer, 2003; Young & Kylander-Clark, 2015). Fluid acts as a reactant, catalyst or transport vector

within metamorphic reactions (Austrheim & Griffin, 1985; Proyer, 2003; Rubie, 1983; Wain et al., 2001). An absence of fluid has been shown to contribute to reaction overstepping (where unfavourable reaction kinetics stall metamorphic reactions) between 5 and 13 kbar in the Flatraket Complex, Nordfjord (Figure 1; Proyer, 2003; Wain et al., 2001; Young & Kylander-Clark, 2015). A lack of fluid availability may contribute to the inability of felsic gneiss in the WGC to react beyond amphibolite-facies conditions during prograde metamorphism (Wain et al., 2001; Young & Kylander-Clark, 2015). The absence of fluid offers a plausible explanation for the paucity of UHP mineral assemblages observed in anhydrous felsic rocks from the WGC and other UHP metamorphic terranes (e.g. the Dabie-Sulu terrane; Wain et al., 2000, 2001; Young & Kylander-Clark, 2015).

The complexity of the WGC makes it an ideal location to further understand the conflicting metamorphic responses of differing lithologies to subduction processes. This study will focus on the little-studied Sognefjord region, which contains mafic eclogite facies assemblages (~20–22 kbar, 650–700 °C) and limited metamorphic reworking (Cuthbert et al., 2000; Skår & Pedersen, 2003; Wain et al., 2001; Young & Kylander-Clark, 2015).

The aims of this study are to:

1. Construct a geological face map of a spatially restricted area to establish the relationships between mafic eclogites and their felsic amphibolite host rocks.

2. Use mineral equilibria forward modelling to compare the *P–T* evolution recorded by mafic eclogites and felsic amphibolites.

The geological face map will act as a framework to understand the pressure evolution recorded by these differing lithologies. Understanding how different lithologies in the Sognefjord (Figures 1, 2) reacted to changing *P–T* conditions will provide insight into their reliability as metamorphic indicators. This, ultimately, has implications for how similar rocks in other UHP metamorphic terranes might respond to *P–T* changes, possibly indicating whether they also (a) remain metastable (and thus make unreliable geodynamic indicators) or (b) experience retrograde recrystallisation.

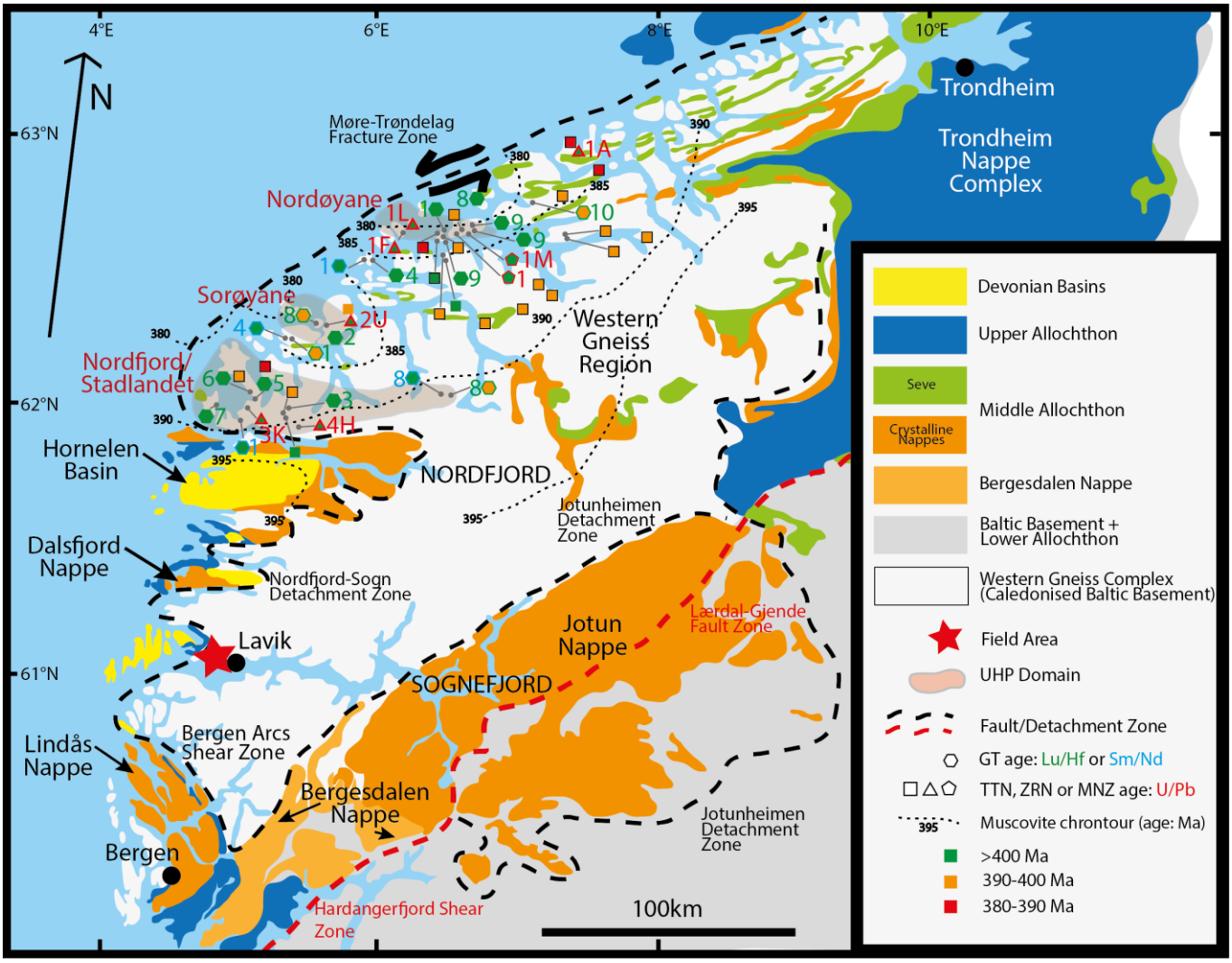

Figure 1: Geological and thermochronological map of the Western Gneiss Complex. The field area near Lavik is indicated by a red star. The extensively studied UHP domains (Nordøyane, Sorøyane and Nordfjord/Stadlandet) are located much further north. Image modified from Brueckner and Cuthbert (2013). Red dashed lines are UHP domains bounded by the ~ 2.8GPa quartz-coesite transition (Garber, Hacker, Kylander-Clark, Stearns and Seward, 2017; Root et al., 2005). Major autochthonous and allochthonous units, basins, major nappes, and fault/detachment zones are shown (refer to key). Note colours (dashed red and black lines) for different shear zones serve only to differentiate them. White mica chrontours are from Walsh, Hacker, Gans, Wong & Andersen (2013); titanite data (squares; solid black boundary = gneiss, no boundary = leucosome) are from Garber et al., (2017). All zircon, monazite and garnet ages are from eclogites. Zircon (triangles - U-Pb), monazite (pentagons - U-Pb) and garnet (hexagons - Lu/Hf or Sm/Nd) data are sourced from various studies indicated by superscript (Brueckner & Cuthbert, 2013). These studies are: Sm/Nd: (1) Mørk and Mearns (1986); (2) Jamtveit, Carswell & Mearns (1991); (3) Mearns (1986); (4) Kylander-Clark et al. (2007); (5) Carswell, Brueckner, Cuthbert, Mehta and O'Brien (2003); (6) Kylander Clark and Hacker (2014); (7) Griffin and Brueckner (1980); (8) Kylander-Clark et al. (2009); (9) Spengler, Brueckner, van Roermund, Drury and Mason (2009) and (10) Vrijmoed, van Roermund and Davies (2006). U/Pb zircon superscripts refer to locations (letter identification) and studies (number identification). 1A = Averøya; 1F = Flemsøya; 1H = Hjelmelandsdalen; 1K = Flatraket; 1L = Lepsøya; 1M = Midsund Bruk; 1U = Ulsteinvik. (1) Krogh, Kamo, Robinson, Terry and Kwok (2011); (2) Carswell, Tucker, O'Brien and Krogh (2003); (3) Root, Hacker, Mattinson and Wooden (2004) and (4) Young, Hacker, Andersen and Corfu (2007). U/Pb monazite ages are from (1) Terry, Robinson, Hamilton and Jercinovic (2000). Barring titanite, for all shapes, rim indicates isotope system (green = Lu/Hf, blue = Sm/Nd, red = U/Pb). For all data points the inner shape colour indicates age (green = >400 Ma, orange = 390–400 Ma, red = 380–390 Ma).

BACKGROUND

The WGC, southwest Norway, underwent three major orogenic events (Cuthbert et al., 2000; Hacker et al., 2003; Skår & Pedersen 2003; Wain et al., 2000; Young 2018). The Gothian Orogeny ca. 1660–1520 Ma metamorphosed the bulk regional protolith (dioritic/granitic migmatitic orthogneisses; Gaál & Gorbatschev, 1987; Kullerud et al., 1986; Skår, 2000; Skår & Pedersen, 2003). Mafic dykes and plutons intruded the Gothian orthogneisses ca. 1250–900 Ma during the granulite-facies (10 kbar, 900℃) Sveconorwegian Orogeny (Hacker et al., 2010). The Sveconorwegian Orogeny produced the NW-SE regional foliation (Hacker et al., 2010; Kylander-Clark, Hacker & Mattinson, 2008; Skår & Pedersen, 2003) while simultaneously reworking and dehydrating Gothian protolith (Krabbendam & Wain, 1997; Skår & Pedersen, 2003). The northern WGC has been the subject of numerous studies (e.g. Braathen & Erambert, 2014; Cuthbert et al., 2000; Garber et al., 2017; Hacker et al., 2003, 2010; Root et al., 2005; Walsh & Hacker 2004; Young et al., 2011) due to its structural and mineralogical complexities. The study area is located near Lavik, Sognefjord, approximately 100 km south of the Nordfjord/Stadlandet UHP domain (Figures 1, 2). Here, elongate granodioritic-dioritic felsic orthogneiss belts, which constitute ~95% of the bulk terrane and are parallel to Sveconorwegian foliation (Skår, 2000; Skår & Pedersen, 2003), display no evidence of deep burial. Approximately 2% of the area consists of lensoid, mafic, eclogitic boudins forming gneiss-parallel fabrics. The surrounding amphibolitic gneisses occasionally display preferential migmatisation (Skår & Pedersen, 2003). Eclogite-facies minerals are restricted to mafic boudins and adjacent felsic rocks (Hacker et al., 2010; Wain et al., 2000).

WGC: *P–T* Conditions and Exhumation

The collision of Baltica and Laurentia caused the Caledonian Orogeny, which involved (i) Iapetus Ocean closure (~430–410 Ma); (ii) UHP westward-directed Baltican subduction (~425–400 Ma); and (iii) lower-crustal level exhumation (~400–385 Ma) (Chauvet, Kienast, Pinardon & Brunel, 1992; Hacker et al., 2003, 2010). Exhumation dates vary from ~400–385 Ma (Zircon U-Pb; Chauvet et al., 1992; Garber et al., 2017; Hacker et al., 2010; Walsh & Hacker, 2004) to complete exhumation by ~400 Ma (Muscovite Ar closure; Chauvet & Dallmeyer, 1992; Hacker et al., 2003). Nordfjord eclogites have been dated at 381–423 Ma (direct HP mineral (Sm-Nd, Lu-Hf) and U-Pb zircon dating; Kylander-Clark & Hacker, 2014). The Northern WGC records early Caledonian *P–T* conditions of 12 kbar, 725 ℃, with the later UHP phase recording 18–36 kbar, 600–750 ℃ (Hacker et al., 2010). Limited *P–T* estimates from eclogites near the study area constrain peak conditions of 22.1 ± 2.2 kbar, 687 ± 77 ℃, and 24.7 ± 2.4 kbar, 718 ± 83°C (Chauvet et al., 1992; Hacker et al., 2003; Wiest et al., 2019).

Study Area: The Eclogite Outcrop

‘The Eclogite Outcrop’ contains felsic and mafic rocks. Amphibolite-facies and eclogite-facies mineral assemblages are present. It is located near Lavik, the Sognefjord, grid coordinates 32V 308364 6776922 (WGC2019J-16J location; Figure 2). Mafic lithologies include eclogitised or partially retrogressed dykes. Mapped diatexitic fabrics extend into deformational fabrics of a scale 100m+, outside the study scope (Figure 3a).

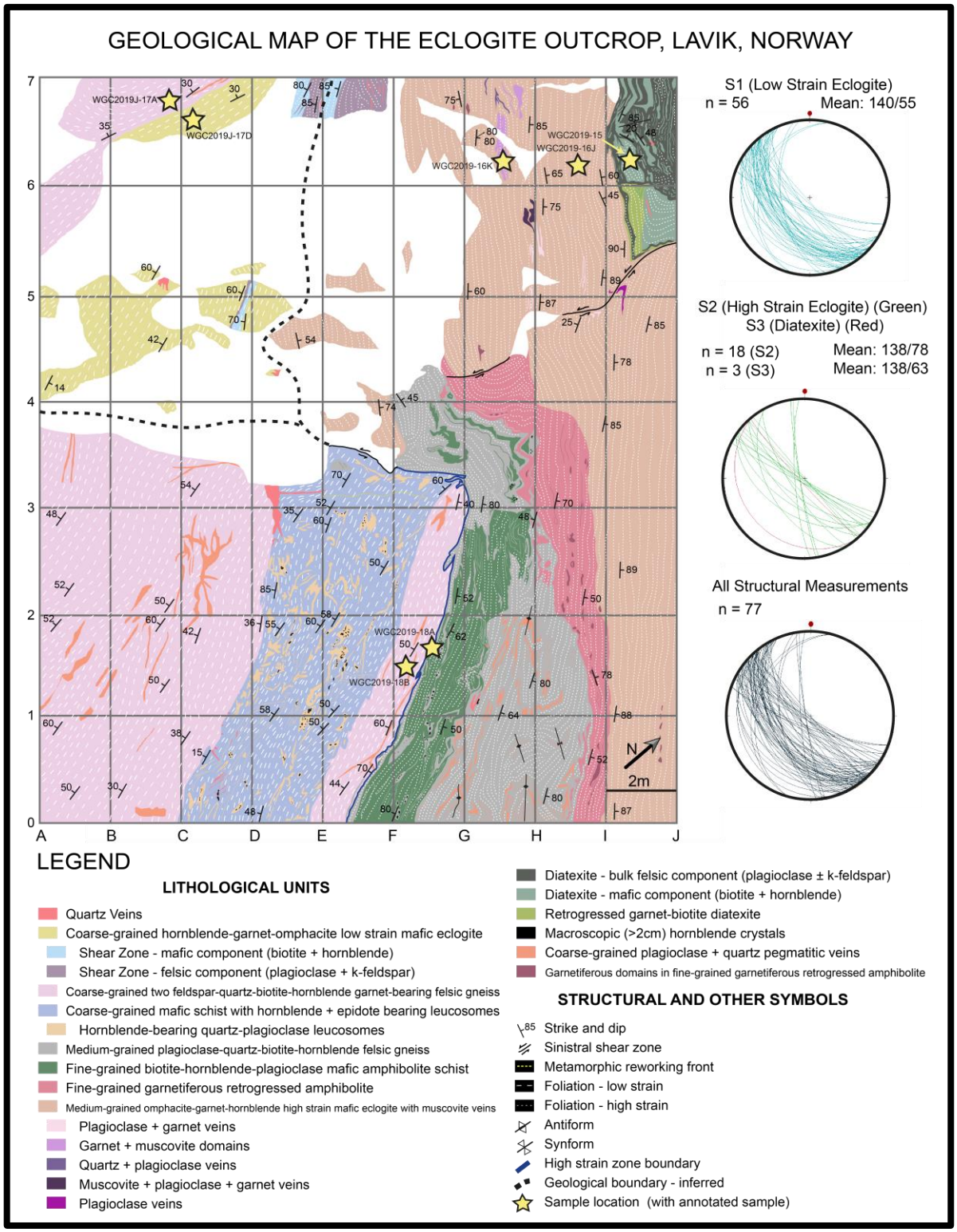

Figure 2: Face map of 'the Eclogite Outcrop', Lavik, Sognefjord, Norway. Inset stereonets illustrate outcrop foliations. Yellow stars refer to collected sample locations, two of which (WGC2019J-16J - high strain eclogite, and WGC2019J-17A – garnet-bearing felsic gneiss) were subject to mineral equilibria modelling. White areas are unmapped. Grid spacing between adjacent letters (horizontal) is 2m; between adjacent numbers (vertical) is 3m. Note that in text, samples are referred to by major distinguishing features only (e.g. 'high strain eclogite' rather than 'medium-grained omphacite–garnet–hornblende high strain mafic eclogite with muscovite veins'). Refer to legend for lithological units and structural, other features. Two feldspar = plagioclase and k-feldspar.

Structural data reveals four deformational fabrics in the area. S1/D1 is defined by a NNW-SSE striking foliation (mean: 140/55) consisting of both coarse-grained two feldspar–quartz–biotite–hornblende–garnet felsic gneiss (defined by biotite and pegmatitic veins up to ~2 m in length) and low strain mafic eclogite. Low strain mafic eclogite is defined by garnet–biotite–hornblende in thin section; in the field, low-intensity biotite foliation overprints eclogite-facies garnet–clinopyroxene±phengite coronae. The medium-grained plagioclase–quartz–biotite–hornblende gneiss next to the mafic lithology did not transform to eclogite-facies. The mafic unit contains coarse-grained hornblende-rich (2-4 cm) quartz–plagioclase leucosomes (Figures 3b, c). A quartz fracture set also crosscuts the foliation. The S1/D1 foliation is generally parallel to lithological boundaries (grids A7-B7-B6-A6; Figure 2). A shear zone of variable width (0.2-3 m) separates S1/D1 and S2/D2 in grids E7-G7-G6-E6 (Figure 2).

Garnet-bearing domains were more numerous in retrogressed amphibolite adjacent to high strain eclogite (Figure 3d). S2/D2 foliation in high strain eclogite is NW-SE trending and typically NE dipping (grids G7-I7-I5-G5; Figure 2). S2/D2 lineation was obvious in high strain eclogite (L_x = 80 → NW), which contained foliation-parallel macroscopic garnet crystals ≥ 1 cm in diameter mantled by omphacite and amphibole (Figure 3e). Interference between S2/D2 and S4/D4, where the latter extends into shear zones several km wide (Milnes et al., 1997), causes a dip change from SW/W to E from gridlines A to J (Stereonet 2, Figure 2, records both S2/D2 and S4/D4 foliations in green). The meter-scale S2/D2 eclogite-facies (garnet–clinopyroxene–phengite–rutile–quartz rich veins) shear zones are overprinted by tightly folded S3/D3 diatexitic fabrics (grids I7-J7-J6-I6; Figures 2, 3a). The S4/D4 structural fabric is recorded in both felsic

and mafic lithologies, overprinting S2/D2 and S3/D3. The felsic rocks do not record eclogite-facies mineral assemblages. D4/S4 overprinting produces sparse garnet coronae around pre-Caledonian biotite, or as small matrix grains, within the felsic orthogneiss. This overprinting converts mafic units into biotite–hornblende–plagioclase amphibolite schists. Appendix 1 holds field descriptions and sample list. Appendix 2 holds the list of all mapped data points.

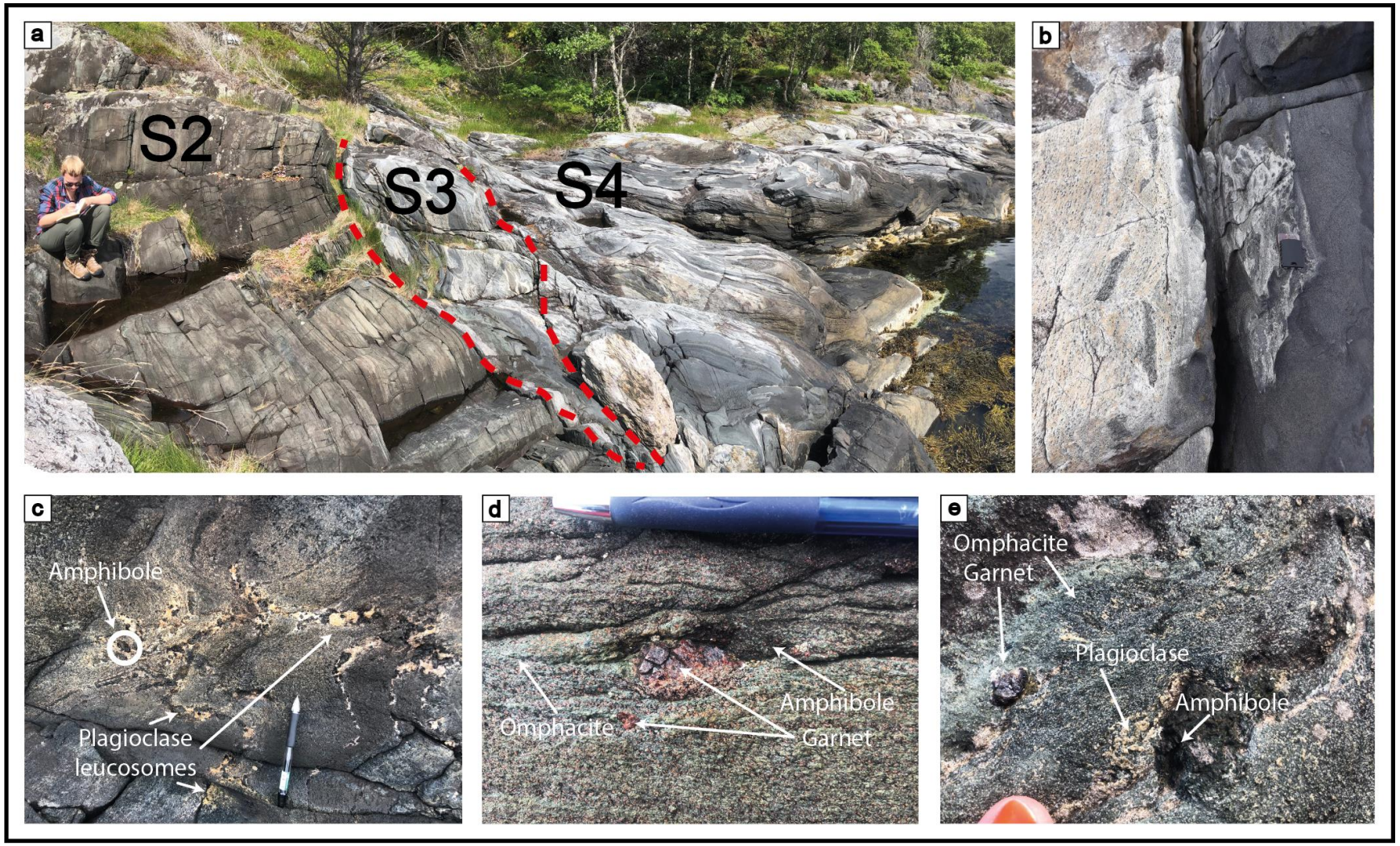

Figure 3: Field photos of the eclogite outcrop. (a) Observed foliations (S2, S3, S4) near outcrop. Note that S4 extends outside map boundary beyond grids 6I-7I-7J-6J. (b) Medium-grained plagioclase–quartz–biotite–hornblende gneiss and fine-grained biotite–hornblende–plagioclase mafic schist. Compass-clinometer for scale. (c) Coarse, hornblende-bearing leucosomes in mafic amphibolite. (d) Garnet-bearing domains in retrogressed amphibolite directly adjacent to high strain eclogite WGC2019J-16J. (e) Omphacite, garnet and amphibole in high strain eclogite WGC2019J-16J; fingertip for scale. Photos courtesy of author, Tamblyn, R.J. and Hand, M.

Felsic Gneiss Reactivity in the WGC

Eclogite-facies mineral assemblages are rare but present in the northern WGC within the Nordøyane, Sorøyane and Nordfjord/Stadlandet UHP domains (Figure 1; Engvik, Austrheim & Andersen, 2000; Krabbendam & Wain, 1997; Krabbendam, Wain & Andersen, 2000; Wain, 1997; Wain et al., 2001; Young & Kylander-Clark, 2015). On the Nordfjord (Figure 1), calcic plagioclase persists up to 22 kbar before anhydrous breakdown to grossular garnet, kyanite and quartz occurs (Wain et al., 2001). A greater calcium content within the bulk rock composition helps form additional HP phases (e.g. garnet) and stabilises net-transfer reactions which alter muscovite composition (Proyer, 2003; Young & Kylander-Clark, 2015).

The prograde net-transfer reactions of felsic gneisses undergoing UHP metamorphism are well constrained from field observations and thermobarometric experiments, and include: (i) muscovite and garnet after biotite and plagioclase (Ghent & Stout, 1981), (ii) garnet/zoisite, kyanite and quartz after (calcic) plagioclase (Goldsmith, 1982) and (iii) jadeite and quartz after (sodic) plagioclase (Goldsmith, 1982; Holland, 1980; Wain et al., 2001).

In the WGC, net-transfer reactions produce distinct (though rare) eclogite-facies mineral assemblages in felsic orthogneiss. Felsic eclogites recorded in the Stadlandet UHP domain (Figure 1) contain omphacite–garnet–quartz–rutile–clinozoisite–

zoisite±kyanite±phengite±coesite (Krabbendam & Wain, 1997; Wain, 1997; Wain et al., 2001; Young & Kylander-Clark, 2015), with some containing quartz–kyanite±grossular±zoisite pseudomorphs after plagioclase (Wain et al., 2001). In garnet, amphibole, paragonite, epidote and quartz inclusions (Krogh, 1982; Wain, 1997) record prograde amphibolite-facies metamorphism. Peak eclogite-facies conditions are shown by rim omphacite and quartz inclusions (Krogh, 1982; Wain, 1997). The presence of albitic plagioclase and high-Si muscovite, plus low modal abundance of biotite, plagioclase and k-feldspar, are other indicators of eclogite-facies metamorphism in felsic WGC lithologies (Wain, 1997; Wain et al., 2001; Young & Kylander-Clark, 2015). The Dabie-Sulu, another highly studied UHP terrane, is often compared to the WGC (Ernst, 1999; Massonne, 2009). There, experimental mineral equilibria modelling of felsic rocks in the NCKFMASH system indicates that for a prograde path typical of a continental subduction environment (as in the WGC), hydrous reactions across 21–37 kbar, 500–650 °C consume grossular garnet (Massonne, 2009). However, in anhydrous reactions, garnet mode increases (Massonne, 2009).

Previous studies have highlighted the role water plays as a reactant, catalyst and transport vector during prograde (Proyer, 2003; Rubie, 1983) and retrograde (Martin & Duchêne 2015) metamorphism. Protolith dehydration prior to UHP metamorphism, as occurs within the WGC, would preferentially preserve HP rather than UHP mineral assemblages during eclogite-facies metamorphism (Liu, Jahn, Long, Li & Oberhänsli, 2003; Massonne, 2009; Proyer, 2003; Young & Kylander-Clark, 2015). Two observations support the proposition that UHP mineral assemblages in the WGC form more readily when water is available to facilitate metamorphic reactions. These two

observations are: (i) the association of rare felsic eclogites with hydrous mafic boudins or shear zones (Krabbendam & Wain, 2000; Skår & Pedersen, 2003; Wain, 1997; Wain et al., 2000, 2001), and (ii) the pervasive amphibolite-facies assemblages preserved by most felsic gneisses (including in the study area; Krabbendam et al., 2000; Krabbendam & Wain, 2000; Skår & Pedersen, 2003; Wain, 1997; Wain et al., 2000, 2001; Young & Kylander-Clark, 2015).

METHODS

Whole-rock geochemistry

WGC2019J-16J (high strain eclogite), WGC2019J-17A (garnet-bearing felsic gneiss), WGC2019J-17D (low strain eclogite) and WGC2019J-18A (felsic gneiss) were sent to Bureau Veritas, Adelaide, for whole rock geochemical analysis. Appendix 3 contains geochemical assays and extended methods.

Electron Probe Micro Analyses (EPMA)

The CAMECA SXFive Electron Microprobe at Adelaide Microscopy was used with a 20 nA beam current, 15 kV accelerating voltage and 5 µm spot size for quantitative mineral compositional analysis of WGC2019J-16J, WGC2019J-17D, WGC2019J-18A, WGC2019J-18B (pristine felsic gneiss) and WGC2019J-17A. Qualitative x-ray compositional maps for garnet were undertaken using a 300 nA beam current, 20 kv accelerating voltage and 1 µm step size for WGC2019J-16J. The three garnets selected

for analysis were: (a) ~900 µm, inclusion-rich, foliation-aligned; (b) ~700 µm, inclusion-poor, foliation-unaligned; and (c) ~600 µm, foliation-aligned garnet with amphibole inclusions. Appendix 4a contains extended methods, Appendix 4b representative analyses, Appendix 5a <600 µm garnet traverse backscatter images and Appendix 5b supplementary x-ray compositional maps.

Trace element LA–ICP–MS: Zircon and Rutile

Laser Ablation-Inductively Coupled Plasma-Mass Spectrometry (LA-ICP-MS) using a RESOlution LR 193nm Excimer laser system with a coupled Agilent 7700s ICP-MS at Adelaide Microscopy was used to acquire zircon full trace element data from WGC2019-15 (diatexite), WGC2019J-16J and WGC2019-17D. Rutile trace element data was acquired for WGC2019J-16J and WGC2019J-17D. Iolite 3.6 (Hellstrom, Paton, Woodhead & Hergt, 2008; Paton, Hellstrom, Woodhead & Hergt, 2011) was employed for data processing. Appendix 6a contains extended methods, Appendix 6b contains zircon trace element data, Appendix 6c zircon trace element graphs and Appendix 7 rutile trace element data.

U–Pb LA–ICP–MS Geochronology: Zircon and Rutile

LA-ICP-MS with a RESOlution LR 193nm Excimer laser system and coupled Agilent 7700s ICP-MS at Adelaide Microscopy was used to acquire zircon U-Pb isotopic data from WGC2019J-15, WGC2019J-16J and WGC2019-17D. Poured (WGC2019J-15) and picked (WGC2019J-16J, WGC2019J-17D) mounted zircon grains were analysed. Rutile U-Pb isotopic data was collected for WGC2019J-16J (mounts and thin section in-

situ analysis) and WGC2019J-17D (mounts). The methods of Payne, Hand, Barovich and Wade (2008) were followed. Iolite 3.6 software was used for data processing and reduction (Hellstrom et al., 2008; Paton et al., 2011). Appendix 7 contains processed rutile U-Pb age data. Appendix 8a expands on sample preparation and analytical procedures. Appendix 8b contains zircon U-Pb age data.

Mineral Equilibria Forward Modelling

THERMOCALC v.3.40 (WGC2019J-17A) and v.3.45 (WGC2019J-16J) were used to calculate *P–T* and pressure-composition (*P–X*) pseudosections (mineral equilibria forward models). The most recent *a–x* (activity-composition) solid solution mineral models were utilised (Diener & Powell, 2012; Green et al., 2016; Holland & Powell, 2003, 2011; White, Powell & Johnson, 2014; White, Powell, Holland, Johnson & Green 2014; White, Powell, Holland & Worley, 2000) along with the internally consistent thermodynamic dataset ds62 (Green et al. 2016; Holland & Powell 2011). Fe^{3+} in iron-bearing phases was calculated using stoichiometric charge balancing via the AX62 program (Droop, 1987; Holland, Green & Powell 2018; Holland & Powell, 1990, 1998; Jennings & Holland, 2015).

WGC2019J-16J was modelled in the MnNCFMASHTO ($MnO–Na_2O–CaO–FeO–MgO–Al_2O_3–SiO_2– H_2O–TiO_2–O_2$) system. WGC2019J-17A was modelled in the NCKFMASHTO ($Na_2O–CaO–K_2O–FeO–MgO–Al_2O_3–SiO_2– H_2O–TiO_2–O_2$) system.

Apatite and zircon were removed from modal proportion calculations prior to creating bulk THERMOCALC composition, negating the need for a CaO correction (in the case of apatite) necessitated by the inability of THERMOCALC to compute phosphorus-bearing systems. Volumetrically minor biotite (<1 wt%) was removed from the WGC2019J-16J model. Water content was determined by subtracting halogen totals from hydrous minerals (WGC2019J-16J – hornblende; WGC2019J-17A – biotite, chlorite).

For WGC2019J-17A, wt% oxide values for ilmenite were taken from WGC2019J-18A. Ilmenite comprised <1% of the WGC2019J-17A thin section and was initially not analysed. Epidote values from felsic amphibolite WGC2018-38a were used.

Mineral forward equilibria model calculation is a months-long process involving 300+ individual calculations per diagram. The user must identify stable mineral assemblages and understand how they alter in response to pressure, temperature, composition, hydration and oxidation. Completed models were interrogated using TCInvestigator v1.0 (Pearce, White & Gazley, 2015). Appendix 9 outlines extended methods.

RESULTS

Petrography

Sample	Mafic/felsic, description (related to map)	Grid Reference UTM
WGC2019-16J	Mafic. Unaltered high strain eclogite.	32V 308364 6776922
WGC2019-17A	Felsic. Garnet-bearing felsic gneiss within contact between retrograde and fresh S1 eclogite.	32V 308356 6776917
WGC2019-17D	Mafic. Low strain eclogite.	32V 308356 6776917
WGC2019-18A	Felsic. Displays S3 and S4 fabrics.	32V 308373 6776911
WGC2019J-18B	Felsic. Pristine felsic gneiss 20cm SW of WGC2019J-18A.	32V 308373 6776911

Table 1: Summary of analysed samples. WGC2019J-16J (high strain mafic eclogite) and WGC2019J-17A (garnet-bearing felsic gneiss) were subjected to mineral equilibria modelling.

WGC2019J-16J: High strain eclogite

The observed mineral assemblage is garnet–amphibole–biotite–rutile–ilmenite (Figure 4a, b). The matrix is dominated by fine grained (as fine as ~5 μm) omphacite–albite–magnetite symplectites. Poikiloblastic garnets contain biotite and zircon inclusions, with larger grains (~1 mm) also containing muscovite and amphibole. Rutile (>1 mm) is associated with magnetite and rimmed by plagioclase. Biotite occurs as blades (up to 1 mm in length) and sieve-textured grains. Blastic, coarse, primary green (up to 1 mm along the c-axis) and garnet-rimming, blue, secondary amphibole (typically <500 μm) are present (Figure 4a, b).

WGC2019J-17A: Garnet-bearing felsic gneiss

The observed mineral assemblage is quartz–plagioclase–orthoclase–microcline±epidote±titanite (Figure 4c). Biotite (up to ~1 mm long blades), k-feldspar

(~500 μm) and plagioclase grains (~500 μm) define the foliation. Rare titanite is either (a) biotite associated, (b) included in/rimming/adjacent to magnetite, or (c) included in quartz. Rare poikiloblastic garnet grains are present with associated magnetite and become more xenoblastic with decreasing size (Figure 4c). Plagioclase and titanite inclusions occur in magnetite. Ilmenite inclusions occur within titanite, with relict chlorite (~100 μm) and zircon also present. Titanite rims around magnetite indicate magnetite crystallised first; accessory apatite is also present.

WGC2019J-17D: Low strain eclogite

WGC2019J-17D is texturally similar to WGC2019J-16J. Xenoblastic and hypidioblastic titanite typically rims poikiloblastic garnet, which has quartz and apatite inclusions (Figure 4d). Garnet is also included in amphiboles. Amphiboles occur as (1) macroscopic green grains up to ~1.5 mm along the c-axis (sometimes containing zircon inclusions), (2) macroscopic blue grains (100-200 μm) and (3) as a symplectite (as fine as 5 μm). Fine-grained albite–amphibole (hornblende)–magnetite–omphacite symplectites are present, likely after peak omphacite. Albitic plagioclase rims symplectite; magnetite is rimmed by titanite and plagioclase. Biotite occurs both in sieve-like textures and as large (~1 mm) blades. Magnetite occurs as (1) rims around various minerals, (2) as symplectite and (3) as large xenoblastic grains. Quartz persists as small grains.

WGC2019J-18A: Felsic gneiss

Quartz occurs as (1) prograde, 1-2 mm, inclusion-free macroscopic grains, and (2) recrystallised aggregates of smaller quartz grains with heavily deformed biotite and rare zircon inclusions (Figure 4e). Potassium feldspar and plagioclase are quartz-associated. Biotite occurs as (1) macroscopic (~2 mm), green pleochroic, radial clusters and (2) <1 mm, darkly brown pleochroic inclusions in quartz. Garnet crystals are small (50 μm) and numerous, forming aggregates associated with quartz, magnetite and amphibole in the S4 fabric. Titanite rims magnetite. Accessory apatite is present.

WGC2019J-18B: Pristine felsic gneiss

Quartz occurs as (a) prograde macroscopic grains, (b) recrystallised grains with biotite inclusions and (c) inclusions in plagioclase (Figure 4f). The matrix consists of microcline, orthoclase, quartz and plagioclase. Plagioclase contains biotite and quartz inclusions. Biotite occurs as (a) bladed, radial clusters (b) small, retrograde grains and (c) thin inclusions in plagioclase. Titanite forms (a) in association with biotite clusters, (b) as isolated grains and (c) rimming magnetite. Zircon and epidote are also present, the latter as small grains edging plagioclase. Accessory apatite grains (up to ~200 μm) are present, included in biotite mats and scattered throughout the matrix.

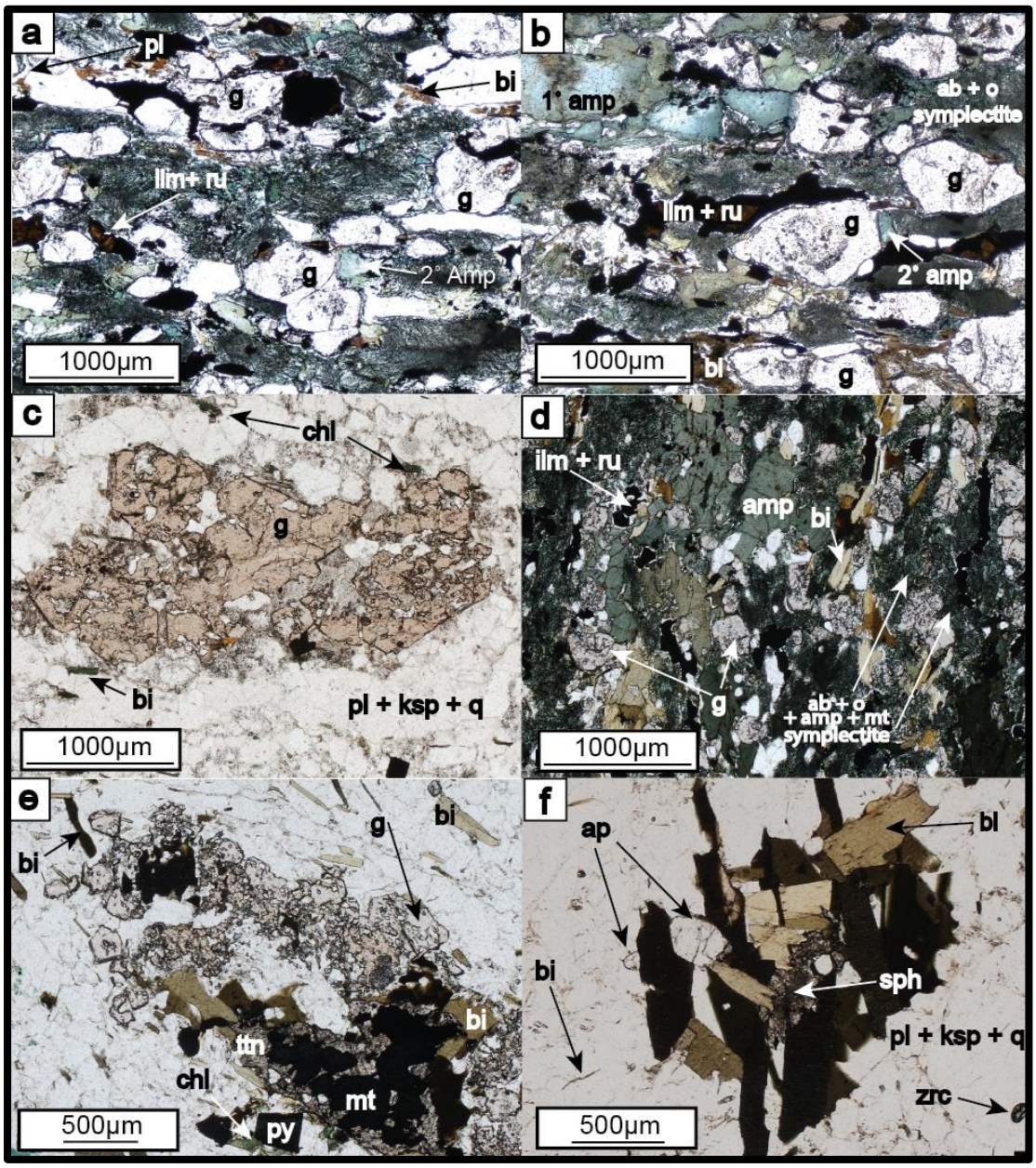

Figure 4: Selected photomicrographs of analysed samples. (a, b) WGC2019J-16J. Poikiloblastic garnet porphyroblasts with omphacite–albite–magnetite symplectites, biotite, primary (green) and secondary (blue) amphibole, rutile with exsolved ilmenite. Note range of garnet sizes (500-1000µm) evident in photograph and rutile + ilmenite mantling plagioclase coronae around garnet, with sieve and bladed biotite textures. (c) WGC2019J-17A. Garnet grains in plagioclase, k-feldspar and quartz dominated matrix. Chlorite, biotite and magnetite also visible. (d) WGC2019J-17D. Fine grained symplectites (amphibole–omphacite–albite–magnetite) with foliation defining biotite and coarse primary amphibole. Ilmenite and rutile visible along with poikiloblastic garnet. (e) WGC2019J-18A. Aggregates of poikiloblastic garnet. Deformed and non-deformed biotite generations. Opaque oxides include magnetite and pyrite. (f) WGC2019J-18B. Quartz and plagioclase dominant matrix with biotite mats, often with included apatite and titanite grains. Apatite grains range up to 200 µm in size. Zircon visible. Abbreviations mostly follow THERMOCALC conventions, excluding 1° amp (primary green amphibole) and 2° amp (secondary blue amphibole): bi (biotite), ab (albitic plagioclase), pl (plagioclase), ksp (potassium feldspar), q (quartz), zrc (zircon), mt (magnetite), py (pyrite), sph (titanite/sphene), chl (chlorite), g (garnet), ilm (ilmenite), ru (rutile), o (omphacitic clinopyroxene).

Mineral Chemistry

Representative mineral compositions relevant for phase equilibria modelling are presented in Table 2.

Garnet composition was principally almandine (55-68%). One traverse in a garnet grain <600 μm in WGC2019J-17D (Figure 5a, b) showed coreward-increasing grossular and rimward increasing almandine. Qualitative mapping of mafic eclogitic garnets >600 μm displayed grossular content decreasing and then increasing from core to rim (progradational zoning) (Figure 6). Almandine content increase then decrease from core to rim. These patterns were most obvious in foliation unaligned garnet (Figure 6c). In garnets >600 μm, manganese enrichment along rims and grain fractures evidenced resorption and compositional wiping after retrograde diffusion (Hollister, 1966; Tracy, Robinson & Thompson, 1976; Krogh, 1982). Symplectitic clinopyroxene and/or amphibole displayed lower MnO concentrations than the garnet they consumed (Table 2). Garnet in felsic gneiss was unzoned.

Amphibole in WGC2019J-17D was more halogen rich (0.83 wt%) than WGC2019J-16J (0.36 wt%). In WGC2019J-17D, primary green amphibole contained higher halogen content (0.83 wt%) than secondary blue (0.56 wt%) and symplectitic amphibole (0.49 wt%). No significant difference in halogen content was observed between the two blastic amphibole types in WGC2019J-16J (0.36 wt%). Primary amphibole in WGC2019J-16J preserved progradational TiO_2 zoning, averaging 0.63 wt% at the rim and 0.24 wt% at core (Table 2, Figure 5c). The t(hb) parameter (Ti on the M2 site, as

calculated by THERMOCALC) varied from 0.035 at the rim to 0.013 at core (Table 2, Figure 5c, d). Secondary amphibole in WGC2019J-16J displayed x(hb) = 0.33 (relevant for later mineral equilibria modelling). Symplectitic clinopyroxene in mafic eclogite was omphacitic (10-19% jadeite, 53-55% diopside). Plagioclase was dominantly albitic (91-97% albite). For felsic samples, apatites in WGC2019J-18A displayed the highest Cl concentration (2.97 wt%) and WGC2019J-18B the highest F concentration (0.19 wt%), which was over double that of WGC2019J-17A (0.06 wt%).

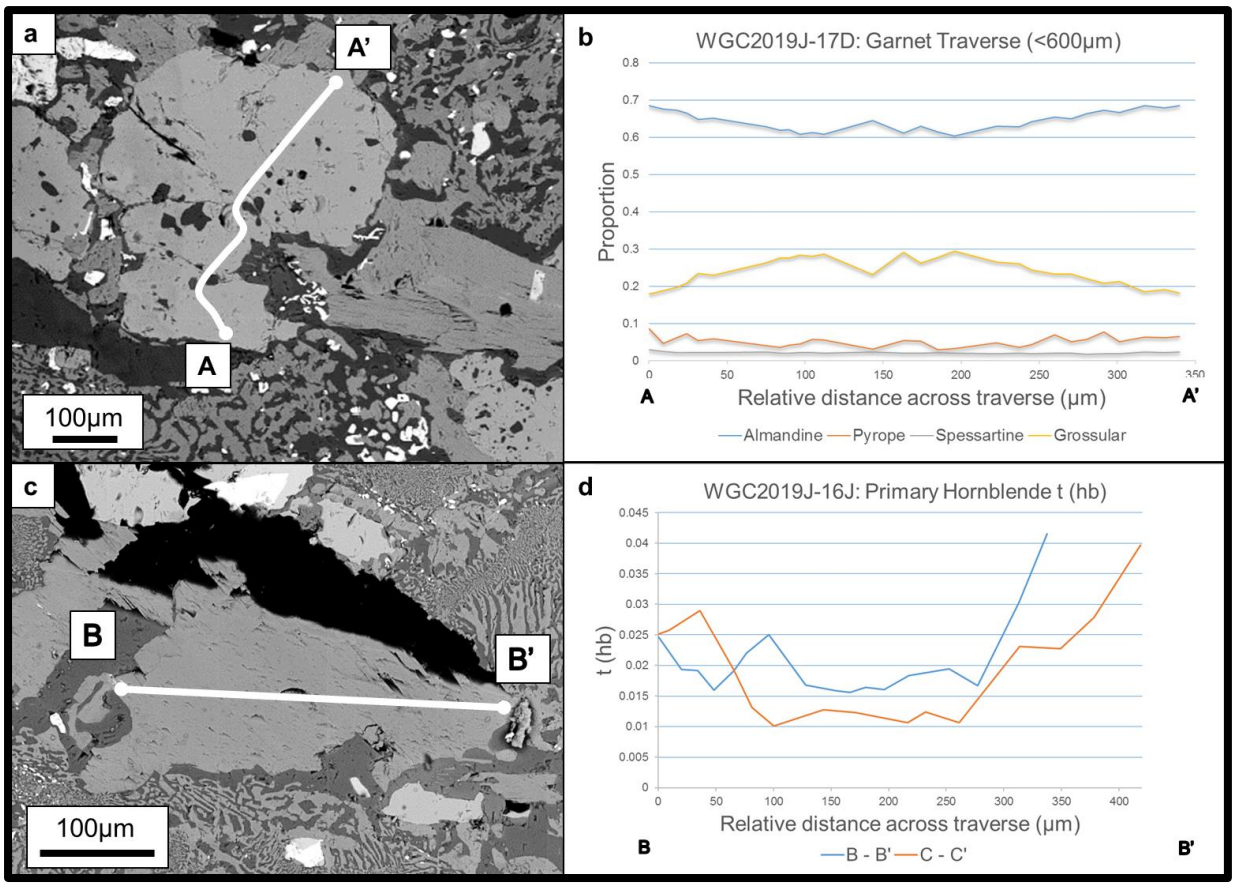

Figure 5: (a) Backscatter electron image of garnet traverse A-A' in low strain mafic eclogite WGC2019J-17D. This was the only traverse to display zonation for garnets <600 µm in mafic eclogite. (b) Garnet zonation, shown as proportion endmembers, from traverse shown in (a). Almandine proportion increases from core to rim. Grossular proportion decreases from core to rim (refer to text). (c) Backscatter electron image of primary green hornblende traverse B-B'. This was one of two traverses taken in high strain mafic eclogite WGC2019J-16J. (d) Primary amphibole titanium progradational zoning in WGC2019J-16J, presented in terms of the t(hb) parameter as calculated by THERMOCALC (relevant for determination of peak *P–T* conditions in WGC2019J-16J, discussed later). Blue and orange lines indicate two different traverses within WGC2019J-16J (C-C' backscatter electron image not shown). Traverse B-B' is shown in blue.

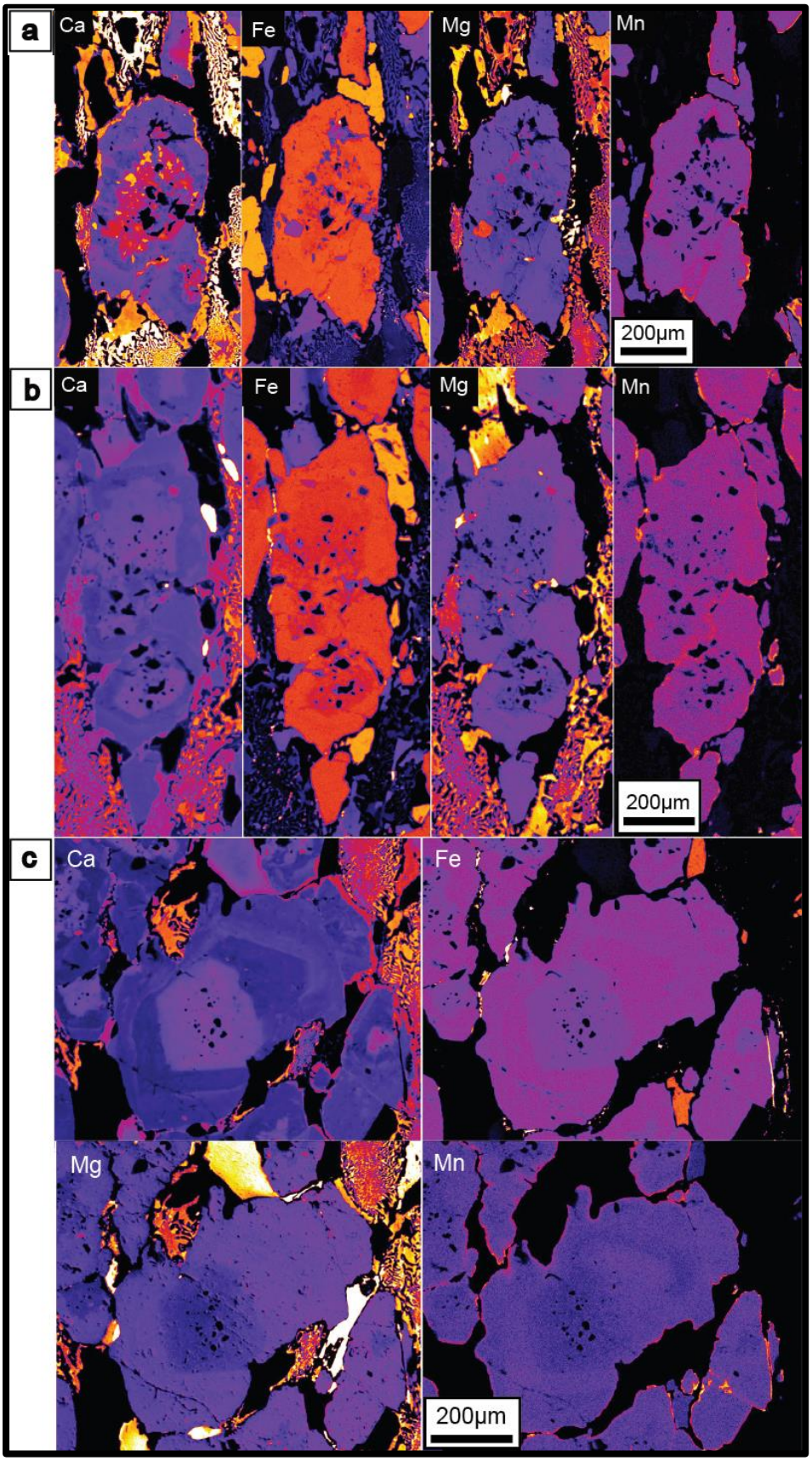

Figure 6: EPMA X-ray compositional maps of garnet in WGC2019J-16J. Cooler, darker colours indicate low and warmer, lighter colours indicate high elemental concentration. Maps show zonation in Ca (grossular), Fe (almandine), Mg (pyrope) and Mn (spessartine) for (a) a small (~600 µm) foliation aligned garnet with amphibole inclusions (b) a large (~900 µm) inclusion rich and foliation aligned and (c) medium sized (~700 µm) inclusion poor and foliation unaligned garnet. Grossular zoning is progradational; spessartine zoning demonstrates retrograde diffusion.

MINERAL	16J	17D	17A	18A	18B
GARNET					
Almandine	0.65	0.68	0.55	0.55	-
Pyrope	0.16	0.09	0.00	0.00	-
Grossular	0.14	0.18	0.42	0.43	-
Spessartine	0.01	0.03	0.02	0.01	-
XFe	0.77	0.86	0.97	0.99	-
MnO	0.56	1.10	0.96	0.55	-
CLINOPYROXENE					
XFe	0.28	0.31	-	-	-
Jadeite	0.19	0.10	-	-	-
Diopside	0.55	0.53	-	-	-
Hedenbergite	0.17	0.24	-	-	-
Aegirine	0.09	0.13	-	-	-
MnO	0.05	0.14	-	-	-
PLAGIOCLASE					
Albite - Symplectite	0.91	0.97	-	-	-
Anorthite – Symplectite	0.08	0.03	-	-	-
Sanidine – Symplectite	0.01	0.01	-	-	-
Albite – Matrix	0.94	-	0.83	-	-
Anorthite – Matrix	0.05	-	0.16	-	-
Sanidine - Matrix	0.01	-	0.01	-	-
AMPHIBOLE - PRIMARY					
Halogen (Cl + F)	0.36	0.83	-	-	-
TiO_2 – core	0.24	-	-	-	-
TiO_2 – rim	0.63	-	-	-	-
t(hb) – core	0.035	-	-	-	-
t(hb) – rim	0.013	-	-	-	-
AMPHIBOLE - SECONDARY					
Halogen (Cl + F)	0.36	0.56	-	-	-
x(hb)	0.33	-	-	-	-
AMPHIBOLE - SYMPLECTITE					
Halogen (Cl + F)	-	0.49	-	-	-
MnO	-	0.19	-	-	-
APATITE					
Cl	-	-	2.75	2.97	2.37
F	-	-	0.06	0.11	0.19

Table 2: Representative end-member compositions (as endmember proportions) for garnet, clinopyroxene, biotite and plagioclase, along with TiO_2 (wt%) core and rim concentrations in primary amphibole. Halogen content in amphibole and apatite is also shown in wt%. Note all samples have had the prefix 'WGC2019J-' removed, leaving only the identification after the hyphen, to conserve space. XFe = the ratio $Fe^{2+}/(Fe^{2+} + Mg)$ as defined by *a–x* THERMOCALC models; the x(hb) parameter is an identical ratio that accounts for cation distribution across M13, M2 and M4 sites in amphibole. t(hb) = proportion of Ti on the M2 site, as defined by THERMOCALC.

Zircon Trace Element Data

Zircon grains from sample WGC2019J-17D (S1) had almost non-existent negative Eu anomalies (0.139 to 0.345) while those from WGC2019J-16J (S2) and WGC2019J-15 (S3) had small Eu anomalies (0.108 to 0.502; 1.44 to 15.10). All three samples displayed HREE enrichment. HREE values of WGC2019J-15 were most elevated. Appendix 6b contains trace element data. Appendix 6c contains trace element graphs.

Zircon U-Pb Geochronology

Cathodoluminescence (CL) images of mounted zircons for WGC2019J-15, WGC2019J-16J and WGC2019J-17D revealed rounded metamorphic zircons with inherited cores (Corfu, Hanchar, Hoskin & Kinney, 2003). Untargeted cores were surrounded by a secondary inner zone ranging from black to grey in CL (Figure 7a) and an outer, lighter rim (Figure 7a, b, c). The secondary zone and outer rim were targeted for analysis.

LA-ICP-MS analysis of secondary inner rims produced Sveconorwegian ages (weighted $^{207}Pb/^{206}Pb$ ages: diatexite WGC2019J-15, 968 ± 20 Ma; high strain eclogite WGC2019J-16J, 926 ± 17 Ma; low strain eclogite WGC2019J-17D, 961 ± 14 Ma; Figure 7a, d). Analysis of outer metamorphic rims was less successful as rims were often smaller than spot size (29 μm; Figure 7a, b). A larger spot size was originally selected to increase precision. Several analyses in high strain eclogite WGC2019J-16J returned ages approaching the Caledonian, though contained large errors (Figure 7b, c). While concordia in WGC2019J-16J and WGC2019J-17D also tracked towards Caledonian ages (~400 Ma; Figure 8b, c), lower intercepts contained large errors (± 230

Ma, WGC2019J-16J; ± 550 Ma, WGC2019J-17D). Therefore, the data were unsuccessful in determining the age of the youngest metamorphic overprint. 95% concordant age data is displayed on Tera-Wasserberg plots (Figure 8 a, b, c). All error ellipses are 2σ.

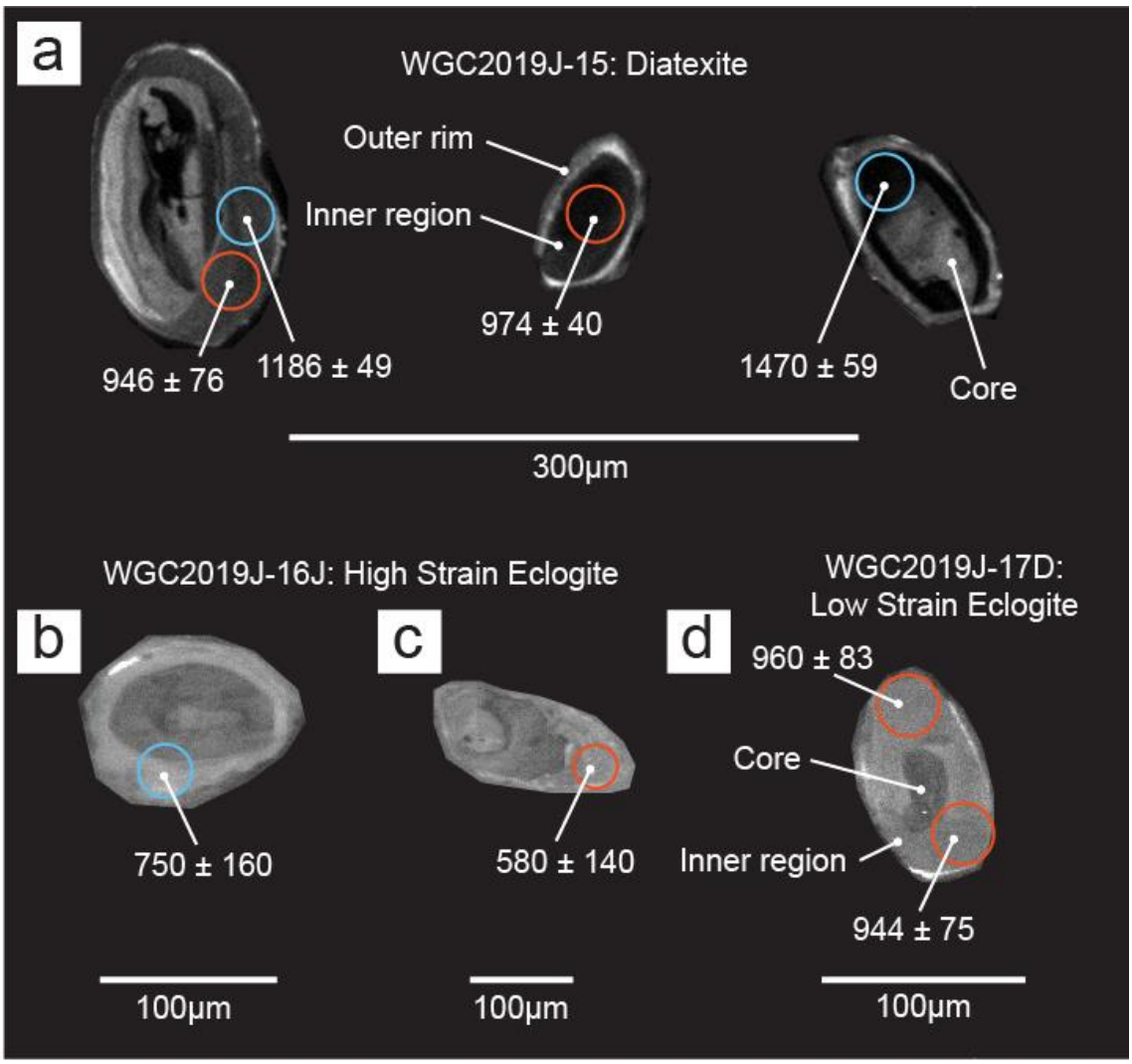

Figure 7: Three distinct zones were identified in zircons using cathodoluminescence (CL) imaging. Outer rims and inner regions were targeted for analysis. Ages (in Ma) are $^{207}Pb/^{206}Pb$ with 2σ errors. Scales are shown below grains. Red circles are concordant, and blue samples discordant, analyses. (a) Zircon in diatexite WGC2019J-15. Outer rim, inner region and inherited core are highlighted. (b, c) Zircon in high strain eclogite WGC2019J-16J. These zircons displayed ages younger than Sveconorwegian (ca. 900 Ma). (d) Zircon in low strain eclogite WGC2019J-17D. Core and inner region are highlighted.

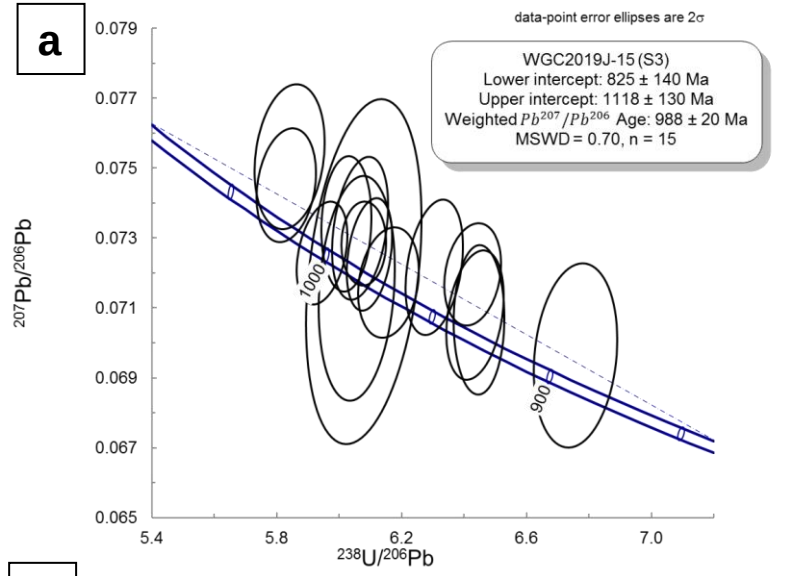

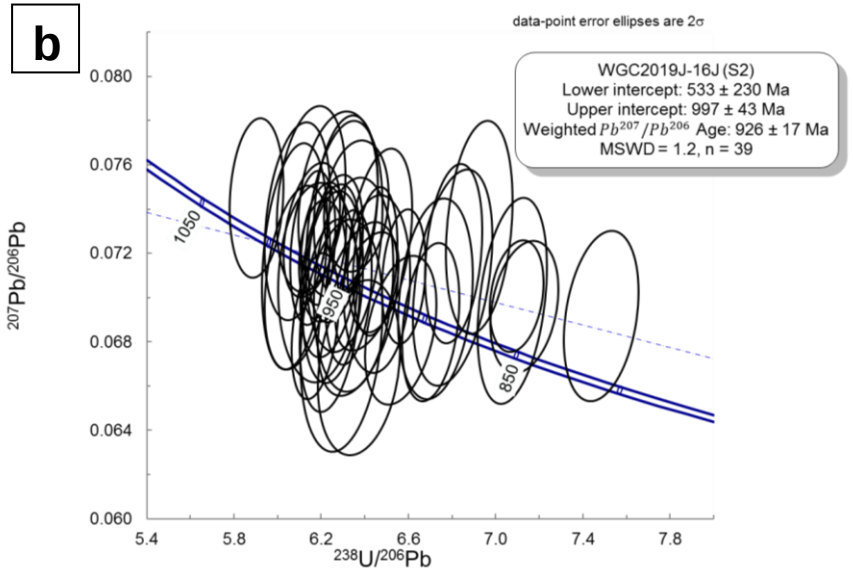

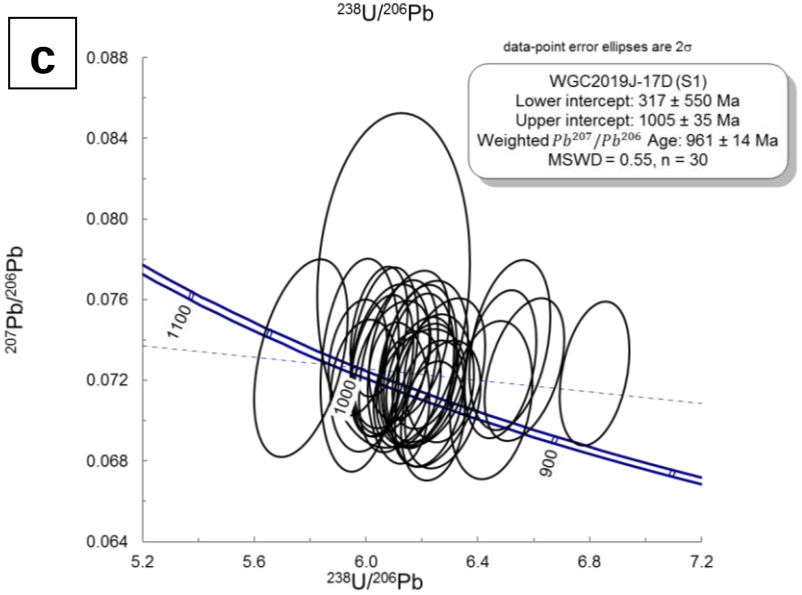

Figure 8: Zircon Tera-Wasserberg plots for (a) diatexite WGC2019J-15, (S3), with lower intercept 825 ± 140 Ma and upper intercept 1118 ± 130 Ma. MSWD = 0.7, n = 15. Weighted $^{207}Pb/^{206}Pb$ age: 968 ± 20 Ma. (b) High strain eclogite WGC2019J-16J (S2), with lower intercept = 533 ± 230 Ma and upper intercept = 997 ± 43 Ma. MSWD = 1.2, n = 39. Weighted $^{207}Pb/^{206}Pb$ age: 926 ± 17 Ma. (c) Low strain eclogite WGC2019J-17D (S1), with lower intercept 317 ± 550 Ma and upper intercept 1005 ± 35 Ma, MSWD = 0.55, n = 30. Weighted $^{207}Pb/^{206}Pb$ age: 961 ± 14 Ma. Data point error ellipses are 2σ. Data points are 95% concordant.

Rutile U-Pb Geochronology and Trace Element Analysis

Rutile grains >51 µm from high strain eclogite WGC2019J-16J (Figure 9a, b) and low strain eclogite WGC2019J-17D (Figure 9b) were analysed for geochronological and trace element data. Back-scatter electron (BSE) images showed ilmenite exsolution, amphibole, petrovskite and titanite inclusions, which were avoided during analysis (Figure 9c). All rutile grains had U contents > 1 ppm, suitable for U-Pb dating (Zack et al., 2011; Zack & Kooijman, 2017). Mounts (Figure 9b; WGC2019J-17D, WGC2019J-16J) and thin sections (Figure 9a; WGC2019J-16J) were analysed.

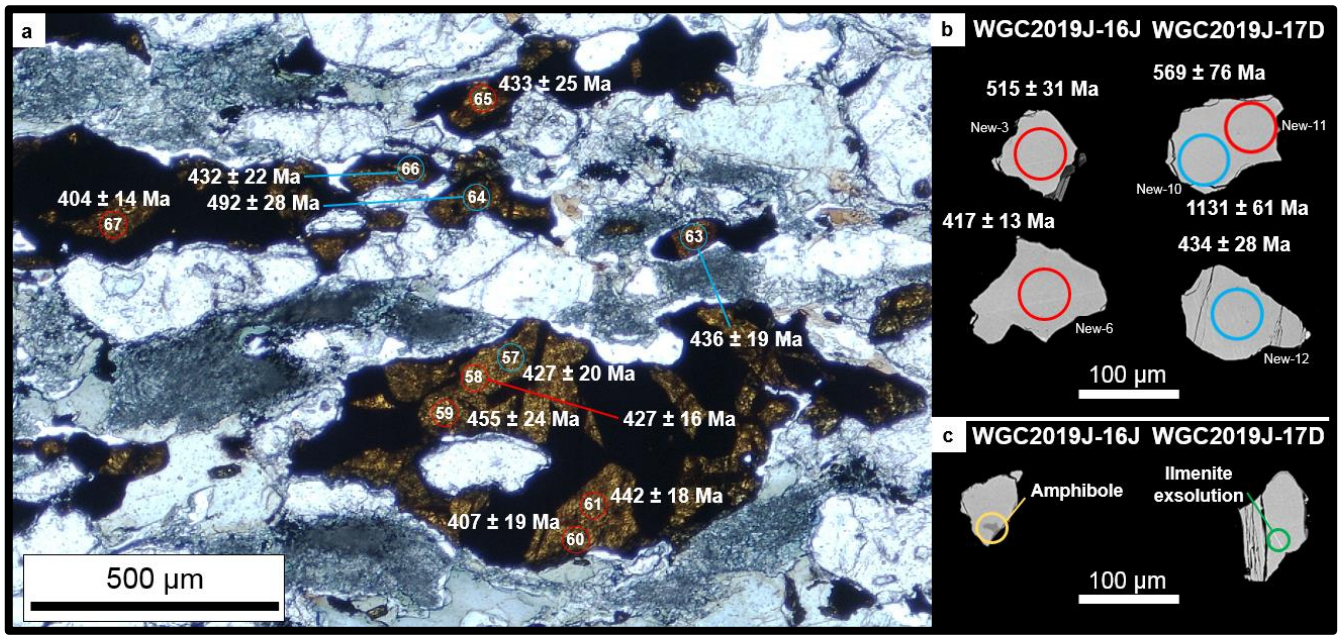

Figure 9: Selected rutile analyses. Plotted analyses are shown in red; analyses removed due to Pb, Ca or Fe content are shown in blue. Reported ages, shown adjacent to relevant analyses, are $^{206}Pb/^{238}U$, errors 2σ. (a) WGC2019J-16J, thin section photomicrograph. Numbers indicate analysis spot number (see Appendix 7). (b) WGC2019J-16J (left column; analyses New-3 and New-6) and WGC2019J-17D (right column; analyses New-10, New-11 and New-12) backscatter electron images of picked and mounted grains (see Appendix 7). (c) Amphibole inclusions (yellow circle) and ilmenite exsolution (green circle), among other inclusions, were actively avoided during analysis.

Caledonian ages (~430–385 Ma; Young & Kylander-Clark, 2015) were found for both eclogites when plotted on Tera-Wasserberg plots (Figure 10). For high strain eclogite WGC2019J-16J (Figure 10a), data points with high common lead (^{204}Pb or ^{208}Pb > 0.2 ppm) were removed (Zack et al., 2011; Zack & Kooijman, 2017). Data points with a clear lead loss trend (ellipse elongation along the x-axis) were also removed (Fielding et al., 2016). Data points with Ca > 0 ppm or Fe ≥ 3600 ppm indicated mixed analyses and were removed (Jedlicka & Faryad, 2017; Luvizotto et al., 2009). All error ellipses are 2σ. With filtering, a lower intercept of 399.8 ± 7.8 Ma (MSWD = 1.7, n = 51) was found (Figure 10b).

For low strain eclogite WGC2019J-17D (Figures 10c, d), identical filtering procedures produced a lower intercept age of 427 ± 13 Ma (MSWD = 0.83, n = 6). ^{208}Pb is preferentially used as a common lead proxy in rutile over ^{204}Pb as ^{208}Pb is more abundant (Zack et al., 2011, Zack & Kooijman 2017). Despite this, ^{204}Pb still remains an effective common lead proxy (Zack et al., 2011). When plotted data included ^{204}Pb < 1 ppm, a lower intercept of 416 ± 18 Ma (MSWD = 2.2, n = 15) was found (Figure 10d).

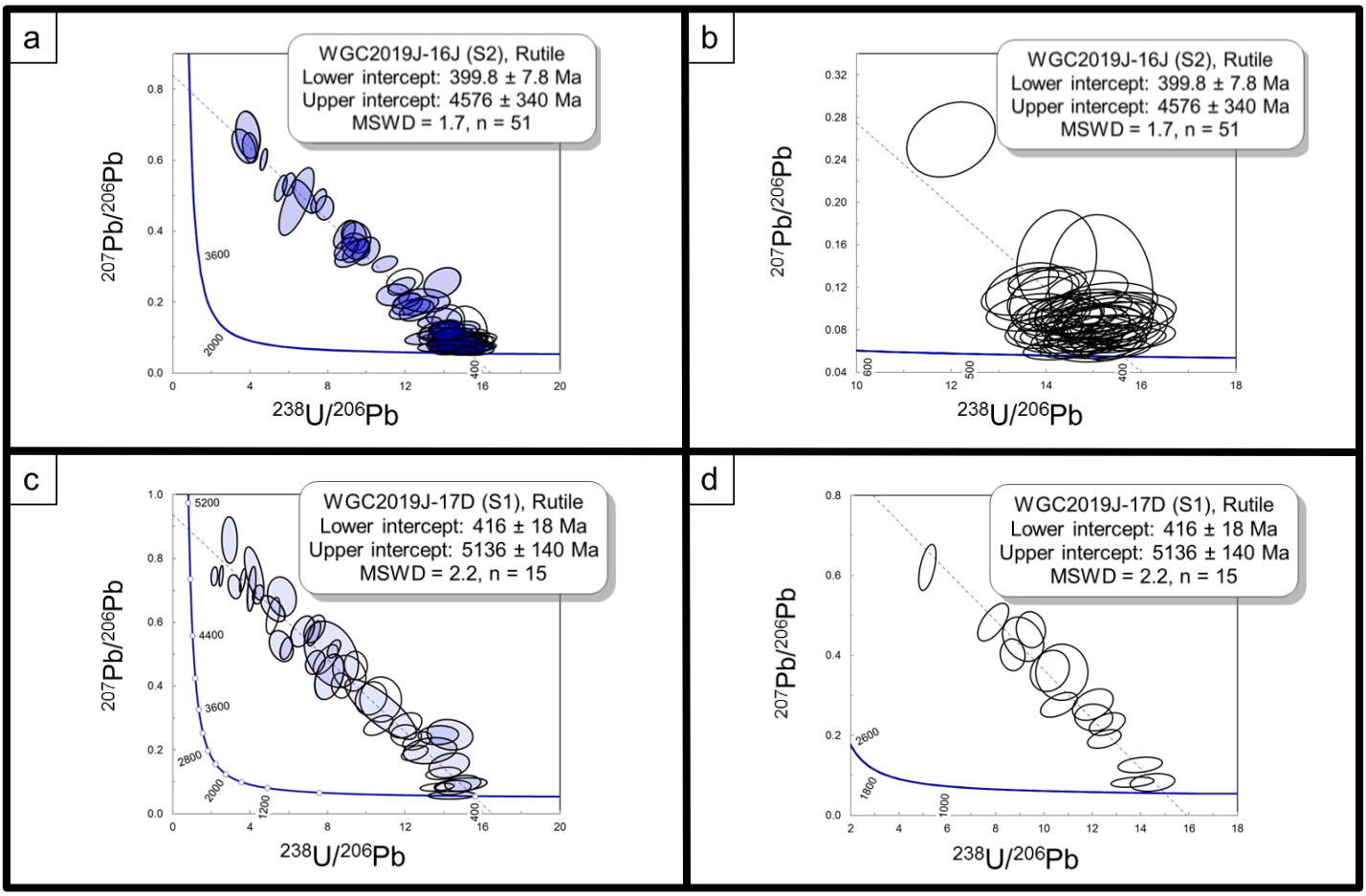

Figure 10: U-Pb Terra-Wasserberg Concordia diagrams for rutile analyses. All error ellipses are 2σ. Blue ellipses indicate analyses that were removed due to high Fe, Ca or common Pb contents. (a) WGC2019J-16J high strain eclogite (S2 foliation). With filtering, a lower intercept of 399.8 ± 7.8 Ma (MSWD = 1.7, n = 51) was found. (b) WGC2019J-16J high strain eclogite (S2 foliation). This plot indicates included analyses only. (c) WGC2019J-17D low strain eclogite (S1 foliation). With filtering, a lower intercept of 416 ± 18 Ma (MSWD = 2.2, n = 15) was found. Note that for this sample, plotted analyses were broadened to include ^{204}Pb < 1ppm; otherwise, identical filtering procedures were followed as for WGC2019J-16J. (d) WGC2019J-17D low strain eclogite (S1 foliation). This plot indicates included analyses only.

Mineral Equilibria Forward Modelling

P–T pseudosections were calculated for high strain mafic eclogite WGC2019J-16J and garnet-bearing felsic gneiss WGC2019J-17A (Figures 12, 14). An additional *P–X* pseudosection was calculated for WGC2019J-16J (Figure 11) to constrain oxidation state (bulk rock Fe_2O_3 content) as this can significantly impact modelling results (Carson, Powell & Clark, 1999; Johnson & White, 2011; Palin et al. 2016a; Rapp & Watson, 1995; Rebay, Powell & Diener, 2010). A *P–X* model fixes temperature (here, 700 °C) while varying pressure and oxidation state.

Oxidation state limits for the *P–X* diagram were defined by complete reduction (x axis lower limit = 0% Fe^{3+}) and ~40% increase in Fe_2O_3 concentration relative to the original composition calculated from microprobe analysis. Bulk rock composition was found at 0.22 (Figure 11). Oxidation state for WGC2019J-17A was calculated using stoichiometric charge balancing via the AX62 program (Droop, 1987; Holland et al., 2018; Holland & Powell, 1990, 1998; Jennings & Holland 2015). Completed pseudosections were inputted into TCInvestigator v1.0, confirming mineral assemblage stability.

WGC2019J-16J: High strain eclogite

High strain eclogite WGC2019J-16J had an inferred peak assemblage omphacite–garnet–rutile–quartz–H_2O–hornblende (Figure 12; peak field is highlighted by white dashed line). The lower-pressure bound of this field was defined by the introduction of glaucophane-like amphibole and calcic hornblende; and up-temperature by the solidus. There was no field evidence this rock crossed the solidus (e.g. leucosomes). Thus, the peak assemblage is reported as water-bearing (rather than water and liquid or liquid bearing). This field was defined up-pressure by lawsonite-in and hornblende-out boundaries.

Peak temperature conditions were constrained by the zirconium-in-rutile geothermometer after Tomkins, Powell and Ellis (2007) as the peak field edges >28 kbar extended beyond the modelled P window. This geothermometer accounts for pressure and temperature dependence on zirconium-in-rutile stability. Rutile from high strain eclogite WGC2019J-16J was used under the assumption that zircon and quartz grew together, permitting rutile zirconium content to change throughout prograde metamorphism. In rutile-stable fields, this geothermometer had a maximum value of 656 °C (at 28 kbar) and a minimum of 577 °C (at 8.3 kbar) (Figure 12). The lower boundary of the peak field intersects the geothermometer at ~20.5 kbar, 626 °C. Thus, the peak temperatures for this sample are constrained between 626°C and 656°C.

Primary hornblendes in WGC2019J-16J displayed progradational Ti zoning. Hornblende Ti content is temperature dependent, increasing with metamorphic grade (Raase, 1974). The slow diffusivity rate of Ti (often two orders of magnitude less than Fe^{2+} and Mg^{2+}; van Orman, Grove, Shimzu & Layne, 2002) ensures established TiO_2 growth patterns remain even up to granulite-facies conditions (Storkey, Hermann, Hand & Buick, 2005).

The TCInvestigator t(hb) parameter (indicating hornblende Ti concentration) decreased from 0.08 to 0.01 across the diagram with increasing *P–T*. Hornblende mode decreased across the diagram from 12% to 3% with increasing *P–T*. Selected analyses from rim and core compositions showed primary hornblende t(hb) decreased from 0.035 to 0.013 (Figure 13). Therefore, rim compositions reflect a *P–T* point lower than peak conditions and provided a minimum constraint for peak metamorphism at ~650 °C; only a combination of (a) growth zoning and (b) mineral growth generates crystal rims reflective of peak metamorphic conditions. A-site Na content in primary amphibole also helped constrain minimum *P–T* conditions for the prograde assemblage. Peak pressures were therefore inferred at ~20–22 kbar.

The retrograde path of WGC2019J-16J is defined by the appearance of albitic plagioclase and clinopyroxene symplectites after omphacite and garnet. While amphibole may form a part of these symplectites, none was identified in EPMA and is not assumed to be part of the retrograde assemblage. The appearance of secondary (blue) hornblende, typically rimming peak garnet, is another aspect of the sample's evolution down pressure. A retrograde assemblage of garnet–omphacite–albite–

hornblende–quartz–rutile–ilmenite–magnetite was found, with the latter oxide very minor in abundance (and not appearing on the calculated pseudosection; Figure 12). Secondary amphibole XFe (defined as x(hb) in THERMOCALC outputs) is the only temperature-sensitive parameter for the retrograde assemblage, placing this part of the rock's path at ~610 °C, where it intersects the calculated omphacite mode (o (mode); Figure 13). Along with calculated garnet mode, omphacite mode constrains retrograde pressures ~8–10.5 kbar (Figure 13). Appendix 10 holds data for zirconium-in-rutile geothermometry. Appendix 11 holds extended TCInvestigator outputs.

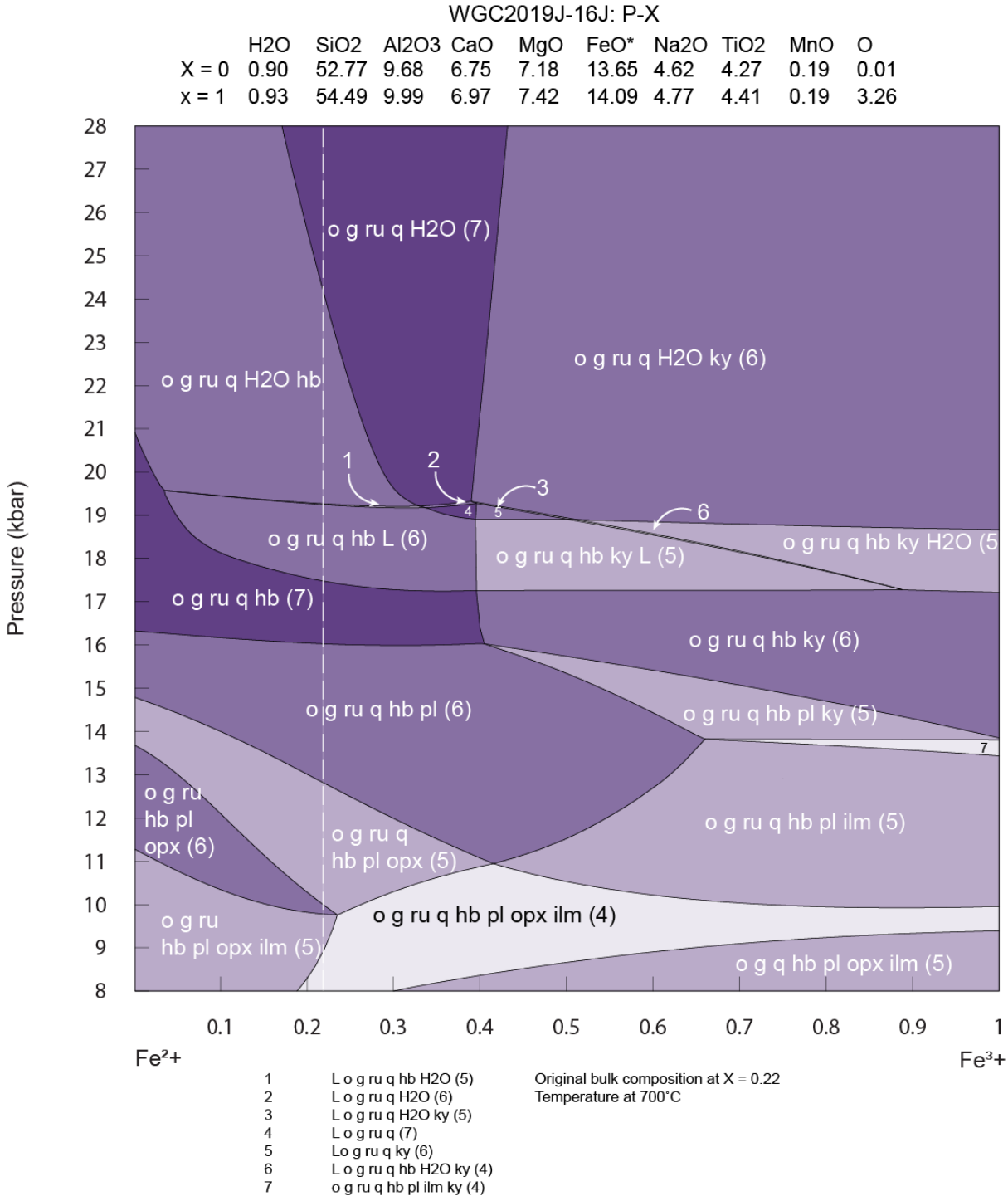

Figure 11: *P–X* model for sample WGC2019J-16J, fixed at T = 700°C and showing bulk composition at X = 0.22. Abbreviations: L (liquid), o (omphacite), g (garnet), ru (rutile), q (quartz), hb (hornblende), H2O (water), ky (kyanite), ilm (ilmenite), opx (orthopyroxene), hb (hornblende). Composition used for calculations is shown above diagram (units: mol%). FeO* = FeO + (2xO). Variance (components – phases + 2) increases with darker shading and is indicated by bracketed number (e.g. (6)) next to field assemblage. System modelled in MnNCFMASHTO.

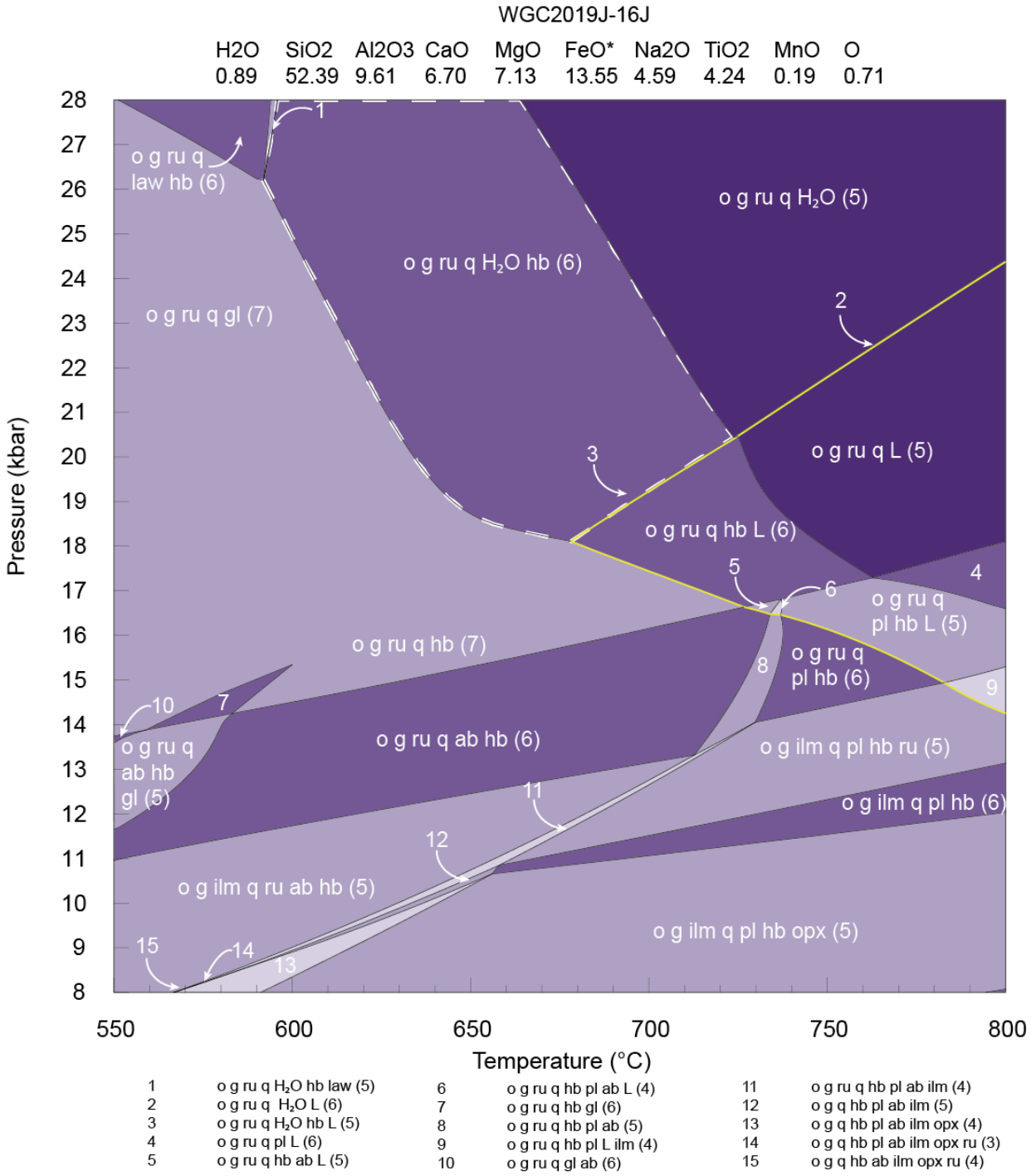

Figure 12: *P-T* pseudosection for sample WGC2019J-16J. Peak field is highlighted by white dashed line. Solidus indicated by yellow line. Field labelled '7' (o g ru q hb gl) defines an amphibole solvus, with adjacent field containing amphibole in a solid solution of hornblende and glaucophane; regions where hornblende or glaucophane are more modally dominant are indicated by label (gl – up pressure; hb – down pressure). Abbreviations: L (liquid), o (omphacite), g (garnet), ru (rutile), q (quartz), H2O (water), ky (kyanite), ilm (ilmenite), opx (orthopyroxene), hb (hornblende), gl (glaucophane), ab (albite), pl (plagioclase). Composition used for calculations is shown above diagram (units: mol%). FeO* = FeO + (2xO). Variance (components – phases + 2) increases with darker shading and is indicated by bracketed number (e.g. (6)) next to field assemblage. System modelled in MnNCFMASHTO (refer to text).

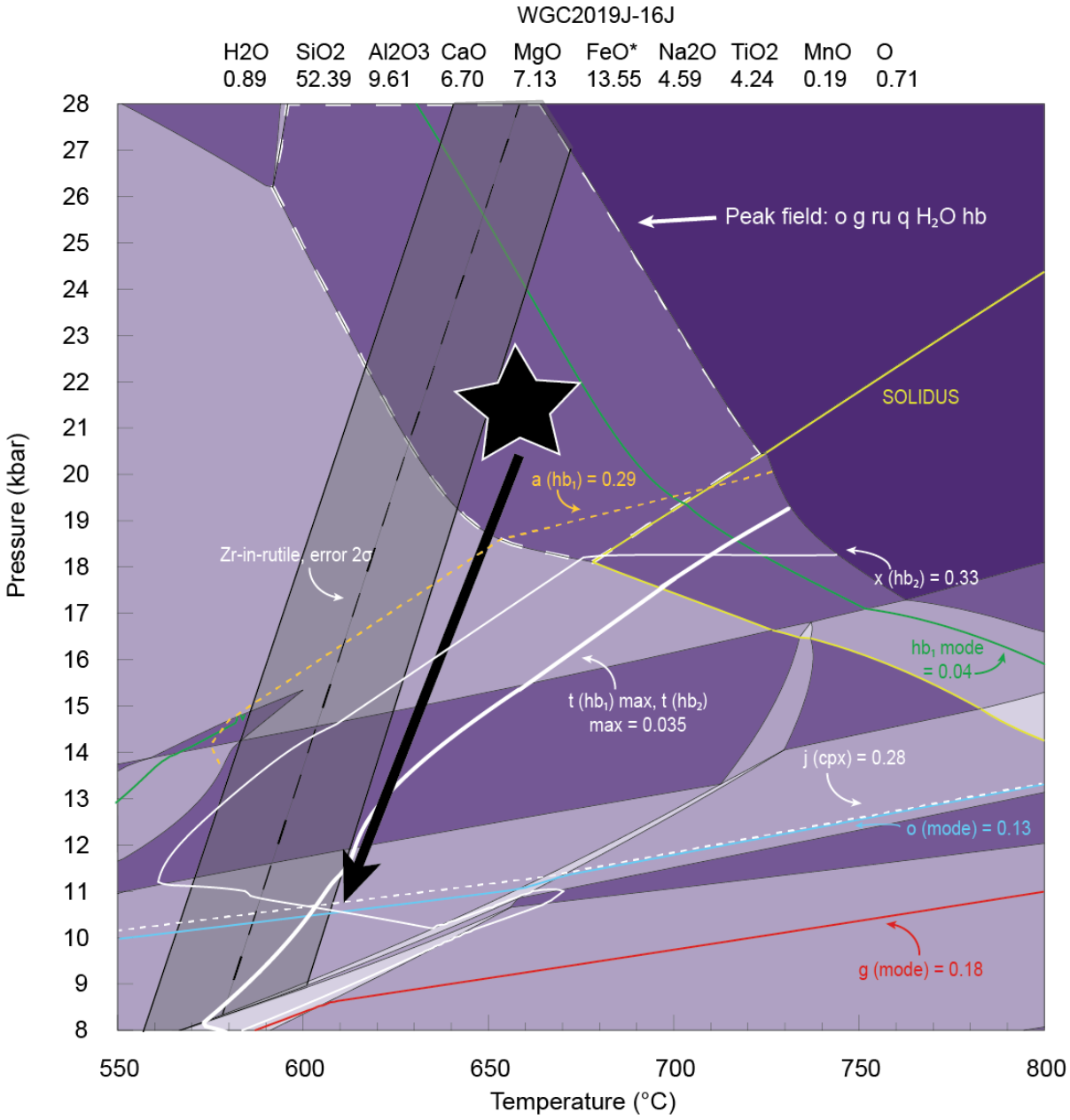

Figure 13: Annotated *P-T* pseudosection for mafic eclogite WGC2019J-16J with inferred peak *P-T* and retrograde path. Peak field is indicated by white dashed line. Black star indicates interpreted peak *P-T* conditions, with black arrow showing retrograde path. Solidus is highlighted in yellow. Zirconium-in-rutile geothermometry is shown as a black dashed line, with associated 2σ error bars shown as a grey field. Composition used for calculations is shown above diagram (units: mol%). FeO* = FeO + (2xO). Variance (components – phases + 2) increases with darker shading. G (mode) = modal garnet proportion (solid red line); o (mode) = modal omphacite proportion (solid blue line); j(cpx) = M2 site Na on omphacite (thin white dotted line); x (hb_2) = secondary hornblende XFe (solid thin white line); hb_1 mode = modal primary hornblende proportion (solid green line); t (hb_1) max = maximum primary hornblende Ti proportion (defined by THERMOCALC; solid bold white line), a (hb_1) = primary amphibole a-site Na (orange dotted line). System modelled in MnNCFMASHTO.

WGC2019J-17A: Garnet-bearing felsic gneiss

Garnet-bearing felsic gneiss WGC2019J-17A was modelled in the same *P–T* window as WGC2019J-16J to determine whether it recorded similar *P–T* conditions (Figure 14). Sub-solidus assemblages alone are presented as there was no evidence in the field that the solidus was crossed.

The peak assemblage for WGC2019J-17A was inferred to be garnet–k-feldspar–plagioclase–quartz–biotite–titanite±zircon from sample, with a retrograde path encompassing magnetite, epidote and chlorite. A garnet-bearing, muscovite-absent peak field was not found. Garnets were sparse in hand sample. The thin section used for analysis was deliberately chosen to include garnet in order to be more representative of the outcrop. The lack of garnet within lower-pressure assemblages may be due to the removal of Mn from the model composition. Manganese (Mn) was removed from the model composition due to low bulk concentrations (0.04 mol%). Clinopyroxene could not be stabilised at high pressures.

More important is the appearance of muscovite up-pressure. No muscovite was present in outcrop or thin section, providing an upper pressure sub-solidus constraint for WGC2019J-17A at ~9 kbar and an upper peak temperature limit of ~640 °C–650 °C (Figure 14).

TCInvestigator mineral modal proportions for garnet range from 0 to 9% across the modelled *P*–*T* range. For muscovite, the maximum at 28 kbar is 8%; for kyanite and rutile, <1%; and plagioclase varies from 38% to 48% across the model. While plagioclase stability >26 kbar is unexpected, TCInvestigator outputs demonstrate that across a pressure range of 20 kbar mineral modal proportion increase is low for muscovite and kyanite. The calculated garnet mode was 0.03%, and at the same point calculated muscovite mode would be ~3% (Figure 14). Muscovite was not present in thin section, reflecting its rarity in host rock lithology.

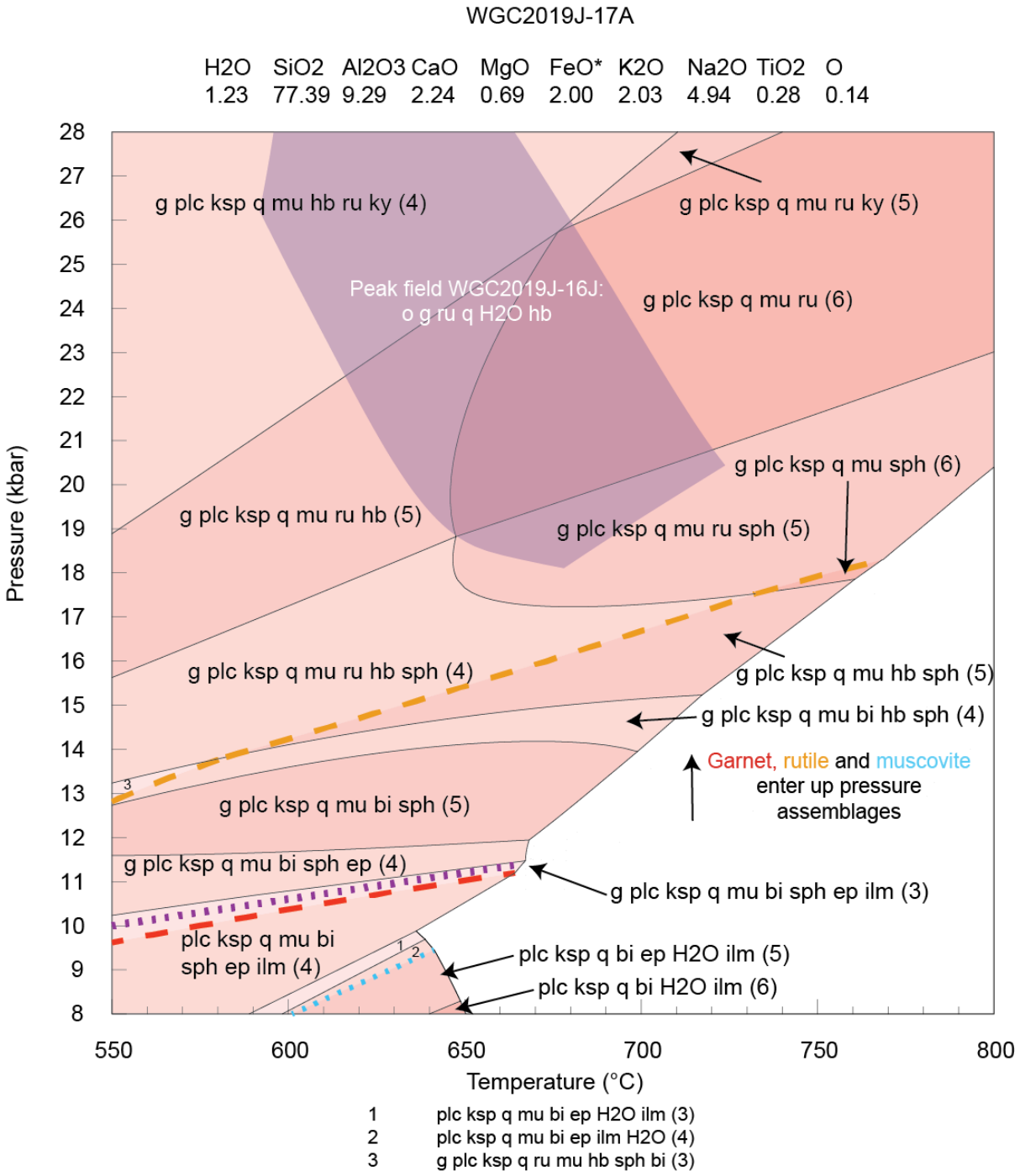

Figure 14: Calculated *P-T* pseudosection for sample WGC2019J-17A. The peak field of WGC2019J-16J (o g ru H2O hb) is shown in purple. Abbreviations: g (garnet), plc (plagioclase), q (quartz), mu (muscovite), ru (rutile), hb (hornblende), bi (biotite), sph (sphene (titanite)), ep (epidote), ilm (ilmenite), H2O (water), ksp (potassium feldspar). Red dashed line represents the garnet-in reaction, orange dashed line represents the rutile-in reaction and blue dotted line represents the muscovite-in reaction. All phases enter assemblages up-pressure. The muscovite-in reaction (blue dotted line) represents the maximum possible peak conditions recorded by this sample. Purple dotted line represents calculated garnet mode from modelled sample (0.03%); at the same point, muscovite mode would be 3%. Variance (V) for each assemblage is indicated in brackets, with variance = (components – phases) + 2. Components = oxides, phases = minerals. System modelled in NCKFMASHTO (refer to text).

DISCUSSION

U-Pb geochronology: Zircon and rutile

Analysis of zircon in mafic eclogite and diatexite was conducted to confirm the study area recorded Caledonian metamorphism rather than the earlier Sveconorwegian (ca. 900 Ma) or Gothian (ca. 1660-1520 Ma) events. Such analysis was essential as the Caledonian Orogeny converted WGC rocks to eclogite-facies, forming the basis of this study.

Geochronological results on zircon grains were not consistent with Caledonian ages. Although three zones were distinguished in zircon from CL imaging (Figure 7a), the rims interpreted as Caledonian overprinting (Corfu et al., 2003; Young & Kylander-Clark, 2015) were too thin (<29 μm) to be effectively targeted. Analysed spots from the inner region confirmed only that the analysed eclogites underwent Sveconorwegian metamorphism (Figure 8). Texturally, the presence of thin metamorphic rims (Figure 7) indicates a later metamorphic overprint. Rutile geochronology of in-situ and picked grains from mafic eclogite (Figure 9a, b) was more successful.

Geochronological results from rutile indicate Caledonian resetting (Figure 10), with S1 foliation dated at 416 ± 18 Ma (WGC2019J-17D; Figure 10c, d) and S2 foliation at 399.8 ± 7.8 Ma (WGC2019J-16J; Figure 10a, b). Though the analysed grains contained common lead and evidence of lead loss (Figure 10), these ages are Caledonian (~430–385 Ma; Kylander-Clark & Hacker, 2014). Assuming the metamorphic overprint on zircon is consistent with the Caledonian ages recorded by rutile grains, these results

provide the basis for the use of zirconium-in-rutile geothermometry to constrain peak *P–T* conditions in high strain eclogite during mineral equilibria modelling. Future analysis with a reduced spot size (9 μm) may allow metamorphic rims on zircon grains to be dated, providing additional evidence to support this assumption.

Mineral equilibria modelling

The ages recorded by rutile in mafic eclogite indicate the study area underwent eclogite-facies metamorphism during the Caledonian, permitting the overarching question of felsic metastability during continental subduction to be addressed. The peak assemblage (omphacite–garnet–rutile–quartz–H_2O–hornblende) of high strain eclogite was constrained at 20–22 kbar, ~650 °C through (i) hornblende Ti content, (ii) hornblende mode and (iii) zirconium-in-rutile geothermometry (Figures 12, 13). Rim Ti concentrations (0.24 wt%) in prograde-zoned hornblende provide a minimum *P–T* constraint as hornblende mode decreases with increasing temperature (Figures 5d, 12). Retrograde temperature conditions ~610 °C were constrained primarily through secondary hornblende XFe; symplectitic omphacite and garnet modes provided retrograde pressure constraints between 8–10.5 kbar. The modelled retrograde path is almost completely isothermal, agreeing with literature (e.g. Kylander-Clark et al., 2012; Young & Kylander-Clark, 2015). These *P–T* conditions establish a baseline for what adjacent garnet-bearing felsic gneiss WGC2019J-17A should record in response to eclogite-facies metamorphism.

P–T conditions recorded by WGC2019J-17A do not indicate eclogite-facies conditions and provide a case for felsic metastability during continental subduction. The peak field

of garnet-bearing felsic gneiss WGC2019J-17A could not be determined from mineral equilibria modelling (Figure 14). The absence of muscovite in thin section, along with garnet scarcity, indicate a low-pressure peak assemblage bound up-pressure by a muscovite-in reaction. The model instead predicts a muscovite-bearing garnet-absent assemblage (Figure 14). Given the low modal proportions of garnet in WGC2019J-17A (0.3%), this may only reflect the inability of THERMOCALC to compute low modal garnet proportions. Instead, the muscovite-in reaction provides a constraint for maximum *P*–*T* recorded by garnet-bearing felsic gneiss (~8–9 kbar, 650 °C).

The forward equilibria model for garnet-bearing felsic gneiss was subject to two limitations. Firstly, the removal of Mn from the model likely decreased garnet stability at lower pressures and temperatures (Proyer & Dachs, 2000; Tinkham, Zuluaga & Stowell, 2003; White, Powell & Johnson 2014). The removal of Mn from the model would provide an explanation for the garnet-in reaction appearing at higher pressure than the muscovite-in reaction (Figure 14). The model could be improved by including Mn in the model system. Secondly, clinopyroxene, a UHP metamorphism indicator, could not be stabilised at high pressure. It is possible there were faults within the *a*–*x* models used, or that clinopyroxene was simply not part of a stable mineral assemblage. Nevertheless, the model contains evidence supporting textural observations made in thin section and outcrop.

Felsic metastability during continental subduction

This study seeks to examine whether felsic rocks react during eclogite-facies conditions or rather remain metastable. Paradoxically, both possibilities would produce amphibolite-facies assemblages in UHP metamorphic terranes. This first order observation was made at the Eclogite Outcrop (Figure 2), observed in thin section (Figure 3 c, e, f) and is extensively recorded in the literature (e.g. Cuthbert et al., 2000; Skår & Pedersen, 2003; Wain et al., 2000).

Rare UHP felsic gneisses do exist within the northern WGC, which underwent the deepest subduction during the Caledonian (Skår & Pedersen, 2003). The textural evidence of UHP metamorphism in felsic gneiss includes the presence of eclogite-facies assemblages with rutile, kyanite and muscovite after plagioclase (Krogh, 1982; Liu & Massonne, 2019; Wain et al., 2000; Young & Kylander-Clark, 2015). Garnet-bearing felsic gneiss had an observed assemblage of plagioclase–k-feldspar–quartz–biotite–epidote–garnet±ilmenite±apatite±titanite±magnetite. It did not contain eclogite-facies minerals (e.g. muscovite, kyanite) indicative of UHP metamorphism. At peak conditions reached at the Eclogite Outcrop – as modelled by WGC2019J-16J – WGC2019J-17A had kyanite and rutile modes <1% (Figure 15). At the same conditions (~20–22 kbar, 650 °C), garnet and muscovite each constituted ~8% of the bulk rock composition (Figure 15). Similar modal proportions have been calculated in garnet-bearing gneisses from other UHP metamorphic terranes (e.g. Liu & Massonne, 2019). Garnet and muscovite should have been easily observed if the garnet-bearing felsic gneiss recorded UHP conditions. The fact that no muscovite was observed supports

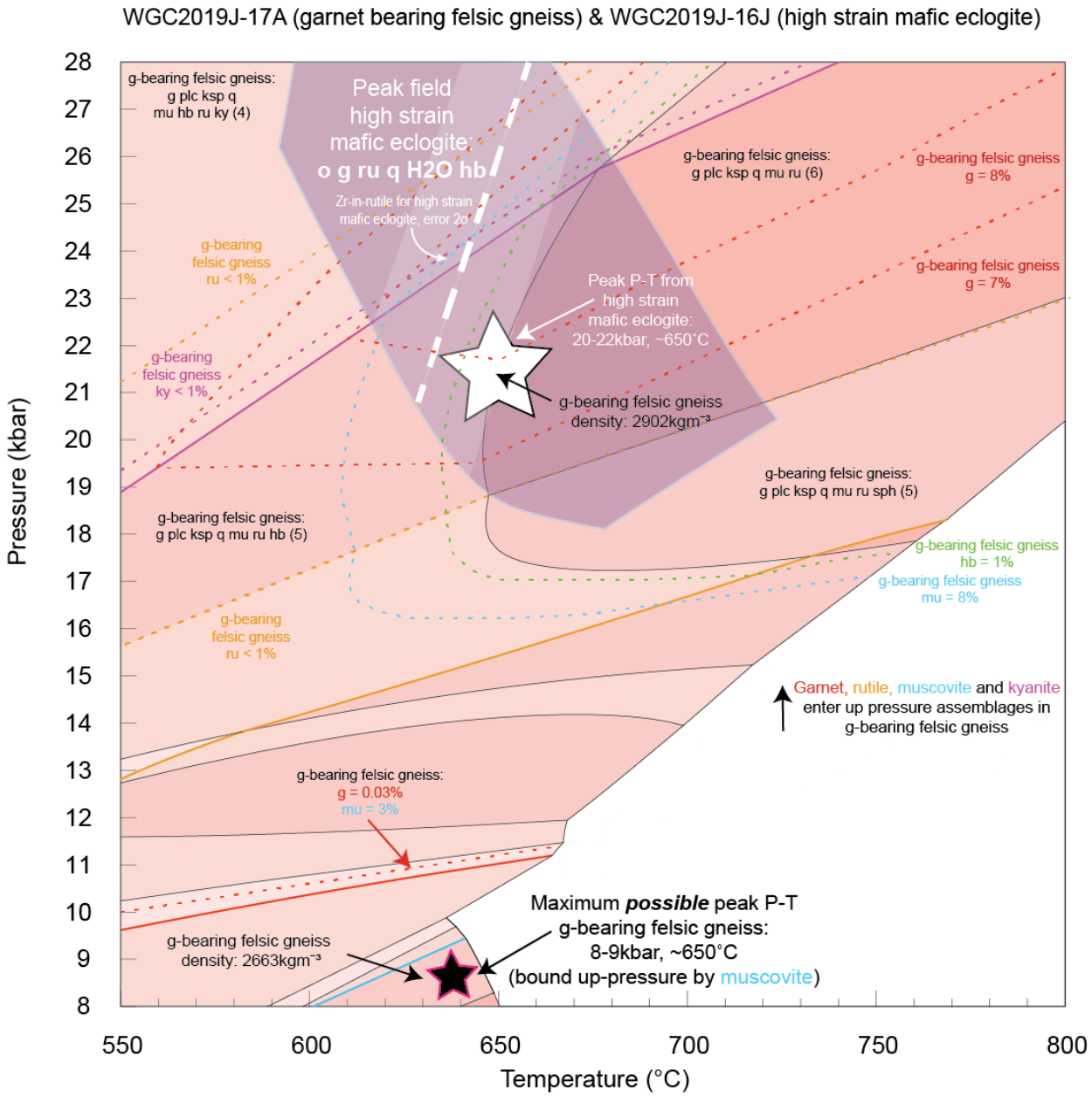

Figure 15: Composite *P-T* pseudosection comparing garnet-bearing felsic gneiss WGC2019J-17A (black annotations) and high strain mafic eclogite WGC2019J-16J (white annotations). Peak field for high strain mafic eclogite WGC2019J-16J is shown in purple, with zirconium-in-rutile geothermometer constraint from WGC2019J-16J shown as a white dashed line; 2σ errors are shown as a pale white region within peak field for high strain eclogite WGC2019J-16J. Mineral modes (as mol%) calculated for WGC2019J-17A, garnet-bearing felsic gneiss, are shown as dashed coloured lines; field boundaries where minerals enter up-pressure are shown as solid coloured lines (red = garnet, blue = muscovite, green = hornblende, purple = kyanite, orange = rutile). Peak *P-T* conditions as modelled by high strain mafic eclogite WGC2019J-16J are shown as a white star. Maximum possible *P-T* conditions modelled for ganet-bearing felsic gneiss WGC2019J-17A are shown as a black star. Approximated density calculations, based on mineral modal proportions from garnet-bearing felsic gneiss WGC2019J-17A, are annotated next to recorded (~8–9kbar) and true (~20–22kbar) peak *P-T* stars. Fields within model for garnet-bearing felsic gneiss are annotated with variance in brackets (e.g. (6)), with variance = (components – phases) + 2. Components = oxides, phases = minerals. Abbreviations: g = garnet, mu = muscovite, hb = hornblende, ky = kyanite, pl = plagioclase, ksp = k-feldspar, ru = rutile, o = omphacite, H_2O = water, q = quartz.

the proposition that the region remained metastable, despite the ambiguity surrounding the location of the modelled garnet-in reaction (Figure 14).

Felsic metastability and UHP metamorphic terrane density

It is important to consider the implications of mass transformation on the bulk metamorphic terrane if reactivity did occur, even though the evidence from this study indicates felsic metastability is more likely. Mass transformation of felsic rocks to eclogite-facies mineral assemblages in metamorphic terranes should increase terrane density (Massonne et al., 2007; Young & Kylander-Clark, 2015). If the mineral assemblage (garnet–plagioclase–K-feldspar–quartz–muscovite–hornblende–rutile) and modal proportions in garnet-bearing felsic gneiss at ~20–22 kbar, 650 °C (peak *P–T* reached at the Eclogite Outcrop, as modelled by high strain eclogite) are used, the overall terrane density at these conditions can be estimated at 2902 kgm^{-3} (Figure 15). This density is slightly lower than literature estimates for dry metapelites (3000 kgm^{-3}; Massonne et al., 2007; Young & Kylander-Clark, 2015) but still greater than the upper mantle (~3310 kgm^{-3}; Massonne et al., 2007). The bulk density of WGC2019J-17A is 2663 kgm^{-3} at maximum possible *P–T* conditions recorded by the gneiss itself (~8–9 kbar, 650 °C). This results in a density increase of ~8% for the bulk metamorphic terrane due to HP mineral phase presence at peak metamorphism (as calculated from this study), falling within the accepted literature range of 3-20% (Walsh & Hacker, 2004; Massonne et al., 2007; Young & Kylander-Clark, 2015). The fact that at ~20–22 kbar, 650 °C, the bulk terrane was less dense than the upper mantle explains why this UHP terrane would be exhumed even if areas did eclogitise and subsequently retrogress. If WGC2019J-17A did convert to eclogite, the low modal proportions of some UHP

minerals (e.g. kyanite, rutile) produced up-pressure (Figure 15) would leave scarce evidence of UHP metamorphism (Massonne et al., 2007; Young & Kylander-Clark, 2015); however, as previously discussed, the presence of muscovite should remain a clear indicator of UHP conditions.

It is possible the scarcity of HP-UHP mineral assemblages at the Eclogite Outcrop reflects their complete destruction during retrograde recrystallisation (Young & Kylander-Clark, 2015). However, if pervasive retrograde recrystallisation did occur, it would be expected that WGC2019J-17A would record textural evidence of it, as WGC2019J-17A lies adjacent to WGC2019J-17D – with which it shares S1 foliation (NNW-SSE striking, 416 ± 18 Ma). Given the modelled rarity of kyanite and rutile it is plausible the sample was not representative. However, large-scale retrogression is still unlikely, as indicated by the scarcity of UHP felsic gneisses in literature (e.g. Wain et al., 2000, 2001) and this study (Figures 2, 3) not associated with hydrous boudins or shear zones (e.g. Wain et al., 2000, 2001).

While WGC2019J-17A contained apatite with average halogen content (Cl = 2.75 wt%, F = 0.06 wt %) greater than WGC2019J-18B (Cl = 2.37 wt%, F = 0.19 wt%), the modal apatite within these gneisses remains unconstrained. Thus, it is possible WGC2019J-18B contains a higher percentage of halogen as a function of bulk rock composition relative to WGC2019J-17A but possesses lower modal apatite. Halogen content within apatite alone is therefore insufficient to determine whether the felsic gneisses were subjected to periods of halogen-rich fluid flow which catalysed metamorphic reactions. A future, more detailed analysis of halogen in felsic apatite from the Eclogite Outcrop

may reveal more about the nature of retrogressive fluids (if present) in catalysing reactions within felsic gneisses.

Garnet zoning and its implications for felsic gneiss metastability

Garnet zoning can indicate progradational isobaric increase (accompanied by garnet, muscovite and rutile growth) or retrograde diffusion, providing insight into metamorphic conditions and duration (Caddick, Konopásek & Thompson, 2010; Young & Kylander-Clark, 2015). Compositional garnet zoning is often given greater importance than warranted as it is not possible to track compositional changes with growth, making compositional resetting difficult to determine (Reyes, Alarcón & Takasu, 2008). Garnet growth zonation (in garnets which grow < 650 °C, as is the case here) is indicated by high Ca and/or Mn cores and high Mg and/or Fe rims (Hollister, 1966; Krogh, 1982; Tracy et al., 1976). Analysed garnets displayed Ca growth zonation (Figure 5b, 6) and Mn retrograde diffusional zonation (Figure 6) (Hollister, 1966; Krogh, 1982; Liu & Massonne, 2019; Tracy et al. 1976).

Garnet cation endmembers (Ca, Fe, Mg, Mn) diffuse through the crystal lattice at different rates during thermal relaxation, providing time constraints for peak conditions (Caddick et al., 2010; Chakraborty, 2006). Caddick et al. (2010) modelled diffusional garnet relaxation (the process by which garnets become chemically homogeneous) as a function of crystal diameter and temperature (modelling temperatures 500–850 °C). In this study, the suspected peak and retrograde temperatures for WGC2019J-16J are ~650 °C and ~610 °C respectively. For garnet to have experienced diffusional relaxation over

a length scale equal to half their diameter (~450 μm), grains must have remained at peak conditions (or closure temperature) between ~10–20 Myr in order to preserve Ca but wipe Mn growth zoning (Caddick et al., 2010; Chakraborty, 2006). This timeframe agrees with established literature (Hacker et al., 2010; Walsh & Hacker, 2004; Young & Kylander-Clark, 2015).

The average Mn concentration in garnet increases as garnet is consumed during metamorphism because the same proportion of Mn is contained within a smaller unit area (Caddick et al., 2010; Krogh, 1982). In WGC2019J-16J, as Mn diffuses towards crystal rims, surrounding symplectitic clinopyroxene is unable to incorporate greater proportions of Mn (Petrakakis, Schuster-Bourgin, Habler & Abart, 2018). Mn enrichment in garnet rims occurs (Ikeda, 1993). Interrogation of the phase equilibria forward model for high strain eclogite revealed a maximum garnet mode of 38%, over double the final mode calculated (18%). WGC2019J-16J demonstrated inner garnet Mn concentrations (0.56 wt%) greater than the surrounding symplectitic clinopyroxene (0.05 wt%) and recorded retrograde temperatures post-symplectite formation of ~610 °C. These results indicate the garnets were compositionally wiped on the retrograde path at temperatures ~610 °C as they were modally halved by the symplectites, producing Mn enriched rims and preserving Ca growth zoning.

If high strain eclogite was subjected to peak conditions for ~10–20 Myr, adjacent felsic gneisses must have remained metastable for this time period at ~650 °C. As this study finds more evidence in support of felsic gneiss metastability (lack of HP mineral phases,

low garnet abundance), it then remains to find a plausible mechanism for this phenomenon.

Felsic gneiss metastability: A mechanism

Brueckner (2018), Krogh (1982) and Wain et al. (2001), along with many others, have found limited volumes of omphacite in HP/UHP felsic gneisses within the WGC. However, these assemblages are generally found within the direct vicinity of eclogitic boudins or shear zones (Krabbendam et al., 2000; Krabbendam & Wain, 2000; Skår & Pedersen 2003; Wain et al., 2000, 2001), which may generate external fluid that catalyses metamorphic reactions and generates HP/UHP mineral assemblages. Muscovite production in felsic gneisses during HP/UHP metamorphism is a consequence of water content (Proyer, 2003). At the Eclogite Outcrop, the paucity of hydrous minerals within felsic gneiss as compared to adjacent mafic eclogite may kinetically inhibit felsic gneiss from reacting at higher *P–T*. Studies in the WGC have shown that rock hydration decreases the pressure at which muscovite, epidote and garnet-producing reactions occur in rocks of a similar bulk composition (Young & Kylander-Clark, 2015). The preservation of prograde assemblages in WGC gneisses may therefore be a result of kinetic inhibition at pressures ~9 kbar (Young & Kylander-Clark, 2015).

A lack of external fluid may also contribute to metastability through reaction overstepping, where reactions fail due to a large Gibbs free-energy difference between stable products and metastable reactants (Pattison, de Capitaini & Gaidies, 2011; Wain et al., 2001). Anhydrous reactions experience greater overstepping (Pattison et al. 2011).

WGC2019J-17A had a dry bulk composition (H_2O = 0.34 wt%) and displayed limited evidence of external fluid influx. It is likely there was insufficient fluid (H_2O = 0.4-1 wt%; Young & Kylander-Clark, 2015) to catalyse metamorphic reactions. If felsic gneiss reactivity is a function of distance from fluid-rich mafic eclogite, it is reasonable to assume WGC2019J-17A would demonstrate mineralogical evidence of this. The fact it does not indicates the adjacent low strain eclogite (not modelled) may either have (i) not contained enough fluid to induce reactivity in WGC2019J-17A or (ii) have contained enough fluid, but been prevented by some other mechanism from inducing reactivity in WGC2019J-17A. While the role of fluid in felsic gneiss reactivity warrants further investigation (perhaps through apatite halogen analysis), the findings of this study support a model of felsic gneiss metastability within the WGC.

CONCLUSIONS

1. The study area near Lavik, Norway, experienced eclogite-facies metamorphism during the Caledonian Orogeny, based on rutile U-Pb geochronology (dates: 399.8 ± 7.8 Ma and 416 ± 18 Ma).

2. Mineral equilibria modelling indicated peak *P–T* conditions for high strain mafic eclogite WGC2019J-16J at 20–22 kbar, ~650 °C, with retrograde conditions at 8–10.5 kbar, ~610 °C marking near isothermal decompression.

3. Mineral equilibria modelling of garnet-bearing felsic gneiss WGC2019J-17A did not locate a garnet-bearing, muscovite-absent peak field. The sub-solidus muscovite-in reaction up-pressure constrained maximum possible peak *P–T* at ~8–9 kbar, ~650 °C.

4. Progradational grossular zoning and compositional wiping of spessartine zoning was observed in garnets >600 μm in high strain mafic eclogite, indicating prolonged exposure to temperatures 600–650 °C for between ~10–20 Myr based on differing rates of cation diffusion.

5. No substantial textural evidence was found within garnet-bearing felsic gneiss indicating transformation to eclogite facies during the Caledonian Orogeny, supporting maximum recorded peak *P–T* conditions calculated by mineral equilibria modelling. Evidence indicates the garnet-bearing felsic gneiss remained metastable as it was subjected to UHP conditions (~20–22 kbar, ~650°C) recorded by nearby high strain mafic eclogite.

6. The implications of these findings are that, along the Sognefjord, anhydrous felsic gneisses likely remain metastable when subjected to eclogite-facies conditions and are thus poor recorders of UHP conditions in comparison to nearby mafic eclogite.

ACKNOWLEDGMENTS

I would like to thank my supervisors, Martin Hand, Karin Barovich and Renee Tamblyn, for their unending explanations, patience and assistance throughout this project. Special acknowledgement must be given to the GSA and Playford Trust; their financial assistance allowed me to complete fieldwork in Norway. I would also like to thank Kiara Alessio, Mitchell Bockmann, Dillon Brown, Brad Cave, Jie Liu, Sean Makin, George Symonds, Kalimna Roe-Simons, Benjamin Kowaluk, Sandra Williamson, Romana Dew, Jonathan Berthiaume, Derrick Hasterok and Celina Sanso for their advice and support. Thanks must be extended to the legends at Adelaide Microscopy, Benjamin Wade, Aoife McFadden and Sarah Gilbert. I wish I could shoot lasers at rocks for a living. Special mention must be given to Brigitta Merriman-McKay and Melanie Irvine. Last – but not least – I would like to thank my fellow mid-year Honours cohort. Matt Linke, Rachel Atkins, Andrew Chua, and Brooke Lorincz – thanks for sharing the journey with me.

REFERENCES

ANDERSEN, T. B. (1998). Extensional tectonics in the Caledonides of southern Norway, an overview. *Tectonophysics, 285*(3-4), 333-351. doi: 10.1016/S0040-1951(97)00277-1

AUSTRHEIM H. & GRIFFIN W. L. (1985). Shear deformation and eclogite formation within granulite-facies anorthosites of the Bergen Arcs, western Norway. *Chemical Geology, 50*(1-3), 267-281. doi: 10.1016/0009-2541(85)90124-X

BAXTER E. F. & CADDICK M. J. (2013). Garnet growth as a proxy for progressive subduction zone dehydration, *Geology, 41*(6), 643-646. doi: 10.1130/G34004.1

BAXTER, E. F., CADDICK, M. J., & AGUE, J. J. (2013). Garnet: Common mineral, uncommonly useful. *Elements, 9*(6), 415-419. doi:10.2113/gselements.9.6.415

BODUR, Ö. F., GÖĞÜŞ, O. H., PYSKLYWEC, R. N., & OKAY, A. I. (2018). Mantle lithosphere rheology, vertical tectonics, and the exhumation of (U)HP rocks. *Journal of Geophysical Research: Solid Earth*, *123*(2), 1824-1839. doi:10.1002/2017JB014546

BOYNTON, W.V. (1984). Cosmochemistry of the rare earth elements: meteorite studies. In P. Henderson (Ed.), *Rare Earth Element Geochemistry* (pp. 63-114). New York, NY: Elsevier.

BRAATHEN, A., & ERAMBERT, M. (2014). Structural and metamorphic history of the Engebøfjellet Eclogite and the exhumation of the Western Gneiss Region, Norway. *Norsk Geologisk Tidsskrift, 94*(1), 53-76.

BRUECKNER, H. K. (2018). The great eclogite debate of the Western Gneiss Region, Norwegian Caledonides: The in situ crustal v. exotic mantle origin controversy. *Journal of Metamorphic Geology, 36*(5), 517-527. doi:10.1111/jmg.12314

BRUECKNER, H. K., & CUTHBERT, S. J. (2013). Extension, disruption, and translation of an orogenic wedge by exhumation of large ultrahigh-pressure terranes: Examples from the Norwegian Caledonides. *Lithosphere, 5*(3), 277-289. doi:10.1130/L256.1

CADDICK, M. J., KONOPÁSEK, J., & THOMPSON, A. B. (2010). Preservation of garnet growth zoning and the duration of prograde metamorphism. *Journal of Petrology, 51*(11), 2327-2347. doi:10.1093/petrology/egq059

CARSON, C.J., POWELL, R. & CLARKE, G.L. (1999). Calculated mineral equilibria for eclogites in CaO–Na2O–FeO–MgO–Al2O3–SiO2–H2O: application to the Pouébo Terrane, Pam Peninsula, New Caledonia. *Journal of Metamorphic Geology*, *17*(1), 9–24. doi: 10.1046/j.1525-1314.1999.00177.x

CARSWELL, D. A., BRUECKNER, H. K., CUTHBERT, S. J., MEHTA, K., & O'BRIEN, P. J. (2003). The timing of stabilisation and the exhumation rate for ultra-high pressure rocks in the Western Gneiss Region of Norway. *Journal of Metamorphic Geology, 21*(6), 601-612. doi:10.1046/j.1525-1314.2003.00467.x

CARSWELL, D. A., TUCKER, R. D., O'BRIEN, P. J., & KROGH, T. E. (2003). Coesite micro-inclusions and the U/Pb age of zircons from the Hareidland Eclogite in the Western Gneiss Region of Norway. *Lithos, 67*(3-4), 181-190. doi:10.1016/S0024-4937(03)00014-8

CAVE, B. J., STEPANOV, A. S., LARGE, R. R., HALPIN, J. A., & THOMPSON, J. (2015). Release of trace elements through the sub-greenschist facies breakdown of detrital rutile to metamorphic titanite in the Otago Schist, New Zealand. *Canadian Mineralogist, 53*(3), 379-400. doi:10.3749/canmin.1400097

CHAKRABORTY, S. (2006). Diffusion modeling as a tool for constraingin timescales of evolution of metamorphic rocks. *Mineral and Petrology, 88*(1-2), 7-27. doi: 10.1007/s00710-006-0152-6

CHAUVET, A., & DALLMEYER, R. D. (1992). 40Ar/39Ar mineral dates related to Devonian extension in the southwestern Scandinavian Caledonides. *Tectonophysics, 210*(1-2), 155-177. doi: 10.1016/0040-1951(92)90133-Q

CHAUVET, A., KIENAST, J. R., PINARDON, J. L., & BRUNEL, M. (1992). Petrological constraints and PT path of Devonian collapse tectonics within the Scandian mountain belt (Western Gneiss Region, Norway). *Journal of the Geological Society, London, 149*(3), 383-400. doi: 10.1144/gsjgs.149.3.0383

CHERNIAK, D.J. (2000). Pb diffusion in rutile, *Contributions to Mineralogy and Petrology, 139*, 198-207. doi: 10.1007/PL00007671

CORFU, F., HANCHAR, J.M., HOSKIN, P.W.O. & KINNY, P. (2003). Atlas of Zircon Textures. *Reviews in Mineralogy and Geochemisty, 53*(1), 469-500. doi: 10.2113/0530469

CUTHBERT, S. J., CARSWELL, D. A., KROGH-RAVNA, E. J., & WAIN, A. (2000). Eclogites and eclogites in the Western Gneiss region, Norwegian Caledonides. *Lithos, 52*(1-4), 165-195. doi:10.1016/S0024-4937(99)00090-0

DIENER, J. F. A., & POWELL, R. (2012). Revised activity-composition models for clinopyroxene and amphibole. *Journal of Metamorphic Geology, 30*(2), 131-142. doi:10.1111/j.1525-1314.2011.00959.x

DIETLER, T. N., KOESTLER, A. G., & MILNES, A. G. (1985). A preliminary structural profile through the Western Gneiss complex, Sognefjord, southwestern Norway. *Norsk Geologisk Tidsskrift, 65*(3), 233-235.

DROOP, G. T. R. (1987). A general equation for estimating Fe3+ concentrations in ferromagnesian silicates and oxides from microprobe analyses, using stoichiometric criteria. *Mineralogical Society,* 51(361), 431-435. doi:10.1180/minmag.1987.051.361.10

ENGVIK, A.K., AUSTRHEIM, H. & ANDERSEN, T.B. (2000). Structural, mineralogical and petrophysical effects on deep crustal rocks of fluid-limited polymetamorphism, Western Gneiss Region, Norway. *Journal of the Geological Society, 157*(1), 121-134.

ERNST, W. G. (1999). Metamorphism, partial preservation, and exhumation of ultrahigh-pressure belts. *Island Arc, 8*(2), 125-153. doi:10.1046/j.1440-1738.1999.00227.x

FIELDING, L., NAJMAN, Y., MILLAR, I., BUTTERWORTH, P., ANDO, S., PADOAN, M., BARFORD, D. & KNELLER, B. (2016). A detrital record of the Nile River and its catchment. *Journal of the Geological Society*, *174*(2), 301-317. doi: 10.1144/jgs2016-075

GAAL, G., & GORBATSCHEV, R. (1987). An Outline of the precambrian evolution of the baltic shield. *Precambrian Research, 35*(C), 15-52. doi:10.1016/0301-9268(87)90044-1

GAO, X., & ZHENG, Y. (2011). On the Zr-in-rutile and Ti-in-zircon geothermometers. *Acta Petrologica Sinica, 27*(2), 417-432.

GARBER, J. M., HACKER, B. R., KYLANDER-CLARK, A. R. C., STEARNS, M., & SEWARD, G. (2017). Controls on Trace Element Uptake in Metamorphic Titanite: Implications for Petrochronology. *Journal of Petrology, 58*(6), 1031-1057. doi:10.1093/petrology/egx046

GHENT, E. D., & STOUT, M. Z. (1981). Geobarometry and geothermometry of plagioclase-biotite-garnet-muscovite assemblages. *Contributions to Mineralogy and Petrology, 76*(1), 92-97. doi:10.1007/BF00373688

GOLDSMITH, J. R. (1982). Review of the behavior of plagioclase under metamorphic conditions. *American Mineralogist, 67*(7-8), 643-652.

GREEN, E. C. R., WHITE, R. W., DIENER, J. F. A., POWELL, R., HOLLAND, T. J. B., & PALIN, R.M. (2016). Activity-composition relations for the calculation of partial melting equilibria in metabasic rocks. *Journal of Metamorphic Geology, 34*(9), 845-869. doi:10.1111/jmg.12211

GRIFFIN, W. L., & BRUECKNER, H. K. (1980). Caledonian Sm-Nd ages and a crustal origin for Norwegian eclogites. *Nature, 285*(5763), 319-321. doi:10.1038/285319a0

GRIFFIN, W. L., & BRUECKNER, H. K. (1985). REE, RbSr and SmNd studies of Norwegian eclogites. *Chemical Geology: Isotope Geoscience Section, 52*(2), 249-271. doi:10.1016/0168-9622(85)90021-1

HACKER, B. R., ANDERSEN, T. B., JOHNSTON, S., KYLANDER-CLARK, A. R. C., PETERMAN, E. M., WALSH, E. O., & YOUNG, D. (2010). High-temperature deformation during continental-margin subduction & exhumation: The ultrahigh-pressure Western Gneiss Region of Norway. *Tectonophysics, 480*(1-4), 149-171. doi:10.1016/j.tecto.2009.08.012

HACKER, B. R., ANDERSEN, T. B., ROOT, D. B., MEHL, L., MATTINSON, J. M., & WOODEN, J. L. (2003). Exhumation of high-pressure rocks beneath the Solund Basin, Western Gneiss Region of Norway. *Journal of Metamorphic Geology, 21*, 613-629. doi:https://doi.org/10.1046/j.1525-1314.2003.00468.x

HELLSTROM, J., PATON, C., WOODHEAD, J., & HERGT, J. (2008). Iolite: software for spatially resolved LA-(quad and MC) ICPMS analysis. In P. Sylvester (Ed.), *Laser Ablation ICP–MS in the Earth Sciences: Current Practices and Outstanding Issues, Mineralogical Association of Canada Short Course Series, 40*, (pp. 343-348). Vancouver, VN: Mineralogical Association of Canada.

HOLLAND, T. J. B., & POWELL, R. (1990). An enlarged and updated internally consistent thermodynamic dataset with uncertainties and correlations: the system K2O–Na2O–CaO–MgO–MnO–FeO–Fe2O3–Al2O3–TiO2–SiO2–C–H2–O2. *Journal of Metamorphic Geology, 8*(1), 89-124. doi:10.1111/j.1525-1314.1990.tb00458.x

HOLLAND, T. J. B., & POWELL, R. (2003). Activity–composition relations for phases in petrological calculations: an asymmetric multicomponent formulation. *Contributions to Mineralogy and Petrology, 145*, 492-501. doi:10.1007/s00410-003-0464-z

HOLLAND, T. J. B., & POWELL, R. (2011). An improved and extended internally consistent thermodynamic dataset for phases of petrological interest, involving a new equation of state for solids. *Journal of Metamorphic Geology, 29*(3), 333-383. doi:10.1111/j.1525-1314.2010.00923.x

HOLLAND, T. J. B., GREEN, E. C. R., & POWELL, R. (2018). Melting of peridotites through to granites: A simple thermodynamic model in the system KNCFMASHTOCr. *Journal of Petrology, 59*(5), 881-900. doi:10.1093/petrology/egy048

HOLLAND, T., BAKER, J., & POWELL, R. (1998). Mixing properties and activity-composition relationships of chlorites in the system MgO-FeO-Al2O3-SiO2-H2O. *European Journal of Mineralogy, 10*(3), 395-406. doi:10.1127/ejm/10/3/0395

HOLLISTER, L. S. (1966). Garnet zoning: An interpretation based on the Rayleigh fractionation model. *Science, 154*(3757), 1651-1653. doi:10.1126/science.154.3757.1647

HOLNESS, M. B. (1995). The effect of feldspar on quartz-H2O-CO2 dihedral angles at 4 kbar, with consequences for the behaviour of aqueous fluids in migmatites. *Contributions to Mineralogy and Petrology, 118*(4), 356-364. doi:10.1007/s004100050020

IKEDA, T. (1993). Compositional zoning patterns of garnet during prograde metamorphism from the Yanai district, Ryoke metamorphic belt, southwest Japan. *Lithos, 30*(2), 109-121. doi:10.1016/0024-4937(93)90010-A

JACKSON, S. E., PEARSON, N. J., GRIFFIN, W. L., & BELOUSOVA, E. A. (2004). The application of laser ablation-inductively coupled plasma-mass spectrometry to in situ U–Pb zircon geochronology. *Chemical Geology, 211*(4), 47-69. doi: 10.1016/j.chemgeo.2004.06.017

JAMTVEIT, B., CARSWELL, D. A., & MEARNS, E. W. (1991). Chronology of the high-pressure metamorphism of Norwegian garnet peridotites/pyroxenites. *Journal of Metamorphic Geology, 9*(2), 125-139. doi:10.1111/j.1525-1314.1991.tb00509.x

JEDLICKA, R., & FARYAD, S. W. (2017). Felsic granulite with layers of eclogite facies rocks in the Bohemian Massif; did they share a common metamorphic history? *Lithos,* 286-287, 408-425. doi:10.1016/j.lithos.2017.06.027

JENNINGS, E. S., & HOLLAND, T. J. B. (2015). A simple thermodynamic model for melting of peridotite in the system NCFMASOCr. *Journal of Petrology, 56*(5), 869-892. doi:10.1093/petrology/egv020

JOCHUM, K. P., WEIS, U., STOLL, B., KUZMIN, D., YANG, Q., RACZEK, I., FRICK, D. A., GUNTHER, D. & ENZWEILER, J. (2011). Determination of reference values for NIST SRM 610–617 glasses

following ISO guidelines. *Geostandards and Geoanalytical Research, 35*(4), 397-429. doi: 10.1111/j.1751-908X.2011.00120.x

JOHNSON, T. E., & WHITE, R. W. (2011). Phase equilibrium constraints on conditions of granulite-facies metamorphism at Scourie, NW Scotland. *Journal of the Geological Society, 168*(1), 147-158. doi:10.1144/0016-76492010-069

KOOIJMAN, E., MEZGER, K., & BERNDT, J. (2010). Constraints on the U-Pb systematics of metamorphic rutile from in situ LA-ICP-MS analysis. *Earth and Planetary Science Letters, 293*(3-4), 321-330. doi:10.1016/j.epsl.2010.02.047

KOONS, P. O., RUBIE, D. C., & FRUCH-GREEN, G. (1987). The effects of disequilibrium and deformation on the mineralogical evolution of quartz diorite during metamorphism in the eclogite facies. *Journal of Petrology, 28*(4), 679-700. doi:10.1093/petrology/28.4.679

KRABBENDAM, M. & WAIN, A. (1997). Late-Caledonian structures, differential retrogression and structural position of (ultra)high-pressure rocks in the Nordfjord – Stadlandet area, Western Gneiss Region. *Norgesqeoloqiske undersekelse Bulletin, 432*(1), 27-139.

KRABBENDAM, M., WAIN, A., & ANDERSEN, T. B. (2000). Pre-Caledonian granulite and gabbro enclaves in the Western Gneiss Region, Norway: Indications of incomplete transition at high pressure. *Geological Magazine, 137*(3), 235-255. doi:10.1017/S0016756800004015

KROGH, T. E., KAMO, S. L., ROBINSON, P., TERRY, M. P., & KWOK, K. (2011). U-Pb zircon geochronology of eclogites from the Scandian Orogen, Northern Western Gneiss Region, Norway: 14-20 million years between eclogite crystallization and return to amphibolitefacies conditions. *Canadian Journal of Earth Sciences, 48*(2), 441-472. doi: 10.1139/E10-076

KROGH, T.E. (1982). Improved accuracy of U–Pb zircon ages by the creation of more concordant systems using an air abrasion technique. *Geochimica et Cosmochimica Acta, 46*(4): 637–649. doi:10.1016/0016-7037(82)90165-X.

KULLERUD, L., TORUDBAKKEN, B. O., & ILEBEKK, S. (1986). A compilation of radiometric age determinations from the Western Gneiss Region, South Norway. *Norges Geologiske Undersøkelse Bulletin, 406*(1742).

KYLANDER-CLARK, A. R. C., & HACKER, B. R. (2014). Age and significance of felsic dikes from the UHP western gneiss region. *Tectonics, 33*(12), 2342-2360. doi:10.1002/2014TC003582

KYLANDER-CLARK, A. R. C., HACKER, B. R., & MATTINSON, J. M. (2008). Slow exhumation of UHP terranes: Titanite and rutile ages of the Western Gneiss Region, Norway. *Earth and Planetary Science Letters, 272*(3-4), 531-540. doi:10.1016/j.epsl.2008.05.019

KYLANDER-CLARK, A. R. C., HACKER, B. R., JOHNSON, C. M., BEARD, B. L., & MAHLEN, N. J. (2009). Slow subduction of a thick ultrahigh-pressure terrane. *Tectonics, 28*(2). doi:10.1029/2007TC002251

KYLANDER-CLARK, A. R. C., HACKER, B. R., JOHNSON, C. M., BEARD, B. L., MAHLEN, N. J., & LAPEN, T. J. (2007). Coupled Lu-Hf and Sm-Nd geochronology constrains prograde and exhumation histories of high- and ultrahigh-pressure eclogites from western Norway. *Chemical Geology, 242*(1-2), 137-154. doi:10.1016/j.chemgeo.2007.03.006

LIU, P., & MASSONNE, H. J. (2019). Tectonic implications of *P–T* paths derived for garnet-bearing felsic gneisses from the dabie and sulu ultrahigh pressure terranes, East-Central China. *American Journal of Science, 319*(9), 788-817. doi:10.2475/09.2019.03

LIU, P., MASSONNE, H. J., JIN, Z., WU, Y., & ZHANG, J. (2017). Diopside, apatite, and rutile in an ultrahigh pressure impure marble from the Dabie Shan, eastern China: A record of eclogite-facies metasomatism during exhumation. *Chemical Geology*, 466, 123-139. doi:10.1016/j.chemgeo.2017.06.001

LIU, X., FU, B., LI, Q., ZHAO, Y., LIU, J., & CHEN, H. (2020). The impact of the Pan-African-aged tectonothermal event on high-grade rocks at Mount Brown, East Antarctica. *Antarctic Science, 32*(1), 45-57. doi:10.1017/S0954102019000518

LIU, X., JAHN, B. M., DONG, S., LI, H., & OBERHÄNSLI, R. (2003). Neoproterozoic granitoid did not record ultrahigh-pressure metamorphism from the southern Dabieshan of China. *Journal of Geology, 111(*6), 719-732. doi:10.1086/378336

LUVIZOTTO, G. L., ZACK, T., MEYER, H. P., LUDWIG, T., TRIEBOLD, S., KRONZ, A., . . . VON EYNATTEN, H. (2009). Rutile crystals as potential trace element and isotope mineral standards for microanalysis. *Chemical Geology, 261(*3-4), 346-369. doi:10.1016/j.chemgeo.2008.04.012

MALLMANN, G. & O'NEILL, H.S.C. (2009). The crystal/melt partitioning of V during mantle melting as a function of oxygen fugacity compared with some other elements (Al, P, Ca, Sc, Ti, Cr, Fe, Ga, Y, Zr and Nb), *Journal of Petrology, 50*(9), 1765–1794.

MARTIN, C & DUCHÊNE, S (2015). Residual water in hydrous minerals as a kinetic factor for omphacite destabilization into symplectite in the eclogites of Vårdalsneset (WGR, Norway). *Lithos,* (232), 162-173. doi: 10.1016/j.lithos.2015.06.021

MASSONNE, H. J. (2009). Hydration, dehydration, and melting of metamorphosed granitic and dioritic rocks at high- and ultrahigh-pressure conditions. *Earth and Planetary Science Letters, 288*(1-2), 244-254. doi:10.1016/j.epsl.2009.09.028

MASSONNE, H., WILLNER, A., & GERYA, T. (2007). Densities of metapelitic rocks at high to ultrahigh pressure conditions: What are the geodynamic consequences? *Earth and Planetary Science Letters, 256*(1-2), 12-27. doi:10.1016/j.epsl.2007.01.013

MEARNS, E. W. (1986). SmNd ages for norwegian garnet peridotite. *Lithos, 19*(3-4), 269-278. doi:10.1016/0024-4937(86)90027-7

MEZGER, K., ESSENE, E. J., & HALLIDAY, A. N. (1992). Closure temperatures of the SmNd system in metamorphic garnets. *Earth and Planetary Science Letters, 113*(3), 397-409. doi:10.1016/0012-821X(92)90141-H

MILNES, A. G., WENNBERG, O. P., SKÅR, Ø., & KOESTLER, A. G. (1997) Contraction, extension and timing in the South Norwegian Caledonides: the Sognefjord transect. In*: Vol. 121. Geological Society Special Publication* (pp. 123-148).

MØRK, M. B. E., & MEARNS, E. W. (1986). SmNd isotopic systematics of a gabbro-eclogite transition. *Lithos, 19*(3-4), 255-267. doi:10.1016/0024-4937(86)90026-5

MORRISSEY, L. J., HAND, M., KELSEY, D. E., & WADE, B. P. (2016). Cambrian high-temperature reworking of the Rayner-Eastern ghats terrane: Constraints from the Northern Prince Charles Mountains region, East Antarctica. *Journal of Petrology, 57*(1), 53-91. doi:10.1093/petrology/egv082

MORRISSEY, L.J., HAND, M., KELSEY, D.E. & WADE, B.P. (2016). Cambrian high-temperature reworking of the Rayner-Eastern ghats terrane: Constraints from the Northern Prince Charles Mountains region, East Antarctica. *Journal of Petrology, 57*(1), 53–91. https://doi.org/10.1093/petrology/egv082

PALIN, R.M., WHITE, R.W. & GREEN, E.C.R. (2016a). Partial melting of metasbasic rocks and the generation of tonalitic-trondhjemitic-granodioritic (TTG) crust in the Archaean: Constraints from phase equilibrium modelling. *Precambrian Research, 287,* 73-90. doi: 10.1016/j.precamres.2016.11.001.

PALIN, R.M., WHITE, R.W., GREEN, E.C.R., DIENER, J.F.A., POWELL, R. & HOLLAND, T.J.B. (2016b). High-grade metamorphism and partial melting of basic and intermediate rocks, *Journal of Metamorphic Geology, 34*(9), 871-892. doi:10.1111/jmg.12212

PATON, C., HELLSTROM, J., PAUL, B., WOODHEAD, J., & HERGT, J. (2011). Iolite: Freeware for the visualisation and processing of mass spectrometic data. *Journal of Analytical Atomic Spectrometry, 26*(12), 2508-2518. doi:10.1039/C1JA10172B

PATTISON, D. R. M., DE CAPITANI, C., & GAIDIES, F. (2011). Petrological consequences of variations in metamorphic reaction affinity. *Journal of Metamorphic Geology, 29*(9), 953-977. doi:10.1111/j.1525-1314.2011.00950.x

PAYNE, J. L., HAND, M., BAROVICH, K., & WADE, B. (2008). Temporal constraints on the timing of high-grade metamorphism in the norther Gawler Craton: implications for assembly of the Australian Proterozoic. *Australian Journal of Earth Sciences, 55*(5), 623-640. doi: 10.1080/08120090801982595

PEARCE, M. A., WHITE, A. J. R., & GAZLEY, M. F. (2015). TCInvestigator: automated calculation of mineral mode and composition contours for thermocalc pseudosections. *Journal of Metamorphic Geology, 33*(4), 413-425. doi:10.1111/jmg.12126

PETERMAN, E. M., HACKER, B. R., & BAXTER, E. F. (2010). Phase transformations of continental crust during subduction and exhumation: Western Gneiss Region, Norway. *European Journal of Mineralogy, 21*(6), 1097-1118. doi:10.1127/0935-1221/2009/0021-1988

PETRAKAKIS, K., SCHUSTER-BOURGIN, N., HABLER, G. & ABART, R (2018). Ca-rich garnets and associated symplectites in mafic peraluminous granulites from the Gföhl Nappe System, Austria. *Solid Earth, 9,* 797-819. doi: 10.5194/se-9-797-2018

PROYER, A. (2003). The preservation of high-pressure rocks during exhumation: metagranites and metapelites. *Lithos, 70*(3-4), 183-194. doi:10.1016/s0024-4937(03)00098-7

RAASE, P (1974). Al and Ti Contents of Hornblende, Indicators of Pressure and Temperature of Regional Metamorphism. *Contributions to Mineralogy and Petrology, 45,* 231-236. doi: 10.1007/BF00383440

RAPP, R.P. & WATSON, E.B. (1995). Dehydration melting of metabasalt at 8–32 kbar: implications for continental growth and crust–mantle recycling. *Journal of Petrology, 36*(4), 891–931. doi: 10.1093/petrology/36.4.891

REBAY, G., POWELL, R., DIENER & J.F.A. (2010). Calculated phase equilibria for a MORB composition in a P–T range, 450–650°C and 18–28 kbar: the stability of eclogite. *Journal of Metamorphic Geology, 28*(6), 635–645. doi:10.1111/j.1525-1314.2010.00882.x

REYES, C.A.R., ALARCÓN, O.M.C., & TAKASU, A (2008). A new interpretation for the garnet zonign in metapelitic rocks of the Silgará Formation, southwestern Santander Massif, Colombia. *Earth Sciences Research Journal, 12*(1), 7-30.

RØHR, T. S., BINGEN, B., ROBINSON, P., & REDDY, S. M. (2013). Geochronology of Paleoproterozoic Augen Gneisses in the Western Gneiss Region, Norway: Evidence for Sveconorwegian Zircon Neocrystallization and Caledonian Zircon Deformation. *The Journal of Geology, 121*(2), 105-128. doi:10.1086/669229

ROOT, D. B., HACKER, B. R., GANS, P. B., DUCEA, M. N., EIDE, E. A., & MOSENFELDER, J. L. (2005). Discrete ultrahigh-pressure domains in the Western Gneiss Region, Norway: implications for formation and exhumation. *Journal of Metamorphic Geology, 23*(1), 45-61. doi:10.1111/j.1525-1314.2005.00561.x

ROOT, D. B., HACKER, B. R., MATTINSON, J. M., & WOODEN, J. L. (2004). Zircon geochronology and ca. 400 Ma exhumation of Norwegian ultrahigh-pressure rocks: An ion microprobe and chemical abrasion study. *Earth and Planetary Science Letters, 228*(3-4), 325-341. doi:10.1016/j.epsl.2004.10.019

RUBIE, D. C. (1983). Reaction-enhanced ductility: The role of solid-solid univariant reactions in deformation of the crust and mantle. *Tectonophysics, 96*(3-4), 331-352. doi:10.1016/0040-1951(83)90225-1

SCHILLING, J.-G., ZAJEC, M., EVANS, R., JOHNSTON, T., WHITE, W., DEVINE, J.D. & KINGSLEY, R. (1983). Petrologic and geochemical variations along the Mid-Atlantic Ridge from 27°N to 73°N. *American Journal of Science, 283*(6), 510–586. doi:10.2475/ajs.283.6.510

SKAR, Ø. (1998). *The Proterzoic and Early Paleozoic evolution of the southern parts of the Western Gneiss Complex, Norway.* (PhD), University of Bergen,

SKAR, Ø. (2000). Field relations and geochemical evolution of the Gothian rocks in the KvamsØy area, southern Western Gneiss Complex, Norway. *Norges Geologiske Undersøkelse Bulletin, 437*, 5-23.

SKAR, Ø., & PEDERSEN, R. B. (2003). Relations between granitoid magmatism and migmatization: U - Pb geochronological evidence from the Western Gneiss Complex, Norway. *Journal of the Geological Society, 160*(6), 935-946. doi:10.1144/0016-764901-121

SLÁMA, J., KOŠLER, J., CONDON, D. J., CROWLEY, J. L., GERDES, A., HANCHAR, J. M.,… WHITEHOUSE, M.J. (2008). Plešovice zircon—a new natural reference material for U–Pb and Hf isotopic microanalysis. *Chemical Geology, 249*(1), 1-35. doi:10.1016/j.chemgeo.2007.11.005

SPENGLER, D., BRUECKNER, H. K., VAN ROERMUND, H. L. M., DRURY, M. R., & MASON, P. R. D. (2009). Long-lived, cold burial of Baltica to 200 km depth. *Earth and Planetary Science Letters, 281*(1-2), 27-35. doi:10.1016/j.epsl.2009.02.001

STORKEY, A.C., HERMANN, J, HAND, M & BUICK, I.S. (2005). Using In Situ Trace-Element Determinations to Monitor Partial-Melting Processes in Metabasites. *Journal of Petrology, 46*(6), 1283-1308. doi: 10.1093/petrology/egi017

SUN, S.S. & McDONOUGH, W.F. (1989). Chemical and isotopic systematics of oceanic basalts: implications for mantle composition and processes. In A.D. Saunders & M.J. Norry (Eds.), *Magmatism in ocean basins.* Geological Society of London Special Publication 42 (pp. 313-345). London, UK: Geological Society of London.

TAMBLYN, R., HAND, M., KELSEY, D., ANCZKIEWICZ, R., & OCH, D. (2020). Subduction and accumulation of lawsonite eclogite and garnet blueschist in eastern Australia. *Journal of Metamorphic Geology, 38*(2), 157-182. doi: 10.111/jmg.12516.

TERRY, M. P., ROBINSON, P., HAMILTON, M. A., & JERCINOVIC, M. J. (2000). Monazite geochronology of UHP and HP metamorphism, deformation, and exhumation Nordøyane, Western Gneiss Region, Norway. *American Mineralogist, 85*(11-12), 1651-1664. doi:10.2138/am-2000-11-1208

TINKHAM, D. K., ZULUAGA, C. A., & STOWELL, H. H. (2003). Metapelite phase equilibria modeling in MnNCKFMASH: The effect of variable Al2O3 and MgO/(MgO + FeO) on mineral stability. *American Mineralogist, 88*(7), 1174.

TOMKINS, H. S., POWELL, R., & ELLIS, D. J. (2007). The pressure dependence of the zirconium-in rutile thermometer. Journal of Metamorphic Geology, 25(6), 703-713. doi:10.1111/j.1525-1314.2007.00724.x

TRACY, R. J., ROBINSON, P & THOMPSON, A. B. (1976). Garnet composition and zoning in the determination of temperature and pressure of metamorphism, central Massachusetts. *American Mineralogist, 61*(7-8): 762–775.

TUCKER, R. D., KROGH, T. E., & RAHEIM, A. (1990). Proterozoic evolution and age province boundaries in the central part of the Western Gneiss Region, Norway: results of U-Pb dating of accessory minerals from Trondheimsfjord to Geiranger. In C. F. Gower, T. Rivers, & B. Ryan (Eds.), *Mid-Proterozoic Geology of the Southern Margin of ProtoLaurentia-Baltica* (Vol. 38, pp. 149-173): Geological Association of Canada.

TUCKER, R. D., RAHEIM, A., KROGH, T. E., & CORFU, F. (1987). Uranium-lead zircon and titanite ages from the northern portion of the Western Gneiss Region, south-central Norway. *Earth and Planetary Science Letters, 81*(2-3), 203-211. doi:10.1016/0012-821X(87)90156-7

VAN ORMAN, J. A., GROVE, T. L., SHIMIZU, N. & LAYNE, G. D. (2002). Rare earth element diffusion in a natural pyrope single crystal at 2·8 GPa. *Contributions to Mineralogy and Petrology*, *142*(4), 416–424. doi:10.1007/s004100100304

VRIJMOED, J. C., VAN ROERMUND, H. L. M., & DAVIES, G. R. (2006). Evidence for diamond-grade ultra-high pressure metamorphism and fluid interaction in the Svartberget Fe-Ti garnet peridotite-websterite body, Western Gneiss Region, Norway. *Mineralogy and Petrology, 88*(1-2), 381-405. doi:10.1007/s00710-006-0160-6

WAIN, A. (1997). New evidence for coesite in eclogite and gneisses: Defining an ultrahigh-pressure province in the Western Gneiss region of Norway. *Geology, 25*(10), 927-930. doi:10.1130/0091-7613(1997)025<0927:NEFCIE>2.3.CO;2

WAIN, A. (1998). *Ultrahigh-pressure metamorphism in the Western Gneiss Region of Norway.* (Doctor of Philosophy PhD), University of Oxford.

WAIN, A. L., WATERS, D. J., & AUSTRHEIM, H. (2001). Metastability of granulites and processes of eclogitisation in the UHP region of Western Norway. *Journal of Metamorphic Geology, 19*(5), 607-623. doi:10.1046/j.0263-4929.2001.00333.x

WAIN, A., WATERS, D., JEPHCOAT, A., & OLIJYNK, H. (2000). The high-pressure to ultrahigh-pressure eclogite transition in the Western Gneiss Region, Norway. *European Journal of Mineralogy, 12*(3), 667-687. doi:10.1127/0935-1221/2000/0012-0667

WALSH, E. O., & HACKER, B. R. (2004). The fate of subducted continental margins: Two-stage exhumation of the high-pressure to ultrahigh-pressure Western Gneiss Region, Norway. *Journal of Metamorphic Geology, 22*(7), 671-687. doi:10.1111/j.1525-1314.2004.00541.x

WALSH, E. O., HACKER, B. R., GANS, P. B., WONG, M. S., & ANDERSEN, T. B. (2013). Crustal exhumation of the Western Gneiss Region UHP terrane, Norway: 40Ar/39Ar thermochronology and fault-slip analysis. *Tectonophysics, 608*(26), 1159-1179. doi:10.1016/j.tecto.2013.06.030

WHITE, R. W., POWELL, R., & JOHNSON, T. E. (2014). The effect of Mn on mineral stability in metapelites revisited: new a-x relations for manganese-bearing minerals. *Journal of Metamorphic Geology, 32*(8), 809-828. doi:10.1111/jmg.12095

WHITE, R. W., POWELL, R., HOLLAND, T. J. B., & WORLEY, B. A. (2000). The effect of TiO2 and Fe2O3 on metapelitic assemblages at greenschist and amphibolite facies conditions: mineral equilibria calculations in the system K2O–FeO–MgO–Al2O3–SiO2–H2O–TiO2–Fe2O3. *Journal of Metamorphic Geology, 18*(5), 497-511. doi:10.1046/j.1525-1314.2000.00269.x

WHITE, R. W., POWELL, R., HOLLAND, T. J. B., JOHNSON, T. E., & GREEN, E. C. R. (2014). New mineral activity-composition relations for thermodynamic calculations in metapelitic systems. *Journal of Metamorphic Geology, 32*(3), 261-286. doi:10.1111/jmg.12071

WIEDENBECK, M., ALLE, P., CORFU, F., GRIFFIN, W. L., MEIER, M., OBERLI, F., . . . SPIEGEL, W. (1995). Three natural zircon standards for U-Th-Pb, Lu-Hf, trace ele-ment and REE analyses. *Geostandards Newsletter, 19*, 1-23. doi: 10.1111/j.1751-908X.1995.tb00147.x.

WIEST, J. D., JACOBS, J., KSIENZYK, A. K., & FOSSEN, H. (2018). Sveconorwegian vs. Caledonian orogenesis in the eastern Øygarden Complex, SW Norway – Geochronology, structural constraints and tectonic implications. *Precambrian Research, 305*, 1-18. doi:10.1016/j.precamres.2017.11.020

WIEST, J. D., OSMUNDSEN, P. T., JACOBS, J., & FOSSEN, H. (2019). Deep crustal flow within post-orogenic metamorphic core complexes – Insights from the southern Western Gneiss Region of Norway. *Tectonics, 38*(12), 4267-4289. doi:10.1029/2019tc005708

YOUNG, D. J. (2018). Structure of the (ultra)high-pressure Western Gneiss Region, Norway: Imbrication during Caledonian continental margin subduction. *Bulletin of the Geological Society of America, 130*(5-6), 926-940. doi:10.1130/B31764.1

YOUNG, D. J., & KYLANDER-CLARK, A. R. C. (2015). Does continental crust transform during eclogite facies metamorphism? *Journal of Metamorphic Geology, 33*(4), 331-357. doi:10.1111/jmg.12123

YOUNG, D. J., HACKER, B. R., ANDERSEN, T. B., & CORFU, F. (2007). Prograde amphibolite facies to ultrahigh-pressure transition along Nordfjord, western Norway: Implications for exhumation tectonics. *Tectonics, 26*(1), n/a-n/a. doi:10.1029/2004tc001781

YOUNG, D. J., HACKER, B. R., ANDERSEN, T. B., & GANS, P. B. (2011). Structure and 40Ar/39Ar thermochronology of an ultrahigh-pressure transition in western Norway. *Journal of the Geological Society, 168*(4), 887-898. doi:10.1144/0016-76492010-075

ZACK, T. & KOOIJMAN, E (2017). Petrology and Geochronology of Rutile, *Reviews in Mineralogy and Geochemistry, 83*(1), 443-467. doi:10.2138/rmg.2017.83.14.

ZACK, T., STOCKLI, D. F., LUVIZOTTO, G. L., BARTH, M. G., BELOUSOVA, E., WOLFE, M. R., & HINTON, R. W. (2011). In situ U–Pb rutile dating by LA-ICP-MS: 208Pb correction and prospects for geological applications. *Contributions to Mineralogy and Petrology, 162*(3), 515-530. doi:10.1007/s00410-011-0609-4

ZHANG, R. Y., & LIOU, J. G. (1997). Partial transformation of gabbro to coesite-bearing eclogite from Yangkou, the Sulu terrane, eastern China. *Journal of Metamorphic Geology, 15*(2), 183-202. doi:10.1111/j.1525-1314.1997.00012.x

Appendix 1: Eclogite Outcrop Sample List and Description

Note that for sample descriptions, lithological unit names may differ slightly from those in Figure 2. This indicates assumptions that were made in the field regarding the age of specific lithological units (e.g. Caledonian gneiss), which aided in discussion but were not scientifically proven at the time. The following Appendix aims to record the evolution of thought with respect to outcrop geology over the project's duration.

Sample	Description (direct from field)	Grid Reference		
WGC 2019J-1	Opx-bearing mafic gneiss	32V	308232	6776799
WGC 2019J-2	Gt-bearing leucosome in mafic gneiss	32V	308232	6776799
WGC-2019J-3	Cpx-hbl felsic gneiss with titanite coronas around ilm	32V	308232	6776799
WGC2019J-4	Retrogressed opx-bearing mafic gneiss with gt-cpx coronas - shear zone on the edge of the mafic gneiss.	32V	308232	6776799
WGC2019-5	Transitional-prograde features; toward eclogite	32V	308333	6776880
WGC2019J-6	Sample ~15m east of eclogite high strain zone- titanite target	32V	308375	6776935
WGC2019J-7	Titanite target	32V	308406	6776959
WGC 2019J-8A	Garnet veins	32V	308443	6776988
WGC 2019J-8B	Garnet veins	32V	308443	6776988
WGC 2019J-8C	Garnet veins	32V	308443	6776988
WGC 2019J-8D	Garnet veins	32V	308443	6776988
WGC 2019J-8E	Garnet veins	32V	308443	6776988
WGC2019J-GA	Relic eclogite here	32V	308382	6776945
WGC 2019J-GB	Garnet-bearing amphibolite that overprints the eclogite	32V	308382	6776945
WGC 2019J-10	Same location as WGC2018-38. Eclogite with overprinting hbd-mu vein assemblage	32V	308571	6777183
WGC 2019J-11	Gt-mu veins with retrogressed eclogite and orthoamphibole? Vein	32V	308571	6777183
WGC 2019J-12	Eclogite with bt (is the bt part of the peak?)	32V	308571	6777183
WGC 2019J-13	Mu-gt-omph vein assemblages in eclogite the protolith eclogite is sample WGC2019J-12	32V	308538	6777152
WGC 2019J-14	Coarse hbd- weak(>) mu and wall rock of gt-omph	32V	308538	6777152
WGC 2019J-15	Inside Teagan's Map. Sample of diatexite melt phase to look for zircons. The age of the diatexite and the PT of the reworked rocks will give a good retrograde PTt constraint. The sample contains gt-bt; modelling PT with zircon would give a nice constraint. i.e. where the melt hits the solidus.	32V	308364	6776922

WGC2019-16A	0cm. Felsic diatexite. NE corner of map where diatexite comes into contact with retrogressed margin of eclogite. Samples on a traverse from A to B (i.e. from E to W) to track transition from diatexite melt to retrogressed eclogite to see if fluids are coming from melt. Samples measured on traverse starting at 0cm for the diatexite melt.	32V	308364	6776922
WGC2019-16B	9cm. Composite gt-bearing diatexite + mafic	32V	308364	6776922
WGC2019-16C	17cm Edge of diatexite (mafic derived from eclogite)	32V	308364	6776922
WGC2019-16D	23cm Edge of eclogite shear zone	32V	308364	6776922
WGC2019-16E	28cm Samples progressively further into eclogite	32V	308364	6776922
WGC2019-16F	34cm	32V	308364	6776922
WGC2019-16G	38cm	32V	308364	6776922
WGC2019-16H	45cm Essentially eclogite	32V	308364	6776922
WGC2019-16I	58cm Essentially eclogite	32V	308364	6776922
WGC2019-16J	Unaltered high strain eclogite. Mylonitic S2 eclogite/is this pk eclogite (i.e. no biotite)	32V	308364	6776922
WGC2019-16K	mu-vein eclogite in the core of the eclogite high strain zone	32V	308364	6776922
WGC2019-17A	Geochemical traverse 2 between felsic gneiss and eclogite. 0cm to middle of sample. Gt-bearing felsic gneiss within contact between retrograte of S1 eclogite and fresh S1 eclogite	32V	308356	6776917
WGC2019-17B	Geochemical traverse 2 between felsic gneiss and eclogite. 7cm to middle of sample. Retrograde eclogite	32V	308356	6776917
WGC2019-17C	Geochemical traverse 2 between felsic gneiss and eclogite. 16cm to middle of sample. Retrograde eclogite	32V	308356	6776917
WGC2019-17D	Geochemical traverse 2 between felsic gneiss and eclogite. 30cm to middle of sample. Sample with retrograde eclogite on margin and transition to S1 eclogite	32V	308356	6776917
WGC2019-18A	Large sample of transition from pre-Caledonian felsic gneiss to S3 Caledonian fabric showing gt coronas in S4	32V	308373	6776911
WGC2019-18B	Pristine pre-Caledonian felsic gneiss 20cm SW of edge of 18A	32V	308373	6776911
WGC2019-18C	Pristine pre-Caledonian migmatitic hbd gneiss	32V	308373	6776911
WGC2019-19A	S1 eclogite with garnet coronas on bt (is this prograde?)	32V	308359	6776909
WGC2019-19B	S1 eclogite with muscovite (is this prograde?)	32V	308359	6776909

Lithological unit	Abbreviated title	Sample ID	Mineralogy (field)	Features: Textural, structural, lithological relationships
Coarse-grained hornblende-garnet-omphacite low strain eclogite	Low strain eclogite	WGC2019J-17D	Garnet + hornblende + biotite	Shares S1 foliation with -17A, garnet-bearing felsic gneiss. Contains shear zone with distinct felsic (plagioclase + quartz rich) and retrogressed mafic (biotite + hornblende(?)) rich intercalated sections. Foliation is steep (~85°). Shear zone is surrounded by retrogressed amphibole-rich material and crosscuts eclogite. Rare hornblende-rich veins (<5mm) crosscut foliation, forming NE striking sets. Felsic sections of shear zone display same mineralogy/appearance as Caledonian felsic gneiss. Southern edge of unit is retrogressed (no visible garnet + omphacite) but swiftly grades to more eclogitic (~10cm from southern boundary).
Coarse-grained two feldspar-quartz-biotite-hornblende garnet-bearing felsic gneiss	Garnet-bearing felsic gneiss / Sveconorwegian felsic gneiss	**WGC2019J-17A** (on traverse) WGC2019J-18B (pristine felsic gneiss)	Plagioclase + k-feldspar + quartz + hornblende + magnetite	-17A shares S1 foliation with -17D, low strain eclogite. Foliation tends to follow lithological boundaries. Sharp contact with low strain eclogite. Hornblende is weathered, creating foliation-defining pits. Foliation NW-Se striking. Coarse, pegmatitic quartz veins present. Eastern edge of unit displays Caledonian reworking when in contact with salt and pepper mafic dyke. Younger, steeper (~40°) salt and pepper mafic dyke foliation cross-cuts older (~60°, Sveconorwegian?) garnet-bearing felsic gneiss foliation. Foliation crosscuts brown ilmenite / rutile domains.
Coarse-grained mafic schist with hornblende and epidote bearing leucosomes	Hornblende leucosome rich dyke		Biotite + plagioclase + hornblende	Quartz leucosomes crosscut foliation, which follows boundary with garnet-bearing felsic gneiss. Felsic, plagioclase rich domains without hornblende crystals are also present. Defining feature is quartz + plagioclase leucosomes with macroscopic (2-4cm) hornblende crystals.
Medium-grained plagioclase-quartz-biotite-hornblende felsic gneiss	S3/S4 transition felsic gneiss / Caledonian felsic gneiss	WGC2019J-18A	Plagioclase + biotite + quartz	Steeply NE dipping foliation. Finer-grained than garnet-bearing felsic gneiss; can be distinguished from older garnet-bearing felsic gneiss by dull grey colour when compared to pinker, more k-feldspar rich garnet-bearing felsic gneiss. Coarse veins are folded with apexes following foliation.
Fine-grained biotite-hornblende-plagioclase mafic amphibolite schist	Salt and pepper mafic dyke	-	Biotite + hornblende + plagioclase	NW-SE striking foliation, steeply NE dipping. Western unit edge appears to have reworked adjacent garnet-bearing felsic gneiss during the Caledonian. Caledonian inclusions prolific, ranging from plagioclase-rich domains (adjacent to garnet-bearing felsic gneiss) to thinner veins (adjacent to Caledonian felsic gneiss). Veins typically follow foliation, which is defined by biotite. Plagioclase-rich domains from garnet-bearing felsic gneiss contain garnets up to 2mm in diameter that 'stain' parts of the outcrop pink.
Fine-grained garnetiferous retrogressed amphibolite	Garnetiferous retrogressed amphibolite	-	Biotite + hornblende + garnet	Extremely diffuse contact with high strain eclogite. Retrogressed amphibolite displays garnet-rich domains with macroscopic garnet crystals.
Medium-grained omphacite-garnet-hornblende high strain mafic eclogite with muscovite veins	High strain eclogite	**WGC2019J-16J** WGC2019J-16K	Hornblende + plagioclase + omphacite + garnet	Contains veins of white plagioclase parallel to foliation, some of which are thicker and more garnetiferous. Sinistral shear zone cross-cuts unit. As in garnetiferous retrogressed amphibolite, pure garnetiferous domains parallel to foliation occur. Also contains muscovite veins, garnet + muscovite domains, quartz + plagioclase veins, muscovite + plagioclase + garnet veins and plagioclase veins. Garnetiferous domains are up to 5cm wide and 10cm long along strike, joining up with muscovite + garnet + plagioclase veins.
Diatexite	Diatexite	WGC2019J-15	Plagioclase + quartz + biotite + hornblende	Consists mainly of heavily deformed, intermingled felsic (plagioclase + quartz-rich) and mafic (biotite + hornblende (?)) rich domains of random geometry. SW unit edge is defined by a sinistral shear zone, possibly retrogressing southern edge of diatexite. Contains S3 foliation; diatexite overprints high strain eclogite (-16J). Diatexite overprinted by S4 foliation (outside mapping area). High strain eclogite (-16J) contains foliation which dips towards diatexite boundary.

Appendix 2: Eclogite Outcrop Structural Data

Note lineation in high strain eclogite: 125 (or 205) /80N, Lx 80 → NW. For grid number reference, please refer to grid schematic on the following page.

Grid #	Strike	Dip	Direc	*Grid #*	Strike	Dip	Direc	*Grid #*	Strike	Dip	Direc
1	154	50	SW	*2*	140	50	SW	*5*	136	42	SW
1	120	38	SW	*2*	130	80	NE	*6*	132	45	NE
1	-	30	SW	*2*	150	52	NE	*6*	128	25	SW
1	124	60	SW	*2*	140	80	NE	*6*	138	87	NE
1	142	42	SW	*2*	132	64	NE	*6*	116	75	NE
1	136	60	SW	*2*	110	80	NE	*6*	120	60	NE
3	136	50	S	*2*	110	78	NE	*6*	130	45	NE
1	120	52	SW	*2*	140	62	NE	*7*	194	35	W
3	140	52	S	*2*	142	58	SW	*7*	194	30	NW
1	155	36	SW	*4*	124	74	NE	*7*	120	30	NW
3	136	48	SW	*11*	122	85	N	*7*	176	80	W
3	132	85	SW	*4*	138	70	SW	*7*	172	85	NW
3	144	54	SW	*4*	152	50	SW	*8*	170	85	NW
3	130	35	SW	*4*	140	52	NE	*8*	148	75	SW
3	132	60	SW	*4*	122	50	NE	*8*	124	60	N
1	-	15	SW	*4*	125	48	NW	*8*	136	65	N
1	142	48	SW	*4*	136	80	NE	*8*	116	85	N
1	140	58	SW	*4*	154	40	NE	*9*	138	85	NE
1	140	50	SW	*4*	150	60	SW	*9*	138	20	NE
1	156	55	SW	*4*	125	70	NE	*9*	138	85	NE
1	168	60	SW	*4*	148	52	SW	*10*	140	90	SW
2	148	80	SW	*5*	154	14	NE	*10*	136	89	NNE
2	140	44	SW	*5*	140	70	SW	*10*	136	78	N
2	152	70	NE	*5*	132	54	NE	*10*	128	85	N
2	148	60	SW	*5*	146	60	SW	*11*	130	89	N
2	156	50	SW	*5*	172	60	SW	*12*	120	88	N
								12	125	87	N

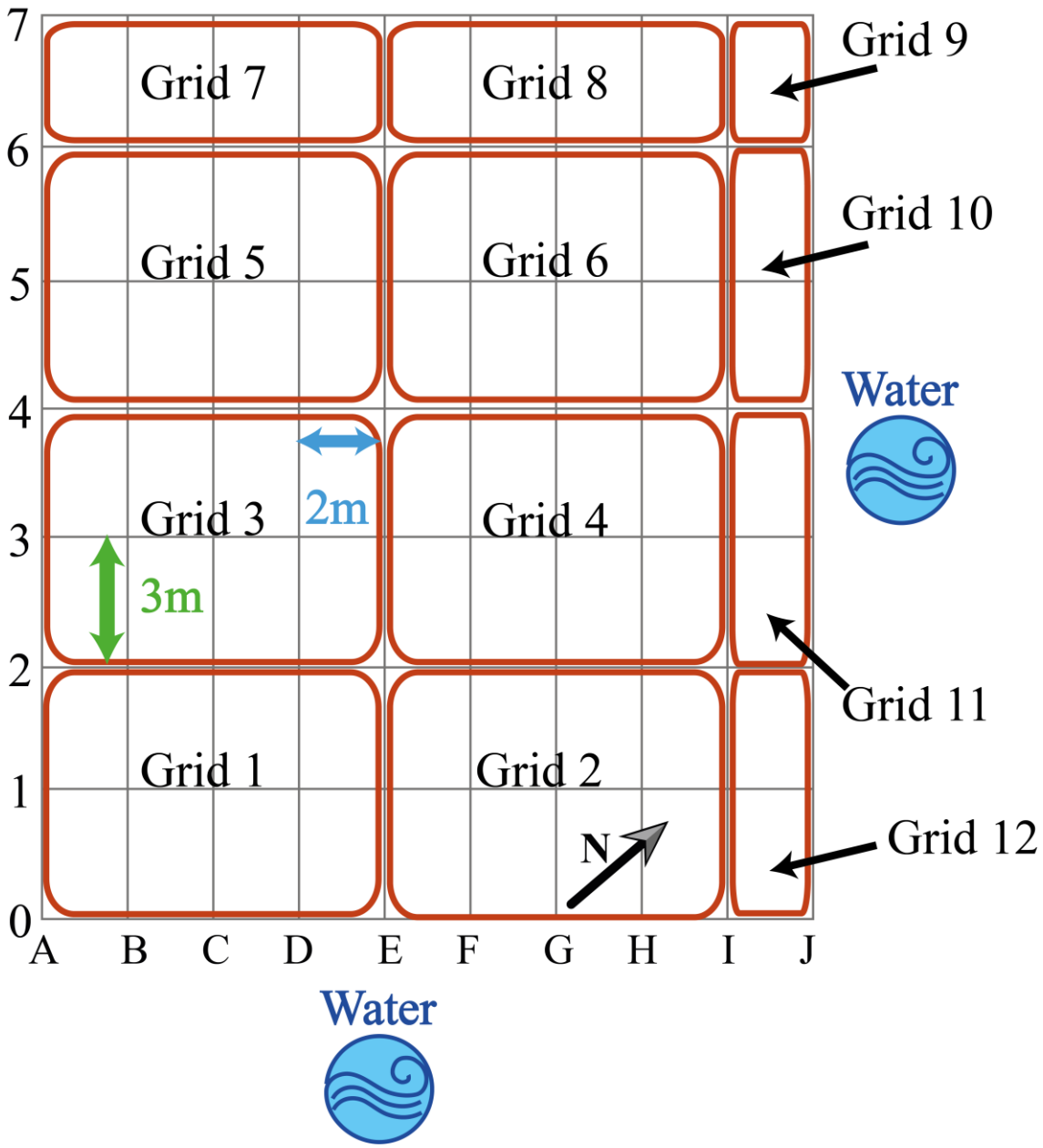

Grid schematic of the Eclogite Outcrop, relevant for structural data point location.

Appendix 3: Eclogite Outcrop Geochemical Assays and Extended Methods

Samples were crushed using a tungsten carbide ring mill at the University of Adelaide lapidary. The samples ranged from ~5g to ~50-100g in size. The samples were then sent to Bureau Veritas Minerals, Adelaide, SA, Australia, for whole and trace element analysis. The samples were digested and refluxed with hydrofluoric, nitric, hydrochloric and perchloric acids. Such extended digest approaches a total digest for many elements. Some refractory minerals are not completely attacked by this digestion. Cu and Ni were determined by Inductively Coupled Plasma (ICP) Optical Emission Spectrometry. Zn was determined by Inductively Coupled Plasma (ICP) Mass Spectrometry. An aliquot of each sample was fused with lithium metaborate at high temperature in a PT crucible, with the resulting fused glass then digested in nitric acid. Complete dissolution of most minerals, including silicates, results from this process, and volatile elements were lost at high fusion temperatures. Al_2O_3, CaO, Cr, Fe_2O_3, K_2O, MgO, MnO, Na_2O, P_2O_5, SiO_2, TiO_2, and V were determined by Inductively Coupled Plasma (ICP) Optical Emission Spectrometry. Ba, Ce, Co, Ga, La, Nb, Rb, Sr, Th, U, Y and Zr were determined by Inductively Coupled Plasma (ICP) Mass Spectrometry after digestion in hydrochloric and hydrofluoric acids. Fe^{2+}, Fe^{3+} and FeO were determined volumetrically.

IDENT	Al2O3	CaO	Fe2O3	K2O	MgO	MnO	Na2O	P2O5	SiO2	TiO2
UNITS	%	%	%	%	%	%	%	%	%	%
DETECTION LIMIT	0.01	0.01	0.01	0.01	0.01	0.01	0.01	0.01	0.01	0.005
WGC 2019J-16J	14.9	7.43	19.6	0.31	5.14	0.26	2.86	0.76	44.7	5.82
WGC 2019J-17A	14.3	1.93	3.72	3.72	0.61	0.06	4.19	0.1	70.2	0.635
WGC 2019J-17D	12.1	8.79	19.4	1.31	4.94	0.31	3.06	0.85	45.4	4.12
WGC 2019J-18A	13.9	2.55	2.93	0.95	0.59	0.05	5.22	0.11	73.8	0.45
WGC 2019J-18A Rpt	13.9	2.53	2.95	0.98	0.57	0.05	5.15	0.11	76.2	0.44
WGC 2019J-33A	14.9	2.9	8.57	2.27	3.5	0.11	2.76	0.16	64.4	1.07
WGC 2019J-33B	16.9	4.53	12.8	1.52	5.17	0.19	2.36	0.1	54.1	1.31
WGC 2019J-34	15.7	1.02	3.96	4.17	1.96	0.15	2.1	0.07	68.7	0.5
WGC 2019J-8D	14.2	3.01	6.08	2.41	0.82	0.15	4.72	0.27	67.6	0.865
WGC 2019J-8E	14.2	2.59	6.23	2.13	0.64	0.14	4.66	0.27	63.8	0.835

IDENT	FeO	Fe2+	FE3PLS	Ba	Ce	Co	Cr	Cu	Ga	La
UNITS	%	%	%	ppm	ppm	ppm	ppm	ppm	ppm	ppm
DETECTION LIMIT	0.1	0.1	0.1	10	0.5	10	20	2	1	1
WGC 2019J-16J	9.2	7.2	29.7	110	67	100	<20	14	24	28
WGC 2019J-17A	2.5	1.9	8	1240	75	80	<20	4	20	38
WGC 2019J-17D	11.1	8.6	35.7	440	99.5	60	100	72	31	39
WGC 2019J-18A	2.6	2	8.3	440	273	<10	160	4	22	142
WGC 2019J-18A Rpt	2.5	1.9	8	430	279	<10	160	6	23	146
WGC 2019J-33A	5.3	4.1	17.1	590	61.5	30	340	62	21	38
WGC 2019J-33B	5.3	4.2	17.2	700	40.5	40	320	130	26	20
WGC 2019J-34	2.3	1.8	7.5	1380	101	<10	180	6	21	31
WGC 2019J-8D	4.3	3.3	13.8	890	251	<10	140	22	23	108
WGC 2019J-8E	4.5	3.5	14.5	820	270	<10	140	14	28	117
IDENT	Nb	Ni	Rb	Sr	Th	U	V	Y	Zn	Zr
UNITS	ppm	ppm	ppm	ppm	ppm	ppm	ppm	ppm	ppm	ppm
DETECTION LIMIT	5	2	0.5	5	0.5	0.5	20	1	2	10
WGC 2019J-16J	25	16	11.5	405	1.5	1	340	49	150	380
WGC 2019J-17A	10	6	84	190	5	1	20	26	76	450
WGC 2019J-17D	20	16	19	245	1	1.5	440	98	212	510
WGC 2019J-18A	10	8	38	320	19.5	1.5	40	22	42	760
WGC 2019J-18A Rpt	10	12	39	330	20	1.5	40	22	42	760
WGC 2019J-33A	20	54	81	85	9	2	180	24	110	280
WGC 2019J-33B	20	68	45.5	145	5	2.5	240	34	140	150
WGC 2019J-34	15	22	97	125	14	2	40	22	52	220
WGC 2019J-8D	80	8	62	380	14	1.5	20	121	72	920
WGC 2019J-8E	95	6	61	320	19.5	1.5	20	135	78	1270

Appendix 4a: Extended Electron Probe Micro Analyses Methods

As an addition to the methods outlined in the main text: Spot analyses of major oxides (SiO_2, ZrO_2, TiO_2, Cr_2O_3, Al_2O_3, FeO, MnO, MgO, CaO, P_2O_5, Na_2O, K_2O, BaO, NiO, F and Cl) were analysed using Wavelength Dispersive Spectrometers (WDS) at Adelaide Microscopy. WDS and Energy Dispersive Spectrometers (EDS) were used to obtain qualitative x-ray compositional maps for Al, Ca, Fe, K, Mg, Mn, Na, P, Si and Ti.

Appendix 4b: Representative EPMA Analyses

WGC2019J-16J (high strain eclogite) and WGC2019J-17A (garnet-bearing felsic gneiss) were subjected to mineral equilibria modelling. For these two samples, values for bulk Fe_2O_3 content were taken from outputs from the AX62 program. Bulk oxide values from the AX62 program were used for modelling in WGC2019J-16J. For WGC2019J-17A, bulk oxide values were taken from stoichiometric charge balancing calculations after Droop (1987). Both methods employ stoichiometric charge balancing. In WGC2019J-17A, where sample values have been taken from a different sample (e.g. WGC2019J-18A), this is denoted in the header, for clarity. For completeness, values obtained through both methods are reported for the two modelled samples.

WGC2019J-17D (low strain eclogite), WGC2019J-18A and WGC2019J-18B were not subjected to phase equilibria modelling. However, they were analysed in terms of their THERMOCALC parameters, which are derived from values calculated simultaneously with the Droop (1987) method; hence, reported here are the oxide values based on that method.

Representative apatite analyses from all felsic samples (WGC2019J-17A, WGC2019J-18A and WGC2019J-18B) are presented in a separate table for ease of reading.

Representative EPMA analyses from samples WGC2019J-18A (abbreviation: 18A) and WGC2019J-18B (abbreviation: 18B) are also included. These were not included in the main thesis body as these samples were not subject to mineral equilibria modelling. However, they are included here for completeness. Note that for WGC2019J-18A, the second generation of biotite did not contain satisfactory analyses; representative values included here are as best possible, but this mineral would require re-analysing should future work on this sample wish to be undertaken.

WGC2019J-16J (AX62)	Biotite	Garnet	Ilmenite	Primary Amphibole	Secondary Amphibole	Omphacite	Sympl Plagioclase	Plagioclase
SiO2	36.89	37.62	0.00	48.08	42.74	53.43	65.97	66.47
TiO2	2.96	0.04	51.61	0.35	0.51	0.15	0.04	0.12
Al2O3	17.55	22.03	0.01	9.55	12.35	5.28	21.01	21.27
Cr2O3	0.01	0.01	0.02	0.00	0.00	0.01	0.00	0.00
Fe2O3	1.02	1.25	1.95	5.48	5.13	4.15	0.45	0.27
FeO	9.57	29.01	43.45	9.51	11.80	5.36	0.00	0.00
MnO	0.02	0.56	0.46	0.08	0.10	0.05	0.00	0.01
MgO	17.47	4.97	1.29	14.04	11.20	10.10	0.29	0.01
CaO	0.05	5.00	0.04	6.50	9.44	17.50	1.82	1.14
Na2O	0.42	0.03	0.03	2.81	2.85	3.91	10.93	11.19
K2O	9.15	0.01	0.01	0.52	1.01	0.02	0.09	0.09
Totals	95.09	100.54	98.85	96.94	97.14	99.96	100.58	100.55
Oxygens	11.00	12.00	3.00	23.00	23.00	6.00	8.00	8.00
Si	2.69	2.95	0.00	6.97	6.38	1.96	2.89	2.90
Ti	0.16	0.00	0.98	0.04	0.06	0.00	0.00	0.00
Al	1.51	2.03	0.00	1.63	2.17	0.23	1.09	1.10
Cr	0.00	0.00	0.00	0.00	0.00	0.00	0.00	0.00
Fe3	0.06	0.07	0.04	0.60	0.58	0.12	0.01	0.01
Fe2	0.58	1.90	0.92	1.15	1.47	0.16	0.00	0.00
Mn	0.00	0.04	0.01	0.01	0.01	0.00	0.00	0.00
Mg	1.90	0.58	0.05	3.03	2.49	0.55	0.02	0.00
Ca	0.00	0.42	0.00	1.01	1.51	0.69	0.09	0.05
Na	0.06	0.00	0.00	0.79	0.83	0.28	0.93	0.95
K	0.85	0.00	0.00	0.10	0.19	0.00	0.00	0.00
Sum	7.82	8.00	2.00	15.33	15.70	4.00	5.03	5.02

WGC2019J-16J	Biotite	Garnet	Ilmenite	Primary Amphibole	Secondary Amphibole	Omphacite	Symplectitic Plagioclase	Plagioclase	Rutile
SiO2	36.88	37.63	0.00	48.08	42.74	53.43	65.97	66.47	0.00
TiO2	2.96	0.04	51.61	0.35	0.51	0.15	0.04	0.12	98.95
Al2O3	17.55	22.03	0.01	9.55	12.35	5.28	21.01	21.26	0.02
Cr2O3	0.01	0.01	0.01	0.00	0.00	0.01	0.00	0.00	0.02
FeO	10.48	30.14	45.20	14.44	16.42	9.09	0.40	0.24	0.27
MnO	0.02	0.56	0.46	0.08	0.10	0.05	0.00	0.01	0.00
MgO	17.46	4.98	1.29	14.04	11.20	10.09	0.29	0.00	0.00
ZnO	0.00	0.00	0.00	0.00	0.00	0.00	0.00	0.00	0.00
CaO	0.05	5.00	0.04	6.50	9.44	17.50	1.81	1.13	0.02
Na2O	0.42	0.03	0.03	2.81	2.85	3.91	10.93	11.19	0.01
K2O	9.15	0.01	0.01	0.53	1.01	0.02	0.09	0.08	0.01
Cl	0.02	0.01	0.00	0.04	0.03	0.01	0.01	0.01	0.00
F	0.54	0.02	0.05	0.32	0.34	0.02	0.01	0.01	0.10
H2O	3.86	0.00	0.00	0.00	0.00	0.00	0.00	0.00	0.00
OH = Cl ("Cl factor")	0.00	0.00	0.00	0.01	0.01	0.00	0.00	0.00	0.00
OH = F ("F factor")	0.23	0.01	0.02	0.13	0.14	0.01	0.00	0.01	0.04
Total	95.85	100.46	98.75	96.60	96.84	99.58	100.55	100.52	99.37
No. Oxygens	11.00	12.00	3.00	23.00	23.00	6.00	8.00	8.00	2.00
Si	2.68	2.95	0.00	6.95	6.33	1.96	2.87	2.89	0.00
Ti	0.16	0.00	0.98	0.04	0.06	0.00	0.00	0.00	1.00
Al	1.50	2.03	0.00	1.63	2.15	0.23	1.08	1.09	0.00
Cr	0.00	0.00	0.00	0.00	0.00	0.00	0.00	0.00	0.00
Fe3+	0.03	0.07	0.03	0.56	0.81	0.11	0.00	0.00	0.00
Fe2+	0.60	1.91	0.92	1.18	1.22	0.17	0.01	0.01	0.00
Mn2+	0.00	0.04	0.01	0.01	0.01	0.00	0.00	0.00	0.00
Mg	1.89	0.58	0.05	3.02	2.47	0.55	0.02	0.00	0.00
Zn	0.00	0.00	0.00	0.00	0.00	0.00	0.00	0.00	0.00
Ca	0.00	0.42	0.00	1.01	1.50	0.69	0.08	0.05	0.00
Na	0.06	0.00	0.00	0.79	0.82	0.28	0.92	0.94	0.00
K	0.85	0.00	0.00	0.10	0.19	0.00	0.00	0.00	0.00
Cl	0.00	0.00	0.00	0.01	0.01	0.00	0.00	0.00	0.00
F	0.13	0.01	0.00	0.15	0.16	0.00	0.00	0.00	0.00
OH-	1.87	0.00	0.00	0.00	0.00	0.00	0.00	0.00	0.00
Total cations (S)	7.78	8.00	2.00	15.28	15.56	4.00	5.00	5.00	1.00

WGC2019J-16J	Primary Hornblende	Primary Hornblende	Secondary Hornblende	Secondary Hornblende
	Maximum	Minimum	Maximum	Minimum
SiO2	45.01	48.98	42.70	41.62
TiO2	0.63	0.24	0.62	0.45
Al2O3	9.94	9.85	11.13	12.68
Cr2O3	0.00	0.00	0.00	0.01
FeO	14.27	14.64	16.56	16.19
MnO	0.10	0.09	0.09	0.10
MgO	12.97	14.11	11.15	10.75
ZnO	0.00	0.00	0.00	0.00
CaO	9.78	5.23	9.33	9.11
Na2O	2.51	3.14	2.85	2.94
K2O	0.78	0.47	1.02	1.10
Cl	0.04	0.02	0.07	0.18
F	0.35	0.30	0.33	0.31
H2O	0.00	0.00	0.00	0.00
OH = Cl ("Cl factor")	0.01	0.01	0.02	0.04
OH = F ("F factor")	0.15	0.13	0.14	0.13
Total	96.24	96.93	95.69	95.26
No. Oxygens	23.00	23.00	23.00	23.00
Si	6.61	7.03	6.40	6.28
Ti	0.07	0.03	0.07	0.05
Al	1.72	1.66	1.97	2.25
Cr	0.00	0.00	0.00	0.00
Fe3+	0.76	0.53	0.86	0.78
Fe2+	1.00	1.23	1.21	1.26
Mn2+	0.01	0.01	0.01	0.01
Mg	2.84	3.02	2.49	2.42
Zn	0.00	0.00	0.00	0.00
Ca	1.54	0.80	1.50	1.47
Na	0.72	0.87	0.83	0.86
K	0.15	0.09	0.20	0.21
Cl	0.01	0.01	0.02	0.05
F	0.17	0.14	0.16	0.15
OH-	0.00	0.00	0.00	0.00
Total cations (S)	15.42	15.26	15.54	15.59

WGC2019J-17D	Secondary Amphibole	Symplectitic Amphibole	Symplectitic Clinopyroxene	Biotite	Ilmenite	Garnet	Primary Amphibole	Symplectitic Plagioclase
SiO2	38.73	41.37	51.70	35.65	0.00	36.93	38.88	66.93
TiO2	0.44	0.75	0.06	3.61	50.85	0.18	1.10	0.00
Al2O3	13.01	9.98	2.97	14.65	0.02	21.59	13.50	20.86
Cr2O3	0.01	0.01	0.02	0.00	0.01	0.01	0.01	0.00
FeO	22.63	21.93	12.84	20.48	45.91	30.85	20.88	0.39
MnO	0.17	0.19	0.14	0.16	0.93	1.10	0.17	0.00
MgO	6.45	7.61	9.22	10.60	0.78	2.81	6.93	0.00
ZnO	0.00	0.00	0.00	0.00	0.00	0.00	0.00	0.00
CaO	10.96	11.30	18.29	0.02	0.01	6.35	9.63	0.56
Na2O	1.80	1.41	3.12	0.07	0.04	0.03	2.34	10.98
K2O	1.40	1.08	0.01	9.27	0.01	0.01	1.49	0.10
Cl	0.39	0.33	0.01	0.21	0.00	0.01	0.65	0.01
F	0.17	0.16	0.01	0.43	0.05	0.02	0.18	0.02
H2O	0.00	0.00	0.00	3.63	0.00	0.00	0.00	0.00
OH = Cl ("Cl factor")	0.09	0.08	0.00	0.05	0.00	0.00	0.15	0.00
OH = F ("F factor")	0.07	0.07	0.00	0.18	0.02	0.01	0.07	0.01
Total	96.01	95.97	98.37	94.91	98.58	99.88	95.53	99.83
No. Oxygens	23.00	23.00	6.00	11.00	3.00	12.00	23.00	8.00
Si	6.03	6.40	1.96	2.74	0.00	2.95	6.04	2.94
Ti	0.05	0.09	0.00	0.21	0.97	0.01	0.13	0.00
Al	2.39	1.82	0.13	1.33	0.00	2.03	2.47	1.08
Cr	0.00	0.00	0.00	0.00	0.00	0.00	0.00	0.00
Fe3+	0.93	0.83	0.17	0.07	0.05	0.06	0.75	0.00
Fe2+	2.01	2.01	0.24	1.25	0.92	2.00	1.96	0.01
Mn2+	0.02	0.02	0.00	0.01	0.02	0.07	0.02	0.00
Mg	1.50	1.75	0.52	1.22	0.03	0.33	1.61	0.00
Zn	0.00	0.00	0.00	0.00	0.00	0.00	0.00	0.00
Ca	1.83	1.87	0.74	0.00	0.00	0.54	1.60	0.03
Na	0.54	0.42	0.23	0.01	0.00	0.01	0.70	0.93
K	0.28	0.21	0.00	0.91	0.00	0.00	0.30	0.01
Cl	0.10	0.09	0.00	0.03	0.00	0.00	0.17	0.00
F	0.09	0.08	0.00	0.11	0.00	0.01	0.09	0.00
OH-	0.00	0.00	0.00	1.87	0.00	0.00	0.00	0.00
Total cations (S)	15.58	15.43	4.00	7.75	2.00	8.00	15.59	5.00

	SiO2	TiO2	Al2O3	Cr2O3	FeO	MnO	MgO	ZnO	CaO	Na2O	K2O	Cl	F	P2O5	TOTAL
APATITE															
WGC2019J-17A	0.05	0.00	0.00	0.02	0.04	0.13	0.00	0.00	55.78	0.03	0.00	0.07	2.66	42.23	99.89
	0.06	0.00	0.00	0.00	0.12	0.09	0.00	0.00	56.16	0.05	0.00	0.05	2.74	41.66	99.77
	0.04	0.00	0.00	0.00	0.03	0.10	0.02	0.00	55.68	0.01	0.00	0.07	2.84	42.12	99.71
AVERAGE	0.05	0.00	0.00	0.01	0.07	0.10	0.01	0.00	55.87	0.03	0.00	0.06	2.75	42.01	99.79
WGC2019J-18A	0.01	0.00	0.00	0.00	0.05	0.06	0.02	0.00	56.00	0.01	0.01	0.10	2.95	41.74	99.68
	0.00	0.00	0.00	0.00	0.08	0.07	0.00	0.00	56.18	0.02	0.00	0.13	3.01	42.14	100.34
	0.01	0.00	0.00	0.00	0.04	0.07	0.00	0.00	55.71	0.04	0.00	0.09	2.96	42.11	99.79
AVERAGE	0.01	0.00	0.00	0.00	0.06	0.07	0.01	0.00	55.96	0.02	0.00	0.11	2.97	42.00	99.94
WGC2019J-18B	0.06	0.00	0.00	0.00	0.05	0.05	0.00	0.00	55.84	0.03	0.00	0.17	2.37	42.03	99.59
	0.07	0.00	0.00	0.00	0.05	0.04	0.00	0.00	55.81	0.00	0.00	0.19	2.54	42.41	100.00
	0.09	0.01	0.00	0.00	0.03	0.04	0.00	0.00	55.83	0.02	0.00	0.22	2.19	42.54	100.04
AVERAGE	0.08	0.00	0.00	0.00	0.04	0.04	0.00	0.00	55.83	0.02	0.00	0.19	2.37	42.32	99.88

WGC2019J-18A	Biotite	Biotite (2nd Generation)	Plagioclase	Garnet	Ilmenite	Chlorite	Titanite	Amphibole
SiO2	35.03	25.44	64.47	37.67	0.01	24.32	30.47	36.60
TiO2	3.69	3.15	0.01	0.05	48.17	0.00	37.53	0.86
Al2O3	14.65	12.93	22.76	21.56	0.07	18.58	1.58	13.43
Cr2O3	0.01	0.00	0.01	0.00	0.01	0.00	0.02	0.01
FeO	26.63	25.12	0.03	25.29	48.14	41.10	0.48	26.10
MnO	0.25	0.26	0.01	0.55	2.98	0.38	0.03	0.68
MgO	6.46	5.91	0.00	0.20	0.02	3.26	0.00	3.35
ZnO	0.00	0.00	0.00	0.00	0.00	0.00	0.00	0.00
CaO	0.00	0.03	3.49	15.08	0.01	0.10	28.26	10.97
Na2O	0.04	0.07	9.86	0.00	0.03	0.06	0.01	1.43
K2O	8.99	8.34	0.26	0.00	0.00	0.10	0.00	1.69
Cl	0.19	0.22	0.01	0.00	0.00	0.04	0.00	0.49
F	0.10	0.09	0.00	0.00	0.02	0.00	0.46	0.06
H2O	3.71	3.02	0.00	0.00	0.00	10.38	0.00	0.00
OH = Cl ("Cl factor")	0.04	0.05	0.00	0.00	0.00	0.01	0.00	0.11
OH = F ("F factor")	0.04	0.04	0.00	0.00	0.01	0.00	0.19	0.02
Total	96.76	82.09	100.93	100.43	99.47	88.50	98.73	95.57
No. Oxygens	11.00	11.00	8.00	12.00	3.00	14.00	5.00	23.00
Si	2.75	2.43	2.81	2.98	0.00	2.77	1.00	5.87
Ti	0.22	0.23	0.00	0.00	0.91	0.00	0.93	0.10
Al	1.35	1.45	1.17	2.01	0.00	2.49	0.06	2.54
Cr	0.00	0.00	0.00	0.00	0.00	0.00	0.00	0.00
Fe3+	0.09	0.20	0.00	0.03	0.17	0.35	0.00	0.97
Fe2+	1.66	1.80	0.00	1.64	0.85	3.57	0.01	2.53
Mn2+	0.02	0.02	0.00	0.04	0.06	0.04	0.00	0.09
Mg	0.75	0.84	0.00	0.02	0.00	0.55	0.00	0.80
Zn	0.00	0.00	0.00	0.00	0.00	0.00	0.00	0.00
Ca	0.00	0.00	0.16	1.28	0.00	0.01	0.99	1.89
Na	0.01	0.01	0.83	0.00	0.00	0.01	0.00	0.45
K	0.90	1.01	0.01	0.00	0.00	0.01	0.00	0.35
Cl	0.02	0.04	0.00	0.00	0.00	0.01	0.00	0.14
F	0.03	0.03	0.00	0.00	0.00	0.00	0.05	0.03
OH-	1.95	1.94	0.00	0.00	0.00	7.99	0.00	0.00
Total Cations (S)	7.74	8.00	5.00	8.00	2.00	9.82	3.00	15.58

WGC2019J-18B	Titanite	Biotite	Biotite (2nd Generation)	K-Feldspar	Plagioclase
SiO2	30.58	35.48	34.47	64.25	64.41
TiO2	38.55	3.46	3.19	0.01	0.01
Al2O3	1.14	14.51	14.78	18.73	18.85
Cr2O3	0.00	0.00	0.00	0.00	0.02
FeO	0.41	25.96	25.92	0.00	0.00
MnO	0.09	0.36	0.41	0.00	0.00
MgO	0.01	6.98	6.78	0.00	0.00
ZnO	0.00	0.00	0.00	0.00	0.00
CaO	28.29	0.03	0.05	0.04	0.04
Na2O	0.03	0.05	0.02	0.95	0.82
K2O	0.00	9.06	9.12	14.61	14.84
Cl	0.00	0.14	0.14	0.01	0.01
F	0.19	0.02	0.04	0.00	0.00
H2O	0.00	3.78	3.71	0.00	0.00
OH = Cl ("Cl factor")	0.00	0.03	0.03	0.00	0.00
OH = F ("F factor")	0.08	0.01	0.02	0.00	0.00
Total	99.27	96.29	95.08	99.51	99.80
No. Oxygens	5.00	11.00	11.00	8.00	8.00
Si	1.00	2.77	2.74	3.01	3.00
Ti	0.95	0.20	0.19	0.00	0.00
Al	0.04	1.34	1.38	1.03	1.04
Cr	0.00	0.00	0.00	0.00	0.00
Fe3+	0.00	0.08	0.09	0.00	0.00
Fe2+	0.01	1.61	1.63	0.00	0.00
Mn2+	0.00	0.02	0.03	0.00	0.00
Mg	0.00	0.81	0.80	0.00	0.00
Zn	0.00	0.00	0.00	0.00	0.00
Ca	0.99	0.00	0.00	0.00	0.00
Na	0.00	0.01	0.00	0.09	0.07
K	0.00	0.90	0.92	0.87	0.88
Cl	0.00	0.02	0.02	0.00	0.00
F	0.02	0.01	0.01	0.00	0.00
OH-	0.00	1.98	1.97	0.00	0.00
Total Cations (S)	3.00	7.76	7.79	5.00	5.00

WGC2019J-17A	Garnet	Plagioclase	K Feldspar	Magnetite	Ilmenite	Biotite 2nd Generation	Biotite 1st Generation	Epidote	Chlorite	Titanite
ID number	WGC2019J-17A	WGC2019J-17A	WGC2019J-17A	WGC2019J-17A	WGC2019J-18A	WGC2019J-17A	WGC2019J-17A	WGC2018-38A	WGC2019J-17A	WGC2019J-17A
SiO2	37.39	64.12	64.19	0.01	0.02	34.78	35.12	37.41	24.61	30.70
TiO2	0.07	0.00	0.00	0.58	47.56	3.23	3.17	0.14	0.21	38.47
Al2O3	20.49	22.72	18.91	0.23	0.04	15.42	15.65	23.37	20.19	1.15
Cr2O3	0.01	0.01	0.00	0.01	0.01	0.00	0.00	0.00	0.01	0.00
FeO	26.29	0.06	0.01	99.10	48.21	27.39	25.32	11.19	29.93	0.63
MnO	0.96	0.00	0.00	0.11	2.92	0.63	0.55	0.16	1.07	0.13
MgO	0.39	0.01	0.00	0.02	0.02	5.37	6.75	0.02	11.19	0.00
ZnO	0.00	0.00	0.00	0.00	0.00	0.00	0.00	0.01	0.00	0.00
CaO	14.70	3.54	0.01	0.01	0.01	0.07	0.00	22.25	0.09	28.29
Na2O	0.00	9.99	0.47	0.02	0.06	0.04	0.06	0.00	0.00	0.01
K2O	0.00	0.19	15.60	0.00	0.03	8.89	9.32	0.00	0.01	0.00
Cl	0.00	0.00	0.00	0.00	0.03	0.05	0.06	0.00	0.00	0.00
F	0.00	0.00	0.00	0.00	0.02	0.03	0.03	0.03	0.00	0.23
H2O	0.00	0.00	0.00	0.00	0.00	3.76	3.80	1.78	10.96	0.00
OH = Cl ("Cl factor")	0.00	0.00	0.00	0.00	0.01	0.01	0.01	0.00	0.00	0.00
OH = F ("F factor")	0.00	0.00	0.00	0.00	0.01	0.01	0.01	0.01	0.00	0.10
Total	100.35	100.67	99.20	100.15	98.91	96.10	96.22	94.58	87.30	99.67
No. Oxygens	12.00	8.00	8.00	4.00	3.00	11.00	11.00	12.50	14.00	5.00
Si	2.97	2.80	2.99	0.00	0.00	2.74	2.74	3.04	2.66	1.00
Ti	0.00	0.00	0.00	0.02	0.91	0.19	0.19	0.01	0.02	0.94
Al	1.92	1.17	1.04	0.01	0.00	1.43	1.44	2.24	2.57	0.04
Cr	0.00	0.00	0.00	0.00	0.00	0.00	0.00	0.00	0.00	0.00
Fe3+	0.13	0.00	0.00	1.96	0.18	0.09	0.08	0.66	0.37	0.00
Fe2+	1.61	0.00	0.00	1.01	0.84	1.72	1.57	0.10	2.33	0.02
Mn2+	0.06	0.00	0.00	0.00	0.06	0.04	0.04	0.01	0.10	0.00
Mg	0.05	0.00	0.00	0.00	0.00	0.63	0.78	0.00	1.80	0.00
Zn	0.00	0.00	0.00	0.00	0.00	0.00	0.00	0.00	0.00	0.00
Ca	1.25	0.17	0.00	0.00	0.00	0.01	0.00	1.94	0.01	0.99
Na	0.00	0.85	0.04	0.00	0.00	0.01	0.01	0.00	0.00	0.00
K	0.00	0.01	0.93	0.00	0.00	0.89	0.93	0.00	0.00	0.00
Cl	0.00	0.00	0.00	0.00	0.00	0.01	0.01	0.00	0.00	0.00
F	0.00	0.00	0.00	0.00	0.00	0.01	0.01	0.01	0.00	0.02
OH-	0.00	0.00	0.00	0.00	0.00	1.99	1.99	0.99	8.00	0.00
Total cations (S)	8.00	5.00	5.00	3.00	2.00	7.75	7.77	8.00	9.86	3.00

WGC2019J-17A (AX62)	Garnet	Plagioclase	K Feldspar	Magnetite	Ilmenite	Biotite 2nd Generation	Biotite 1st Generation	Epidote	Chlorite
ID number	WGC2019J-17A	WGC2019J-17A	WGC2019J-17A	WGC2019J-17A	WGC2019J-18A	WGC2019J-17A	WGC2019J-17A	WGC2018-38A	WGC2019J-17A
SiO2	37.39	64.13	64.20	0.01	0.02	34.78	35.12	37.41	24.61
TiO2	0.07	0.00	0.01	0.58	47.56	3.23	3.17	0.14	0.22
Al2O3	20.49	22.72	18.91	0.22	0.04	15.42	15.65	23.38	20.19
Cr2O3	0.01	0.01	0.00	0.01	0.01	0.00	0.00	0.00	0.01
Fe2O3	2.25	0.07	0.01	72.73	9.78	0.00	0.00	12.29	0.00
FeO	24.27	0.00	0.00	33.66	39.40	27.38	25.31	0.13	29.93
MnO	0.96	0.00	0.00	0.11	2.92	0.63	0.55	0.02	1.07
MgO	0.39	0.01	0.00	0.02	0.02	5.37	6.75	0.16	11.19
CaO	14.70	3.54	0.01	0.01	0.01	0.07	0.00	22.26	0.09
Na2O	0.00	10.00	0.48	0.02	0.06	0.04	0.06	0.00	0.00
K2O	0.00	0.19	15.61	0.00	0.03	8.89	9.32	0.00	0.01
Totals	100.52	100.66	99.21	107.36	99.87	95.83	95.94	95.80	87.29
Oxygens	12.00	8.00	8.00	4.00	3.00	11.00	11.00	12.50	14.00
Si	2.97	2.82	2.98	0.00	0.00	2.75	2.75	3.03	2.69
Ti	0.00	0.00	0.00	0.02	0.91	0.19	0.19	0.01	0.02
Al	1.92	1.18	1.04	0.01	0.00	1.44	1.45	2.23	2.60
Cr	0.00	0.00	0.00	0.00	0.00	0.00	0.00	0.00	0.00
Fe3	0.13	0.00	0.00	1.96	0.19	0.00	0.00	0.75	0.00
Fe2	1.61	0.00	0.00	1.01	0.84	1.81	1.66	0.01	2.74
Mn	0.06	0.00	0.00	0.00	0.06	0.04	0.04	0.00	0.10
Mg	0.05	0.00	0.00	0.00	0.00	0.63	0.79	0.02	1.82
Ca	1.25	0.17	0.00	0.00	0.00	0.01	0.00	1.93	0.01
Na	0.00	0.85	0.04	0.00	0.00	0.01	0.01	0.00	0.00
K	0.00	0.01	0.92	0.00	0.00	0.90	0.93	0.00	0.00
Sum	8.00	5.03	4.99	3.00	2.00	7.79	7.81	7.98	9.99

Appendix 5a: Extended <600 µm Garnet Traverses

Quantitative EPMA garnet traverses for mafic eclogites WGC2019J-16J and WGC2019J-17D are presented. Concentration is given in terms of wt% oxide outputs direct from probe analyses.

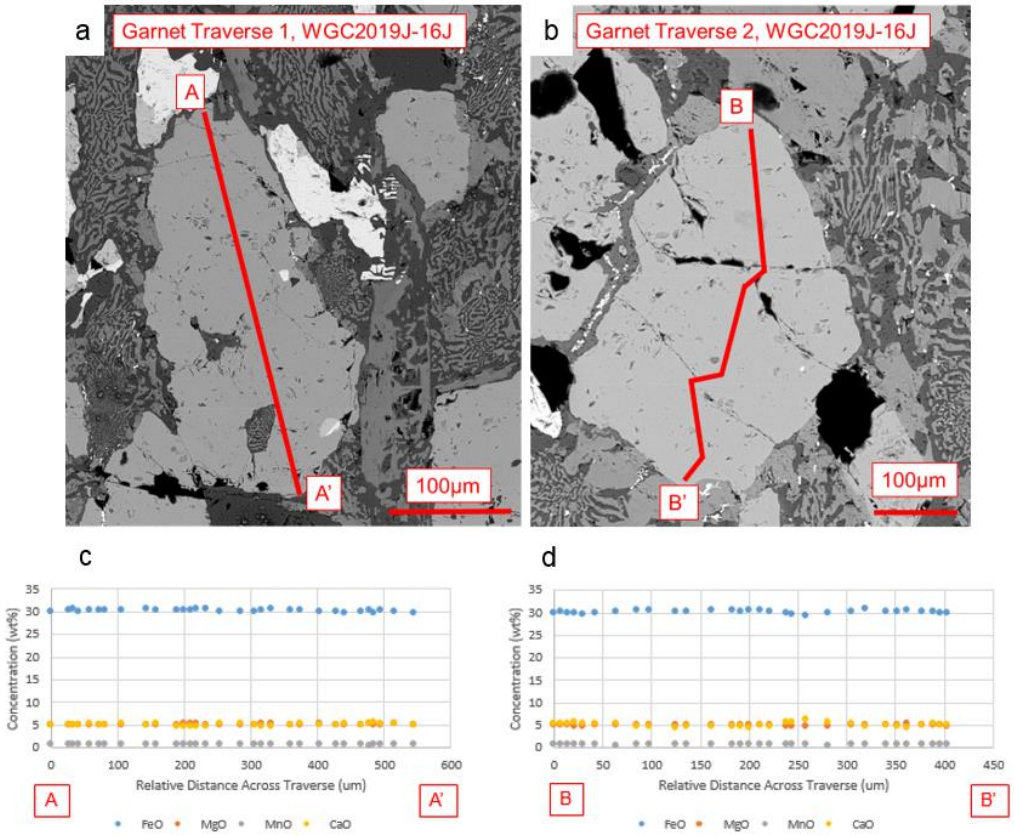

(a), (b) Backscatter electron images of garnet traverses A-A' and B-B' in sample WGC2019J-16J, with resulting cation endmember concentrations shown in (c), (d). Graphs show oxide concentrations on the y-axis and relative distance across traverse (µm) on the x-axis.

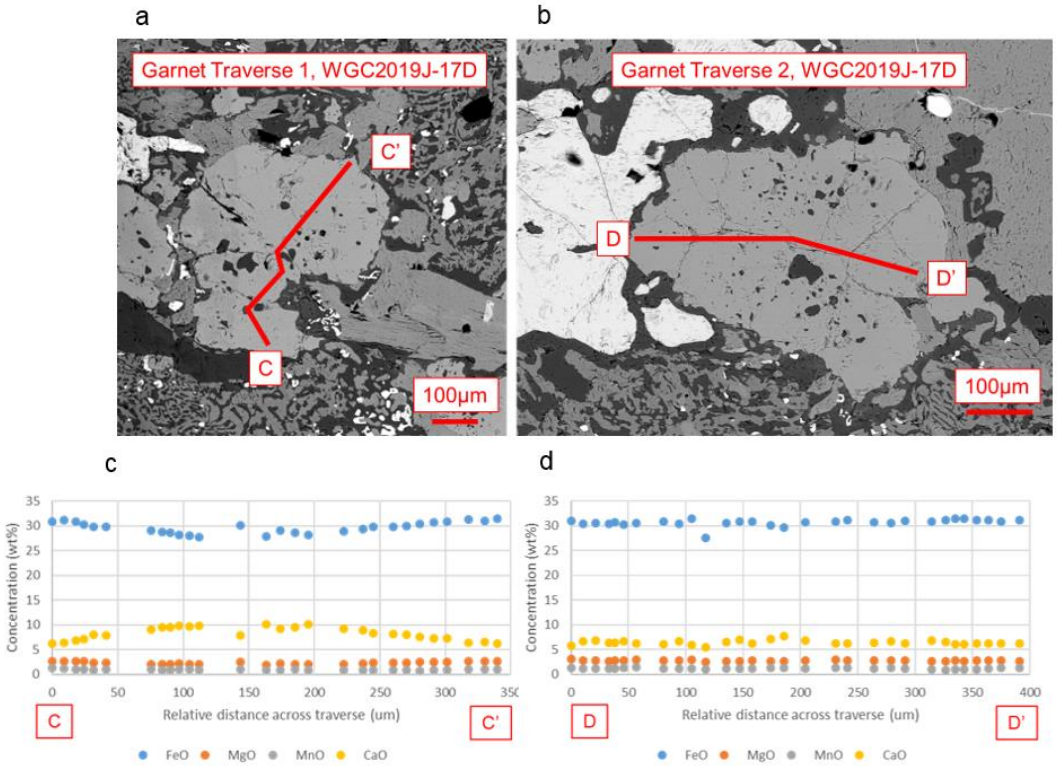

(a), (b) Backscatter electron images of garnet traverses C-C' and D-D' in sample WGC2019J-16J, with resulting cation endmember concentrations shown in (c), (d). Graphs show oxide concentrations on the y-axis and relative distance across traverse (µm) on the x-axis.

Appendix 5b: Extended >600 µm X-ray Garnet Maps

Image processing from original greyscale x-ray maps was undertaken using ImageJ, a freely available software.

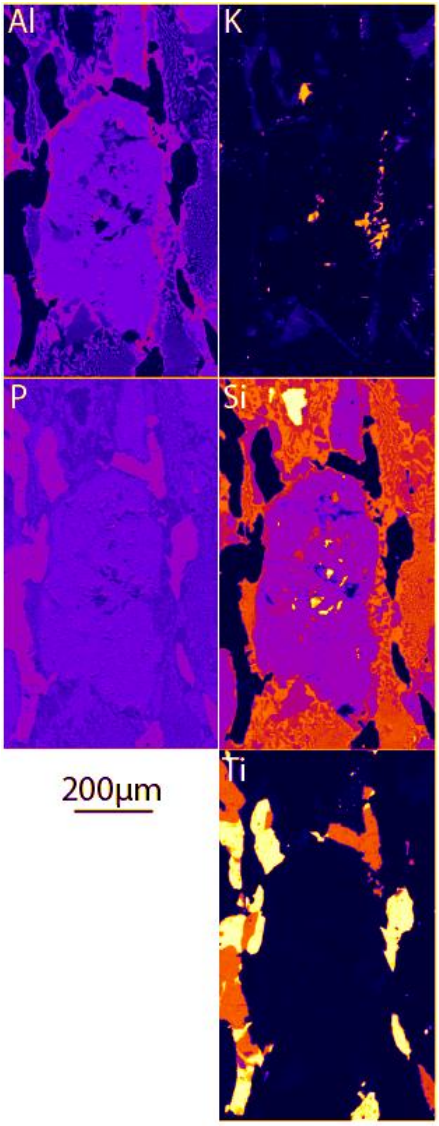

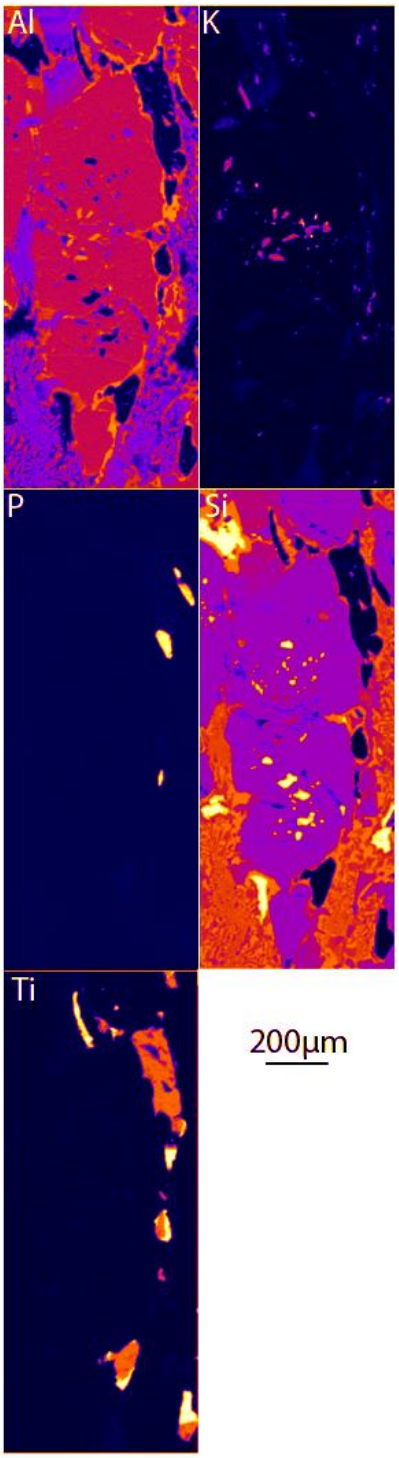

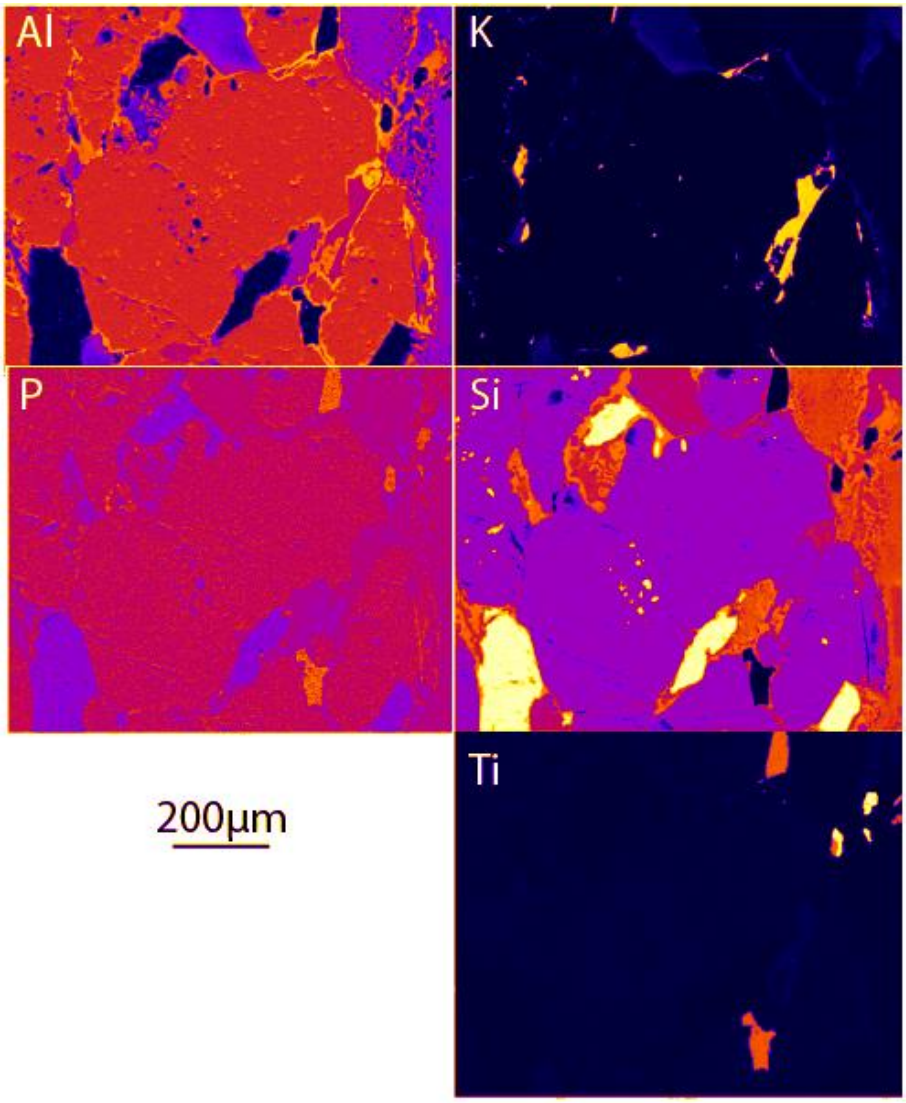
Al
K
P
Si
Ti
200µm

Appendix 6a: Extended Trace Element LA-ICP-MS Methods

LA-ICP-MS Analysis

Laser Ablation-Inductively Coupled Plasma-Mass Spectrometry (LA-ICP-MS) using a RESOlution LR 193nm Excimer laser system with a coupled Agilent 7700s ICP-MS at Adelaide Microscopy was used to acquire zircon full trace element and titanium data from samples WGC2019-15 (diatexite), WGC2019J-16J (high strain eclogite) and WGC2019-17D (low strain eclogite). A He-ablation atmosphere with an ablation fluence of 2J/cm^2 fluence, 35mJ Ar-F laser energy, and 50% attenuation at a 5 Hz frequency was used to ablate zircons. A 29 μm spot size was used on the three grain mounts. For WGC2019-15, both 'white' outer rims and 'black' inner regions were targeted on the smaller zircons, which were selected due to the larger sizes of desired target areas. Inherited detrital zircons were not analysed in any of the three samples. For WGC2019J-16J and WGC2019J-17D, only zircon rims were analysed. Fractures, inclusions, resin, and interior zoned areas were actively avoided while selecting spots for both rutile and zircon grains. In the case of rutiles, BSE imaging allowed for ilmenite exsolution to be avoided during target selection. Laser refocussing occurred every ~5-10 spots.

A 60s total acquisition time was used for each zircon analysis, subdivided into 30s of background acquisition and sample ablation. For rutiles, a 72s acquisition time was subdivided into ~30s background and ~40s sample ablation. The standard NIST SRM610 (P = 413 ± 46 ppm, La = 440 ± 10 ppm, Lu = 439 ± 8 ppm, Zr = 448 ± 9 ppm) (Jochum et al. 2011) was used to correct for elemental fractionation and mass bias in trace element analyses for both minerals. For zircon analysis, the NIST SRM610 standard displayed P = 413 ± 3.7 ppm, La = 440 ± 1.2 ppm and Lu = 439 ± 1.2 ppm. For rutile analysis, this study had a standard with concentrations of Zr = 448.0 ± 1.0ppm.

A spot size of 29 μm and fluence of 3.5J/cm^2 was employed throughout nine runs for zircons. A 51 μm spot size and 5J/cm^2 fluence was used for rutiles from samples WGC2019J-16J and WGC2019J-17D. A combination of mounts and thin sections were used for the former and mounts alone for the latter to maximise collectable data.

Data Processing and Reduction

Iolite 3.6 was used to reduce trace element data (Paton et al. 2011). The methods employed were identical to those outlined in **Data Processing and Reduction, Appendix 8a.** Consistency between chemistry and age was assured by collecting trace element and U-Pb data synchronously. Internal element standards, consistent with the mineral being processed, are used while processing trace element data. Zircon trace element data were processed to an internal standard element value of Zr = 43.14%. Rutile trace element data were processed to an internal standard element value of Ti = 59.94%.

Appendix 6b: Zircon Trace Element Data

For standards, not normalised values are presented. For data, not normalised values are presented, separated into concordant and discordant analyses, with normalisation values provided also. Normalisation was done to Boynton (1984) and Sun and McDonough (1989).

	Si	2σ	P	2σ	Ti	2σ	Y	2σ	Nb	2σ	La	2σ	Ce	2σ
G_NIST610_1	326100.00	4800.00	402.00	16.00	454.00	11.00	458.20	6.40	461.50	6.90	435.80	5.60	448.20	5.70
G_NIST610_2	327500.00	4000.00	414.00	14.00	449.00	11.00	461.80	5.00	464.90	5.20	440.50	4.30	452.30	4.50
G_NIST610_3	326400.00	3800.00	408.00	16.00	450.00	10.00	458.80	5.00	460.40	5.60	437.50	4.80	450.80	4.90
G_NIST610_4	327800.00	4500.00	425.00	18.00	458.00	11.00	465.20	6.90	468.20	6.40	441.70	5.60	456.10	6.50
G_NIST610_5	327700.00	4000.00	411.00	17.00	451.40	9.60	463.30	5.50	466.50	5.40	440.10	4.50	453.40	4.80
G_NIST610_6	330300.00	4300.00	425.00	15.00	456.00	11.00	470.10	6.30	469.60	5.70	446.00	5.30	459.50	5.50
G_NIST610_7	324000.00	4400.00	410.00	17.00	443.30	9.70	460.50	6.10	463.60	6.20	440.30	5.60	453.80	6.00
G_NIST610_8	327200.00	4800.00	416.00	15.00	459.60	9.90	465.00	6.30	472.90	6.90	445.60	6.20	459.10	6.20
G_NIST610_9	328000.00	4100.00	404.00	15.00	449.00	11.00	460.00	5.10	464.50	5.70	440.00	4.90	452.60	4.80
G_NIST610_10	325700.00	4000.00	409.00	16.00	448.80	9.30	463.60	5.30	464.30	5.50	440.40	4.60	453.60	4.70
G_NIST610_11	329400.00	4300.00	420.00	14.00	457.00	12.00	459.80	5.90	462.00	5.60	437.00	5.10	450.40	5.60
G_NIST610_12	326100.00	4000.00	411.00	16.00	444.00	11.00	457.40	5.00	460.00	4.70	435.30	4.30	448.80	4.50
G_NIST610_13	326700.00	4200.00	412.00	17.00	448.00	12.00	461.10	5.70	464.40	6.00	438.30	5.40	451.50	5.40
G_NIST610_14	327800.00	4200.00	410.00	17.00	452.00	12.00	468.60	5.90	471.50	5.90	444.40	5.10	457.20	5.20
G_NIST610_15	328000.00	4100.00	430.00	16.00	453.00	11.00	463.90	5.80	466.20	6.20	439.50	5.20	451.30	5.40
G_NIST610_16	326700.00	4800.00	422.00	16.00	463.00	12.00	463.20	5.70	467.10	6.50	440.20	5.40	453.60	5.80
G_NIST610_17	329300.00	3900.00	403.00	16.00	456.00	11.00	460.70	5.40	465.60	5.30	440.70	4.90	454.10	5.40
G_NIST610_18	325100.00	3600.00	405.00	14.00	447.00	11.00	460.30	5.20	462.60	5.20	440.20	4.50	452.50	4.70

	Pr	2σ	Nd	2σ	Sm	2σ	Eu	2σ	Gd	2σ	Tb	2σ	Dy	2σ
G_NIST610_1	445.60	5.50	426.80	6.00	447.50	6.10	444.70	5.90	446.90	6.30	434.50	5.80	434.40	5.80
G_NIST610_2	448.90	4.10	430.20	5.10	452.60	5.00	447.20	4.70	449.80	5.40	436.50	4.90	437.50	5.20
G_NIST610_3	445.60	4.80	428.60	5.40	451.40	5.40	446.20	5.00	447.60	5.70	435.30	5.00	435.20	5.60
G_NIST610_4	451.40	6.50	433.20	6.40	455.90	7.70	448.60	6.10	450.20	6.90	439.30	6.50	440.40	6.70
G_NIST610_5	446.40	4.80	429.20	5.00	454.20	5.60	445.80	4.50	448.60	6.20	434.20	5.30	434.10	5.50
G_NIST610_6	452.20	5.30	435.30	5.50	460.40	5.90	451.70	5.70	453.20	6.00	443.80	4.70	442.10	5.50
G_NIST610_7	446.90	5.70	427.20	5.30	454.10	6.00	443.20	5.40	445.30	5.90	435.70	5.90	437.20	6.70
G_NIST610_8	451.20	6.00	433.70	6.70	459.50	6.90	453.10	6.00	452.00	6.30	441.70	5.80	438.70	6.10
G_NIST610_9	448.10	4.80	428.80	4.80	451.40	5.70	447.30	5.00	449.30	5.90	436.40	5.20	435.70	5.50
G_NIST610_10	448.30	4.80	431.50	5.00	452.80	4.80	447.90	5.10	449.80	5.20	435.20	5.30	438.30	5.40
G_NIST610_11	447.10	5.50	429.30	6.00	451.60	6.50	445.10	5.60	447.30	6.00	434.80	5.40	435.50	5.30
G_NIST610_12	444.50	4.30	426.50	4.90	447.00	4.70	443.60	4.60	446.10	5.40	433.30	4.70	435.00	4.60
G_NIST610_13	446.40	5.40	428.90	5.20	451.30	5.90	444.60	5.70	447.50	5.90	435.60	5.60	434.50	6.00
G_NIST610_14	453.40	5.20	434.20	5.90	457.90	6.20	452.00	5.40	454.60	6.00	441.60	5.50	440.80	5.70
G_NIST610_15	447.20	5.50	429.40	5.60	453.90	6.00	445.50	5.30	447.30	5.70	436.20	5.50	436.40	5.80
G_NIST610_16	448.40	5.60	429.70	5.60	451.50	5.90	447.90	5.90	449.00	5.90	437.20	5.70	437.40	6.70
G_NIST610_17	448.30	5.20	432.30	4.90	453.50	5.70	448.10	5.50	450.30	5.40	436.80	5.40	437.40	5.70
G_NIST610_18	447.80	4.70	428.70	4.50	454.00	5.50	446.90	5.10	448.20	5.60	438.30	5.10	437.30	5.40

	Ho	2σ	Er	2σ	Tm	2σ	Yb	2σ	Lu	2σ	Hf	2σ	Hg	2σ
G_NIST610_1	445.60	6.00	454.00	6.20	431.00	5.10	446.80	5.90	436.90	5.90	433.80	6.10	49.00	29.00
G_NIST610_2	449.10	4.90	454.90	5.20	436.60	5.00	452.40	5.90	438.80	4.50	436.20	5.50	75.00	34.00
G_NIST610_3	448.30	5.10	453.70	5.30	433.30	5.40	447.50	5.20	436.80	5.30	431.50	6.10	56.00	29.00
G_NIST610_4	452.10	6.80	458.40	6.80	439.10	6.60	452.80	6.60	442.30	6.20	435.90	6.30	64.00	33.00

G_NIST610_5	447.50	5.00	452.70	5.70	434.20	4.80	450.50	5.50	438.80	4.80	433.70	5.30	34.00	27.00
G_NIST610_6	454.60	5.80	457.60	5.50	440.10	5.90	453.10	6.40	443.70	5.50	439.60	6.20	49.00	32.00
G_NIST610_7	448.10	6.10	452.50	6.40	433.70	5.70	447.60	6.50	436.10	5.70	433.10	5.90	53.00	31.00
G_NIST610_8	452.30	5.90	459.20	6.90	440.40	6.10	453.30	6.90	442.90	6.20	440.60	6.30	72.00	31.00
G_NIST610_9	448.60	5.70	454.70	5.30	434.00	5.30	449.30	5.70	436.50	5.30	434.90	5.80	57.00	27.00
G_NIST610_10	448.40	4.70	455.50	4.70	434.10	4.90	450.60	6.00	440.00	5.10	433.60	5.00	53.00	29.00
G_NIST610_11	446.20	5.70	453.60	5.70	432.60	5.60	448.20	6.60	437.90	6.00	433.10	5.50	23.00	26.00
G_NIST610_12	446.50	5.10	453.20	4.80	432.90	4.60	447.30	5.40	437.00	4.80	434.40	5.10	41.00	28.00
G_NIST610_13	447.40	5.90	453.50	6.20	432.20	5.20	447.70	5.40	436.40	5.20	431.30	5.90	45.00	30.00
G_NIST610_14	453.60	5.60	458.90	5.80	439.60	5.20	456.70	5.60	443.50	4.90	440.60	5.40	56.00	29.00
G_NIST610_15	447.00	5.80	454.50	5.50	434.80	5.30	447.50	5.50	437.20	5.40	434.30	6.20	35.00	27.00
G_NIST610_16	449.80	6.40	455.40	6.20	435.10	5.30	450.00	6.90	439.50	6.00	433.60	6.20	49.00	30.00
G_NIST610_17	450.20	4.80	454.60	5.20	435.70	5.50	450.70	6.00	439.00	5.40	435.20	5.60	49.00	30.00
G_NIST610_18	448.50	5.10	455.30	5.40	435.10	5.30	450.50	5.40	439.50	4.60	435.90	5.90	13.00	23.00

	Pb (204)	2σ	Pb (206)	2σ	Pb (207)	2σ	Pb (208)	2σ	Th (232)	2σ	U (238)	2σ
G_NIST610_1	419.50	9.40	421.10	6.10	422.40	6.10	420.40	6.00	454.70	5.80	457.40	6.00
G_NIST610_2	428.40	8.60	426.00	4.80	427.30	4.80	427.80	4.80	457.70	5.00	462.90	4.80
G_NIST610_3	423.30	8.70	425.00	4.70	424.30	4.70	423.90	5.10	455.10	5.30	459.70	5.30
G_NIST610_4	432.00	10.00	430.90	6.40	428.70	6.00	429.90	6.50	461.60	6.70	464.90	6.90
G_NIST610_5	425.10	7.90	425.10	5.00	425.00	4.80	425.20	4.90	455.70	5.10	460.50	5.50
G_NIST610_6	430.20	9.50	431.60	5.30	430.60	5.20	431.40	5.30	461.70	5.80	466.40	5.70
G_NIST610_7	419.10	9.80	423.80	5.70	422.50	5.50	422.40	5.80	454.50	6.30	460.10	6.20
G_NIST610_8	428.50	9.20	428.20	6.30	427.60	6.40	429.30	6.70	461.00	6.40	463.20	6.40
G_NIST610_9	426.40	9.40	427.60	5.20	428.30	4.80	427.20	4.90	456.00	5.20	461.70	5.40

G_NIST610_10	435.70	7.80	426.30	5.00	426.60	5.20	427.60	5.40	457.70	4.90	460.50	5.20
G_NIST610_11	425.60	7.80	423.00	5.50	423.70	5.50	423.60	5.40	456.60	6.00	460.00	6.00
G_NIST610_12	419.60	7.50	422.40	4.90	423.20	4.60	422.40	4.50	455.30	4.50	459.50	4.80
G_NIST610_13	422.80	9.50	425.10	5.70	425.80	5.70	425.50	5.80	455.60	5.80	461.20	6.00
G_NIST610_14	424.20	8.10	428.10	4.90	429.20	4.90	429.90	5.30	461.50	5.60	466.10	6.00
G_NIST610_15	427.50	8.20	425.50	4.90	424.10	4.90	424.80	4.80	456.60	5.20	460.90	5.70
G_NIST610_16	425.50	8.90	424.70	5.70	425.50	5.60	424.10	5.80	455.40	5.80	459.40	6.10
G_NIST610_17	428.50	7.80	428.00	5.00	428.30	5.00	428.60	5.40	458.50	5.50	462.00	5.70
G_NIST610_18	425.50	7.40	425.90	4.80	425.20	4.50	425.80	5.20	457.40	5.40	462.10	5.40

Element	La	Ce	Pr	Nd	Sm	Eu	Gd	Tb	Dy	Ho	Er	Tm	Yb	Lu
Units	ppm	ppm	ppm	ppm	ppm	ppm	ppm	ppm	ppm	ppm	ppm	ppm	ppm	ppm
Normalisation Value	0.31	0.81	0.12	0.60	0.20	0.07	0.26	0.05	0.32	0.07	0.21	0.03	0.21	0.03
WGC2019-15 CONCORDANT														
WGC2019-15 - 2	4.40	11.20	0.98	3.48	1.86	0.33	10.90	4.11	50.30	19.58	87.30	16.41	136.80	26.33
WGC2019-15 - 3	0.00	7.94	0.02	0.59	1.47	0.11	9.67	3.23	43.60	16.79	83.60	17.13	153.50	31.23
WGC2019-15 - 5	0.00	3.47	0.02	0.20	0.51	0.20	3.15	1.37	18.40	8.24	46.30	11.46	118.90	27.31
WGC2019-15 - 10	0.12	9.83	0.15	1.26	1.95	0.43	12.05	4.40	53.20	18.58	88.00	17.31	154.90	30.27
WGC2019-15 - 11	0.71	10.65	0.40	2.36	2.42	0.59	11.43	3.77	48.40	17.91	84.60	18.70	169.30	34.10
WGC2019-15 - 20	1.67	7.25	0.62	2.88	1.80	0.44	6.90	3.75	59.60	27.70	174.40	46.40	521.00	116.00
WGC2019-15 - 22	24.40	43.60	5.56	23.20	5.70	1.11	9.00	3.01	50.50	27.10	171.10	46.90	518.00	116.30
WGC2019-15 - 24	0.24	9.89	0.21	1.59	2.30	0.55	9.97	3.36	42.30	14.51	65.20	12.72	113.00	21.71
WGC2019-15 - 32	0.01	4.49	0.05	0.76	1.38	0.17	7.25	2.61	35.80	15.10	81.00	19.20	202.00	49.30
WGC2019-15 - 39	0.01	2.11	0.00	0.24	0.55	0.19	2.86	1.18	16.09	6.97	37.00	9.28	95.10	21.55
WGC2019-15 - 40	0.01	1.78	0.02	0.21	0.76	0.11	6.48	3.58	65.10	31.80	199.00	56.10	623.00	137.30

WGC2019-15 - 45	0.29	9.37	0.16	1.37	1.31	0.20	6.83	2.55	36.20	14.90	81.10	19.18	194.50	42.90
WGC2019-15 - 55	0.16	7.25	0.17	1.39	1.41	0.36	5.10	1.98	23.90	9.09	47.80	10.36	104.30	23.00
WGC2019-15 - 57	0.04	2.37	0.05	0.68	0.69	0.30	3.39	1.06	15.73	6.60	39.00	9.42	102.20	22.89
WGC2019-15 - 60	0.11	8.36	0.13	0.60	1.62	0.24	13.30	6.46	104.60	47.10	260.00	60.20	533.00	103.50
WGC2019-15 DISCORDANT														
WGC2019-15 - 1	0.19	5.67	0.23	1.74	2.09	0.45	8.90	2.28	18.70	5.11	24.40	6.44	76.90	23.50
WGC2019-15 - 4	0.01	9.56	0.08	1.70	3.42	0.32	18.90	6.41	78.60	29.00	134.20	26.35	229.40	45.80
WGC2019-15 - 6	491.30	699.00	76.30	268.30	28.00	4.61	27.80	6.83	73.60	28.20	137.30	27.10	248.10	49.80
WGC2019-15 - 7	33.10	85.00	10.30	48.10	16.20	4.51	22.40	5.53	67.50	25.72	141.60	36.00	394.50	90.00
WGC2019-15 - 8	1.82	12.50	1.43	9.00	4.10	1.10	8.50	2.44	28.60	11.28	66.20	17.30	190.40	49.40
WGC2019-15 - 9	0.68	8.77	0.83	5.12	3.00	0.68	6.22	1.82	23.00	10.22	61.30	15.84	178.00	43.90
WGC2019-15 - 12	0.40	7.60	0.35	2.74	2.80	0.70	10.09	3.42	43.50	17.60	91.10	22.00	214.00	46.60
WGC2019-15 - 13	0.07	5.00	0.03	0.35	0.64	0.15	4.15	1.72	23.20	10.05	54.30	13.15	130.60	29.19
WGC2019-15 - 14	0.07	1.97	0.04	0.28	0.54	0.10	4.54	2.68	46.80	20.36	124.00	32.20	354.00	77.80
WGC2019-15 - 15	83.00	154.00	17.40	69.00	12.40	3.13	15.50	4.15	51.60	22.44	128.10	32.13	349.00	79.90
WGC2019-15 - 16	1.36	17.01	1.56	9.40	6.88	1.84	18.30	5.64	76.60	31.60	169.20	41.10	432.00	95.90
WGC2019-15 - 17	0.34	18.30	0.50	3.79	5.60	0.77	22.80	8.00	93.50	36.50	172.50	35.90	309.60	63.40
WGC2019-15 - 18	5.10	25.00	2.30	11.40	6.60	0.87	22.50	7.14	84.80	32.40	159.00	34.00	323.60	70.30
WGC2019-15 - 19	185.00	313.00	40.50	151.00	24.60	5.17	23.00	4.94	53.60	19.70	94.50	19.90	183.00	37.10
WGC2019-15 - 21	0.67	7.74	0.57	3.16	2.09	0.81	5.07	2.29	42.60	22.79	158.10	44.50	501.00	113.50
WGC2019-15 - 23	0.01	2.97	0.01	0.10	0.35	0.03	3.02	1.44	19.80	9.40	53.90	13.76	148.20	36.80
WGC2019-15 - 25	0.52	4.73	0.54	3.91	1.94	0.40	3.05	0.83	12.10	6.27	44.60	12.44	155.80	45.80
WGC2019-15 - 26	333.00	605.00	73.90	265.00	30.90	5.84	19.20	3.26	43.60	17.38	93.40	22.40	224.00	47.30
WGC2019-15 - 27	9.70	29.00	2.90	14.50	6.20	1.19	15.00	4.88	52.80	19.60	95.40	20.10	191.70	40.10
WGC2019-15 - 28	1.21	19.70	1.00	5.81	3.55	0.79	12.78	4.17	48.60	18.30	87.70	18.00	170.00	34.10
WGC2019-15 - 29	0.59	13.50	0.57	4.39	3.62	0.81	12.84	5.80	88.10	37.30	197.50	43.80	382.40	75.50
WGC2019-15 - 30	15.70	31.00	3.70	16.30	5.10	1.13	9.50	2.59	31.60	11.80	57.20	12.17	113.40	23.60

WGC2019-15 - 31	0.02	6.95	0.05	0.81	2.21	0.12	12.30	4.10	43.10	13.78	55.20	9.51	73.10	14.07
WGC2019-15 - 33	0.12	4.82	0.13	1.03	1.23	0.22	5.79	2.10	31.30	13.52	75.60	19.35	208.60	51.10
WGC2019-15 - 34	0.20	7.38	0.19	1.32	1.39	0.44	7.60	2.60	35.60	14.80	74.90	15.80	147.00	31.70
WGC2019-15 - 35	1.81	16.70	1.21	6.86	4.17	1.32	16.70	6.37	97.60	40.49	221.80	49.80	471.00	98.80
WGC2019-15 - 36	0.13	3.40	0.17	0.81	0.99	0.37	3.85	1.28	18.69	7.43	41.10	10.19	108.30	25.82
WGC2019-15 - 37	0.08	3.58	0.12	1.11	1.14	0.43	3.63	1.08	13.78	5.83	31.90	7.56	77.90	17.13
WGC2019-15 - 38	1.95	14.50	1.08	6.69	3.69	0.76	13.50	6.12	101.20	47.00	271.60	66.60	653.00	134.20
WGC2019-15 - 41	0.29	14.50	0.35	3.19	5.75	0.66	30.00	9.45	116.70	43.10	203.40	42.10	389.00	80.30
WGC2019-15 - 42	0.04	5.97	0.04	0.44	1.05	0.47	7.19	2.56	33.20	12.25	61.30	13.42	127.00	25.60
WGC2019-15 - 43	1.64	25.65	0.95	7.57	5.65	1.19	24.00	8.25	94.80	37.60	182.90	38.80	351.60	71.40
WGC2019-15 - 44	1.31	17.50	1.04	6.82	3.92	0.96	10.90	3.36	38.60	14.40	66.30	13.97	127.50	25.65
WGC2019-15 - 46	2.74	21.30	2.32	14.10	6.19	2.18	14.20	5.49	87.10	38.20	227.00	61.60	679.00	153.20
WGC2019-15 - 47	0.19	3.38	0.15	1.60	1.00	0.56	3.33	1.10	12.81	5.10	29.00	7.05	74.80	18.73
WGC2019-15 - 48	2.05	15.65	1.47	9.20	4.57	1.46	10.89	3.38	42.50	18.40	99.60	23.20	237.00	53.10
WGC2019-15 - 49	0.46	8.94	0.48	3.05	2.48	0.83	10.70	5.11	72.10	33.70	194.00	48.30	505.00	113.80
WGC2019-15 - 50	0.18	3.22	0.11	0.55	0.59	0.31	3.40	1.34	14.64	5.34	28.60	7.00	73.90	16.58
WGC2019-15 - 51	15.70	142.00	14.00	80.00	46.00	11.80	90.00	23.00	225.00	71.60	307.50	59.40	493.30	91.20
WGC2019-15 - 52	0.02	1.99	0.02	0.20	0.81	0.12	7.40	4.21	76.30	35.10	221.00	59.20	642.00	142.40
WGC2019-15 - 53	4.60	12.60	1.08	4.90	1.07	0.23	2.65	1.07	16.40	7.11	37.60	9.38	100.30	22.76
WGC2019-15 - 54	0.48	7.90	0.48	2.92	2.27	0.56	9.70	4.02	60.80	28.09	159.70	45.10	490.00	109.70
WGC2019-15 - 56	0.27	8.01	0.30	2.20	2.59	0.51	9.07	3.14	39.90	15.95	82.30	18.03	174.90	39.39
WGC2019-15 - 58	0.04	5.25	0.04	0.56	2.03	0.16	11.90	3.74	37.10	11.44	44.90	7.51	58.10	11.03
WGC2019-15 - 59	17.90	49.20	4.95	20.70	6.05	0.93	11.39	3.43	43.90	17.65	93.60	22.51	224.60	48.00
WGC2019J-16J CONCORDANT														
WGC2019J-16J - 1	0.00	0.86	0.00	0.00	0.17	0.11	1.35	0.47	6.53	2.64	14.01	3.19	33.30	7.52
WGC2019J-16J - 2	0.00	1.89	0.00	0.10	0.25	0.18	1.73	0.59	8.96	3.88	20.80	4.88	50.90	12.41
WGC2019J-16J - 3	0.01	1.76	0.02	0.18	0.39	0.28	1.95	0.71	8.70	3.59	17.36	3.68	37.40	7.63

WGC2019J-16J - 4	0.02	1.54	0.02	0.20	0.31	0.16	1.90	0.62	8.77	3.33	18.20	4.25	44.00	10.07
WGC2019J-16J - 5	0.27	7.90	0.20	1.03	1.15	0.50	5.51	1.98	24.00	10.22	51.20	12.60	128.30	29.80
WGC2019J-16J - 7	0.00	0.86	0.00	0.16	0.30	0.20	1.68	0.64	8.12	3.00	14.08	2.60	21.40	3.99
WGC2019J-16J - 8	0.00	0.80	0.01	0.10	0.28	0.13	1.58	0.52	7.13	2.73	14.89	3.38	33.50	7.61
WGC2019J-16J - 9	0.00	0.76	0.00	0.07	0.20	0.14	1.36	0.56	8.01	2.89	14.75	3.18	31.10	7.17
WGC2019J-16J - 10	0.00	2.06	0.01	0.25	0.57	0.27	2.88	1.10	13.68	4.95	24.19	5.37	48.90	10.05
WGC2019J-16J - 11	0.00	1.46	0.01	0.23	0.39	0.21	2.06	0.79	10.09	4.33	21.30	5.04	48.90	11.78
WGC2019J-16J - 13	0.00	1.57	0.01	0.16	0.36	0.27	2.88	0.96	11.86	4.95	26.30	5.91	62.40	15.00
WGC2019J-16J - 14	0.00	1.42	0.01	0.12	0.36	0.19	1.95	0.75	9.31	3.69	19.80	4.41	51.20	11.80
WGC2019J-16J - 18	0.01	1.64	0.02	0.19	0.56	0.28	2.22	0.78	8.97	3.70	19.61	4.64	50.10	11.60
WGC2019J-16J - 19	0.00	0.96	0.01	0.07	0.33	0.17	1.90	0.66	7.62	2.82	12.67	2.24	17.92	3.30
WGC2019J-16J - 21	0.00	2.21	0.01	0.13	0.32	0.21	2.13	0.86	11.28	4.95	28.40	6.96	74.60	18.27
WGC2019J-16J - 23	0.00	1.91	0.01	0.27	0.50	0.30	2.91	0.99	10.72	3.86	16.55	3.40	27.40	5.69
WGC2019J-16J - 24	0.00	1.59	0.01	0.23	0.36	0.26	1.94	0.57	7.13	2.89	15.09	3.32	34.70	8.01
WGC2019J-16J - 25	0.00	0.88	0.01	0.12	0.33	0.16	1.50	0.51	6.10	2.26	10.63	2.22	21.10	4.08
WGC2019J-16J - 26	0.00	1.88	0.01	0.07	0.27	0.23	1.71	0.60	8.35	3.47	20.00	5.09	53.70	13.06
WGC2019J-16J - 27	0.01	0.79	0.01	0.12	0.31	0.22	1.69	0.48	6.75	2.49	11.07	2.33	19.04	3.92
WGC2019J-16J - 28	0.00	0.74	0.00	0.13	0.29	0.14	1.50	0.46	6.09	2.47	11.83	2.65	25.20	5.66
WGC2019J-16J - 31	0.00	0.90	0.01	0.05	0.16	0.11	1.33	0.55	7.50	3.58	19.74	4.65	50.00	12.12
WGC2019J-16J - 32	0.00	0.83	0.01	0.04	0.17	0.13	1.47	0.66	8.46	3.48	19.36	4.65	49.60	11.68
WGC2019J-16J - 33	0.00	1.86	0.00	0.17	0.48	0.28	2.75	0.66	8.24	2.73	12.74	2.15	18.40	3.53
WGC2019J-16J - 34	0.08	2.47	0.04	0.47	0.39	0.25	1.43	0.59	7.02	2.73	15.54	3.65	36.50	8.43
WGC2019J-16J - 35	0.00	1.81	0.01	0.00	0.47	0.20	1.81	0.71	10.10	4.42	21.90	5.58	57.10	12.98
WGC2019J-16J - 37	0.00	0.83	0.00	0.12	0.14	0.17	1.56	0.60	6.92	2.47	12.51	2.61	25.50	5.05
WGC2019J-16J - 38	0.00	0.83	0.01	0.15	0.36	0.21	2.03	0.64	8.33	3.06	15.15	2.88	25.50	4.94
WGC2019J-16J - 39	0.00	1.58	0.01	0.14	0.24	0.24	1.77	0.63	9.01	3.52	17.51	4.26	42.40	9.97
WGC2019J-16J - 40	0.00	1.40	0.01	0.09	0.24	0.17	1.55	0.50	7.79	2.94	15.94	3.94	38.80	9.04

WGC2019J-16J - 41	0.11	2.31	0.07	0.98	1.70	0.25	7.10	2.07	19.50	5.81	23.70	5.05	48.00	9.61
WGC2019J-16J - 43	0.00	0.70	0.01	0.08	0.10	0.13	1.22	0.44	6.33	2.64	15.05	3.63	37.20	9.79
WGC2019J-16J - 44	0.00	0.60	0.00	0.06	0.16	0.13	1.53	0.48	6.98	3.03	16.64	4.23	43.00	10.61
WGC2019J-16J - 45	0.01	2.02	0.02	0.25	0.52	0.20	2.40	0.90	10.46	4.27	21.25	5.13	56.40	12.45
WGC2019J-16J - 46	0.00	1.72	0.01	0.24	0.27	0.21	2.11	0.76	11.43	4.74	26.20	6.18	65.30	15.68
WGC2019J-16J - 47	0.00	1.87	0.01	0.08	0.13	0.17	2.09	0.74	10.34	4.17	24.16	6.33	67.20	16.92
WGC2019J-16J - 49	0.00	2.49	0.02	0.31	0.63	0.24	3.49	1.20	14.92	6.24	31.60	6.96	67.00	14.45
WGC2019J-16J - 50	0.00	2.22	0.01	0.11	0.41	0.12	2.99	0.97	12.60	5.07	25.10	5.60	55.20	11.78
WGC2019J-16J - 51	0.00	5.09	0.02	0.46	0.80	0.29	5.36	1.56	19.20	6.38	26.70	4.97	42.80	8.58
WGC2019J-16J DISCORDANT														
WGC2019J-16J - 6	0.06	1.36	0.03	0.35	0.44	0.31	2.40	0.77	10.42	3.87	19.50	4.45	45.10	10.06
WGC2019J-16J - 12	0.01	1.20	0.02	0.19	0.26	0.22	2.16	0.74	11.00	4.42	21.60	4.38	45.10	9.17
WGC2019J-16J - 15	0.04	1.45	0.04	0.30	0.37	0.25	1.75	0.72	9.31	3.82	19.60	4.65	53.00	12.28
WGC2019J-16J - 16	0.00	2.43	0.00	0.17	0.46	0.32	3.61	1.12	11.41	3.58	16.60	3.26	30.70	6.88
WGC2019J-16J - 17	0.00	9.31	0.03	0.77	2.38	0.26	14.10	4.55	52.70	20.20	97.00	21.19	181.70	35.80
WGC2019J-16J - 20	0.05	2.25	0.03	0.16	0.61	0.27	2.46	0.78	9.80	3.87	21.70	5.19	56.30	13.39
WGC2019J-16J - 22	0.00	1.84	0.01	0.10	0.71	0.36	3.33	0.89	10.20	3.40	15.40	2.79	24.90	4.94
WGC2019J-16J - 29	0.00	2.11	0.01	0.20	0.24	0.17	2.40	0.91	10.60	3.76	19.50	4.64	43.30	10.62
WGC2019J-16J - 30	0.01	2.52	0.03	0.19	0.40	0.20	2.56	0.82	11.33	4.81	25.20	5.94	60.70	13.36
WGC2019J-16J - 36	0.02	1.06	0.02	0.16	0.33	0.42	3.21	0.79	6.80	1.78	7.17	1.52	15.40	3.63
WGC2019J-16J - 42	0.23	54.30	4.94	68.80	68.40	9.36	135.00	30.10	241.50	61.60	208.80	34.50	241.10	36.27
WGC2019J-16J - 48	0.01	5.93	0.10	1.51	2.81	0.58	14.70	5.03	64.90	23.60	104.40	23.20	204.00	38.00
WGC2019J-17D CONCORDANT														
WGC2019J-17D - 1	0.00	3.33	0.01	0.18	0.56	0.25	3.47	1.31	17.90	7.76	42.10	9.95	106.70	24.41
WGC2019J-17D - 2	0.00	3.33	0.01	0.27	0.62	0.27	4.16	1.65	23.10	9.38	51.30	12.92	130.80	31.11
WGC2019J-17D - 3	0.00	3.22	0.01	0.12	0.44	0.23	2.92	1.29	15.77	7.38	39.20	9.46	100.20	22.79

WGC2019J-17D - 6	0.00	3.48	0.02	0.26	0.58	0.28	4.14	1.78	22.70	9.80	55.40	13.44	135.40	30.54
WGC2019J-17D - 8	0.00	3.88	0.01	0.22	0.35	0.14	3.59	1.40	19.80	8.60	46.10	11.34	117.50	26.43
WGC2019J-17D - 10	0.00	3.93	0.02	0.25	0.49	0.17	3.86	1.35	19.17	8.25	45.60	10.67	111.90	24.74
WGC2019J-17D - 11	0.00	3.72	0.01	0.24	0.64	0.15	3.52	1.36	19.50	7.70	41.20	9.74	98.40	21.72
WGC2019J-17D - 12	0.01	3.77	0.01	0.12	0.54	0.27	3.76	1.53	22.30	8.79	47.30	11.18	110.40	23.90
WGC2019J-17D - 13	0.00	3.20	0.01	0.00	0.42	0.23	3.59	1.34	19.20	7.60	41.90	9.81	104.40	22.10
WGC2019J-17D - 17	0.00	3.51	0.01	0.13	0.44	0.20	3.58	1.50	20.60	9.14	49.20	11.78	124.70	28.56
WGC2019J-17D - 18	0.00	3.74	0.01	0.14	0.48	0.15	3.32	1.25	17.96	8.09	46.00	10.81	113.20	25.73
WGC2019J-17D - 19	0.00	2.49	0.01	0.00	0.26	0.16	2.16	1.01	13.58	5.77	34.60	8.29	92.10	21.04
WGC2019J-17D - 22	0.00	3.58	0.01	0.23	0.53	0.21	4.24	1.73	22.88	9.43	51.80	11.89	118.80	27.43
WGC2019J-17D - 23	0.00	3.22	0.01	0.07	0.39	0.15	2.85	1.12	17.41	6.95	37.80	8.99	92.10	19.93
WGC2019J-17D - 24	0.00	3.46	0.01	0.14	0.44	0.18	3.09	1.34	17.90	7.60	41.70	9.89	102.30	23.00
WGC2019J-17D - 25	0.00	3.34	0.01	0.25	0.45	0.21	3.24	1.30	17.99	7.50	40.60	9.83	100.10	23.27
WGC2019J-17D - 26	0.00	3.12	0.01	0.18	0.31	0.16	2.78	1.05	14.79	6.24	35.10	8.04	83.10	19.49
WGC2019J-17D - 28	0.00	2.63	0.00	0.06	0.27	0.16	2.08	0.84	11.91	5.08	29.50	7.19	75.80	17.82
WGC2019J-17D - 30	0.01	3.57	0.01	0.25	0.48	0.16	3.56	1.32	18.10	8.23	44.80	10.20	101.90	22.84
WGC2019J-17D - 32	0.01	4.09	0.03	0.18	0.63	0.35	5.42	2.02	24.80	10.81	58.00	13.74	140.90	31.13
WGC2019J-17D - 33	0.00	3.96	0.01	0.24	0.45	0.23	3.97	1.58	22.30	9.33	51.60	12.22	130.50	29.48
WGC2019J-17D - 35	0.00	3.10	0.00	0.19	0.37	0.21	3.45	1.26	19.00	7.38	42.50	10.32	107.30	24.69
WGC2019J-17D - 39	0.00	3.34	0.01	0.21	0.53	0.15	3.51	1.30	17.24	7.33	40.90	9.67	100.50	22.36
WGC2019J-17D - 41	0.00	3.36	0.01	0.17	0.36	0.20	3.15	1.17	16.89	7.24	39.10	9.40	100.60	22.19
WGC2019J-17D - 43	0.00	3.50	0.01	0.21	0.32	0.20	3.45	1.26	17.30	7.33	39.30	9.49	99.90	22.80
WGC2019J-17D - 44	0.00	3.56	0.01	0.12	0.50	0.20	3.69	1.43	20.08	8.47	46.20	10.64	113.20	25.17
WGC2019J-17D - 45	0.01	3.69	0.03	0.19	0.47	0.26	3.22	1.27	16.17	6.85	36.00	8.69	91.10	20.56
WGC2019J-17D - 46	0.00	3.54	0.01	0.17	0.40	0.20	3.33	1.27	16.56	7.34	39.60	9.73	98.70	22.23
WGC2019J-17D - 47	0.00	3.60	0.01	0.14	0.73	0.20	4.45	1.43	22.30	9.47	51.00	12.39	126.30	27.39
WGC2019J-17D - 49	0.00	2.94	0.00	0.18	0.51	0.18	3.30	1.20	18.43	7.65	43.00	10.05	105.70	24.99

WGC2019J-17D DISCORDANT														
WGC2019J-17D - 4	0.01	2.71	0.02	0.12	0.38	0.29	2.91	1.18	16.30	7.48	40.70	9.42	101.80	24.03
WGC2019J-17D - 5	0.01	3.05	0.06	0.33	0.89	0.35	3.98	1.65	19.60	8.10	43.20	10.80	112.40	27.00
WGC2019J-17D - 7	0.03	2.74	0.02	0.37	0.32	0.21	2.89	1.13	16.03	6.73	38.30	8.98	97.70	22.93
WGC2019J-17D - 9	0.00	2.89	0.00	0.14	0.55	0.18	3.55	1.33	19.60	8.01	44.90	10.80	117.40	27.54
WGC2019J-17D - 14	0.00	3.08	0.01	0.12	0.41	0.15	3.45	1.28	18.40	7.38	39.90	9.81	101.00	22.80
WGC2019J-17D - 15	0.00	4.41	0.01	0.18	0.70	0.25	4.80	1.77	25.40	10.50	57.50	13.37	133.80	29.17
WGC2019J-17D - 16	0.06	4.15	0.05	0.15	0.65	0.24	5.30	2.12	25.00	10.99	60.20	13.11	129.20	28.30
WGC2019J-17D - 20	0.00	2.87	0.02	0.12	0.39	0.21	3.26	1.36	18.70	7.68	44.10	11.25	116.50	27.47
WGC2019J-17D - 21	93.10	244.00	33.30	134.60	22.70	3.11	14.90	2.23	20.10	8.19	45.10	10.35	109.10	25.30
WGC2019J-17D - 27	0.01	2.83	0.02	0.17	0.40	0.20	2.37	1.02	13.90	5.93	34.90	8.37	89.70	21.80
WGC2019J-17D - 29	0.01	3.77	0.02	0.23	0.58	0.15	3.29	1.48	20.30	8.90	44.90	10.64	102.90	23.18
WGC2019J-17D - 31	0.00	3.66	0.01	0.13	0.51	0.27	3.54	1.45	19.04	8.39	44.30	10.49	110.20	24.01
WGC2019J-17D - 34	0.00	4.28	0.01	0.19	0.93	0.31	5.83	2.30	30.10	12.53	71.30	16.71	163.20	35.92
WGC2019J-17D - 36	0.00	3.60	0.01	0.26	0.52	0.17	3.66	1.29	19.60	8.45	46.10	10.96	111.30	25.33
WGC2019J-17D - 37	0.01	3.01	0.01	0.13	0.27	0.17	2.76	0.98	15.80	6.38	35.40	8.79	89.50	20.74
WGC2019J-17D - 38	0.01	3.90	0.02	0.16	0.55	0.18	4.17	1.66	23.89	10.25	56.80	13.27	139.70	31.07
WGC2019J-17D - 40	0.02	3.45	0.02	0.19	0.50	0.34	4.70	1.69	24.90	10.39	57.80	13.88	136.30	31.54
WGC2019J-17D - 42	0.00	3.01	0.02	0.35	0.46	0.25	3.75	1.35	19.20	7.82	43.70	10.84	112.50	26.33
WGC2019J-17D - 48	0.00	3.20	0.01	0.10	0.40	0.16	2.89	1.24	16.65	6.92	39.20	9.23	92.50	21.25

Element	Y	Th 232	U 238	Nb	La	Ce	Nd	Hf	Ti	Y	Pb 204	Pb 206	Pb 207	Pb 208
Units	ppm	ppm	ppm	ppm	ppm	ppm	ppm	ppm	ppm	ppm	ppm	ppm	ppm	ppm
Normalisation Value	0.00	0.08	0.02	0.71	0.71	1.83	1.37	0.31	1280.00	4.55	0.07	0.07	0.07	0.07
WGC2019-15 CONCORDANT														
WGC2019-15 - 2	560.00	75.00	750.00	2.49	4.40	11.20	3.48	10360.00	6.20	560.00	0.00	488.50	38.85	7.07
WGC2019-15 - 3	521.60	49.60	144.60	1.01	0.00	7.94	0.59	9710.00	2.60	521.60	0.00	90.80	7.12	4.45
WGC2019-15 - 5	278.60	114.20	443.00	0.56	0.00	3.47	0.20	8590.00	4.10	278.60	0.00	276.00	21.82	10.70
WGC2019-15 - 10	605.30	76.70	537.70	3.32	0.12	9.83	1.26	9510.00	7.90	605.30	0.00	346.00	27.39	6.85
WGC2019-15 - 11	553.00	60.10	495.20	2.81	0.71	10.65	2.36	9720.00	6.90	553.00	0.00	310.90	25.02	5.72
WGC2019-15 - 20	918.00	17.10	722.00	4.25	1.67	7.25	2.88	11070.00	27.00	918.00	0.00	458.00	37.80	2.56
WGC2019-15 - 22	877.00	28.64	1284.00	12.13	24.40	43.60	23.20	11670.00	7.60	877.00	0.00	757.00	59.80	2.86
WGC2019-15 - 24	462.90	68.60	404.40	1.92	0.24	9.89	1.59	9350.00	7.20	462.90	0.00	244.60	18.96	5.92
WGC2019-15 - 32	479.00	25.40	507.00	2.48	0.01	4.49	0.76	9660.00	4.10	479.00	0.00	337.00	27.40	3.22
WGC2019-15 - 39	233.20	53.10	212.80	0.31	0.01	2.11	0.24	8494.00	4.40	233.20	0.00	126.20	9.66	4.55
WGC2019-15 - 40	1014.00	10.04	816.00	2.74	0.01	1.78	0.21	11280.00	7.40	1014.00	0.00	527.00	42.10	1.22
WGC2019-15 - 45	500.00	93.70	510.00	4.27	0.29	9.37	1.37	10910.00	9.30	500.00	0.00	339.00	27.20	8.92
WGC2019-15 - 55	289.70	26.01	142.00	1.89	0.16	7.25	1.39	9520.00	7.00	289.70	0.00	93.10	7.36	2.01
WGC2019-15 - 57	230.90	72.50	291.80	0.28	0.04	2.37	0.68	8803.00	3.70	230.90	0.00	178.00	13.86	6.48
WGC2019-15 - 60	1543.00	45.10	1247.00	13.47	0.11	8.36	0.60	11500.00	8.00	1543.00	0.00	763.00	60.20	4.05
WGC2019-15 DISCORDANT														
WGC2019-15 - 1	159.70	38.18	301.70	1.78	0.19	5.67	1.74	10300.00	5.90	159.70	0.00	175.70	13.90	3.52
WGC2019-15 - 4	845.00	65.70	159.00	1.35	0.01	9.56	1.70	9290.00	7.80	845.00	0.00	118.40	10.49	7.63
WGC2019-15 - 6	847.00	50.70	120.90	1.61	491.30	699.00	268.30	8200.00	13.10	847.00	0.00	103.80	10.46	6.77
WGC2019-15 - 7	797.00	52.20	804.00	3.54	33.10	85.00	48.10	10600.00	43.00	797.00	0.00	385.00	29.65	4.29
WGC2019-15 - 8	390.00	32.70	1377.00	12.20	1.82	12.50	9.00	10970.00	1790.00	390.00	2.50	601.00	44.90	3.40
WGC2019-15 - 9	356.60	32.10	1342.00	3.61	0.68	8.77	5.12	10780.00	11.70	356.60	1.80	590.70	44.80	3.84
WGC2019-15 - 12	545.00	44.80	491.00	2.10	0.40	7.60	2.74	9560.00	8.00	545.00	0.00	256.00	20.90	4.52

WGC2019-15 - 13	333.30	65.00	340.60	1.82	0.07	5.00	0.35	9470.00	33.00	333.30	0.00	190.90	15.54	5.72
WGC2019-15 - 14	649.00	7.01	511.00	1.80	0.07	1.97	0.28	10970.00	8.90	649.00	0.00	283.00	23.10	1.20
WGC2019-15 - 15	713.00	41.60	725.00	6.06	83.00	154.00	69.00	10520.00	21.20	713.00	1.50	371.00	30.70	4.39
WGC2019-15 - 16	977.00	50.90	615.00	2.91	1.36	17.01	9.40	10280.00	30.90	977.00	0.00	326.00	27.30	5.16
WGC2019-15 - 17	1067.00	132.60	283.40	3.40	0.34	18.30	3.79	8940.00	114.00	1067.00	0.00	297.10	30.00	19.38
WGC2019-15 - 18	985.00	97.30	628.00	2.90	5.10	25.00	11.40	9820.00	5.10	985.00	0.00	425.00	36.30	12.00
WGC2019-15 - 19	602.00	62.80	392.00	2.30	185.00	313.00	151.00	9670.00	19.90	602.00	0.00	243.00	19.90	5.73
WGC2019-15 - 21	795.00	17.36	1289.00	14.10	0.67	7.74	3.16	11760.00	9.60	795.00	0.00	771.00	61.70	1.92
WGC2019-15 - 23	310.90	15.90	323.00	2.18	0.01	2.97	0.10	9880.00	4.30	310.90	0.00	202.40	16.54	1.75
WGC2019-15 - 25	238.70	5.60	645.00	1.18	0.52	4.73	3.91	11620.00	8.60	238.70	0.00	397.90	32.01	0.65
WGC2019-15 - 26	538.00	44.00	455.00	6.20	333.00	605.00	265.00	10510.00	5.80	538.00	15.50	278.00	36.00	20.40
WGC2019-15 - 27	622.00	57.40	243.00	2.10	9.70	29.00	14.50	9080.00	5.90	622.00	0.00	176.00	16.70	7.50
WGC2019-15 - 28	567.00	71.00	395.00	3.93	1.21	19.70	5.81	10210.00	8.80	567.00	0.00	257.00	22.00	8.06
WGC2019-15 - 29	1194.00	44.60	620.50	20.30	0.59	13.50	4.39	10018.00	1010.00	1194.00	0.00	309.60	23.64	3.32
WGC2019-15 - 30	372.00	30.60	581.00	1.02	15.70	31.00	16.30	10250.00	8.40	372.00	0.00	322.00	25.70	2.92
WGC2019-15 - 31	409.00	40.50	129.30	0.51	0.02	6.95	0.81	9750.00	7.90	409.00	1.60	82.80	7.88	4.88
WGC2019-15 - 33	447.00	25.00	560.00	3.58	0.12	4.82	1.03	10080.00	3.70	447.00	0.00	342.00	28.10	2.89
WGC2019-15 - 34	437.00	27.80	45.60	1.37	0.20	7.38	1.32	9400.00	6.60	437.00	0.00	24.00	1.98	2.49
WGC2019-15 - 35	1306.00	42.20	1025.00	8.59	1.81	16.70	6.86	10890.00	29.30	1306.00	0.00	512.00	39.59	3.65
WGC2019-15 - 36	250.20	173.70	1018.00	0.26	0.13	3.40	0.81	8041.00	7.30	250.20	0.00	634.00	50.40	16.01
WGC2019-15 - 37	193.60	91.60	317.30	0.36	0.08	3.58	1.11	8600.00	9.60	193.60	0.00	141.90	10.43	6.19
WGC2019-15 - 38	1513.00	29.10	1039.00	10.42	1.95	14.50	6.69	10940.00	15.80	1513.00	0.00	617.00	49.50	2.46
WGC2019-15 - 41	1299.00	96.50	288.00	2.26	0.29	14.50	3.19	8890.00	10.60	1299.00	0.00	236.00	22.70	13.55
WGC2019-15 - 42	400.00	44.26	396.00	1.66	0.04	5.97	0.44	9760.00	5.50	400.00	0.00	140.40	9.73	2.31
WGC2019-15 - 43	1134.00	283.30	657.00	6.16	1.64	25.65	7.57	9480.00	650.00	1134.00	0.00	301.10	24.62	19.60
WGC2019-15 - 44	480.00	108.90	643.00	3.87	1.31	17.50	6.82	10570.00	18.40	480.00	0.00	394.00	31.20	9.85
WGC2019-15 - 46	1207.00	33.80	1341.00	4.34	2.74	21.30	14.10	11280.00	41.50	1207.00	2.40	656.00	51.00	2.65

WGC2019-15 - 47	177.60	123.10	535.00	0.42	0.19	3.38	1.60	8320.00	10.40	177.60	0.00	170.00	11.07	5.80
WGC2019-15 - 48	600.00	52.30	826.00	3.04	2.05	15.65	9.20	10300.00	9.70	600.00	0.00	433.00	33.30	4.09
WGC2019-15 - 49	1089.00	73.60	1751.00	9.14	0.46	8.94	3.05	10250.00	11.60	1089.00	1.50	614.00	44.00	5.67
WGC2019-15 - 50	186.50	35.30	160.20	0.23	0.18	3.22	0.55	9016.00	3.00	186.50	0.00	81.60	6.38	3.03
WGC2019-15 - 51	2209.00	558.00	3230.00	14.20	15.70	142.00	80.00	9120.00	90.00	2209.00	5.40	862.00	59.10	28.25
WGC2019-15 - 52	1158.00	9.90	721.00	3.23	0.02	1.99	0.20	11100.00	5.80	1158.00	0.00	435.50	34.78	0.98
WGC2019-15 - 53	228.40	114.00	368.50	0.38	4.60	12.60	4.90	9050.00	6.80	228.40	0.00	196.10	15.22	9.52
WGC2019-15 - 54	876.00	29.70	717.00	2.61	0.48	7.90	2.92	10670.00	7.70	876.00	0.00	421.00	33.60	2.73
WGC2019-15 - 56	497.00	43.40	400.00	1.74	0.27	8.01	2.20	9350.00	7.70	497.00	0.00	236.00	19.00	4.68
WGC2019-15 - 58	339.60	31.81	199.20	0.89	0.04	5.25	0.56	9898.00	3.50	339.60	0.00	116.50	9.45	2.85
WGC2019-15 - 59	587.00	114.40	714.00	3.80	17.90	49.20	20.70	10160.00	10.80	587.00	0.00	340.00	26.00	8.48
WGC2019J-16J CONCORDANT														
WGC2019J-16J - 1	91.60	20.26	81.40	0.15	0.00	0.86	0.00	6631.00	3.70	91.60	0.00	51.70	4.06	1.85
WGC2019J-16J - 2	121.70	30.60	59.21	0.27	0.00	1.89	0.10	7235.00	4.80	121.70	0.00	36.27	2.76	2.71
WGC2019J-16J - 3	117.10	25.27	61.57	0.25	0.01	1.76	0.18	7311.00	5.50	117.10	0.00	34.94	2.82	2.25
WGC2019J-16J - 4	112.50	25.63	68.60	0.21	0.02	1.54	0.20	7183.00	33.00	112.50	0.00	42.00	3.36	2.39
WGC2019J-16J - 5	330.00	102.40	298.00	0.21	0.27	7.90	1.03	9410.00	1.90	330.00	0.00	172.00	13.23	8.92
WGC2019J-16J - 7	105.40	32.90	110.60	0.23	0.00	0.86	0.16	7130.00	4.40	105.40	0.00	70.10	5.31	2.95
WGC2019J-16J - 8	94.90	26.63	110.30	0.24	0.00	0.80	0.10	6262.00	5.60	94.90	0.00	67.30	5.22	2.19
WGC2019J-16J - 9	97.80	26.43	92.60	0.14	0.00	0.76	0.07	6351.00	6.60	97.80	0.00	58.50	4.61	2.58
WGC2019J-16J - 10	162.00	15.64	55.78	0.32	0.00	2.06	0.25	7284.00	5.30	162.00	0.00	33.52	2.55	1.39
WGC2019J-16J - 11	136.10	24.39	58.40	0.21	0.00	1.46	0.23	7260.00	5.20	136.10	0.00	36.19	2.81	2.39
WGC2019J-16J - 13	162.10	36.98	94.20	0.30	0.00	1.57	0.16	7223.00	5.50	162.10	0.00	58.70	4.77	3.48
WGC2019J-16J - 14	127.20	29.14	79.50	0.20	0.00	1.42	0.12	7260.00	5.30	127.20	0.00	50.80	3.94	2.57
WGC2019J-16J - 18	125.20	32.67	81.90	0.23	0.01	1.64	0.19	7064.00	5.00	125.20	0.00	48.27	3.66	2.79
WGC2019J-16J - 19	93.10	23.54	133.50	0.27	0.00	0.96	0.07	7440.00	5.70	93.10	0.00	86.00	6.92	2.10
WGC2019J-16J - 21	172.40	35.20	94.20	0.31	0.00	2.21	0.13	7383.00	5.50	172.40	0.00	63.90	5.25	3.53

WGC2019J-16J - 23	121.20	15.98	56.96	0.27	0.00	1.91	0.27	7438.00	4.20	121.20	0.00	37.10	2.93	1.40
WGC2019J-16J - 24	96.10	24.63	80.70	0.23	0.00	1.59	0.23	7553.00	5.20	96.10	0.00	42.75	3.26	2.20
WGC2019J-16J - 25	79.40	16.03	72.82	0.17	0.00	0.88	0.12	6404.00	6.10	79.40	0.00	42.43	3.36	1.42
WGC2019J-16J - 26	121.40	18.94	67.80	0.32	0.00	1.88	0.07	7150.00	4.00	121.40	0.00	40.40	3.09	1.72
WGC2019J-16J - 27	78.60	37.26	122.60	0.17	0.01	0.79	0.12	6328.00	7.40	78.60	0.00	66.00	5.04	2.87
WGC2019J-16J - 28	81.40	34.79	105.60	0.22	0.00	0.74	0.13	6260.00	7.30	81.40	0.00	65.40	5.15	3.10
WGC2019J-16J - 31	113.00	21.29	92.40	0.21	0.00	0.90	0.05	6493.00	5.70	113.00	0.00	59.49	4.73	2.03
WGC2019J-16J - 32	119.60	28.17	113.00	0.22	0.00	0.83	0.04	6516.00	4.20	119.60	0.00	72.20	5.68	2.84
WGC2019J-16J - 33	92.10	12.05	66.15	0.27	0.00	1.86	0.17	7566.00	8.40	92.10	0.00	37.28	2.92	1.04
WGC2019J-16J - 34	95.20	27.63	84.10	0.25	0.08	2.47	0.47	7532.00	5.90	95.20	0.00	47.90	3.69	2.57
WGC2019J-16J - 35	139.30	21.04	56.48	0.26	0.00	1.81	0.00	7567.00	6.60	139.30	0.00	35.74	2.66	2.06
WGC2019J-16J - 37	88.90	18.37	69.80	0.19	0.00	0.83	0.12	6128.00	4.40	88.90	0.00	43.37	3.29	1.75
WGC2019J-16J - 38	106.70	15.83	64.30	0.28	0.00	0.83	0.15	6262.00	5.40	106.70	0.00	40.80	3.29	1.43
WGC2019J-16J - 39	118.10	23.04	63.51	0.14	0.00	1.58	0.14	7126.00	3.30	118.10	0.00	39.84	3.24	2.05
WGC2019J-16J - 40	99.60	20.44	61.26	0.25	0.00	1.40	0.09	7064.00	3.50	99.60	0.00	38.81	3.15	1.90
WGC2019J-16J - 41	181.00	32.40	129.60	0.43	0.11	2.31	0.98	6630.00	7.10	181.00	0.00	79.10	6.35	3.20
WGC2019J-16J - 43	90.80	43.99	145.90	0.22	0.00	0.70	0.08	5958.00	4.20	90.80	0.00	86.80	6.78	4.10
WGC2019J-16J - 44	104.00	42.45	133.20	0.18	0.00	0.60	0.06	5823.00	3.00	104.00	0.00	83.90	6.64	4.11
WGC2019J-16J - 45	141.40	37.27	76.20	0.27	0.01	2.02	0.25	7190.00	5.40	141.40	0.00	40.90	3.16	3.41
WGC2019J-16J - 46	162.10	35.64	67.00	0.21	0.00	1.72	0.24	7300.00	5.30	162.10	0.00	41.30	3.16	3.01
WGC2019J-16J - 47	148.50	19.25	120.40	0.27	0.00	1.87	0.08	7300.00	2.90	148.50	0.00	73.00	5.72	1.66
WGC2019J-16J - 49	196.90	9.28	52.67	0.22	0.00	2.49	0.31	7830.00	4.70	196.90	0.00	31.86	2.55	0.92
WGC2019J-16J - 50	163.60	7.52	44.29	0.35	0.00	2.22	0.11	7911.00	4.20	163.60	0.00	27.52	2.06	0.70
WGC2019J-16J - 51	193.40	13.99	46.66	0.36	0.00	5.09	0.46	8290.00	4.80	193.40	0.00	30.42	2.39	1.39
WGC2019J-16J DISCORDANT														
WGC2019J-16J - 6	132.70	20.04	85.31	0.16	0.06	1.36	0.35	7328.00	6.30	132.70	0.00	43.60	3.71	1.98
WGC2019J-16J - 12	138.20	26.43	92.60	0.20	0.01	1.20	0.19	7200.00	10.80	138.20	0.00	36.20	2.73	1.59

WGC2019J-16J - 15	123.40	38.20	102.30	0.17	0.04	1.45	0.30	7329.00	4.90	123.40	0.00	37.90	2.56	2.03
WGC2019J-16J - 16	117.40	7.81	55.59	0.24	0.00	2.43	0.17	8050.00	6.80	117.40	0.00	29.29	2.15	0.66
WGC2019J-16J - 17	617.00	47.20	131.30	1.26	0.00	9.31	0.77	8720.00	5.50	617.00	0.00	94.90	8.51	5.24
WGC2019J-16J - 20	134.90	15.84	58.70	0.27	0.05	2.25	0.16	7590.00	4.80	134.90	0.00	28.63	2.31	1.41
WGC2019J-16J - 22	109.40	15.50	64.20	0.29	0.00	1.84	0.10	7530.00	11.90	109.40	0.00	34.10	3.38	2.26
WGC2019J-16J - 29	125.70	20.09	76.10	0.30	0.00	2.11	0.20	8540.00	4.70	125.70	0.00	35.60	2.85	1.73
WGC2019J-16J - 30	154.60	26.88	72.20	0.42	0.01	2.52	0.19	7768.00	5.40	154.60	0.00	33.90	2.58	1.99
WGC2019J-16J - 36	59.50	20.77	168.00	0.25	0.02	1.06	0.16	9690.00	2.40	59.50	0.00	48.90	3.27	1.43
WGC2019J-16J - 42	1629.00	117.20	572.10	6.30	0.23	54.30	68.80	8378.00	36.60	1629.00	0.00	422.80	36.60	13.09
WGC2019J-16J - 48	697.00	213.00	240.30	0.72	0.01	5.93	1.51	7580.00	4.20	697.00	0.00	164.20	14.65	22.10
WGC2019J-17D CONCORDANT														
WGC2019J-17D - 1	256.60	17.92	74.83	0.35	0.00	3.33	0.18	8310.00	5.70	256.60	0.00	48.59	3.88	1.72
WGC2019J-17D - 2	323.50	19.86	79.00	0.39	0.00	3.33	0.27	8368.00	4.60	323.50	0.00	48.83	3.96	1.83
WGC2019J-17D - 3	242.70	22.30	85.80	0.39	0.00	3.22	0.12	8590.00	3.00	242.70	0.00	54.60	4.40	2.21
WGC2019J-17D - 6	336.60	33.80	121.20	0.44	0.00	3.48	0.26	8410.00	2.80	336.60	0.00	74.80	5.93	2.97
WGC2019J-17D - 8	286.10	37.76	130.30	0.49	0.00	3.88	0.22	8780.00	3.10	286.10	0.00	79.00	6.15	3.25
WGC2019J-17D - 10	275.80	31.60	104.10	0.45	0.00	3.93	0.25	8530.00	5.10	275.80	0.00	66.00	5.26	3.21
WGC2019J-17D - 11	258.80	25.60	96.90	0.31	0.00	3.72	0.24	8680.00	6.60	258.80	0.00	60.90	4.87	2.41
WGC2019J-17D - 12	288.00	28.82	107.20	0.53	0.01	3.77	0.12	8810.00	5.40	288.00	0.00	68.10	5.47	2.71
WGC2019J-17D - 13	253.10	16.20	71.30	0.36	0.00	3.20	0.00	8300.00	5.80	253.10	0.00	45.40	3.82	2.09
WGC2019J-17D - 17	300.80	34.40	112.80	0.43	0.00	3.51	0.13	8516.00	4.10	300.80	0.00	71.50	5.68	3.09
WGC2019J-17D - 18	270.10	37.12	122.50	0.43	0.00	3.74	0.14	8708.00	3.70	270.10	0.00	77.50	5.94	3.37
WGC2019J-17D - 19	196.10	33.40	91.80	0.39	0.00	2.49	0.00	7830.00	2.50	196.10	0.00	57.80	4.63	3.13
WGC2019J-17D - 22	310.70	32.09	101.40	0.49	0.00	3.58	0.23	8592.00	5.80	310.70	0.00	63.10	4.93	3.08
WGC2019J-17D - 23	228.90	25.13	102.30	0.31	0.00	3.22	0.07	8703.00	5.30	228.90	0.00	65.10	5.15	2.42
WGC2019J-17D - 24	253.30	23.13	98.50	0.37	0.00	3.46	0.14	8472.00	3.30	253.30	0.00	63.20	4.98	2.30
WGC2019J-17D - 25	250.40	23.46	94.20	0.39	0.00	3.34	0.25	8309.00	5.40	250.40	0.00	61.90	4.89	2.30

WGC2019J-17D - 26	209.80	19.34	86.12	0.38	0.00	3.12	0.18	8423.00	3.60	209.80	0.00	51.71	4.12	1.73
WGC2019J-17D - 28	172.20	24.94	81.90	0.29	0.00	2.63	0.06	8132.00	3.70	172.20	0.00	51.53	4.13	2.22
WGC2019J-17D - 30	267.20	25.49	91.40	0.48	0.01	3.57	0.25	8646.00	5.20	267.20	0.00	57.90	4.59	2.44
WGC2019J-17D - 32	353.80	27.50	94.00	0.49	0.01	4.09	0.18	8300.00	6.40	353.80	0.00	61.40	4.93	2.92
WGC2019J-17D - 33	317.50	35.47	102.60	0.33	0.00	3.96	0.24	8246.00	7.30	317.50	0.00	67.20	5.48	3.40
WGC2019J-17D - 35	250.20	30.77	93.10	0.36	0.00	3.10	0.19	8397.00	2.70	250.20	0.00	60.20	4.68	2.93
WGC2019J-17D - 39	252.70	29.10	107.20	0.45	0.00	3.34	0.21	8360.00	6.90	252.70	0.00	64.30	5.16	2.42
WGC2019J-17D - 41	244.00	17.34	80.11	0.39	0.00	3.36	0.17	8330.00	4.70	244.00	0.00	51.71	4.15	1.65
WGC2019J-17D - 43	243.20	26.60	85.20	0.34	0.00	3.50	0.21	8211.00	6.60	243.20	0.00	55.20	4.42	2.44
WGC2019J-17D - 44	279.40	17.83	55.08	0.38	0.00	3.56	0.12	8680.00	4.50	279.40	0.00	35.70	2.85	1.76
WGC2019J-17D - 45	224.50	28.69	101.00	0.56	0.01	3.69	0.19	8513.00	10.30	224.50	0.00	58.90	4.69	2.45
WGC2019J-17D - 46	239.80	28.71	94.70	0.45	0.00	3.54	0.17	8579.00	4.40	239.80	0.00	61.30	4.80	2.68
WGC2019J-17D - 47	313.10	29.86	99.30	0.52	0.00	3.60	0.14	8480.00	4.00	313.10	0.00	61.90	4.88	2.60
WGC2019J-17D - 49	254.70	18.89	72.30	0.48	0.00	2.94	0.18	8140.00	3.70	254.70	0.00	46.10	3.69	1.72
WGC2019J-17D DISCORDANT														
WGC2019J-17D - 4	237.20	21.40	71.40	0.32	0.01	2.71	0.12	8090.00	4.80	237.20	0.00	42.10	3.85	2.25
WGC2019J-17D - 5	270.00	38.70	118.30	0.46	0.01	3.05	0.33	8390.00	20.20	270.00	0.00	70.40	6.09	4.30
WGC2019J-17D - 7	229.70	21.91	81.20	0.64	0.03	2.74	0.37	8090.00	8.70	229.70	0.00	52.50	4.80	2.68
WGC2019J-17D - 9	267.70	61.00	140.50	0.42	0.00	2.89	0.14	8100.00	5.60	267.70	0.00	82.30	6.77	5.69
WGC2019J-17D - 14	249.80	14.22	64.90	0.39	0.00	3.08	0.12	8324.00	5.20	249.80	0.00	39.50	3.57	1.59
WGC2019J-17D - 15	352.70	36.96	102.90	0.70	0.00	4.41	0.18	8578.00	4.10	352.70	0.00	67.30	5.64	3.55
WGC2019J-17D - 16	364.00	29.90	102.00	0.45	0.06	4.15	0.15	8850.00	0.00	364.00	0.00	60.60	5.84	3.82
WGC2019J-17D - 20	266.90	32.11	94.20	0.42	0.00	2.87	0.12	8214.00	5.40	266.90	0.00	55.40	4.63	2.87
WGC2019J-17D - 21	273.00	31.86	98.70	0.50	93.10	244.00	134.60	8340.00	27.80	273.00	3.30	63.80	7.80	5.67
WGC2019J-17D - 27	207.00	37.80	108.20	0.70	0.01	2.83	0.17	8206.00	40.50	207.00	0.00	63.90	5.62	4.03
WGC2019J-17D - 29	281.60	31.45	117.10	1.63	0.01	3.77	0.23	8810.00	17.50	281.60	12.50	84.10	17.10	14.80
WGC2019J-17D - 31	266.20	35.29	120.70	0.50	0.00	3.66	0.13	8248.00	10.30	266.20	0.00	77.70	6.53	3.73

WGC2019J-17D - 34	432.20	48.89	131.20	0.48	0.00	4.28	0.19	8268.00	6.10	432.20	0.00	85.80	7.11	4.86
WGC2019J-17D - 36	276.20	26.53	99.60	0.41	0.00	3.60	0.26	8790.00	4.40	276.20	0.00	57.80	5.03	2.45
WGC2019J-17D - 37	211.50	28.60	103.90	0.36	0.01	3.01	0.13	8108.00	8.30	211.50	0.00	69.70	6.96	4.41
WGC2019J-17D - 38	335.30	42.44	142.10	0.35	0.01	3.90	0.16	8851.00	8.60	335.30	0.00	86.50	7.17	3.99
WGC2019J-17D - 40	343.10	27.36	106.40	0.50	0.02	3.45	0.19	8470.00	16.70	343.10	0.00	66.90	5.63	2.87
WGC2019J-17D - 42	268.00	32.66	104.90	0.39	0.00	3.01	0.35	7871.00	3.90	268.00	0.00	66.10	5.57	3.17
WGC2019J-17D - 48	231.10	26.70	90.80	0.56	0.00	3.20	0.10	8570.00	6.00	231.10	0.00	57.00	4.95	2.93

Appendix 6c: Zircon Trace Element Graphs

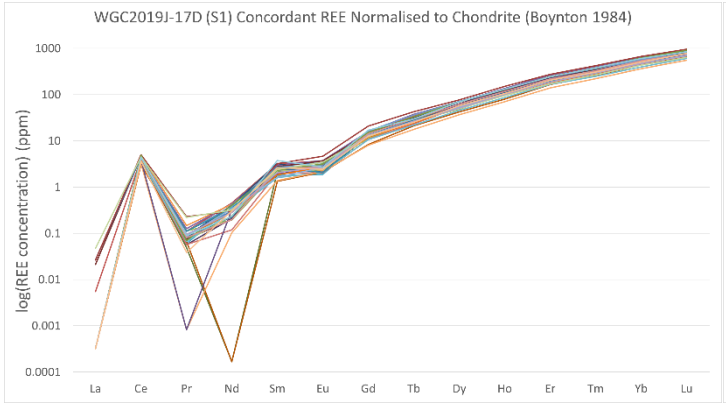

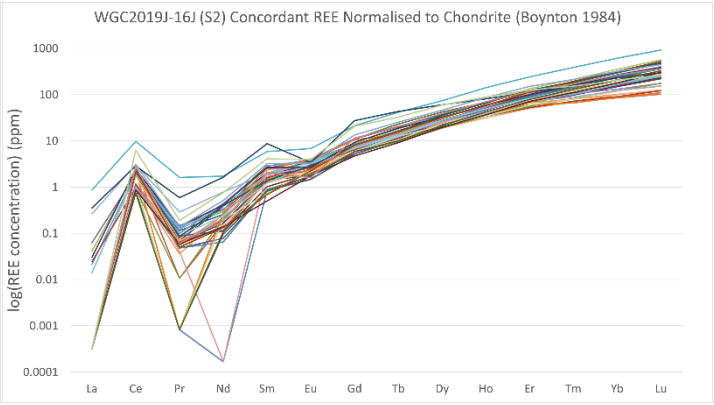

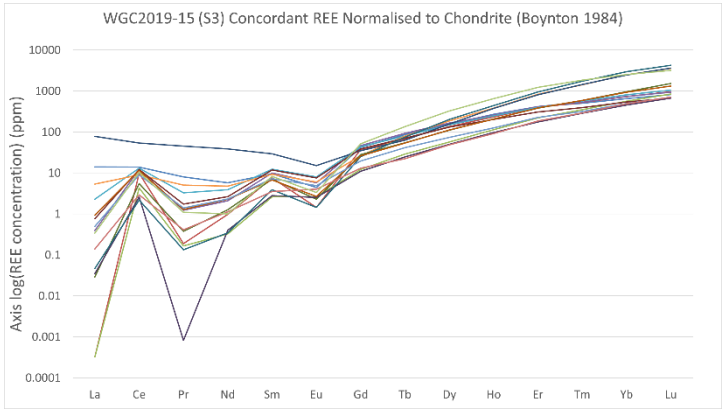

Appendix 7: Rutile U-Pb And Trace Element Data

Rutile U-Pb age data for samples WGC2019J-16J and WGC2019J-17D. Crossed out analyses indicate those that were removed due to high Ca, Fe or common lead contents. For WGC2019J-17D, italicised values indicate the six analyses that were also filtered by the same standards. To increase the size of the dataset, analyses with $^{204}Pb < 1$ were included.

Sample	Pb207/U235	2σ	Pb206/U238	2σ	ρ	Pb 207/Pb206	2σ	Pb207/U235 Age	2σ
~~WGC2019J-16J_New - 1~~	~~1.53~~	~~0.25~~	~~0.0713~~	~~0.0038~~	~~0.42314~~	~~0.152~~	~~0.022~~	~~886~~	~~99~~
~~WGC2019J-16J_New - 2~~	~~12.17~~	~~0.68~~	~~0.1661~~	~~0.0074~~	~~0.52997~~	~~0.535~~	~~0.025~~	~~2592~~	~~53~~
WGC2019J-16J_New - 3	2.98	0.34	0.0834	0.0053	0.32424	0.261	0.027	1348	85
~~WGC2019J-16J_New - 4~~	~~17.64~~	~~0.62~~	~~0.2125~~	~~0.0068~~	~~0.256~~	~~0.606~~	~~0.019~~	~~2964~~	~~34~~
~~WGC2019J-16J_New - 5~~	~~1.05~~	~~0.13~~	~~0.0685~~	~~0.0036~~	~~0.226~~	~~0.11~~	~~0.013~~	~~696~~	~~67~~
WGC2019J-16J_New - 6	0.581	0.045	0.0669	0.0022	0.038043	0.0638	0.0049	457	29
~~WGC2019J-16J_New - 7~~	~~5.03~~	~~0.34~~	~~0.1057~~	~~0.006~~	~~0.20244~~	~~0.35~~	~~0.026~~	~~1809~~	~~60~~
~~WGC2019J-16J_New - 8~~	~~2.21~~	~~0.27~~	~~0.0825~~	~~0.0043~~	~~0.086438~~	~~0.193~~	~~0.023~~	~~1146~~	~~82~~
~~WGC2019J-16J_New - 9~~	~~2.85~~	~~0.21~~	~~0.0845~~	~~0.0041~~	~~0.13377~~	~~0.25~~	~~0.02~~	~~1351~~	~~55~~
~~WGC2019J-16J_Old - 01~~	~~2.32~~	~~0.19~~	~~0.0826~~	~~0.0039~~	~~0.17728~~	~~0.213~~	~~0.02~~	~~1189~~	~~56~~
~~WGC2019J-16J_Old - 02~~	~~10.1~~	~~1.4~~	~~0.147~~	~~0.011~~	~~0.90658~~	~~0.144~~	~~0.012~~	~~2330~~	~~130~~
~~WGC2019J-16J_Old - 03~~	~~5.54~~	~~0.65~~	~~0.1051~~	~~0.0065~~	~~0.6098~~	~~0.35~~	~~0.033~~	~~1840~~	~~94~~
~~WGC2019J-16J_Old - 04~~	~~2.04~~	~~0.21~~	~~0.078~~	~~0.0046~~	~~0.03057~~	~~0.383~~	~~0.035~~	~~1106~~	~~65~~
~~WGC2019J-16J_Old - 05~~	~~2.03~~	~~0.23~~	~~0.0816~~	~~0.0057~~	~~0.050449~~	~~0.537~~	~~0.028~~	~~1103~~	~~80~~
~~WGC2019J-16J_Old - 06~~	~~23.9~~	~~4.1~~	~~0.271~~	~~0.037~~	~~0.94447~~	~~0.356~~	~~0.025~~	~~3070~~	~~210~~
~~WGC2019J-16J_Old - 07~~	~~10.4~~	~~1.2~~	~~0.156~~	~~0.018~~	~~0.025899~~	~~0.661~~	~~0.032~~	~~2423~~	~~100~~
~~WGC2019J-16J_Old - 08~~	~~4.74~~	~~0.45~~	~~0.1~~	~~0.0057~~	~~0.33562~~	~~0.633~~	~~0.035~~	~~1747~~	~~83~~
WGC2019J-16J_Old - 09	1.285	0.08	0.0728	0.0023	0.11503	0.126	0.016	832	34
~~WGC2019J-16J_Old - 11~~	~~0.814~~	~~0.083~~	~~0.0662~~	~~0.0029~~	~~0.20296~~	~~0.48~~	~~0.036~~	~~595~~	~~48~~

~~WGC2019J-16J_Old - 12~~	~~1.48~~	~~0.13~~	~~0.0753~~	~~0.0028~~	~~0.18886~~	~~0.378~~	~~0.033~~	~~905~~	~~52~~
~~WGC2019J-16J_Old - 13~~	~~5.03~~	~~0.42~~	~~0.1078~~	~~0.0085~~	~~0.29594~~	~~0.2~~	~~0.024~~	~~1804~~	~~73~~
~~WGC2019J-16J_Old - 14~~	~~5.7~~	~~0.63~~	~~0.1068~~	~~0.006~~	~~0.59497~~	~~0.189~~	~~0.025~~	~~1855~~	~~98~~
~~WGC2019J-16J_Old - 15~~	~~12.85~~	~~0.63~~	~~0.1788~~	~~0.0084~~	~~0.27896~~	~~0.61~~	~~0.049~~	~~2664~~	~~49~~
~~WGC2019J-16J_Old - 16~~	~~5.39~~	~~0.38~~	~~0.1114~~	~~0.0062~~	~~0.3142~~	~~0.496~~	~~0.066~~	~~1861~~	~~61~~
~~WGC2019J-16J_Old - 17~~	~~23.8~~	~~4~~	~~0.257~~	~~0.034~~	~~0.88198~~	~~0.351~~	~~0.033~~	~~3110~~	~~140~~
~~WGC2019J-16J_Old - 18~~	~~21.8~~	~~2.3~~	~~0.249~~	~~0.02~~	~~0.86111~~	~~0.1294~~	~~0.008~~	~~3120~~	~~110~~
~~WGC2019J-16J_Old - 19~~	~~1.19~~	~~0.16~~	~~0.0705~~	~~0.0036~~	~~0.11813~~	~~0.092~~	~~0.01~~	~~777~~	~~76~~
~~WGC2019J-16J_TS - 01~~	~~0.58~~	~~0.075~~	~~0.067~~	~~0.0033~~	~~0.043519~~	~~0.0635~~	~~0.0083~~	~~451~~	~~48~~
~~WGC2019J-16J_TS - 02~~	~~2.67~~	~~0.32~~	~~0.0878~~	~~0.0054~~	~~0.36~~	~~0.087~~	~~0.012~~	~~1286~~	~~91~~
WGC2019J-16J_TS - 03	0.74	0.23	0.0659	0.0049	0.01902	0.083	0.016	530	120
WGC2019J-16J_TS - 04	0.88	0.14	0.0665	0.0046	0.10857	0.077	0.011	617	75
WGC2019J-16J_TS - 05	1.4	0.38	0.0703	0.0034	0.046787	0.117	0.02	800	140
WGC2019J-16J_TS - 06	0.82	0.14	0.0657	0.0037	0.0022939	0.0732	0.0087	564	73
WGC2019J-16J_TS - 07	0.741	0.091	0.0668	0.0034	0.084341	0.0766	0.0093	538	51
WGC2019J-16J_TS - 08	0.92	0.12	0.0709	0.0034	0.071032	0.125	0.017	630	56
WGC2019J-16J_TS - 09	0.81	0.11	0.0667	0.0037	0.12621	0.0709	0.0075	572	61
~~WGC2019J-16J_TS - 10~~	~~1.05~~	~~0.15~~	~~0.0765~~	~~0.0051~~	~~0.014416~~	~~0.221~~	~~0.023~~	~~700~~	~~68~~
WGC2019J-16J_TS - 11	0.86	0.17	0.0668	0.0039	0.2942	0.09	0.028	576	82
~~WGC2019J-16J_TS - 12~~	~~0.767~~	~~0.095~~	~~0.0681~~	~~0.0032~~	~~0.0063797~~	~~0.096~~	~~0.016~~	~~544~~	~~50~~
WGC2019J-16J_TS - 13	0.77	0.12	0.0717	0.0034	0.071676	0.148	0.04	528	52
WGC2019J-16J_TS - 14	0.87	0.16	0.0699	0.0034	0.026151	0.095	0.016	553	61
~~WGC2019J-16J_TS - 15~~	~~2.52~~	~~0.33~~	~~0.0718~~	~~0.004~~	~~0.12821~~	~~0.084~~	~~0.011~~	~~1251~~	~~97~~
~~WGC2019J-16J_TS - 16~~	~~1.07~~	~~0.13~~	~~0.0695~~	~~0.0031~~	~~0.10245~~	~~0.094~~	~~0.013~~	~~691~~	~~57~~
~~WGC2019J-16J_TS - 17~~	~~1.149~~	~~0.096~~	~~0.0745~~	~~0.003~~	~~0.0055933~~	~~0.09~~	~~0.013~~	~~756~~	~~48~~
~~WGC2019J-16J_TS - 18~~	~~0.856~~	~~0.077~~	~~0.0724~~	~~0.0031~~	~~0.0077065~~	~~0.102~~	~~0.015~~	~~619~~	~~44~~
WGC2019J-16J_TS - 19	0.78	0.14	0.0653	0.0033	0.0042907	0.099	0.022	522	68

WGC2019J-16J_TS - 20	0.735	0.087	0.0703	0.0031	0.074884	0.08	0.011	523	48
WGC2019J-16J_TS - 21	0.67	0.1	0.067	0.0036	0.11814	0.094	0.018	491	59
~~WGC2019J-16J_TS - 22~~	~~0.78~~	~~0.1~~	~~0.0699~~	~~0.004~~	~~0.14184~~	~~0.276~~	~~0.043~~	~~554~~	~~61~~
~~WGC2019J-16J_TS - 23~~	~~0.69~~	~~0.12~~	~~0.068~~	~~0.004~~	~~0.035794~~	~~0.113~~	~~0.013~~	~~483~~	~~68~~
WGC2019J-16J_TS - 24	0.76	0.17	0.0672	0.0033	0.012055	0.113	0.0096	516	73
WGC2019J-16J_TS - 25	0.598	0.078	0.0697	0.0033	0.0005352	0.0852	0.0078	467	52
~~WGC2019J-16J_TS - 26~~	~~0.86~~	~~0.12~~	~~0.0699~~	~~0.0037~~	~~0.053961~~	~~0.089~~	~~0.017~~	~~593~~	~~64~~
~~WGC2019J-16J_TS - 27~~	~~0.56~~	~~0.1~~	~~0.0639~~	~~0.0032~~	~~0.093474~~	~~0.081~~	~~0.01~~	~~439~~	~~72~~
~~WGC2019J-16J_TS - 28~~	~~0.63~~	~~0.049~~	~~0.0697~~	~~0.0022~~	~~0.25072~~	~~0.0685~~	~~0.0094~~	~~486~~	~~32~~
WGC2019J-16J_TS - 29	0.97	0.14	0.073	0.0042	0.12018	0.083	0.011	637	70
~~WGC2019J-16J_TS - 30~~	~~0.618~~	~~0.095~~	~~0.0648~~	~~0.0041~~	~~0.012124~~	~~0.082~~	~~0.017~~	~~466~~	~~61~~
WGC2019J-16J_TS - 31	0.78	0.13	0.0648	0.0043	0.039196	0.0663	0.0096	568	75
~~WGC2019J-16J_TS - 32~~	~~1.28~~	~~0.14~~	~~0.0712~~	~~0.0032~~	~~0.011047~~	~~0.094~~	~~0.016~~	~~788~~	~~58~~
~~WGC2019J-16J_TS - 33~~	~~0.687~~	~~0.098~~	~~0.0652~~	~~0.0028~~	~~0.15831~~	~~0.068~~	~~0.014~~	~~491~~	~~55~~
WGC2019J-16J_TS - 34	0.642	0.084	0.0627	0.0025	0.081851	0.0658	0.0049	471	47
WGC2019J-16J_TS - 35	0.81	0.13	0.0715	0.0033	0.0783	0.099	0.014	550	62
WGC2019J-16J_TS - 36	0.553	0.064	0.065	0.0028	0.079641	0.077	0.015	424	42
~~WGC2019J-16J_TS - 37~~	~~8.17~~	~~0.59~~	~~0.1273~~	~~0.006~~	~~0.59123~~	~~0.091~~	~~0.018~~	~~2184~~	~~68~~
WGC2019J-16J_TS - 38	0.63	0.12	0.0667	0.0038	0.19921	0.134	0.015	459	65
WGC2019J-16J_TS - 39	1.22	0.12	0.0713	0.0034	0.16607	0.078	0.011	791	57
WGC2019J-16J_TS - 40	1.09	0.52	0.066	0.0039	0.18642	0.089	0.015	550	100
WGC2019J-16J_TS - 41	1.16	0.16	0.0732	0.0045	0.0032505	0.0648	0.008	754	77
~~WGC2019J-16J_TS - 42~~	~~5.2~~	~~0.58~~	~~0.1056~~	~~0.0065~~	~~0.65231~~	~~0.455~~	~~0.024~~	~~1779~~	~~98~~
~~WGC2019J-16J_TS - 43~~	~~2.17~~	~~0.35~~	~~0.0769~~	~~0.0064~~	~~0.57895~~	~~0.073~~	~~0.015~~	~~1130~~	~~110~~
WGC2019J-16J_TS - 44	0.85	0.14	0.0644	0.0041	0.15473	0.128	0.014	593	75
WGC2019J-16J_TS - 45	1.06	0.18	0.0717	0.0032	0.046906	0.121	0.055	675	72
WGC2019J-16J_TS - 46	0.69	0.13	0.0653	0.0028	0.48936	0.123	0.02	472	60

WGC2019J-16J_TS - 47	1.04	0.25	0.071	0.0035	0.0090435	0.353	0.03	594	74
WGC2019J-16J_TS - 48	0.9	0.15	0.0693	0.0031	0.10823	0.198	0.022	576	65
WGC2019J-16J_TS - 49	0.8	0.11	0.0668	0.0029	0.10757	0.096	0.016	542	56
WGC2019J-16J_TS - 50	0.93	0.13	0.0676	0.0038	0.012336	0.077	0.014	620	65
~~WGC2019J-16J_TS - 51~~	~~1.13~~	~~0.17~~	~~0.0668~~	~~0.0033~~	~~0.034267~~	~~0.105~~	~~0.025~~	~~710~~	~~66~~
WGC2019J-16J_TS - 52	0.7	0.1	0.0641	0.0027	0.057072	0.099	0.017	501	45
WGC2019J-16J_TS - 53	0.639	0.072	0.067	0.0025	0.10809	0.09	0.013	476	40
WGC2019J-16J_TS - 54	0.848	0.099	0.0681	0.003	0.0064482	0.106	0.017	581	51
WGC2019J-16J_TS - 55	0.74	0.15	0.0655	0.0033	0.19136	0.13	0.021	523	76
WGC2019J-16J_TS - 56	0.693	0.08	0.0679	0.0027	0.057239	0.08	0.011	505	47
~~WGC2019J-16J_TS - 57~~	~~0.74~~	~~0.11~~	~~0.0685~~	~~0.0033~~	~~0.030159~~	~~0.0682~~	~~0.007~~	~~533~~	~~53~~
WGC2019J-16J_TS - 58	0.774	0.084	0.0686	0.0026	0.031002	0.09	0.01	562	49
WGC2019J-16J_TS - 59	1.17	0.22	0.0733	0.004	0.044367	0.08	0.016	700	84
WGC2019J-16J_TS - 60	0.72	0.1	0.0652	0.0031	0.1094	0.081	0.013	525	57
WGC2019J-16J_TS - 61	0.93	0.12	0.0711	0.0029	0.046169	0.0821	0.0093	626	52
~~WGC2019J-16J_TS - 62~~	~~3.86~~	~~0.23~~	~~0.0912~~	~~0.0044~~	~~0.38663~~	~~0.115~~	~~0.023~~	~~1595~~	~~47~~
~~WGC2019J-16J_TS - 63~~	~~1.07~~	~~0.13~~	~~0.07~~	~~0.0031~~	~~0.052975~~	~~0.081~~	~~0.011~~	~~706~~	~~62~~
~~WGC2019J-16J_TS - 64~~	~~1.94~~	~~0.25~~	~~0.0794~~	~~0.0046~~	~~0.013504~~	~~0.1~~	~~0.013~~	~~1070~~	~~79~~
WGC2019J-16J_TS - 65	0.73	0.14	0.0696	0.0041	0.11297	0.312	0.021	516	67
~~WGC2019J-16J_TS - 66~~	~~0.96~~	~~0.18~~	~~0.0694~~	~~0.0037~~	~~0.21207~~	~~0.114~~	~~0.015~~	~~652~~	~~88~~
WGC2019J-16J_TS - 67	0.661	0.073	0.0647	0.0024	0.000702	0.18	0.023	497	38
WGC2019J-16J_TS - 68	0.588	0.065	0.0685	0.0028	0.010796	0.08	0.016	448	41
WGC2019J-16J_TS - 69	0.623	0.08	0.0644	0.0034	0.015127	0.099	0.017	471	47
WGC2019J-16J_TS - 70	0.94	0.15	0.0657	0.004	0.14349	0.0638	0.0075	652	77
~~WGC2019J-16J_TS - 71~~	~~6.08~~	~~0.42~~	~~0.1126~~	~~0.0058~~	~~0.097498~~	~~0.072~~	~~0.0096~~	~~1964~~	~~55~~
~~WGC2019J-16J_TS - 72~~	~~1.17~~	~~0.21~~	~~0.0704~~	~~0.0036~~	~~0.089593~~	~~0.105~~	~~0.017~~	~~719~~	~~81~~
WGC2019J-16J_TS - 73	0.675	0.094	0.0696	0.0027	0.038236	0.403	0.033	514	58

~~WGC2019J-16J_TS - 74~~	~~0.799~~	~~0.099~~	~~0.0653~~	~~0.0027~~	~~0.10319~~	~~0.124~~	~~0.025~~	~~557~~	~~48~~
~~WGC2019J-16J_TS - 75~~	~~0.76~~	~~0.12~~	~~0.072~~	~~0.0052~~	~~0.033075~~	~~0.0698~~	~~0.0095~~	~~550~~	~~73~~
~~WGC2019J-16J_TS - 76~~	~~8.86~~	~~0.43~~	~~0.1325~~	~~0.0057~~	~~0.24267~~	~~0.0872~~	~~0.0093~~	~~2306~~	~~45~~
WGC2019J-16J_TS - 77	0.88	0.13	0.0691	0.0028	0.057898	0.082	0.015	580	58
WGC2019J-16J_TS - 78	1.08	0.14	0.0673	0.0032	0.027839	0.498	0.027	707	68
~~WGC2019J-16J_TS - 79~~	~~0.684~~	~~0.066~~	~~0.0716~~	~~0.003~~	~~0.051914~~	~~0.09~~	~~0.013~~	~~517~~	~~41~~
Sample	Pb206/U238 Age	2σ	Pb207/Pb206 Age	2σ	U (ppm)	Ca (ppm)	Fe (ppm)	Pb 204 (ppm)	Pb 208 (ppm)
~~WGC2019J-16J_New - 1~~	~~448~~	~~24~~	~~2030~~	~~290~~	~~2.607~~	~~Below LOD~~	~~3699~~	~~Below LOD~~	~~0.107~~
~~WGC2019J-16J_New - 2~~	~~988~~	~~41~~	~~4312~~	~~73~~	~~1.463~~	~~Below LOD~~	~~3224~~	~~0.8~~	~~0.771~~
WGC2019J-16J_New - 3	515	31	3080	180	1.277	Below LOD	3366	Below LOD	0.084
~~WGC2019J-16J_New - 4~~	~~1241~~	~~36~~	~~4509~~	~~48~~	~~2.431~~	~~Below LOD~~	~~2489~~	~~2.01~~	~~1.869~~
~~WGC2019J-16J_New - 5~~	~~427~~	~~21~~	~~1640~~	~~260~~	~~2.363~~	~~Below LOD~~	~~6650~~	~~0.36~~	~~0.161~~
WGC2019J-16J_New - 6	417	13	570	160	4.55	Below LOD	2504	Below LOD	0.0191
~~WGC2019J-16J_New - 7~~	~~647~~	~~35~~	~~3690~~	~~120~~	~~2.173~~	~~Below LOD~~	~~7.00E+03~~	~~140~~	~~9.9~~
~~WGC2019J-16J_New - 8~~	~~510~~	~~25~~	~~2600~~	~~220~~	~~1.961~~	~~56~~	~~2065~~	~~0.39~~	~~0.228~~
~~WGC2019J-16J_New - 9~~	~~522~~	~~25~~	~~3120~~	~~120~~	~~2.029~~	~~78~~	~~2529~~	~~Below LOD~~	~~0.241~~
~~WGC2019J-16J_Old - 01~~	~~511~~	~~23~~	~~2760~~	~~160~~	~~1.922~~	~~130~~	~~1.27E+04~~	~~Below LOD~~	~~0.54~~
~~WGC2019J-16J_Old - 02~~	~~880~~	~~64~~	~~4100~~	~~120~~	~~4.16~~	~~Below LOD~~	~~2344~~	~~2.9~~	~~2.86~~
~~WGC2019J-16J_Old - 03~~	~~650~~	~~40~~	~~3730~~	~~140~~	~~1.686~~	~~830~~	~~4810~~	~~0.38~~	~~0.368~~
~~WGC2019J-16J_Old - 04~~	~~483~~	~~28~~	~~2660~~	~~180~~	~~1.494~~	~~Below LOD~~	~~6055~~	~~0.42~~	~~0.166~~
~~WGC2019J-16J_Old - 05~~	~~505~~	~~34~~	~~2600~~	~~230~~	~~1.69~~	~~Below LOD~~	~~2221~~	~~0.65~~	~~0.548~~
~~WGC2019J-16J_Old - 06~~	~~1520~~	~~190~~	~~4480~~	~~140~~	~~1.71~~	~~Below LOD~~	~~3167~~	~~3.9~~	~~3.98~~
~~WGC2019J-16J_Old - 07~~	~~926~~	~~95~~	~~4090~~	~~220~~	~~0.616~~	~~Below LOD~~	~~2410~~	~~2~~	~~0.71~~
~~WGC2019J-16J_Old - 08~~	~~614~~	~~33~~	~~3640~~	~~150~~	~~1.67~~	~~Below LOD~~	~~2827~~	~~0.74~~	~~0.43~~
WGC2019J-16J_Old - 09	453	14	2010	110	4.409	Below LOD	1161	Below LOD	0.192
~~WGC2019J-16J_Old - 11~~	~~413~~	~~17~~	~~1250~~	~~230~~	~~2.974~~	~~Below LOD~~	~~2688~~	~~Below LOD~~	~~0.367~~
~~WGC2019J-16J_Old - 12~~	~~468~~	~~17~~	~~2160~~	~~150~~	~~3.77~~	~~Below LOD~~	~~1910~~	~~Below LOD~~	~~0.208~~

~~WGC2019J-16J_Old - 13~~	~~659~~	~~49~~	~~3640~~	~~160~~	~~1.557~~	~~Below LOD~~	~~2700~~	~~0.39~~	~~0.292~~
~~WGC2019J-16J_Old - 14~~	~~659~~	~~36~~	~~3710~~	~~150~~	~~1.41~~	~~Below LOD~~	~~2450~~	~~0.39~~	~~0.212~~
~~WGC2019J-16J_Old - 15~~	~~1058~~	~~46~~	~~4314~~	~~78~~	~~1.102~~	~~Below LOD~~	~~3548~~	~~1.6~~	~~1.087~~
~~WGC2019J-16J_Old - 16~~	~~680~~	~~36~~	~~3700~~	~~100~~	~~2.266~~	~~Below LOD~~	~~3240~~	~~0.99~~	~~1.09~~
~~WGC2019J-16J_Old - 17~~	~~1440~~	~~160~~	~~4635~~	~~78~~	~~1.612~~	~~43~~	~~4596~~	~~1.48~~	~~1.5~~
~~WGC2019J-16J_Old - 18~~	~~1423~~	~~100~~	~~4565~~	~~92~~	~~1.75~~	~~52~~	~~3790~~	~~5.7~~	~~6.2~~
~~WGC2019J-16J_Old - 19~~	~~443~~	~~20~~	~~1790~~	~~290~~	~~1.665~~	~~60~~	~~3260~~	~~1.77~~	~~1.94~~
~~WGC2019J-16J_TS - 01~~	~~417~~	~~20~~	~~500~~	~~250~~	~~2.498~~	~~Below LOD~~	~~1946~~	~~0.53~~	~~0.024~~
~~WGC2019J-16J_TS - 02~~	~~541~~	~~32~~	~~2920~~	~~170~~	~~1.46~~	~~68~~	~~1985~~	~~0.64~~	~~0.235~~
WGC2019J-16J_TS - 03	411	30	790	550	1.241	Below LOD	2145	Below LOD	0.08
WGC2019J-16J_TS - 04	414	28	1260	360	2.581	Below LOD	2330	Below LOD	0.08
WGC2019J-16J_TS - 05	437	21	1550	450	1.662	Below LOD	1946	Below LOD	0.12
WGC2019J-16J_TS - 06	409	22	1170	370	1.753	Below LOD	2090	Below LOD	0.032
WGC2019J-16J_TS - 07	416	20	960	260	2.354	Below LOD	1912	Below LOD	0.0279
WGC2019J-16J_TS - 08	441	20	1280	250	2.412	Below LOD	1710	Below LOD	0.055
WGC2019J-16J_TS - 09	415	22	1080	310	1.697	Below LOD	2147	Below LOD	0.066
~~WGC2019J-16J_TS - 10~~	~~474~~	~~30~~	~~1360~~	~~270~~	~~1.988~~	~~Below LOD~~	~~7340~~	~~Below LOD~~	~~0.077~~
WGC2019J-16J_TS - 11	416	23	990	370	1.518	Below LOD	2760	Below LOD	0.03
~~WGC2019J-16J_TS - 12~~	~~424~~	~~19~~	~~920~~	~~270~~	~~1.655~~	~~Below LOD~~	~~6500~~	~~0.35~~	~~0.0195~~
WGC2019J-16J_TS - 13	446	20	800	280	1.932	Below LOD	2135	Below LOD	0.0177
WGC2019J-16J_TS - 14	435	20	870	280	1.692	Below LOD	2350	Below LOD	0.0214
~~WGC2019J-16J_TS - 15~~	~~446~~	~~24~~	~~3120~~	~~220~~	~~1.863~~	~~304~~	~~2337~~	~~0.4~~	~~0.207~~
~~WGC2019J-16J_TS - 16~~	~~433~~	~~19~~	~~1540~~	~~240~~	~~1.917~~	~~47~~	~~2309~~	~~Below LOD~~	~~0.0511~~
~~WGC2019J-16J_TS - 17~~	~~463~~	~~18~~	~~1650~~	~~180~~	~~2.265~~	~~36~~	~~1946~~	~~Below LOD~~	~~0.078~~
~~WGC2019J-16J_TS - 18~~	~~450~~	~~19~~	~~1150~~	~~200~~	~~2.487~~	~~Below LOD~~	~~6701~~	~~Below LOD~~	~~0.055~~
WGC2019J-16J_TS - 19	411	21	850	330	1.39	Below LOD	1859	Below LOD	0.0242
WGC2019J-16J_TS - 20	437	18	820	250	1.828	Below LOD	2578	Below LOD	0.024

WGC2019J-16J_TS - 21	417	22	670	300	2.613	Below LOD	2603	Below LOD	0.0156
~~WGC2019J-16J_TS - 22~~	~~435~~	~~24~~	~~970~~	~~320~~	~~1.624~~	~~Below LOD~~	~~2088~~	~~0.31~~	~~0.0277~~
~~WGC2019J-16J_TS - 23~~	~~423~~	~~24~~	~~610~~	~~350~~	~~1.33~~	~~Below LOD~~	~~2266~~	~~0.37~~	~~0.0421~~
WGC2019J-16J_TS - 24	419	20	770	320	2.158	Below LOD	2378	Below LOD	0.0499
WGC2019J-16J_TS - 25	434	20	510	290	2.732	Below LOD	2910	Below LOD	0.0256
~~WGC2019J-16J_TS - 26~~	~~435~~	~~22~~	~~1080~~	~~310~~	~~2.002~~	~~Below LOD~~	~~2359~~	~~0.34~~	~~0.0234~~
~~WGC2019J-16J_TS - 27~~	~~399~~	~~19~~	~~480~~	~~390~~	~~2.652~~	~~Below LOD~~	~~2072~~	~~0.31~~	~~0.014~~
~~WGC2019J-16J_TS - 28~~	~~434~~	~~13~~	~~630~~	~~160~~	~~2.99~~	~~Below LOD~~	~~6180~~	~~Below LOD~~	~~0.0227~~
WGC2019J-16J_TS - 29	453	25	1140	300	1.424	Below LOD	2248	Below LOD	0.067
~~WGC2019J-16J_TS - 30~~	~~404~~	~~25~~	~~690~~	~~350~~	~~1.685~~	~~Below LOD~~	~~4820~~	~~0.44~~	~~0.0096~~
WGC2019J-16J_TS - 31	404	26	1110	360	1.959	Below LOD	2122	Below LOD	0.0116
~~WGC2019J-16J_TS - 32~~	~~443~~	~~19~~	~~1880~~	~~220~~	~~1.941~~	~~Below LOD~~	~~4.23E+04~~	~~Below LOD~~	~~0.0373~~
~~WGC2019J-16J_TS - 33~~	~~407~~	~~17~~	~~710~~	~~290~~	~~1.787~~	~~Below LOD~~	~~2025~~	~~0.33~~	~~0.01~~
WGC2019J-16J_TS - 34	391	15	800	260	2.042	Below LOD	2325	Below LOD	0.0105
WGC2019J-16J_TS - 35	445	20	840	280	1.561	Below LOD	2744	Below LOD	0.0303
WGC2019J-16J_TS - 36	406	17	480	240	1.555	Below LOD	2805	Below LOD	0.0123
~~WGC2019J-16J_TS - 37~~	~~774~~	~~35~~	~~4023~~	~~84~~	~~1.724~~	~~48~~	~~5.06E+04~~	~~0.78~~	~~0.704~~
WGC2019J-16J_TS - 38	416	23	480	340	1.605	Below LOD	2722	Below LOD	0.036
WGC2019J-16J_TS - 39	444	20	1860	250	2.214	Below LOD	3429	Below LOD	0.045
WGC2019J-16J_TS - 40	411	24	960	480	1.48	Below LOD	3060	Below LOD	0.0325
WGC2019J-16J_TS - 41	454	27	1580	300	1.459	Below LOD	2437	Below LOD	0.06
~~WGC2019J-16J_TS - 42~~	~~645~~	~~38~~	~~3640~~	~~130~~	~~1.617~~	~~64~~	~~2.04E+04~~	~~0.56~~	~~0.309~~
~~WGC2019J-16J_TS - 43~~	~~476~~	~~38~~	~~2750~~	~~210~~	~~2.389~~	~~910~~	~~1937~~	~~0.79~~	~~0.541~~
WGC2019J-16J_TS - 44	402	25	1210	360	1.814	Below LOD	2047	Below LOD	0.05
WGC2019J-16J_TS - 45	445	19	1250	270	1.833	Below LOD	1940	Below LOD	0.0244
WGC2019J-16J_TS - 46	407	17	550	280	1.528	Below LOD	2789	Below LOD	0.03
WGC2019J-16J_TS - 47	441	21	900	300	1.473	Below LOD	2105	Below LOD	0.0216

WGC2019J-16J_TS - 48	431	18	960	300	1.567	Below LOD	2654	Below LOD	0.015
WGC2019J-16J_TS - 49	416	18	920	260	1.625	Below LOD	2810	Below LOD	0.0123
WGC2019J-16J_TS - 50	421	23	1210	280	1.556	Below LOD	2318	Below LOD	0.0217
~~WGC2019J-16J_TS - 51~~	~~416~~	~~20~~	~~1590~~	~~270~~	~~1.857~~	~~Below LOD~~	~~2126~~	~~0.31~~	~~0.0307~~
WGC2019J-16J_TS - 52	400	16	900	260	3.129	Below LOD	1805	Below LOD	0.0105
WGC2019J-16J_TS - 53	418	15	640	200	2.659	Below LOD	1743	Below LOD	0.0128
WGC2019J-16J_TS - 54	427	18	1040	230	1.613	Below LOD	1987	Below LOD	0.0235
WGC2019J-16J_TS - 55	409	20	860	370	3.602	Below LOD	1769	Below LOD	0.036
WGC2019J-16J_TS - 56	423	16	720	240	2.278	Below LOD	2220	Below LOD	0.0291
~~WGC2019J-16J_TS - 57~~	~~427~~	~~20~~	~~870~~	~~260~~	~~2.086~~	~~Below LOD~~	~~4577~~	~~Below LOD~~	~~0.0216~~
WGC2019J-16J_TS - 58	427	16	970	240	1.99	Below LOD	2531	Below LOD	0.034
WGC2019J-16J_TS - 59	455	24	1330	350	1.531	Below LOD	2624	Below LOD	0.0381
WGC2019J-16J_TS - 60	407	19	900	270	2.843	Below LOD	2445	Below LOD	0.043
WGC2019J-16J_TS - 61	442	18	1220	220	2.606	Below LOD	3148	Below LOD	0.044
~~WGC2019J-16J_TS - 62~~	~~568~~	~~29~~	~~3491~~	~~96~~	~~3.841~~	~~823~~	~~3470~~	~~0.73~~	~~0.576~~
~~WGC2019J-16J_TS - 63~~	~~436~~	~~19~~	~~1490~~	~~250~~	~~2.038~~	~~61~~	~~2629~~	~~Below LOD~~	~~0.0469~~
~~WGC2019J-16J_TS - 64~~	~~492~~	~~28~~	~~2580~~	~~240~~	~~2.657~~	~~536~~	~~2202~~	~~0.55~~	~~0.435~~
WGC2019J-16J_TS - 65	433	25	840	340	2.017	Below LOD	1892	Below LOD	0.0148
~~WGC2019J-16J_TS - 66~~	~~432~~	~~22~~	~~1260~~	~~340~~	~~2.154~~	~~31~~	~~3412~~	~~Below LOD~~	~~0.104~~
WGC2019J-16J_TS - 67	404	14	870	200	3.501	Below LOD	3298	Below LOD	0.035
WGC2019J-16J_TS - 68	426	17	450	240	2.198	Below LOD	2431	Below LOD	0.0154
WGC2019J-16J_TS - 69	402	20	740	270	2.672	Below LOD	2575	Below LOD	0.0191
WGC2019J-16J_TS - 70	410	25	1390	320	1.733	Below LOD	2795	Below LOD	0.0322
~~WGC2019J-16J_TS - 71~~	~~687~~	~~34~~	~~3860~~	~~130~~	~~1.725~~	~~425~~	~~2380~~	~~0.36~~	~~0.388~~
~~WGC2019J-16J_TS - 72~~	~~438~~	~~22~~	~~1490~~	~~320~~	~~1.71~~	~~Below LOD~~	~~4.48E+04~~	~~Below LOD~~	~~0.097~~
WGC2019J-16J_TS - 73	434	17	710	280	2.582	Below LOD	3190	Below LOD	0.0206
~~WGC2019J-16J_TS - 74~~	~~407~~	~~16~~	~~1060~~	~~220~~	~~2.102~~	~~Below LOD~~	~~2.86E+04~~	~~Below LOD~~	~~0.033~~

~~WGC2019J-16J_TS - 75~~	~~447~~	~~30~~	~~810~~	~~340~~	~~1.842~~	~~Below LOD~~	~~3620~~	~~Below LOD~~	~~0.0116~~
~~WGC2019J-16J_TS - 76~~	~~801~~	~~32~~	~~4207~~	~~87~~	~~1.287~~	~~328~~	~~2311~~	~~0.49~~	~~0.464~~
WGC2019J-16J_TS - 77	430	17	1000	260	1.962	Below LOD	2970	Below LOD	0.0247
WGC2019J-16J_TS - 78	419	20	1510	270	1.668	Below LOD	2886	Below LOD	0.039
~~WGC2019J-16J_TS - 79~~	~~445~~	~~18~~	~~680~~	~~210~~	~~2.484~~	~~Below LOD~~	~~5684~~	~~Below LOD~~	~~0.0261~~
Sample	Pb207/U235	2σ	Pb206/U238	2σ	ρ	Pb 207/Pb206	2σ	Pb207/U235 Age	2σ
WGC2019J-17D_New - 01	3.59	0.29	0.0941	0.0055	0.15843	0.279	0.024	1508	67
~~WGC2019J-17D_New - 02~~	~~21.4~~	~~1.2~~	~~0.226~~	~~0.012~~	~~0.7938~~	~~0.695~~	~~0.022~~	~~3136~~	~~54~~
~~WGC2019J-17D_New - 03~~	~~2.05~~	~~0.36~~	~~0.0752~~	~~0.0064~~	~~0.29504~~	~~0.217~~	~~0.038~~	~~1080~~	~~110~~
~~WGC2019J-17D_New - 04~~	~~12.9~~	~~1.7~~	~~0.178~~	~~0.016~~	~~0.83806~~	~~0.514~~	~~0.037~~	~~2550~~	~~120~~
~~WGC2019J-17D_New - 05~~	~~7.31~~	~~0.95~~	~~0.1235~~	~~0.0094~~	~~0.2104~~	~~0.435~~	~~0.05~~	~~2080~~	~~120~~
~~WGC2019J-17D_New - 06~~	~~12.19~~	~~0.66~~	~~0.1705~~	~~0.0074~~	~~0.39596~~	~~0.52~~	~~0.024~~	~~2604~~	~~54~~
~~WGC2019J-17D_New - 07~~	~~47.5~~	~~3.2~~	~~0.463~~	~~0.03~~	~~0.88125~~	~~0.75~~	~~0.025~~	~~3919~~	~~68~~
WGC2019J-17D_New - 09	8.44	0.55	0.1267	0.0084	0.27362	0.5	0.039	2250	64
WGC2019J-17D_New - 10	16.5	1.1	0.193	0.011	0.25991	0.624	0.027	2875	61
~~WGC2019J-17D_New - 11~~	~~4.2~~	~~1.5~~	~~0.093~~	~~0.013~~	~~0.91721~~	~~0.23~~	~~0.063~~	~~1160~~	~~270~~
~~WGC2019J-17D_New - 12~~	~~2.38~~	~~0.43~~	~~0.0698~~	~~0.0047~~	~~0.48836~~	~~0.249~~	~~0.041~~	~~1110~~	~~140~~
~~WGC2019J-17D_New - 13~~	~~41~~	~~1.5~~	~~0.399~~	~~0.013~~	~~0.45631~~	~~0.744~~	~~0.02~~	~~3791~~	~~38~~
~~WGC2019J-17D_New - 15~~	~~30.6~~	~~3.2~~	~~0.312~~	~~0.027~~	~~0.91474~~	~~0.703~~	~~0.03~~	~~3430~~	~~100~~
~~WGC2019J-17D_New - 16~~	~~10.9~~	~~0.72~~	~~0.1364~~	~~0.0083~~	~~0.5333~~	~~0.579~~	~~0.035~~	~~2497~~	~~59~~
~~WGC2019J-17D_New - 17~~	~~11.74~~	~~0.92~~	~~0.149~~	~~0.011~~	~~0.58308~~	~~0.604~~	~~0.048~~	~~2588~~	~~81~~
WGC2019J-17D_New - 18	4.86	0.6	0.0976	0.0063	0.35949	0.356	0.039	1720	110
~~WGC2019J-17D_New - 19~~	~~40.2~~	~~5.4~~	~~0.34~~	~~0.038~~	~~0.85598~~	~~0.823~~	~~0.044~~	~~3710~~	~~130~~
~~WGC2019J-17D_New - 20~~	~~24.6~~	~~4.1~~	~~0.237~~	~~0.023~~	~~0.89759~~	~~0.714~~	~~0.049~~	~~3210~~	~~130~~
WGC2019J-17D_New - 21	2.1	0.19	0.08	0.0036	0.036454	0.19	0.017	1112	64
WGC2019J-17D_New - 22	*0.84*	*0.1*	*0.0732*	*0.0039*	*0.11084*	*0.087*	*0.011*	*587*	*58*
~~WGC2019J-17D_New - 23~~	~~8.4~~	~~2.1~~	~~0.122~~	~~0.017~~	~~0.76463~~	~~0.492~~	~~0.078~~	~~2140~~	~~180~~

~~WGC2019J-17D_New - 24~~	~~23.8~~	~~1.7~~	~~0.245~~	~~0.011~~	~~0.080102~~	~~0.727~~	~~0.056~~	~~3247~~	~~69~~
~~WGC2019J-17D_New - 25~~	~~16.6~~	~~2.3~~	~~0.177~~	~~0.019~~	~~0.85108~~	~~0.66~~	~~0.038~~	~~2850~~	~~120~~
WGC2019J-17D_Old - 01	4.59	0.83	0.0931	0.0077	0.4557	0.328	0.05	1560	160
WGC2019J-17D_Old - 02	6.36	0.61	0.1149	0.0055	0.54724	0.4	0.033	1955	89
WGC2019J-17D_Old - 03	*0.78*	*0.17*	*0.069*	*0.0036*	*0.018382*	*0.079*	*0.015*	*498*	*76*
WGC2019J-17D_Old - 04	*6.65*	*0.95*	*0.1095*	*0.0084*	*0.71563*	*0.383*	*0.036*	*1830*	*130*
~~WGC2019J-17D_Old - 06~~	~~3.18~~	~~0.35~~	~~0.0832~~	~~0.0048~~	~~0.15244~~	~~0.29~~	~~0.037~~	~~1423~~	~~79~~
WGC2019J-17D_Old - 07	*1.24*	*0.15*	*0.0715*	*0.0038*	*0.15025*	*0.135*	*0.018*	*780*	*73*
~~WGC2019J-17D_Old - 08~~	~~0.87~~	~~0.19~~	~~0.0667~~	~~0.0034~~	~~0.0431~~	~~0.095~~	~~0.02~~	~~536~~	~~73~~
WGC2019J-17D_Old - 09	2.49	0.23	0.0792	0.0038	0.081952	0.241	0.025	1213	70
WGC2019J-17D_Old - 10	*0.56*	*0.1*	*0.0693*	*0.0048*	*0.28235*	*0.059*	*0.011*	*417*	*64*
~~WGC2019J-17D_Old - 11~~	~~0.84~~	~~0.15~~	~~0.0672~~	~~0.005~~	~~0.057077~~	~~0.095~~	~~0.017~~	~~576~~	~~83~~
~~WGC2019J-17D_Old - 12~~	~~8.88~~	~~0.66~~	~~0.1357~~	~~0.0076~~	~~0.53632~~	~~0.48~~	~~0.027~~	~~2277~~	~~64~~
WGC2019J-17D_Old - 13	6.77	0.66	0.1057	0.0055	0.59123	0.45	0.034	1983	85
~~WGC2019J-17D_Old - 14~~	~~17.1~~	~~2.3~~	~~0.193~~	~~0.019~~	~~0.94665~~	~~0.56~~	~~0.037~~	~~2620~~	~~150~~
WGC2019J-17D_Old - 15	*2.8*	*0.35*	*0.0829*	*0.0044*	*0.44729*	*0.252*	*0.027*	*1258*	*96*
~~WGC2019J-17D_Old - 16~~	~~1.46~~	~~0.3~~	~~0.07~~	~~0.0042~~	~~0.02875~~	~~0.151~~	~~0.03~~	~~810~~	~~100~~
~~WGC2019J-17D_Old - 17~~	~~27.88~~	~~0.94~~	~~0.2766~~	~~0.01~~	~~0.3077~~	~~0.732~~	~~0.025~~	~~3410~~	~~33~~
~~WGC2019J-17D_Old - 18~~	~~8.55~~	~~0.35~~	~~0.12~~	~~0.004~~	~~0.28868~~	~~0.519~~	~~0.019~~	~~2276~~	~~37~~
~~WGC2019J-17D_Old - 19~~	~~10.66~~	~~0.47~~	~~0.1368~~	~~0.0053~~	~~0.083326~~	~~0.575~~	~~0.029~~	~~2480~~	~~41~~
~~WGC2019J-17D_Old - 20~~	~~2.47~~	~~0.28~~	~~0.0728~~	~~0.0045~~	~~0.47642~~	~~0.249~~	~~0.025~~	~~1202~~	~~83~~
Sample	Pb206/U238 Age	2σ	Pb207/Pb206 Age	2σ	U (ppm)	Ca (ppm)	Fe (ppm)	Pb 204 (ppm)	Pb208 (ppm)
WGC2019J-17D_New - 01	578	32	3250	160	1.179	Below LOD	2534	0.62	0.292
~~WGC2019J-17D_New - 02~~	~~1308~~	~~65~~	~~4730~~	~~54~~	~~2.33~~	~~47~~	~~3091~~	~~2.37~~	~~2.33~~
~~WGC2019J-17D_New - 03~~	~~466~~	~~38~~	~~2640~~	~~300~~	~~1.515~~	~~Below LOD~~	~~3957~~	~~0.81~~	~~0.62~~
~~WGC2019J-17D_New - 04~~	~~1044~~	~~89~~	~~4220~~	~~110~~	~~1.385~~	~~Below LOD~~	~~1576~~	~~1.02~~	~~0.817~~
~~WGC2019J-17D_New - 05~~	~~748~~	~~54~~	~~3910~~	~~180~~	~~1.499~~	~~420~~	~~1906~~	~~0.84~~	~~0.61~~

~~WGC2019J-17D_New - 06~~	~~1013~~	~~40~~	~~4284~~	~~78~~	~~1.198~~	~~Below LOD~~	~~2083~~	~~1.05~~	~~0.737~~
~~WGC2019J-17D_New - 07~~	~~2440~~	~~130~~	~~4850~~	~~57~~	~~1.477~~	~~1.24E+04~~	~~6635~~	~~3.8~~	~~3.83~~
WGC2019J-17D_New - 09	775	50	4180	130	0.698	Below LOD	1286	0.67	0.398
WGC2019J-17D_New - 10	1131	61	4548	65	1.126	Below LOD	1645	0.69	0.57
~~WGC2019J-17D_New - 11~~	~~569~~	~~76~~	~~1930~~	~~550~~	~~1.495~~	~~Below LOD~~	~~1839~~	~~1~~	~~1.03~~
~~WGC2019J-17D_New - 12~~	~~434~~	~~28~~	~~2620~~	~~370~~	~~1.458~~	~~Below LOD~~	~~1699~~	~~0.87~~	~~0.493~~
~~WGC2019J-17D_New - 13~~	~~2161~~	~~58~~	~~4834~~	~~46~~	~~1.298~~	~~15180~~	~~4690~~	~~3.54~~	~~3.56~~
~~WGC2019J-17D_New - 15~~	~~1730~~	~~130~~	~~4736~~	~~71~~	~~1.043~~	~~168~~	~~4720~~	~~2.47~~	~~2.75~~
~~WGC2019J-17D_New - 16~~	~~823~~	~~47~~	~~4450~~	~~100~~	~~1.477~~	~~Below LOD~~	~~12980~~	~~1.04~~	~~0.911~~
~~WGC2019J-17D_New - 17~~	~~891~~	~~60~~	~~4480~~	~~120~~	~~1.308~~	~~Below LOD~~	~~1.32E+04~~	~~1.3~~	~~1.23~~
WGC2019J-17D_New - 18	599	37	3600	180	1.32	Below LOD	2130	0.87	0.82
~~WGC2019J-17D_New - 19~~	~~1900~~	~~190~~	~~5010~~	~~100~~	~~1.11~~	~~Below LOD~~	~~2940~~	~~3.49~~	~~2.94~~
~~WGC2019J-17D_New - 20~~	~~1390~~	~~130~~	~~4760~~	~~110~~	~~1.175~~	~~Below LOD~~	~~1437~~	~~2.1~~	~~1.52~~
WGC2019J-17D_New - 21	496	21	2620	180	1.646	Below LOD	2109	0.31	0.286
WGC2019J-17D_New - 22	*454*	*23*	*960*	*280*	*1.365*	*Below LOD*	*2554*	*Below LOD*	*0.0214*
~~WGC2019J-17D_New - 23~~	~~739~~	~~96~~	~~4090~~	~~240~~	~~1.436~~	~~1.05E+04~~	~~2290~~	~~4.09~~	~~4.19~~
~~WGC2019J-17D_New - 24~~	~~1411~~	~~57~~	~~4790~~	~~130~~	~~1.361~~	~~1.78E+04~~	~~5420~~	~~6.62~~	~~6.31~~
~~WGC2019J-17D_New - 25~~	~~1040~~	~~100~~	~~4632~~	~~91~~	~~1.31~~	~~187~~	~~3340~~	~~1.99~~	~~1.53~~
WGC2019J-17D_Old - 01	571	45	3180	290	1.237	Below LOD	1260	0.65	0.344
WGC2019J-17D_Old - 02	700	32	3780	140	1.4	Below LOD	1665	0.29	0.284
WGC2019J-17D_Old - 03	*429*	*22*	*640*	*380*	*1.273*	*Below LOD*	*3000*	*Below LOD*	*0.0127*
WGC2019J-17D_Old - 04	*671*	*49*	*3630*	*170*	*1.299*	*Below LOD*	*1584*	*Below LOD*	*0.114*
~~WGC2019J-17D_Old - 06~~	~~515~~	~~28~~	~~3330~~	~~210~~	~~1.52~~	~~Below LOD~~	~~3900~~	~~Below LOD~~	~~0.194~~
WGC2019J-17D_Old - 07	*444*	*23*	*1700*	*300*	*1.163*	*Below LOD*	*2031*	*Below LOD*	*0.0304*
~~WGC2019J-17D_Old - 08~~	~~415~~	~~20~~	~~790~~	~~330~~	~~1.252~~	~~Below LOD~~	~~4278~~	~~Below LOD~~	~~0.0092~~
WGC2019J-17D_Old - 09	491	23	2930	180	1.365	Below LOD	1577	0.52	0.166
WGC2019J-17D_Old - 10	*431*	*29*	*240*	*340*	*1.477*	*Below LOD*	*1925*	*Below LOD*	*0.0054*

~~WGC2019J-17D_Old - 11~~	~~418~~	~~30~~	~~1040~~	~~410~~	~~1.445~~	~~Below LOD~~	~~1748~~	~~0.34~~	~~0.187~~
~~WGC2019J-17D_Old - 12~~	~~823~~	~~44~~	~~4112~~	~~90~~	~~1.156~~	~~200~~	~~1924~~	~~0.94~~	~~0.481~~
WGC2019J-17D_Old - 13	655	35	3970	120	1.351	Below LOD	2450	0.56	0.386
~~WGC2019J-17D_Old - 14~~	~~1120~~	~~100~~	~~4310~~	~~130~~	~~1.588~~	~~28~~	~~6750~~	~~1.12~~	~~0.83~~
WGC2019J-17D_Old - 15	*512*	*26*	*2820*	*210*	*1.198*	*Below LOD*	*1628*	*Below LOD*	*0.11*
~~WGC2019J-17D_Old - 16~~	~~435~~	~~25~~	~~1810~~	~~360~~	~~1.276~~	~~Below LOD~~	~~3738~~	~~0.3~~	~~0.0342~~
~~WGC2019J-17D_Old - 17~~	~~1572~~	~~52~~	~~4807~~	~~57~~	~~1.514~~	~~3230~~	~~1700~~	~~1.93~~	~~1.89~~
~~WGC2019J-17D_Old - 18~~	~~730~~	~~23~~	~~4262~~	~~56~~	~~1.754~~	~~31~~	~~2234~~	~~0.7~~	~~0.625~~
~~WGC2019J-17D_Old - 19~~	~~825~~	~~30~~	~~4410~~	~~75~~	~~1.679~~	~~420~~	~~2173~~	~~0.92~~	~~0.715~~
~~WGC2019J-17D_Old - 20~~	~~452~~	~~27~~	~~2960~~	~~180~~	~~1.47~~	~~Below LOD~~	~~2429~~	~~Below LOD~~	~~0.131~~

Sample	Pb207/U235	2σ	Pb206/U238	2σ	ρ	Pb 207/Pb206	2σ	Pb207/U235 Age	2σ
NIST610 - 1	29.49	0.7	0.2392	0.0049	0.92186	0.909	0.0017	3469.4	23
NIST610 - 2	29.38	0.7	0.2379	0.0049	0.90629	0.9009	0.0017	3465.7	23
NIST610 - 3	29.23	0.7	0.2365	0.0049	0.92278	0.8943	0.0018	3460.8	23
NIST610 - 4	29.24	0.7	0.2366	0.0049	0.92593	0.8951	0.0019	3461.1	23
NIST610 - 5	29.29	0.7	0.2363	0.0049	0.90543	0.9041	0.0018	3462.6	24
NIST610 - 6	29.45	0.71	0.2381	0.0049	0.92143	0.9027	0.0019	3467.8	24
NIST610 - 7	29.1	0.7	0.2353	0.0049	0.93174	0.8988	0.0021	3456.2	24
NIST610 - 8	29.02	0.7	0.2349	0.0049	0.91921	0.8978	0.002	3453.4	24
NIST610 - 9	28.83	0.7	0.2333	0.0049	0.87347	0.8988	0.0023	3446.9	23
NIST610 - 10	28.9	0.7	0.2338	0.0049	0.79002	0.9006	0.0028	3449.3	24
NIST610 - 11	28.5	0.69	0.2301	0.0048	0.87774	0.8967	0.0026	3436.6	24
NIST610 - 12	28.62	0.69	0.2315	0.0048	0.87498	0.8949	0.0025	3440	24
NIST610 - 13	28.61	0.7	0.2305	0.0049	0.91367	0.9028	0.0023	3439.4	24
NIST610 - 14	28.34	0.68	0.2285	0.0048	0.88249	0.9017	0.0025	3430.1	23
NIST610 - 15	28.61	0.69	0.231	0.0048	0.84858	0.8956	0.0027	3439.4	23
NIST610 - 16	28.62	0.69	0.2315	0.0048	0.8049	0.8953	0.0031	3439.9	23

NIST610 - 17	29.06	0.7	0.2347	0.0049	0.79028	0.9002	0.0035	3454.9	23
NIST610 - 18	29.22	0.7	0.2358	0.0049	0.87917	0.9003	0.0026	3460.3	23
R10 - 1	1.937	0.057	0.1856	0.0042	0.17931	0.0758	0.0016	1091	20
R10 - 2	1.913	0.055	0.1837	0.004	0.14034	0.0757	0.0013	1085	20
R10 - 3	1.934	0.057	0.1834	0.0039	0.16955	0.0762	0.0014	1091	19
R10 - 4	1.95	0.056	0.1863	0.0041	0.36403	0.0757	0.0012	1096	19
R10 - 5	1.941	0.054	0.1861	0.004	0.20536	0.0759	0.0012	1095	19
R10 - 6	1.892	0.055	0.1829	0.0041	0.28169	0.0754	0.0013	1076	19
R10 - 7	1.918	0.053	0.182	0.004	0.33809	0.0761	0.0012	1085.7	18
R10 - 8	1.942	0.052	0.1865	0.004	0.17735	0.0756	0.0012	1094.3	18
R10 - 9	1.943	0.055	0.1847	0.004	0.23769	0.0763	0.0013	1094	19
R10 - 10	1.892	0.053	0.183	0.004	0.093708	0.0751	0.0013	1076	19
R10 - 11	1.942	0.053	0.1853	0.0041	0.10313	0.0758	0.0013	1094.4	18
R10 - 12	1.932	0.055	0.1839	0.004	0.1094	0.076	0.0014	1090	19
R10 - 13	1.93	0.054	0.1863	0.0042	0.14611	0.0757	0.0013	1090	19
R10 - 14	1.933	0.052	0.1856	0.004	0.076617	0.0757	0.0011	1091	18
R10 - 15	1.933	0.053	0.1832	0.004	0.37307	0.0762	0.0011	1091	18
R10 - 16	1.929	0.055	0.1847	0.0041	0.2858	0.0755	0.0013	1089	19
R10 - 17	1.899	0.052	0.1827	0.004	0.27607	0.0755	0.0011	1079.3	18
R10 - 18	1.956	0.056	0.1862	0.0041	0.098717	0.0761	0.0013	1098	19
R19 - 1	0.635	0.062	0.0815	0.0027	-0.029454	0.0579	0.0058	477	37
R19 - 2	0.589	0.048	0.0792	0.0028	0.058465	0.0554	0.0045	456	30
R19 - 3	0.65	0.056	0.0812	0.0028	0.23064	0.0598	0.005	504	37
R19 - 4	0.657	0.059	0.0812	0.0027	0.12045	0.0597	0.0052	494	35
R19 - 5	0.687	0.058	0.079	0.0028	-0.035484	0.0653	0.0055	517	34
R19 - 6	0.694	0.051	0.0796	0.0025	-0.0087642	0.0647	0.0048	525	31
R19 - 7	0.666	0.054	0.0809	0.0026	0.14024	0.0612	0.005	507	34

R19 - 8	0.698	0.052	0.0798	0.0025	0.21468	0.0632	0.0046	522	32
R19 - 9	0.62	0.048	0.0779	0.0029	-0.12074	0.0606	0.0052	480	31
R19 - 10	0.655	0.053	0.0772	0.0027	0.015633	0.0632	0.0054	495	33
R19 - 11	0.687	0.059	0.0794	0.0029	0.0079072	0.0633	0.0052	512	35
R19 - 12	0.645	0.053	0.0784	0.0032	0.047706	0.0617	0.0053	498	34
R19 - 13	0.618	0.052	0.0788	0.0024	0.062796	0.0576	0.0047	473	32
R19 - 14	0.699	0.053	0.0767	0.0025	-0.022346	0.067	0.0052	527	33
R19 - 15	0.68	0.05	0.0787	0.0027	-0.012271	0.0632	0.0046	526	29
R19 - 16	0.675	0.055	0.0791	0.0027	0.074049	0.0621	0.005	507	34
R19 - 17	0.715	0.05	0.0819	0.0031	0.13671	0.0655	0.0047	542	30
R19 - 18	0.692	0.054	0.081	0.0029	-0.078377	0.0642	0.0054	530	35
Sample	Pb206/U238 Age	2σ	Pb207/Pb206 Age	2σ	U (ppm)	Ca (ppm)	Fe (ppm)	Pb 204 (ppm)	Pb_ppm_m208
NIST610 - 1	1382.1	25	5208.1	3.9	417.6	82150	452.7	424.2	422.1
NIST610 - 2	1375.6	26	5189.8	3.9	413.1	82120	461.6	426.3	426.2
NIST610 - 3	1368.4	25	5175	4.1	404.7	82210	453	428.8	430
NIST610 - 4	1368.7	25	5176.7	4.2	408.2	82320	460.4	422.8	427.7
NIST610 - 5	1367.1	25	5197.1	4	398.6	82290	461.1	429.8	429.1
NIST610 - 6	1376.9	26	5194	4.2	399.5	81640	455.1	424	423.8
NIST610 - 7	1361.8	26	5185.1	4.7	386.1	82000	462.1	424.1	425
NIST610 - 8	1359.7	26	5182.8	4.6	391.8	82530	459.7	427.2	425.4
NIST610 - 9	1351.4	25	5185.1	5.3	386	81730	463.3	425.4	426.6
NIST610 - 10	1354.3	26	5189.1	6.4	385.1	82170	458.4	424.8	424.7
NIST610 - 11	1334.9	25	5180.4	5.9	382.5	82000	452.4	428.7	426.3
NIST610 - 12	1342.2	25	5176.2	5.6	380.9	82520	458.7	431	428.8
NIST610 - 13	1336.8	25	5194.2	5.1	374.4	82550	456.6	432	431.4
NIST610 - 14	1326.6	25	5191.6	5.6	380.6	81900	461.4	421.9	419.6
NIST610 - 15	1339.6	25	5178	6	386.4	82560	458.2	423.3	425.1

NIST610 - 16	1342.4	25	5177.2	6.9	387	81890	458.4	421	423
NIST610 - 17	1359.8	26	5188.4	7.9	393.7	81490	455.7	423.2	425.8
NIST610 - 18	1364.5	25	5188.5	5.8	392.2	82490	456.5	429.8	428.8
R10 - 1	1097	23	1084	39	29.67	Below LOD	4788	0.52	0.022
R10 - 2	1087.1	22	1077	37	29.52	Below LOD	4753	0.33	0.0091
R10 - 3	1085.4	21	1084	37	29.28	Below LOD	4711	Below LOD	Below LOD
R10 - 4	1101	22	1074	33	29.38	Below LOD	4866	0.38	Below LOD
R10 - 5	1100.1	22	1095	31	29.33	Below LOD	4748	Below LOD	Below LOD
R10 - 6	1082	22	1071	35	29.75	Below LOD	4680	Below LOD	0.0049
R10 - 7	1077.7	22	1087	31	29.51	Below LOD	4728	Below LOD	0.0061
R10 - 8	1102.1	22	1083	31	29.71	Below LOD	4659	Below LOD	0.0067
R10 - 9	1092.3	22	1091	33	29.71	Below LOD	4722	Below LOD	0.0082
R10 - 10	1083.2	22	1058	35	29.15	Below LOD	4612	Below LOD	0.0043
R10 - 11	1096	22	1078	34	29.71	Below LOD	4704	Below LOD	0.0064
R10 - 12	1088.3	22	1080	37	29.19	Below LOD	4653	0.29	Below LOD
R10 - 13	1098	21	1079	37	29.67	Below LOD	4668	0.28	Below LOD
R10 - 14	1097.1	22	1082	29	29.51	Below LOD	4668	Below LOD	0.0065
R10 - 15	1084.3	22	1094	30	29.75	Below LOD	4691	0.29	Below LOD
R10 - 16	1092	22	1079	33	29.45	Below LOD	4687	Below LOD	0.0054
R10 - 17	1081	22	1070	30	29.09	Below LOD	4675	0.26	0.0065
R10 - 18	1100.4	22	1092	33	29.73	Below LOD	4536	Below LOD	0.0046
R19 - 1	504	16	300	190	2.931	Below LOD	2808	0.32	Below LOD
R19 - 2	491	16	280	160	3.37	Below LOD	2838	0.3	Below LOD
R19 - 3	503	17	410	170	2.814	Below LOD	2911	Below LOD	Below LOD
R19 - 4	503	16	400	170	2.795	Below LOD	2906	Below LOD	Below LOD
R19 - 5	489	17	550	170	2.756	Below LOD	2842	Below LOD	Below LOD
R19 - 6	494	15	590	150	2.732	Below LOD	2828	Below LOD	Below LOD

R19 - 7	501	16	470	170	2.979	Below LOD	2783	Below LOD	Below LOD
R19 - 8	495	15	550	160	3.241	Below LOD	2809	Below LOD	Below LOD
R19 - 9	483	17	450	170	2.757	Below LOD	2824	Below LOD	0.0045
R19 - 10	479	16	480	180	2.711	Below LOD	2849	Below LOD	Below LOD
R19 - 11	492	17	500	170	2.692	Below LOD	2834	Below LOD	Below LOD
R19 - 12	486	19	470	170	2.729	Below LOD	2833	Below LOD	0.0058
R19 - 13	489	15	330	160	3.056	Below LOD	2757	Below LOD	Below LOD
R19 - 14	476	15	660	160	3.14	Below LOD	2770	Below LOD	0.005
R19 - 15	488	16	620	150	2.778	Below LOD	2814	Below LOD	0.0043
R19 - 16	490	16	490	170	2.721	Below LOD	2806	Below LOD	Below LOD
R19 - 17	507	18	610	150	2.817	Below LOD	2860	Below LOD	0.0077
R19 - 18	501	17	560	170	2.816	Below LOD	2772	Below LOD	0.0069

Appendix 8a: Extended Geochronology Methods

Mineral Separate Preparation

Zircon and rutile grains were obtained through crushing and sieving of samples WGC2019-15, WGC2019J-16J and WGC2019J-17D using the jaw crusher, disc mill and ring mill at the University of Adelaide lapidary. Standard panning and frantzing were used to isolate zircon, apatite and rutile grains from the 79-400µm fraction. Approximately 100 zircon and rutile grains were mounted per 25mm- diameter mold. Seven molds were initially made; a zircon mount for WGC2019-15, and two zircon plus one rutile mount for samples WGC2019J-16J and WGC2019J-17D. The zircon mount for sample WGC2019-15 contained one poured and one picked line, while the other six mounts contained ~100 picked grains each. Each mold was filled with epoxy resin and after setting polished with 2500 grit sandpaper until individual grains were exposed. These were then polished with diamond paste using 3µm and 1µm laps in the University of Adelaide lapidary.

The Gatan cathodoluminescence (CL) analyser attached to the FEI Quanta MLA-600 scanning electron microscope (SEM) at Adelaide Microscopy was used to acquire CL images for zircons in WGC2019-15, WGC2019J-16J and WGC2019J-17D. These images illuminated zircon zonation and promising metamorphic rim LA-ICP-MS targets. Zircon grains were distinguishable by their high relief, numerous inclusions and zoning under CL. Apatite grains were noticeably duller and colourless under reflected light. Rutile grains appeared dark under reflected light with sub- to anhedral grain shapes. The E-DAX software on the Quanta MLA-600 SEM allowed these minerals to be distinguished in a first-pass process. Only zircons were targeted for CL imaging.

Two additional mounts were made for rutiles. These were required for samples WGC2019J-16J and WGC2019J-17D as the original mounts used for analysis had incorrectly calibrated standards. This produced nonsensical data on the first run. Subsequently, these later mounts underwent backscatter electron (BSE) imaging using the Philips XL30 Field Emission Scanning Electron Microscope (FESEM) at Adelaide Microscopy. A spot size of 5 and accelerating voltage of 20.0kV was used. Imaging showed ilmenite exsolution (white streaks on typically grey rutile grains) and inclusions (e.g. amphiboles, ilmenite, petrovskite and titanite), which were identified by spectral analysis.

LA-ICP-MS Analysis

Laser Ablation-Inductively Coupled Plasma-Mass Spectrometry (LA-ICP-MS) using a RESOlution LR 193nm Excimer laser system with a coupled Agilent 7700s ICP-MS at Adelaide Microscopy was used to acquire zircon U-Pb data from samples WGC2019-15 (diatexite), WGC2019J-16J (high strain eclogite) and WGC2019-17D (low strain eclogite). The same machine was used to collect rutile U-Pb data from WGC2019J-16J and WGC2019J-17D. A He-ablation atmosphere with an ablation fluence of 2J/cm^2, 35mJ Ar-F laser energy, and 50% attenuation at a 5 Hz frequency was used to ablate zircons. A 29 µm spot size was used on the three grain mounts. For WGC2019-15, both

'white' outer rims and 'black' inner regions were targeted. In mafic eclogites (high and low strain), inner regions were sometimes grey. Inherited detrital zircons were not analysed. For WGC2019J-16J and WGC2019J-17D, only zircon rims were analysed. For zircons, trace element and titanium data were measured simultaneously with U-Pb data.

A 60s total acquisition time was used for each zircon analysis. This was subdivided into 30s each of background acquisition and sample ablation. The standards GJ (206Pb/238U = 608.5 ± 0.4 Ma) (Jackson et al., 2004), Plešovice (206Pb/238U = 337.13 ± 0.37 Ma) (Sláma et al., 2008) and 91500 (1062.4 ± 0.4 Ma) (Wiedenbeck et al., 1995) were used to correct for elemental fractionation/mass bias and monitor data accuracy respectively. A spot size of 29 μm and fluence of 2J/cm^2 was employed throughout. A summary of the various weighted mean averages for the various standards is shown below. In all cases, n=18.

Standard Name	Standard Age (Ma)	2σ	Study: Pb^{206}/U^{238}	2σ	Study: Pb^{207}/U^{235}	2σ
GJ1	608.5	0.4	601	1.8	603.6	3.4
Plesovice	337.13	0.37	339.5	1.5	339.7	2
91500	1062.4	0.4	1058.6	4.2	1054.1	6.7

For rutiles, after the initial disastrous run, a combination of mounts and thin sections were analysed for WGC2019J-16J and mounts for WGC2019J-17D. A 51 μm spot size with 5J/cm^2 fluence, 55mJ energy and 50% attenuation was used. As the mass spectrometer had broken the day before the analysis took place (part of the machine would not close properly), a workaround meant that an apparent 26s background signal collection was in fact 30s long. This workaround also made the laser ablation laboratory have more loose wires than the Millennium Falcon after a particularly difficult Kessel Run. Ablation was 40s, resulting in a ~72s total ablation time per sample. Standards R10 ($^{207}Pb/^{235}U$ = 1085.1 - 1096.2 Ma and $^{206}Pb/^{238}U$ = 1086.3–1096.6 Ma) (Luvizotto et al., 2009) and R19 ($^{206}Pb/^{238}U$ TIMS age 489.5 ± 0.9Ma) (Zack et al., 2011) were used to correct for elemental fractionation/mass bias and monitor data accuracy respectively. A summary of the various standard weighted mean averages is shown below.

Standard Name	Standard: Pb^{206}/U^{238}	Standard: Pb^{207}/U^{235}	Study: Pb^{206}/U^{238}	2σ	Study: Pb^{207}/U^{235}	2σ
R10	1086.3 – 1096.6 Ma	1085.1 - 1096.2 Ma	1091.38 Ma	21.9	1089.26 Ma	18.7
R19	489.5 ± 0.9 Ma	-	492.83 Ma	16.3	505.1 Ma	33.1

Data Processing and Reduction

Iolite 3.6 was used to reduce U-Pb isotopic data (Paton et al., 2011). Iolite 3.6 corrects for instrument drift and down-hole fractionation using data from standards acquired alongside that of analysed zircons. Background signals, which should be flat, are

measured for 30s at the beginning of each analysis. Signals are removed if spikes in the background are observed. Standards and samples are identified and data signals subsequently cropped to remove background data. A data reduction scheme (DRS) is then applied, with the default linear fit typically best suited. The DRS corrects for downhole fractionation and instrument drift in analyses. Standard and data signals are then cropped to avoid nonsensical data. Signal quality is improved by removing low quality analyses. High quality analyses have steady U and Pb isotope readings (i.e. flat slopes); no spikes in signal (indicative of hitting an inclusion); curved or steep slopes (indicating the crossing of zones); and a negative slope towards the end of an analysis (indicating ablation through grains). In the case of bimodal zircon signals, which indicate ablation of multiple zones, the first section of the signal is generally selected preferentially as this is indicative of the pre-planned target. The latter end of the signal is taken towards the end of the ablation and therefore records the bottom of the ablation hole. This is not seen on the CL images used to decide target points. An average of these two halves of the signal produces a meaningless age that is a combination of e.g. a metamorphic rim and inherited core. It is important throughout this correcting process to not bias the data towards desired trends. The same DRS is then applied to the data before exportation from Iolite 3.6 and subsequent concordia plotting

Appendix 8b: Zircon U-Pb Data

95% concordant analyses are shown italicised.

	Pb 207/ U 235	**2σ**	**Pb 206/U 238**	**2σ**	**ρ**	**Pb 207/ U 235 Final Age**	**2σ**	Final Age Pb 206 / U 238	2σ	**Pb 207/ Pb 206**	**2σ**
PRIMARY STANDARDS											
GJ - 1	0.828	0.028	0.0973	0.0013	-0.021269	610	16	598.4	7.8	0.0613	0.0021
GJ - 2	0.813	0.03	0.0982	0.0013	0.32158	602	17	603.7	7.4	0.0597	0.002
GJ - 3	0.796	0.025	0.0968	0.0013	0.29917	593	14	595.4	7.9	0.0594	0.0016
GJ - 4	0.82	0.026	0.0973	0.0014	0.17851	606	15	598.6	8.2	0.0609	0.0019
GJ - 5	0.822	0.027	0.0987	0.0014	0.03262	607	15	606.7	8.3	0.0603	0.002
GJ - 6	0.803	0.025	0.0978	0.0013	0.021494	597	14	601.6	7.3	0.0593	0.0019
GJ - 7	0.814	0.027	0.098	0.0014	0.037744	603	15	602.9	8.2	0.06	0.002
GJ - 8	0.813	0.028	0.0984	0.0013	0.34781	602	16	605.2	7.5	0.0596	0.0018
GJ - 9	0.824	0.025	0.0977	0.0012	0.20976	609	14	600.7	7.2	0.0609	0.0017
GJ - 10	0.831	0.025	0.0992	0.0013	0.028962	613	14	609.8	7.4	0.0605	0.0018
GJ - 11	0.809	0.024	0.0971	0.0013	0.19897	600	14	597.4	7.5	0.0601	0.0017
GJ - 12	0.822	0.028	0.0981	0.0012	0.30653	607	16	603.5	7.1	0.0603	0.0019
GJ - 13	0.813	0.029	0.0978	0.0014	0.19265	602	16	601.7	8.1	0.0598	0.002
GJ - 14	0.812	0.027	0.0979	0.0013	-0.051405	602	15	601.8	7.8	0.06	0.002
GJ - 15	0.81	0.025	0.0979	0.0013	0.15944	603	14	602	7.9	0.0595	0.0018
GJ - 16	0.812	0.022	0.0977	0.0014	0.17812	602	12	600.6	8.2	0.0602	0.0017
GJ - 17	0.841	0.025	0.0982	0.0012	0.3437	618	14	603.9	6.8	0.0615	0.0016
GJ - 18	0.795	0.023	0.0969	0.0012	-0.045732	592	13	596.2	7.3	0.059	0.0017

SECONDARY STANDARDS											
Plesovice - 1	0.4	0.012	0.05463	0.00061	0.077231	340.9	8.4	342.8	3.8	0.053	0.0015
Plesovice - 2	0.411	0.012	0.05465	0.00062	0.26178	349.1	8.6	343	3.8	0.0544	0.0015
Plesovice - 3	0.406	0.013	0.05398	0.00068	0.11968	345.6	9	338.9	4.2	0.054	0.0016
Plesovice - 4	0.398	0.013	0.05381	0.00077	0.18905	339.6	9.4	337.8	4.7	0.0535	0.0016
Plesovice - 5	0.391	0.012	0.05366	0.00068	0.070076	334.5	8.8	336.9	4.2	0.0527	0.0016
Plesovice - 6	0.398	0.011	0.05418	0.00073	-0.073882	339.9	8.3	340.1	4.4	0.0532	0.0016
Plesovice - 7	0.405	0.012	0.05515	0.00071	0.22395	344.7	8.6	346	4.4	0.053	0.0015
Plesovice - 8	0.397	0.011	0.05434	0.00076	0.28958	338.8	8.2	341.1	4.6	0.0525	0.0013
Plesovice - 9	0.403	0.013	0.05459	0.0006	0.11851	342.9	9.1	342.6	3.7	0.0534	0.0017
Plesovice - 10	0.391	0.012	0.05379	0.00072	0.293	334.4	9.1	337.7	4.4	0.0524	0.0015
Plesovice - 11	0.394	0.012	0.05348	0.00067	0.22545	336.8	9	335.8	4.1	0.0528	0.0015
Plesovice - 12	0.397	0.012	0.05399	0.00076	0.10312	338.9	9	339	4.7	0.0531	0.0016
Plesovice - 13	0.4	0.014	0.05419	0.00064	0.010427	341.2	10	340.2	3.9	0.0533	0.0019
Plesovice - 14	0.395	0.011	0.05357	0.00062	0.11841	337.5	8.1	336.4	3.8	0.0532	0.0014
Plesovice - 15	0.399	0.011	0.05388	0.00069	-0.0067157	340.1	7.9	338.3	4.2	0.0533	0.0015
Plesovice - 16	0.4	0.012	0.05368	0.00066	0.22555	340.8	8.7	337.1	4	0.0536	0.0015
Plesovice - 17	0.396	0.012	0.05448	0.00076	0.18741	338.3	8.9	342	4.7	0.0521	0.0017
Plesovice - 18	0.384	0.013	0.05327	0.00072	0.0099592	329.1	9.3	334.5	4.4	0.0519	0.0018
91500 - 1	1.872	0.069	0.1766	0.0033	0.062261	1066	24	1048	18	0.0765	0.0031
91500 - 2	1.866	0.092	0.1813	0.0038	0.08747	1060	33	1074	21	0.0749	0.0038
91500 - 3	1.806	0.082	0.1781	0.0033	0.089037	1040	30	1056	18	0.0736	0.0034
91500 - 4	1.834	0.086	0.1767	0.0033	0.14064	1050	31	1049	18	0.0745	0.0033
91500 - 5	1.841	0.08	0.1774	0.0033	0.207	1053	29	1052	18	0.0751	0.0032
91500 - 6	1.837	0.078	0.1783	0.0037	0.14888	1057	27	1057	20	0.0748	0.0033

91500 - 7	1.877	0.088	0.1787	0.0034	-0.059027	1065	31	1059	18	0.0763	0.0039
91500 - 8	1.871	0.087	0.1817	0.0034	0.24967	1068	32	1076	18	0.0751	0.0035
91500 - 9	1.852	0.087	0.1779	0.0035	0.19034	1056	31	1055	19	0.0753	0.0035
91500 - 10	1.829	0.088	0.1783	0.0037	0.015938	1047	32	1057	20	0.0744	0.0037
91500 - 11	1.84	0.08	0.1817	0.0033	0.32008	1053	29	1076	18	0.0731	0.0029
91500 - 12	1.942	0.083	0.1799	0.0035	0.028994	1089	29	1066	19	0.0776	0.0034
91500 - 13	1.825	0.085	0.178	0.0027	-0.08669	1052	29	1056	15	0.0739	0.0036
91500 - 14	1.807	0.079	0.1785	0.0035	-0.21406	1041	29	1058	19	0.0734	0.0036
91500 - 15	1.802	0.076	0.1767	0.0032	0.02311	1045	26	1049	18	0.0737	0.0032
91500 - 16	1.778	0.068	0.1781	0.0029	0.081303	1032	25	1056	16	0.0721	0.0028
91500 - 17	1.87	0.087	0.1789	0.0032	0.27337	1062	31	1061	18	0.0756	0.0033
91500 - 18	1.818	0.08	0.178	0.0035	0.01927	1045	30	1056	19	0.0739	0.0034
SAMPLES											
WGC2019J-16J - 1	1.573	0.066	0.1602	0.0029	0.045159	954	26	958	16	0.0711	0.0031
WGC2019J-16J - 2	1.504	0.063	0.157	0.0037	0.086003	928	26	940	20	0.0695	0.0032
WGC2019J-16J - 3	1.457	0.076	0.1444	0.0026	-0.087405	905	32	869	15	0.0731	0.0042
WGC2019J-16J - 4	1.547	0.068	0.1546	0.0029	0.053826	943	27	926	16	0.0725	0.0033
WGC2019J-16J - 5	1.361	0.04	0.1409	0.002	0.23864	871	17	850	12	0.0699	0.002
WGC2019J-16J - 6	1.358	0.058	0.1273	0.0028	0.1892	867	25	772	16	0.0773	0.0033
WGC2019J-16J - 7	1.535	0.057	0.162	0.0023	0.034701	945	22	968	13	0.0684	0.0026
WGC2019J-16J - 8	1.536	0.061	0.1581	0.0022	0.10458	941	24	946	12	0.0701	0.0027
WGC2019J-16J - 9	1.589	0.058	0.1596	0.0026	0.14471	962	22	954	15	0.0719	0.0026
WGC2019J-16J - 10	1.439	0.055	0.1523	0.0031	0.17099	906	25	914	18	0.069	0.0029
WGC2019J-16J - 11	1.576	0.088	0.1617	0.0039	0.36318	955	34	966	22	0.0704	0.0037
WGC2019J-16J - 12	0.987	0.076	0.104	0.0026	0.2758	692	39	638	15	0.0684	0.005
WGC2019J-16J - 13	1.607	0.056	0.1572	0.003	0.38506	969	22	941	17	0.0737	0.0023
WGC2019J-16J - 14	1.533	0.087	0.1575	0.0037	-0.23748	937	35	942	21	0.0708	0.0046

WGC2019J-16J - 15	0.828	0.048	0.0977	0.0024	0.026183	609	26	601	14	0.0613	0.0037
WGC2019J-16J - 16	1.252	0.082	0.1369	0.0038	-0.017108	818	38	827	22	0.0665	0.0047
WGC2019J-16J - 17	2.152	0.08	0.1913	0.0037	0.19759	1163	26	1128	20	0.0811	0.003
WGC2019J-16J - 18	1.417	0.058	0.1492	0.0024	0.10011	891	24	896	13	0.0686	0.0028
WGC2019J-16J - 19	1.636	0.052	0.1624	0.0028	0.13888	981	20	970	16	0.0728	0.0024
WGC2019J-16J - 20	1.315	0.083	0.1302	0.0043	0.19192	848	36	789	24	0.073	0.0046
WGC2019J-16J - 21	1.74	0.071	0.1694	0.0029	0.27891	1018	26	1008	16	0.0741	0.0028
WGC2019J-16J - 22	1.75	0.24	0.1418	0.0049	0.33239	1001	84	855	28	0.089	0.011
WGC2019J-16J - 23	1.63	0.091	0.1645	0.0033	0.063082	972	35	982	18	0.0717	0.0041
WGC2019J-16J - 24	1.274	0.056	0.1336	0.0025	0.13261	829	25	808	14	0.0689	0.0031
WGC2019J-16J - 25	1.458	0.065	0.1469	0.0023	0.087617	907	27	883	13	0.0714	0.0032
WGC2019J-16J - 26	1.508	0.073	0.1549	0.003	0.29663	929	29	928	17	0.0699	0.0031
WGC2019J-16J - 27	1.345	0.047	0.1402	0.0025	0.24098	863	20	846	14	0.0692	0.0024
WGC2019J-16J - 28	1.532	0.057	0.1551	0.002	0.09063	939	23	929	11	0.0712	0.0026
WGC2019J-16J - 29	1.248	0.086	0.1242	0.0042	0.30279	817	39	754	24	0.0726	0.0049
WGC2019J-16J - 30	1.129	0.052	0.1182	0.0022	0.057241	762	24	720	13	0.0685	0.0031
WGC2019J-16J - 31	1.617	0.062	0.1623	0.0022	0.10053	972	24	969	12	0.0718	0.0027
WGC2019J-16J - 32	1.592	0.053	0.1611	0.0023	0.33124	963	21	963	13	0.0711	0.0021
WGC2019J-16J - 33	1.437	0.075	0.147	0.0032	-0.011563	898	32	884	18	0.0707	0.0039
WGC2019J-16J - 34	1.434	0.075	0.1487	0.0031	0.16809	898	31	893	17	0.0697	0.0036
WGC2019J-16J - 35	1.446	0.071	0.1569	0.0038	0.27614	908	32	939	21	0.0673	0.0034
WGC2019J-16J - 36	0.638	0.031	0.0776	0.0022	-0.1408	506	23	482	13	0.0595	0.0036
WGC2019J-16J - 37	1.529	0.075	0.1603	0.0029	0.056763	936	31	958	16	0.0689	0.0035
WGC2019J-16J - 38	1.663	0.08	0.1642	0.0033	0.12407	989	30	980	18	0.0731	0.0036
WGC2019J-16J - 39	1.619	0.073	0.1584	0.003	0.19396	971	28	948	17	0.0737	0.0032
WGC2019J-16J - 40	1.668	0.076	0.1625	0.0034	0.20117	991	29	970	19	0.0734	0.0031
WGC2019J-16J - 41	1.63	0.077	0.1593	0.0038	0.29336	978	30	953	21	0.0738	0.0034

WGC2019J-16J - 42	1.998	0.036	0.1841	0.0018	0.21997	1114.1	12	1089.1	9.8	0.0782	0.0012
WGC2019J-16J - 43	1.487	0.052	0.152	0.0019	-0.16546	922	21	912.1	11	0.0706	0.0026
WGC2019J-16J - 44	1.608	0.049	0.161	0.0022	-0.16347	971	19	962	12	0.0721	0.0024
WGC2019J-16J - 45	1.361	0.07	0.1413	0.0026	-0.012257	868	30	852	15	0.0699	0.0038
WGC2019J-16J - 46	1.554	0.077	0.1599	0.0029	0.13736	947	30	956	16	0.0701	0.0034
WGC2019J-16J - 47	1.512	0.042	0.156	0.0029	0.14219	938	19	934	16	0.0711	0.0024
WGC2019J-16J - 48	2.026	0.055	0.1812	0.0029	-0.056588	1123	18	1073	16	0.0807	0.0024
WGC2019J-16J - 49	1.591	0.091	0.1586	0.0036	0.13289	960	37	949	20	0.0725	0.0042
WGC2019J-16J - 50	1.496	0.093	0.1589	0.0039	0.16898	918	37	950	22	0.0681	0.0043
WGC2019J-16J - 51	1.605	0.073	0.1642	0.0033	0.097113	975	32	980	18	0.0712	0.0034
WGC2019J-17D - 1	1.669	0.074	0.1649	0.0027	-0.038273	990	28	984	15	0.0733	0.0034
WGC2019J-17D - 2	1.561	0.069	0.1535	0.0028	-0.056606	950	27	920	15	0.0737	0.0035
WGC2019J-17D - 3	1.652	0.063	0.1625	0.0031	0.091201	987	24	970	17	0.0736	0.0029
WGC2019J-17D - 4	1.86	0.16	0.1608	0.0054	0.27463	1057	58	961	30	0.0838	0.0074
WGC2019J-17D - 5	1.676	0.084	0.156	0.0031	0.34563	995	32	935	17	0.0776	0.0036
WGC2019J-17D - 6	1.588	0.061	0.1597	0.0026	0.35557	962	24	955	15	0.0718	0.0025
WGC2019J-17D - 7	1.937	0.081	0.1694	0.0038	-0.016702	1089	28	1008	21	0.083	0.0038
WGC2019J-17D - 8	1.556	0.055	0.1594	0.0028	0.17676	950	21	953	16	0.0705	0.0024
WGC2019J-17D - 9	1.561	0.069	0.1533	0.0024	0.49597	951	27	919	14	0.0737	0.0028
WGC2019J-17D - 10	1.647	0.054	0.1641	0.003	0.12938	986	21	979	17	0.0727	0.0024
WGC2019J-17D - 11	1.656	0.061	0.1651	0.0025	0.034887	989	24	985	14	0.0726	0.0027
WGC2019J-17D - 12	1.689	0.053	0.1675	0.0024	-0.17673	1007	22	998	13	0.0729	0.0026
WGC2019J-17D - 13	1.74	0.16	0.164	0.006	0.3009	994	58	977	33	0.077	0.0065
WGC2019J-17D - 14	1.698	0.083	0.1505	0.004	-0.012491	1001	32	903	22	0.0821	0.0044
WGC2019J-17D - 15	1.732	0.067	0.1648	0.0029	0.28938	1017	25	983	16	0.0759	0.0027
WGC2019J-17D - 16	1.72	0.12	0.1422	0.0036	0.1101	1011	46	857	20	0.0876	0.0065

WGC2019J-17D - 17	1.603	0.046	0.161	0.0025	0.21901	969	18	962	14	0.072	0.002
WGC2019J-17D - 18	1.547	0.054	0.1603	0.0024	0.24646	945	21	958	13	0.0697	0.0023
WGC2019J-17D - 19	1.678	0.098	0.1673	0.0032	-0.11482	994	37	997	18	0.0727	0.0046
WGC2019J-17D - 20	1.573	0.068	0.1487	0.0027	0.19529	953	27	894	15	0.0756	0.0031
WGC2019J-17D - 21	2.5	0.12	0.1629	0.0032	0.047082	1278	40	973	18	0.1108	0.0052
WGC2019J-17D - 22	1.519	0.068	0.1551	0.0029	0.18484	933	27	929	16	0.0708	0.0031
WGC2019J-17D - 23	1.602	0.055	0.1613	0.0027	0.18624	968	22	964	15	0.0718	0.0024
WGC2019J-17D - 24	1.605	0.051	0.1627	0.0026	0.17594	969	20	971	14	0.0709	0.0022
WGC2019J-17D - 25	1.65	0.063	0.1668	0.0028	0.27709	985	24	994	16	0.0717	0.0026
WGC2019J-17D - 26	1.523	0.055	0.1523	0.0027	-0.018475	935	22	913	15	0.0719	0.0027
WGC2019J-17D - 27	1.68	0.053	0.151	0.003	0.11195	998	20	906	17	0.0807	0.0028
WGC2019J-17D - 28	1.621	0.07	0.1616	0.0029	0.12575	979	29	965	16	0.0733	0.0035
WGC2019J-17D - 29	4.6	0.84	0.1783	0.0083	0.88146	1610	140	1056	45	0.174	0.025
WGC2019J-17D - 30	1.584	0.068	0.1598	0.0035	0.025501	959	27	955	19	0.0719	0.0033
WGC2019J-17D - 31	1.709	0.06	0.163	0.0025	0.40132	1012	24	973	14	0.0761	0.0025
WGC2019J-17D - 32	1.748	0.087	0.1734	0.0041	-0.010849	1022	33	1031	23	0.0731	0.0041
WGC2019J-17D - 33	1.697	0.057	0.1654	0.0023	0.065533	1007	20	987	13	0.0741	0.0026
WGC2019J-17D - 34	1.699	0.054	0.1625	0.0024	-0.024182	1006	20	970	13	0.0756	0.0025
WGC2019J-17D - 35	1.569	0.053	0.1606	0.0026	-0.10149	955	21	960	14	0.0707	0.0026
WGC2019J-17D - 36	1.692	0.098	0.1537	0.0035	0.40931	1000	37	921	19	0.0787	0.0038
WGC2019J-17D - 37	2.21	0.13	0.1772	0.0028	0.27659	1187	44	1052	15	0.09	0.0049
WGC2019J-17D - 38	1.6	0.045	0.154	0.0023	0.18452	968	18	923	13	0.075	0.002
WGC2019J-17D - 39	1.549	0.061	0.1543	0.0025	0.085344	946	24	925	14	0.0726	0.0029
WGC2019J-17D - 40	1.685	0.062	0.1612	0.0031	0.15228	1006	26	963	17	0.0764	0.0031
WGC2019J-17D - 41	1.655	0.067	0.1643	0.0031	0.16822	987	26	980	17	0.0728	0.0029
WGC2019J-17D - 42	1.698	0.065	0.1608	0.0032	0.29004	1003	25	961	18	0.0763	0.0028
WGC2019J-17D - 43	1.615	0.068	0.1616	0.0027	0.12353	971	26	965	15	0.0725	0.0031

WGC2019J-17D - 44	1.639	0.073	0.1635	0.0031	-0.02123	984	27	976	17	0.0727	0.0035
WGC2019J-17D - 45	1.463	0.056	0.1467	0.0022	0.056705	911	23	882	13	0.072	0.0028
WGC2019J-17D - 46	1.609	0.07	0.1635	0.0024	0.38996	968	27	976	14	0.0707	0.0027
WGC2019J-17D - 47	1.594	0.054	0.1614	0.0034	0.33957	966	21	964	19	0.0713	0.0022
WGC2019J-17D - 48	1.75	0.072	0.1637	0.0028	0.16147	1023	27	977	15	0.0773	0.0032
WGC2019J-17D - 49	1.618	0.072	0.1612	0.0034	0.14436	972	28	963	19	0.0727	0.0034
WGC2019-15 - 1	1.476	0.034	0.1481	0.0018	0.45549	919	14	890	10	0.0721	0.0014
WGC2019-15 - 2	1.683	0.028	0.1682	0.0019	0.33985	1001.4	11	1001.9	10	0.0724	0.001
WGC2019-15 - 3	1.629	0.061	0.1651	0.0027	0.25953	983	22	985	15	0.0714	0.0025
WGC2019-15 - 4	2.135	0.071	0.1923	0.0037	0.6313	1160	22	1133	20	0.0802	0.002
WGC2019-15 - 5	1.578	0.034	0.1586	0.0019	0.24333	960	14	948.9	10	0.0719	0.0014
WGC2019-15 - 6	2.715	0.079	0.2121	0.0042	0.13289	1330	22	1240	23	0.0928	0.0029
WGC2019-15 - 7	1.199	0.024	0.1241	0.0017	0.59991	799.3	11	754.2	9.6	0.0701	0.0011
WGC2019-15 - 8	1.095	0.032	0.1164	0.0023	0.78241	750	16	710	13	0.068	0.0012
WGC2019-15 - 9	1.072	0.022	0.1128	0.0016	0.71224	740.8	10	688.6	9.2	0.06894	0.0009
WGC2019-15 - 10	1.64	0.029	0.164	0.0016	0.22693	984.8	11	978.8	8.7	0.0723	0.0011
WGC2019-15 - 11	1.68	0.039	0.166	0.0018	0.37936	1003	13	989.9	10	0.0732	0.0014
WGC2019-15 - 12	1.422	0.031	0.138	0.0019	0.1267	898	13	833	11	0.0752	0.0019
WGC2019-15 - 13	1.51	0.045	0.1466	0.0024	0.44884	933	18	882	14	0.0741	0.0019
WGC2019-15 - 14	1.532	0.056	0.1492	0.003	0.23193	941	22	897	17	0.0743	0.0027
WGC2019-15 - 15	1.452	0.046	0.1388	0.0029	0.76123	909	19	837	16	0.0752	0.0014
WGC2019-15 - 16	1.531	0.042	0.1469	0.0029	0.1669	942	17	883	16	0.0754	0.0023
WGC2019-15 - 17	3.268	0.077	0.2574	0.0031	0.20155	1472	18	1477	16	0.0917	0.002
WGC2019-15 - 18	2.039	0.1	0.1866	0.0052	0.74701	1124	34	1103	28	0.0788	0.0027
WGC2019-15 - 19	1.611	0.037	0.1554	0.0017	0.26574	973	14	930.9	9.7	0.0745	0.0015
WGC2019-15 - 20	1.778	0.044	0.1712	0.0027	0.45831	1037	16	1019	15	0.0751	0.0016

WGC2019-15 - 21	1.606	0.033	0.1596	0.002	0.46046	972	13	954	11	0.0728	0.0012
WGC2019-15 - 22	1.544	0.028	0.1556	0.0018	0.44463	947.6	11	932.2	10	0.0717	0.001
WGC2019-15 - 23	1.661	0.044	0.1618	0.0022	0.18075	992	17	966	12	0.0743	0.0019
WGC2019-15 - 24	1.511	0.04	0.1551	0.0016	0.36256	933	16	929.4	8.9	0.0704	0.0016
WGC2019-15 - 25	1.57	0.033	0.1562	0.0021	0.53963	958	13	936	12	0.073	0.0013
WGC2019-15 - 26	2.695	0.095	0.1647	0.0025	0.62025	1325	26	983	14	0.1181	0.0034
WGC2019-15 - 27	2.34	0.26	0.1954	0.0074	0.59126	1224	77	1150	40	0.0861	0.0077
WGC2019-15 - 28	1.748	0.048	0.1622	0.0025	0.56065	1027	18	969	14	0.0779	0.0015
WGC2019-15 - 29	1.232	0.036	0.1284	0.0019	0.62091	818	18	778.7	11	0.0698	0.0017
WGC2019-15 - 30	1.512	0.048	0.1507	0.0028	0.67386	934	19	905	16	0.0724	0.0016
WGC2019-15 - 31	2.08	0.12	0.1686	0.0031	0.049836	1135	40	1004	17	0.0894	0.0052
WGC2019-15 - 32	1.762	0.035	0.1715	0.0023	0.48163	1030	13	1020	12	0.0742	0.0012
WGC2019-15 - 33	1.631	0.038	0.1581	0.0019	0.37988	981	15	945.9	10	0.0746	0.0014
WGC2019-15 - 34	1.5	0.11	0.1439	0.009	0.47389	922	46	865	50	0.0764	0.0062
WGC2019-15 - 35	1.331	0.051	0.1354	0.003	0.73959	858	22	818	17	0.0709	0.0018
WGC2019-15 - 36	1.582	0.025	0.158	0.0015	0.57671	962.6	9.8	945.6	8.1	0.07231	0.0007
WGC2019-15 - 37	1.044	0.028	0.1134	0.0015	0.23583	727	15	692.5	8.8	0.0667	0.0018
WGC2019-15 - 38	1.595	0.033	0.1578	0.0021	0.64056	968	13	944	12	0.0728	0.001
WGC2019-15 - 39	1.421	0.046	0.148	0.0024	0.3372	896	19	890	13	0.0694	0.002
WGC2019-15 - 40	1.652	0.027	0.1645	0.0016	0.56745	989.8	10	981.4	8.9	0.07241	0.00077
WGC2019-15 - 41	2.507	0.075	0.2078	0.0034	0.43292	1272	22	1217	18	0.0873	0.0022
WGC2019-15 - 42	0.791	0.026	0.0912	0.0016	0.48183	590	15	562.5	9.6	0.0627	0.0017
WGC2019-15 - 43	1.241	0.036	0.1211	0.002	0.3427	818	16	737	11	0.0735	0.0017
WGC2019-15 - 44	1.517	0.033	0.1502	0.0016	0.080724	937	13	902.2	9	0.073	0.0015
WGC2019-15 - 45	1.665	0.037	0.1648	0.002	0.22012	996	13	983.2	11	0.073	0.0015
WGC2019-15 - 46	1.288	0.029	0.1321	0.0025	0.73156	840	13	799	14	0.0704	0.00094
WGC2019-15 - 47	0.627	0.027	0.0766	0.0012	-0.063273	493	17	476	7	0.0591	0.0026

WGC2019-15 - 48	1.337	0.04	0.138	0.0021	0.747	861	17	833	12	0.0696	0.0015
WGC2019-15 - 49	0.849	0.024	0.0951	0.0026	0.77427	627	15	586	15	0.065	0.0012
WGC2019-15 - 50	1.262	0.044	0.1284	0.0019	0.1531	826	20	778.4	11	0.0709	0.0024
WGC2019-15 - 51	0.625	0.034	0.0727	0.0041	0.91737	491	22	452	24	0.0623	0.0013
WGC2019-15 - 52	1.585	0.03	0.1583	0.0018	0.20493	963.9	12	947.1	10	0.0724	0.0012
WGC2019-15 - 53	1.254	0.042	0.1289	0.0021	0.42648	824	19	781	12	0.0702	0.002
WGC2019-15 - 54	1.547	0.031	0.1545	0.0018	0.43962	949	13	926	10	0.0723	0.0012
WGC2019-15 - 55	1.634	0.088	0.1645	0.0041	0.1472	980	33	982	23	0.0721	0.0042
WGC2019-15 - 56	1.511	0.04	0.1505	0.0027	0.59924	936	17	903	15	0.0733	0.0016
WGC2019-15 - 57	1.517	0.032	0.1554	0.0018	0.25472	936	13	930.9	10	0.0702	0.0015
WGC2019-15 - 58	1.513	0.043	0.1488	0.0019	0.18857	933	18	894.1	11	0.0735	0.002
WGC2019-15 - 59	1.246	0.043	0.1301	0.0039	0.75337	821	19	788	22	0.0692	0.0015
WGC2019-15 - 60	1.606	0.032	0.1624	0.0021	0.46723	972	12	970	11	0.0714	0.0011

Appendix 9: Extended Mineral Equilibria Modelling Methods

Concerning Oxidation State

Iron (Fe) exists in two different oxide forms: FeO (Fe^{2+}, reduced, ferrous) and Fe_2O_3 (Fe^{3+}, oxidised, ferric). It is vital to be able to differentiate between these two different oxides in order to produce accurate *P–T* diagrams. This is because oxidation state heavily impacts how rocks react to changing *P–T* environments – and therefore how we model them in *P–T* diagrams, in which we aim to 'fix' rocks in compositional space (Johnson & White, 2011).

In order to 'fix' a rock *correctly* in *P–T* space, it is necessary to first create a PMo (or P-X) diagram. In this instance we fix the rock at a specific temperature and vary pressure and oxidation state. If one is uncertain of the oxidation state, then this means that when the PMo is created it becomes more time-consuming to calculate mineral behaviour over a wider range in oxidation states.

The first order solution to this problem is to simply use geochemical assays. Rocks can be powdered using standard equipment and sent away for analysis, during which ferrous iron (reduced) is oxidised. Although companies such as Bureau Veritas (BV) are the industry standard for doing so, their method of analysis can produce unreliable results which impact *P–T* modelling (as already discussed).

$$Fe_2O_3 = Fe_2O_{3(analysed)} - (FeO \times 1.111)$$

e.g. for sample 16J, $Fe_2O_3 = 19.6 - (9.2 \times 1.111) = 9.2$ wt% FeO and 9.4 wt% Fe_2O_3

In order to fix this problem, we require probe data. Acquiring probe data from minerals within each sample allows for a more direct method of calculating FeO:Fe_2O_3 ratios. This is because it allows us to recalculate cations into the mineral formulae, giving us a stoichiometric estimate of Fe_2O_3 in the rock.

This study faced extensive issues due to the presence of finely grained symplectites. Rock bulk compositions can ordinarily be easily calculated using the following method:

1. Take backscatter electron (BSE) image of the thin section, using the FEI Quanta600 at Adelaide Microscopy and either the GXMaps (high resolution but longer time frame) or XMOD (little extra information but designed for modal mineralogy determination) software to determine the modal mineralogy of each sample after identifying each mineral based on spectral analysis.
2. Take probe data of each mineral (~6 spots per mineral is a good rule of thumb) in order to determine the amount of each oxide within that mineral. The caveat to this is that the probe only provides data for FeO, not Fe_2O_3.
3. Feeding these probe analyses through a program/spreadsheet (e.g. AX62, or using the Droop 1987 method) to split the detected Fe into its ferrous and ferric components. These programs/spreadsheets recast mineral compositions into the oxides required for *P–T* modelling.

4. Creating idealised mineral compositions by averaging the best probe analyses. These form the basis of the *P–T* diagram. At this stage, several modifications may be made as certain minerals are removed from consideration (e.g. apatite, biotite) and the wt% of water calculated from the totals of hydrous minerals (e.g. biotite, chlorite) minus F and Cl contents.
5. Multiplying the percentage of each oxide in the mineral by the percentage of mineral in the rock, one can then determine the amount of each oxide within the rock.
6. Converting these values (which are in wt%) to volume percent (as the thin section image represents a 3D structure rather than a 2D slice), or even just straight to mol%. Mol% is the input required for THERMOCALC.

The presence of symplectites in the mafic samples (WGC2019J-16J, -17D) meant that a thin section image in which modal mineralogies were automatically calculated could not be created. Photoshop was instead used to manually pick apart each sample. Provided that the chemistry of the minerals constituting the symplectites are accurately known it is possible to determine the original chemistry of the peak metamorphic minerals which had broken down to form said symplectites. In reality, the compositions of the symplectites were simplified due to time constraints into several components: clinopyroxene (omphacite), amphibole and small amounts of iron oxides (magnetite). On the microprobe, however, it could be seen that these symplectites were likely zoned beyond the resolution of current analytical techniques.

Concerning THERMOCALC

The calculation of mineral forward equilibria models is time intensive. The user is required to identify stable assemblages and understand how these change as rocks undergo variations in pressure, temperature, mineral composition, water content and oxidation state. Each model can involve more than 300+ individual calculations and take several months to build. These models can be visualised as a minimum five-dimensional physical object. As such it is desirable to 'fix' several of these dimensions (typically water content, oxidation state and mineral composition) to create a more readily interpretable P-T pseudosection. THERMOCALC is a freely available software that comes in various versions; v3.40 and v3.45 were used in this study. The implementation of THERMOCALC also requires a supplementary program, drawpad, which again is available in different versions. The user must remain aware that only certain versions of THERMOCALC are compatible with certain versions of drawpad.

Prior to commencing THERMOCALC mineral equilibria forward modelling, a stable assemblage must be located. This is generally done by using petrological observations to infer a peak mineral assemblage within the rock. After this, a Gibbs free energy minimisation calculation ('dogmin' calculation) is typically conducted at a set temperature over a constrained pressure range. 'Dogmin' calculations work well in felsic rocks but poorly in mafic ones. They also frequently produce erroneous results, and hence the user must use the given outputs with caution. Once a stable assemblage has been established, it is up to the user to input this assemblage into THERMOCALC.

THERMOCALC then draws a line that represents where a phase within that assemblage (as specified by the user) approaches zero abundance, or where a new phase enters the assemblage. The intersection of two lines forms a point, which is surrounded by four stable fields. THERMOCALC cannot specify an exact point where two phases equal zero, so each point must be calculated manually by selecting a line (where one phase is at zero abundance) and then calculating this line across a very small pressure (or temperature) range until a second phase reaches on the order of 10^{-6} or less. THERMOCALC often fails to calculate lines that are (a) nearly vertical or (b) nearly horizontal, so the user must change their approach to suit this. Some lines can be calculated by changing 'calculations done at P' to 'calculations done at T' when prompted by the program.

It is necessary to understand how stable metamorphic assemblages vary across *P–T* space in order to successfully calculate a diagram, as missed phases can prove a time-costly exercise. By incorrectly calculating a mineral assemblage, the user can effectively calculate hundreds of assemblages that THERMOCALC believes are stable but are in fact metastable. When using THERMOCALC, it is often necessary to update 'starting guesses'. 'Starting guesses' are the compositional variables of phases that THERMOCALC uses to calculate lines or points. This process uses an iterative least-squares calculation. Starting guesses must be frequently updated as the user moves across the diagram. Often, THERMOCALC will not recognise a stable line that the user knows exists based on (a) extensive evidence and (b) the existence of other lines indicating that a reaction must be present. Altering starting guesses is often the only way around this issue. Once a mineral equilibria model (either *P–X* or *P–T*) is completed, it is important to determine whether or not the calculated mineral assemblages are stable. It is often possible to completely calculate a metastable diagram. Mineral equilibria models can be inputted into the program TCInvestigator (Pearce et al., 2015) in order to do this. Input requirements include the completed mineral equilibria model and several executable (.exe) files. TCInvestigator, like THERMOCALC, is a program that is constantly updated. Although a more recent version (TCInvestigator v2.0) exists, v1.0 was used in this study due to compatibility issues.

Appendix 10: Rutile Zirconium-In-Rutile Geothermometry

Zr-in-rutile geothermometry was calculated using Zr (ppm) concentrations in WGC2019J-16J. The equation from Tomkins et al. (2007) was utilised:

$$T\ (°C) = \frac{83.9+6.410P}{0.1428-Rln\varphi} - 273$$, where ϕ = Zr (ppm) and P = pressure in kbar.

Zr (ppm) concentrations with 2σ errors are also shown for data run and standard.

Source file	Zr (ppm)	2σ	T (°C) at 8.3kbar	2σ	T (°C) at 20.5kbar	2σ	T (°C) at 28kbar	2σ
NIST610 - 1	446.80	4.10						
NIST610 - 2	447.20	4.10						
NIST610 - 3	449.20	4.20						
NIST610 - 4	448.30	4.10						
NIST610 - 5	450.50	4.20						
NIST610 - 6	445.20	4.60						
NIST610 - 7	449.40	4.50						
NIST610 - 8	450.90	4.60						
NIST610 - 9	445.20	4.10						
NIST610 - 10	444.70	4.00						
NIST610 - 11	448.30	4.20						
NIST610 - 12	451.00	4.10						
NIST610 - 13	450.80	4.10						
NIST610 - 14	446.80	4.40						
NIST610 - 15	448.10	4.20						
NIST610 - 16	447.20	4.60						
NIST610 - 17	444.80	4.70						
NIST610 - 18	449.30	4.90						
WGC2019J-16J_New - 1	137.70	1.50	584.16	34.79	633.28	34.83	663.47	34.86
WGC2019J-16J_New - 2	140.50	2.30	585.58	35.18	634.77	35.25	665.01	35.29
WGC2019J-16J_New - 3	155.50	1.40	592.76	34.71	642.36	34.74	672.85	34.77
WGC2019J-16J_New - 4	130.00	1.40	580.16	34.75	629.04	34.80	659.09	34.82
WGC2019J-16J_New - 5	133.60	1.30	582.05	34.69	631.04	34.73	661.16	34.76
WGC2019J-16J_New - 6	141.80	1.10	586.22	34.58	635.45	34.61	665.71	34.63
WGC2019J-16J_New - 7	146.00	41.00	588.28	56.61	637.63	57.91	667.96	58.71
WGC2019J-16J_New - 8	123.00	1.10	576.34	34.60	625.00	34.64	654.92	34.66
WGC2019J-16J_New - 9	189.50	3.20	607.11	35.38	657.53	35.45	688.53	35.50
WGC2019J-16J_Old - 1	111.20	6.60	569.46	38.05	617.73	38.29	647.41	38.43

WGC2019J-16J_Old - 2	60.30	2.60	530.03	36.46	576.04	36.61	604.33	36.71
WGC2019J-16J_Old - 3	122.40	1.20	576.00	34.66	624.64	34.70	654.55	34.72
WGC2019J-16J_Old - 4	126.90	1.20	578.49	34.65	627.27	34.69	657.26	34.71
WGC2019J-16J_Old - 5	121.60	1.40	575.55	34.77	624.17	34.82	654.06	34.85
WGC2019J-16J_Old - 6	150.70	1.50	590.52	34.76	640.00	34.80	670.41	34.83
WGC2019J-16J_Old - 7	133.70	2.30	582.11	35.22	631.10	35.29	661.22	35.33
WGC2019J-16J_Old - 8	143.50	2.50	587.06	35.27	636.34	35.34	666.63	35.38
WGC2019J-16J_Old - 9	117.50	1.40	573.21	34.79	621.69	34.83	651.49	34.86
WGC2019J-16J_Old - 10	157.70	3.00	593.76	35.44	643.42	35.51	673.95	35.56
WGC2019J-16J_Old - 11	177.40	7.50	602.26	37.24	652.41	37.42	683.24	37.53
WGC2019J-16J_Old - 12	119.10	1.30	574.13	34.72	622.67	34.77	652.50	34.79
WGC2019J-16J_Old - 13	74.50	2.80	543.23	36.25	590.00	36.38	618.75	36.47
WGC2019J-16J_Old - 14	142.20	1.50	586.42	34.78	635.66	34.82	665.93	34.85
WGC2019J-16J_Old - 15	136.50	2.00	583.55	35.05	632.63	35.11	662.80	35.14
WGC2019J-16J_Old - 16	166.30	1.80	597.58	34.87	647.46	34.91	678.12	34.94
WGC2019J-16J_Old - 17	135.50	1.80	583.04	34.95	632.09	35.00	662.24	35.03
WGC2019J-16J_Old - 18	96.90	4.20	560.26	36.82	608.00	36.99	637.35	37.09
WGC2019J-16J_Old - 19	124.30	1.30	577.06	34.71	625.76	34.75	655.70	34.78
WGC2019J-16J_TS - 1	126.20	1.10	578.11	34.60	626.87	34.63	656.85	34.65
WGC2019J-16J_TS - 2	116.30	1.20	572.51	34.67	620.95	34.71	650.73	34.74
WGC2019J-16J_TS - 3	123.80	1.10	576.78	34.60	625.47	34.64	655.40	34.66
WGC2019J-16J_TS - 4	135.10	1.10	582.83	34.59	631.87	34.62	662.01	34.64
WGC2019J-16J_TS - 5	103.40	1.30	564.58	34.77	612.57	34.82	642.07	34.85
WGC2019J-16J_TS - 6	115.10	1.10	571.80	34.62	620.20	34.65	649.96	34.68
WGC2019J-16J_TS - 7	117.70	1.40	573.32	34.79	621.81	34.83	651.62	34.86
WGC2019J-16J_TS - 8	143.20	1.60	586.91	34.83	636.18	34.87	666.47	34.90
WGC2019J-16J_TS - 9	108.13	0.92	567.58	34.52	615.74	34.55	645.34	34.57
WGC2019J-16J_TS - 10	126.40	1.20	578.21	34.65	626.98	34.69	656.97	34.71
WGC2019J-16J_TS - 11	111.40	0.89	569.59	34.50	617.86	34.53	647.54	34.55
WGC2019J-16J_TS - 12	117.60	1.10	573.26	34.61	621.75	34.65	651.56	34.67
WGC2019J-16J_TS - 13	144.50	1.20	587.55	34.63	636.86	34.66	667.17	34.68
WGC2019J-16J_TS - 14	123.60	1.10	576.67	34.60	625.35	34.64	655.28	34.66
WGC2019J-16J_TS - 15	115.00	1.20	571.74	34.68	620.14	34.72	649.89	34.74
WGC2019J-16J_TS - 16	126.40	1.00	578.21	34.54	626.98	34.57	656.97	34.59
WGC2019J-16J_TS - 17	127.30	1.20	578.70	34.65	627.50	34.69	657.50	34.71
WGC2019J-16J_TS - 18	152.20	1.80	591.23	34.90	640.74	34.95	671.18	34.98
WGC2019J-16J_TS - 19	107.07	0.98	566.91	34.56	615.04	34.59	644.62	34.62
WGC2019J-16J_TS - 20	106.50	1.20	566.56	34.70	614.66	34.74	644.23	34.77
WGC2019J-16J_TS - 21	125.70	1.90	577.83	35.04	626.58	35.10	656.55	35.14
WGC2019J-16J_TS - 22	114.10	1.10	571.21	34.62	619.58	34.66	649.31	34.68
WGC2019J-16J_TS - 23	108.04	0.95	567.52	34.54	615.68	34.57	645.28	34.59

WGC2019J-16J_TS - 24	127.90	1.80	579.03	34.98	627.85	35.03	657.86	35.07
WGC2019J-16J_TS - 25	178.60	4.60	602.76	36.01	652.93	36.11	683.78	36.18
WGC2019J-16J_TS - 26	121.50	1.30	575.49	34.72	624.11	34.76	654.00	34.79
WGC2019J-16J_TS - 27	157.70	2.20	593.76	35.07	643.42	35.13	673.95	35.16
WGC2019J-16J_TS - 28	149.30	1.20	589.86	34.62	639.30	34.65	669.69	34.67
WGC2019J-16J_TS - 29	125.60	1.30	577.78	34.71	626.52	34.75	656.49	34.78
WGC2019J-16J_TS - 30	112.40	1.20	570.19	34.68	618.50	34.72	648.20	34.75
WGC2019J-16J_TS - 31	115.10	1.50	571.80	34.85	620.20	34.90	649.96	34.94
WGC2019J-16J_TS - 32	119.40	2.20	574.30	35.24	622.85	35.32	652.69	35.36
WGC2019J-16J_TS - 33	110.92	0.95	569.29	34.53	617.55	34.57	647.22	34.59
WGC2019J-16J_TS - 34	130.30	1.10	580.32	34.59	629.21	34.63	659.26	34.65
WGC2019J-16J_TS - 35	106.00	1.20	566.24	34.70	614.32	34.74	643.88	34.77
WGC2019J-16J_TS - 36	103.70	1.10	564.77	34.64	612.77	34.68	642.28	34.71
WGC2019J-16J_TS - 37	102.80	1.80	564.19	35.10	612.16	35.17	641.64	35.21
WGC2019J-16J_TS - 38	103.90	1.00	564.90	34.58	612.91	34.62	642.42	34.64
WGC2019J-16J_TS - 39	108.80	1.10	567.99	34.63	616.18	34.67	645.80	34.69
WGC2019J-16J_TS - 40	132.83	0.92	581.65	34.49	630.62	34.52	660.72	34.54
WGC2019J-16J_TS - 41	111.80	1.10	569.83	34.62	618.12	34.66	647.80	34.69
WGC2019J-16J_TS - 42	111.70	1.00	569.77	34.56	618.05	34.60	647.74	34.62
WGC2019J-16J_TS - 43	110.90	1.30	569.28	34.75	617.54	34.79	647.21	34.82
WGC2019J-16J_TS - 44	113.40	1.10	570.79	34.62	619.14	34.66	648.86	34.68
WGC2019J-16J_TS - 45	115.60	2.20	572.10	35.27	620.52	35.34	650.28	35.39
WGC2019J-16J_TS - 46	122.28	0.88	575.93	34.48	624.57	34.51	654.47	34.53
WGC2019J-16J_TS - 47	125.96	0.94	577.97	34.51	626.73	34.54	656.70	34.56
WGC2019J-16J_TS - 48	99.75	0.77	562.18	34.43	610.03	34.46	639.45	34.48
WGC2019J-16J_TS - 49	100.15	0.86	562.45	34.49	610.32	34.53	639.74	34.55
WGC2019J-16J_TS - 50	107.79	0.92	567.36	34.52	615.51	34.55	645.11	34.57
WGC2019J-16J_TS - 51	114.10	1.00	571.21	34.56	619.58	34.59	649.31	34.61
WGC2019J-16J_TS - 52	144.10	3.20	587.36	35.61	636.65	35.70	666.95	35.76
WGC2019J-16J_TS - 53	113.70	1.10	570.97	34.62	619.32	34.66	649.05	34.68
WGC2019J-16J_TS - 54	124.20	1.80	577.00	34.99	625.71	35.05	655.64	35.08
WGC2019J-16J_TS - 55	147.30	3.40	588.91	35.69	638.29	35.78	668.65	35.84
WGC2019J-16J_TS - 56	105.80	1.20	566.11	34.70	614.19	34.75	643.75	34.77
WGC2019J-16J_TS - 57	117.70	1.10	573.32	34.61	621.81	34.65	651.62	34.67
WGC2019J-16J_TS - 58	127.55	0.98	578.84	34.53	627.65	34.56	657.65	34.58
WGC2019J-16J_TS - 59	116.60	1.30	572.68	34.73	621.13	34.77	650.92	34.80
WGC2019J-16J_TS - 60	128.91	0.89	579.57	34.48	628.42	34.51	658.45	34.53
WGC2019J-16J_TS - 61	124.10	1.30	576.95	34.71	625.65	34.75	655.58	34.78
WGC2019J-16J_TS - 62	134.20	2.30	582.37	35.21	631.37	35.28	661.50	35.33
WGC2019J-16J_TS - 63	155.20	1.60	592.62	34.80	642.21	34.84	672.70	34.87
WGC2019J-16J_TS - 64	109.40	1.50	568.36	34.88	616.57	34.93	646.20	34.96

WGC2019J-16J_TS - 65	112.33	0.82	570.15	34.45	618.46	34.48	648.15	34.50
WGC2019J-16J_TS - 66	101.90	1.40	563.60	34.85	611.53	34.90	641.00	34.93
WGC2019J-16J_TS - 67	222.40	2.10	619.08	34.90	670.19	34.95	701.61	34.97
WGC2019J-16J_TS - 68	108.84	0.91	568.02	34.51	616.20	34.54	645.83	34.56
WGC2019J-16J_TS - 69	139.80	1.60	585.22	34.83	634.40	34.88	664.63	34.91
WGC2019J-16J_TS - 70	128.30	1.00	579.25	34.54	628.07	34.57	658.09	34.59
WGC2019J-16J_TS - 71	139.60	1.10	585.12	34.58	634.29	34.61	664.52	34.63
WGC2019J-16J_TS - 72	115.50	1.60	572.04	34.91	620.45	34.97	650.22	35.00
WGC2019J-16J_TS - 73	214.80	7.50	616.45	36.83	667.41	36.99	698.74	37.08
WGC2019J-16J_TS - 74	151.00	1.60	590.67	34.81	640.15	34.85	670.57	34.88
WGC2019J-16J_TS - 75	133.80	1.20	582.16	34.64	631.15	34.68	661.28	34.70
WGC2019J-16J_TS - 76	127.30	1.10	578.70	34.60	627.50	34.63	657.50	34.65
WGC2019J-16J_TS - 77	136.10	1.10	583.35	34.59	632.41	34.62	662.57	34.64
WGC2019J-16J_TS - 78	106.48	0.98	566.54	34.56	614.64	34.60	644.21	34.62
WGC2019J-16J_TS - 79	171.00	1.60	599.59	34.78	649.59	34.81	680.32	34.84

Appendix 11: Extended TCInvestigator Outputs

Relevant mineral modal proportions and parameters, as modelled in THERMOCALC, are presented. Note that various parameters involving amphibole include both glaucophane and hornblende as these two amphiboles exist in solid solution in some fields.

TCInvestigator produces outputs in '1-atom-normalised' mol%, referred to in-text as 'mol%' for clarity. The main results included in Figures 13 and 15 were cannibalised from the following TCInvestigator and placed together in the main text.

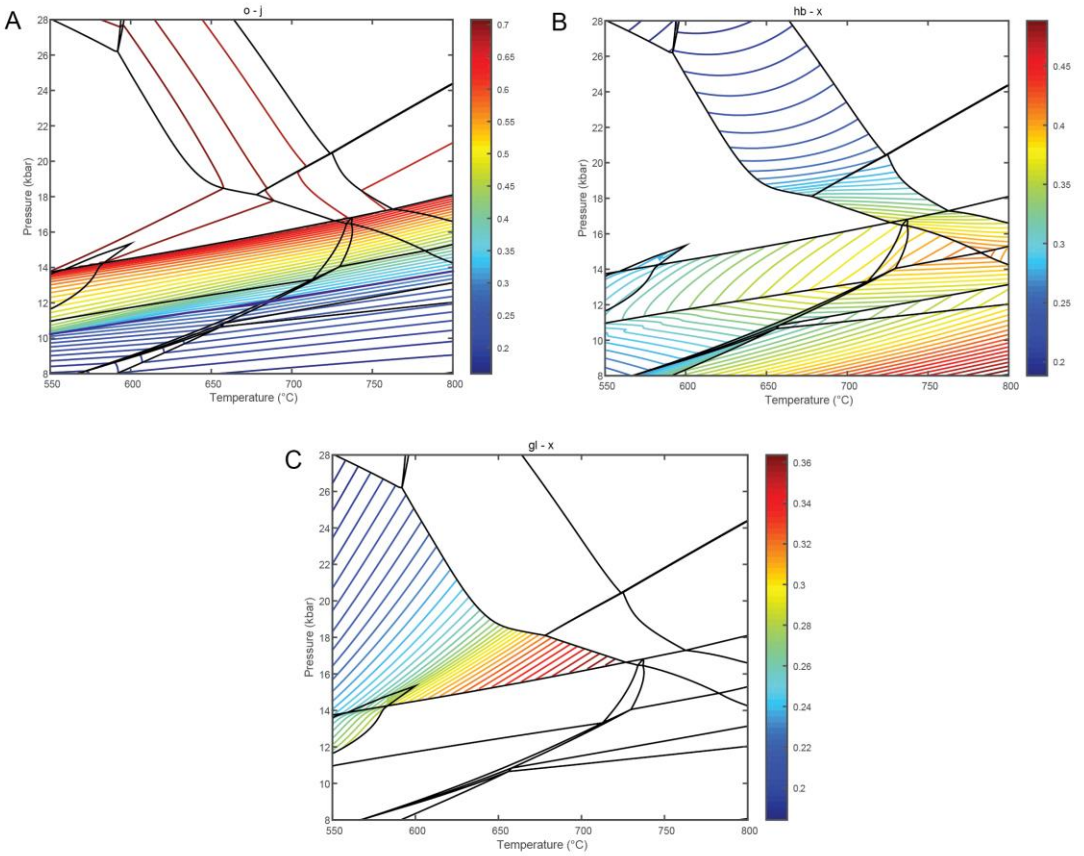

TCInvestigator outputs for mafic eclogite WGC2019J-16J, showing (a) omphacite M2 site Na, (b) hornblende XFe, and (c) glaucophane XFe (as defined by THERMOCALC, XFe = Fe2+ /(Fe2+ + Mg)). Temperature (°C) is shown on the x axis; pressure (kbar) on the y axis; colour scale and modal proportions indicated to the right of each individual output.

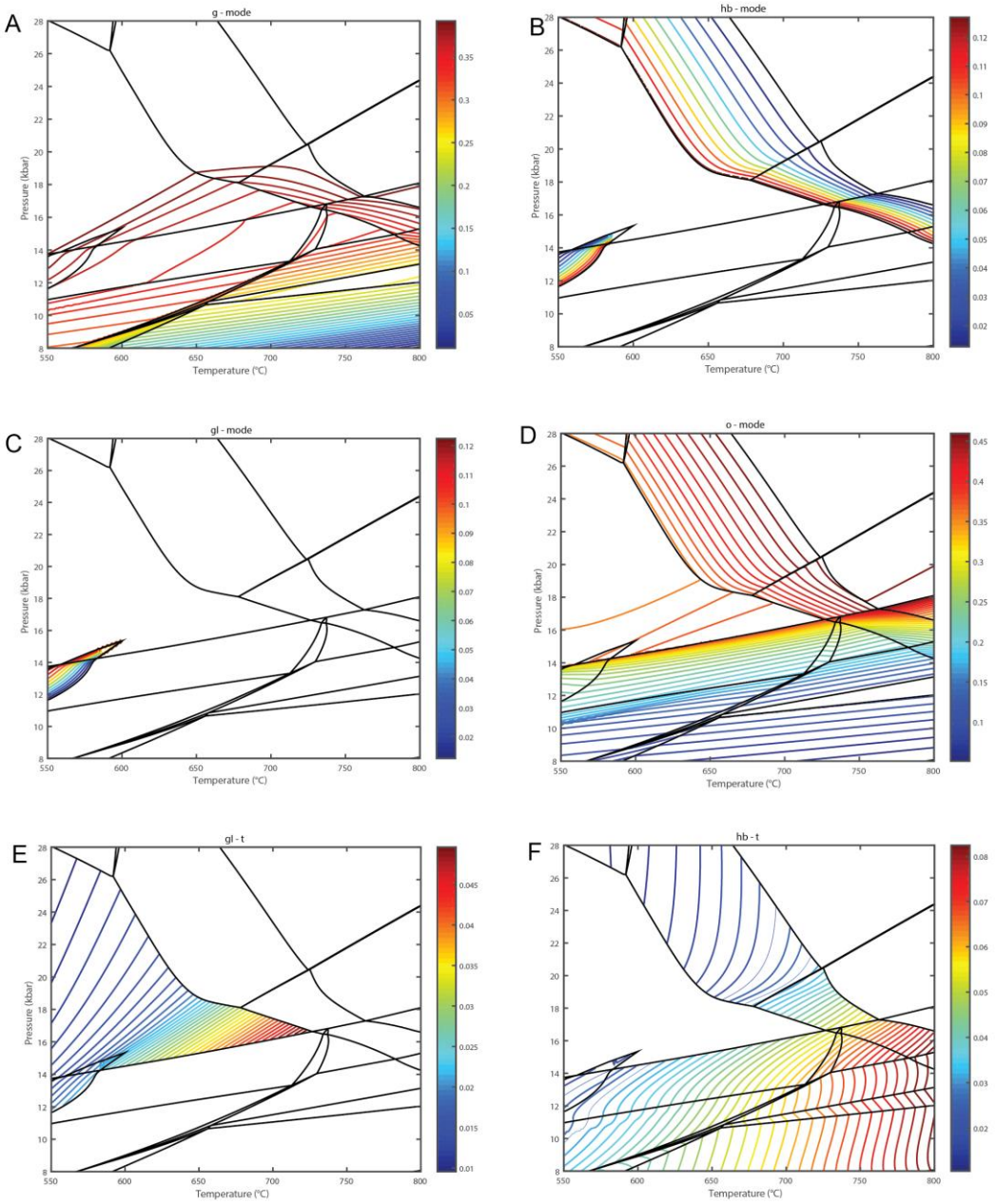

TCInvestigator outputs for mafic eclogite WGC2019J-16J, showing (a) garnet mode, (b) hornblende mode, (c) glaucophane mode, (d) omphacite mode, (e) glaucophane Ti concentrations, (f) hornblende Ti concentrations. Note that due to amphibole solvus, parameters used to constrain peak conditions involved combining hornblende (hb) and glaucophane (gl) readouts. Temperature (°C) is shown on the x axis; pressure (kbar) on the y axis; colour scale and modal proportions indicated to the right of each individual output.

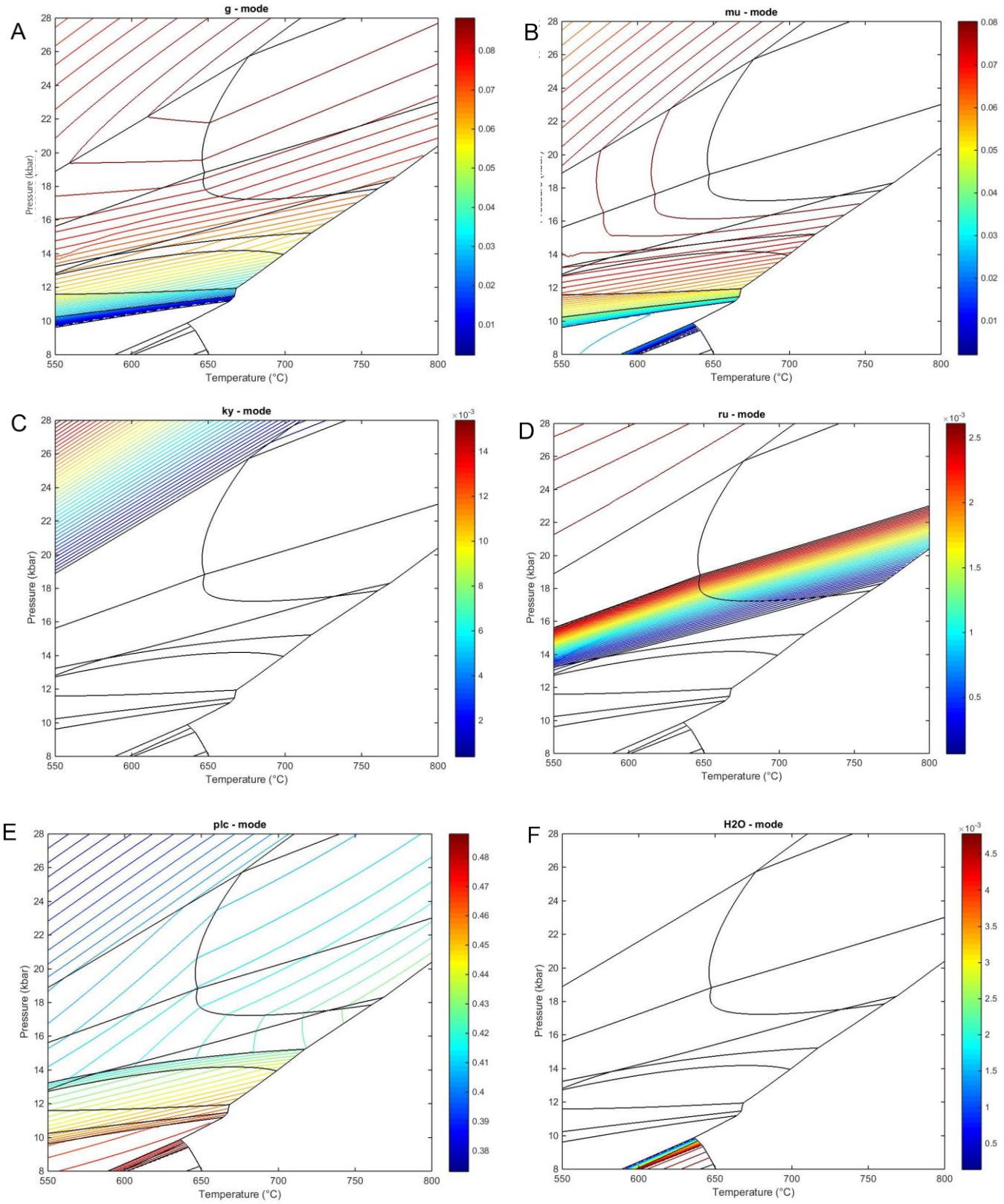

TCInvestigator outputs for felsic garnet-bearing gneiss WGC2019J-17A, showing (a) garnet mode, (b) muscovite mode, (c) kyanite mode, (d) rutile mode, (e) plagioclase mode and (f) H2O modal content. Temperature (°C) is shown on the x axis; pressure (kbar) on the y axis; colour scale and modal proportions indicated to the right of each individual output.

APPENDIX 12: DENSITY CALCULATION

In the discussion, a brief mention is made of the possible density increase within the WGC as a result of bulk felsic orthogneiss to eclogite-facies mineral assemblages. The following Appendix aims to expand upon the methodology of this calculation.

THERMOCALC outputs mineral modes in a unit known as '1-atom-normalised' percentages, often abbreviated to mol%s for clarity (as in the text here). It is possible to convert these modes back to thin section percentages ('TS%') by multiplying them by their '1 atomised normalised modal volume', or 1V (equation 1). E.g. Almandine garnet has a molar volume of 11.525 and is made up 20 'atoms' ($Fe_3Al_2Si_3O_{12}$; 3+2+3+12=20). $1V = \frac{11.525}{20} = 0.57$

$$\text{Area\%} = \text{TS\%} = \frac{THERMOCALC\ Mode}{1V} \quad \ldots\ldots(1)$$

This is an equivalent of area%. To transform this into vol%, therefore, one must multiply by thin section thickness, which is assumed to be 30μm (30×10^{-6} m). While it is realistic to assume that thin section thickness would vary, this error is small enough to be considered negligible. (In addition, one could approximate vol% as area% given that the thin section thickness is so small; here, conversion is merely for completeness' sake; equation 2).

$$\text{Vol\%} = \text{area\%} \times 30\times10^{-6} \quad \ldots\ldots(2)$$

The estimation of THERMOCALC outputs is based on manual calculations, and as such is prone to error. As a result, the total original THERMOCALC modal outputs do not sum exactly to 100% (or 1, as is the case for these calculations). Therefore, the vol%'s are normalised by dividing the vol% by the sum of vol%'s (equation 3).

$$\text{Normalised vol\%} = \frac{vol\%\ mineral}{total\ vol\%\ of\ all\ minerals\ in\ sample} \quad \ldots\ldots(3)$$

These normalised vol%'s are then converted into weight (in g), by multiplying vol% by density (equation 4).

Weight (g) = vol% x ρ……...(4)

These are then converted into wt% by dividing the weight (g) by the total weight (g). For simplicity's sake, these calculations assume $1cm^3$ of rock, and densities are kept in gcm^{-3} (equation 5).

Wt% = $\frac{wt(g)}{total\ weight\ (g)}$……(5)

These wt%s (as decimal proportions, to avoid confusion) are then multiplied by the density of the mineral in question for each assemblage at 8-9kbar and 20-22kbar. Endmember densities, when chosen, were selected based on representative mineral chemistry and highest density endmembers to provide a *theoretical maximum* density increase. The amphiboles analysed in this study were hornblende and glaucophane rather than hastingite; the density of hastingite was selected on greatest density rather than geochemistry. Note that it is the sum of all of these that gives the composite theoretical density of $1cm^3$ of rock at these conditions (equation 6).

Total density of $1cm^3$ rock = $\sum(mineral\ density)x\ (wt\%\ mineral, as\ proportion)$……(6)

The total % density increase as a result of these mineral transformations can then be calculated by dividing the density at 8-9kbar by the density at 20-22kbar, multiplying by 100% (equation 7), and subtracting this number from 100%.

Density increase = 100% - ($\frac{Density\ at\ 8-9kbar}{Density\ at\ 20-22kbar}$ x 100) =100% - ($\frac{2.66}{2.90}$ x 100) = 100% - 92% = 8%.....(7)

MINERAL	Plagioclase	Quartz	K-feldspar	Biotite	Water	Epidote	Ilmenite	TOTAL	SI UNITS (kg/m^3)
1V	0.78	0.76	0.84	0.70	0.49	0.63	0.63		
ENDMEMBER	High-temperature Albite		Microcline	Annite					
TC Mode (8-9kbar)	0.49	0.30	0.14	0.06	0.00	0.00	0.00	1.00	
Percentage TS (i.e. area%; TC Mode/1V)	0.63	0.40	0.17	0.08	0.01	0.01	0.01	1.30	
Vol % (i.e. area%*30μm)	1.88E-05	1.19E-05	5.14E-06	2.47E-06	2.47E-07	1.56E-07	1.89E-07	3.89E-05	
Normalised vol%	0.48	0.31	0.13	0.06	0.01	0.00	0.00	1.00	
Density	2.60	2.62	2.56	3.17	1.00	3.38	4.72		
Weight (g) (normalised vol% * density)	1.26	0.80	0.34	0.20	0.01	0.01	0.02	2.64	
wt% (wt / total weight)	0.48	0.30	0.13	0.08	0.00	0.01	0.01	1.00	
Density of $1cm^3$ of rock (wt% mineral * mineral density in gcm^{-3})	1.24	0.79	0.33	0.24	0.00	0.02	0.04	2.66	2662.94

MINERAL	Garnet	Plagioclase	Quartz	Muscovite	Hornblende	Rutile	K-feldspar	TOTAL	SI UNITS (kg/m^3)
1V	0.58	0.78	0.76	0.67	0.65	0.63	0.84		
ENDMEMBER	Almandine	High-temperature Albite			Hastingite		Microcline		
TC Mode (20-22kbar)	0.08	0.41	0.30	0.08	0.01	0.00	0.13	1.01	
Percentage TS (i.e. area%; TC Mode/1V)	0.14	0.53	0.40	0.12	0.02	0.00	0.15	1.35	
Vol % (i.e. area%*30µm)	4.16E-06	1.58E-05	1.19E-05	3.58E-06	4.63E-07	4.78E-08	4.52E-06	4.05E-05	
Normalised vol%	0.10	0.39	0.29	0.09	0.01	0.00	0.11	1.00	
Density	4.32	2.60000	2.62000	2.82	3.07	4.25	2.56000		
Weight (g) (normalised vol% * density)	0.44	1.02	0.77	0.25	0.04	0.01	0.29	2.81	
wt% (wt / total weight)	0.16	0.36	0.27	0.09	0.01	0.00	0.10	1.00	
Density of $1cm^3$ of rock (wt% mineral * mineral density in gcm^{-3})	0.68	0.94	0.72	0.25	0.04	0.01	0.26	2.90	2902.21
Density increase								8.24	